BIO-INSPIRED MEMS AQUATIC FLOW SENSOR ARRAYS

Nima Izadi

Promotiecommissie:

Voorzitter en Secretaris:

prof. dr. M. C. Elwenspoek	Universiteit Twente

Promotor:

prof. dr. ir. G. J. M. Krijnen	Universiteit Twente

Leden:

prof. dr. ir. Albert van den Berg	Universiteit Twente
prof. dr. Paddy French	Technische Universiteit Delft
prof. C. Liu	Northwestern University
dr. Joachim Mogdans	Universität Bonn
dr. Michel Versluis	Universiteit Twente
dr. ir. H. V. Jansen	Universiteit Twente

The research described in this thesis was carried out at the Transducer Science and Technology Group of the MESA$^+$ research institute, University of Twente, The Netherlands. It has been financially supported by the Future and Emergent Technologies arm of the IST Programme under the Customized Intelligent Life-Inspired Arrays (CILIA) project and by the BioEARS Vici grant of the Dutch Technology Foundation (STW/NWO).

Cover design by Anna Gharibi
Printed by Wöhrmann Print Service, Zutphen, The Netherlands
©N. Izadi, Enschede, The Netherlands, 2011

DOI: 10.3990/1.9789036531405
ISBN: 978-90-365-3140-5

BIO-INSPIRED MEMS AQUATIC FLOW SENSOR ARRAYS

PROEFSCHRIFT

ter verkrijging van
de graad van doctor aan de Universiteit Twente,
op gezag van de rector magnificus,
prof. dr. H. Brinksma,
volgens besluit van het College voor Promoties
in het openbaar te verdedigen
op vrijdag 7 januari 2011 om 16:45 uur

door

Nima Izadi
geboren op 29 augustus 1981
te Shiraz, Iran

Dit proefschrift is goedgekeurd door de promotor,

prof. dr. ir. G. J. M. Krijnen

…so here,
all of this,
to your smile.

Table of Contents

1
Prelude

When it all began…

1.1 Biological Sensors

Appropriate responses to internal and external conditions are the essence of animals' survival. Naturally, the awareness of existing conditions and more precisely the detection of a change, whatever minute, in the environment is, therefore, of utmost importance. Animals collect the necessary information from their environment using their sensory systems. Sensory systems transduce the external energy of stimuli into physiological signals which are carried by the nervous system. Animals' reaction to the relevant changes in their environment is, therefore, based on information encoded in these neuronal signals through their sensory systems.

In many sensory systems, for example ears, sensory organs collect the energy that is transmitted through the medium, the stimulus, and deliver it to the neuronal receptors[1]. The physical structure of these sensory organs and their coupling to the sensory neurons play important roles in filtering relevant information. The "detection threshold" is defined as the minimum energy[2] which can generate neuronal activity when delivered to a sensory organ. It determines the smallest fluctuation that can be sensed and, therefore, is an important property of a sensory system. For example, the detection threshold of cricket mechanoreceptors has proved to border the thermal noise limit [1]. Nature, however, does not stop here. Many sensory systems in members of the animal kingdom are composed of tens to thousands of individual sensory organs. Why does nature provide an animal with such an abundance of sensory units while a single organ provides such fidelity?

One reason of this high level of redundancy could be to provide auxiliary units which ensure continuous operation of the sensory system (robustness), even when some of the sensory organs malfunction (e.g. due to physical damage). On the other hand, there are plenty of uncorrelated sources of noise in nature the power level of which is much higher than the thermal noise level. It is, therefore, important for an animal to detect a relevant stimulus against such background noise as well. The signal to noise (SNR) ratio of a sensory system is improved when correlative input from similar but independent receptors is averaged which reduces some of the uncorrelated noise. Moreover, on top of the medium-structure and structure-neuron transfer

[1] In some cases, e.g. tactile sensing, the information does not transmit through a medium but is directly received by the sensory organs.
[2] The detection threshold is usually expressed in terms of stimulus' unit rather than in terms of energy.

functions of individual sensory organs, the functionality of a sensory system is further determined by the collective properties of the array. The number, spatial distribution and variation of important structural parameters affect the bandwidth, sensitivity and overall the dynamic response of a sensory system. In addition, the localisation of a source, if not more vital, is as important as the recognition of fluctuations. This function, however, can only evolve from a sensory array.

1.1.1 Flow: Sense it? Hear it?

Despite the great diversity in morphology and the detailed characteristics of the transfer function, two categories of sensory systems specialised to sense medium motion are distinguished: those that are sensitive to pressure variations and those that are sensitive to fluid displacements [2]. The sensation of sound pressure is commonly referred to as hearing and the relevant sensory system is called ear. The sensory organs of a pressure sensitive system usually have membrane shapes which deform due to the pressure difference across them. On the other hand, natural organs for detecting the fluid motion tend to be hair-like, small and, therefore, minimally invasive structures. The relevant biological wavelengths are much larger than the diameter of these structures and, therefore, the pressure gradients on the scale of these structures are negligible. It is, however, the frictional contact with the medium that causes fluid particles to drag these hairs along and displace them (i.e. viscous drag).

The energy that a flow source emits spreads over a certain range and frequencies. In chapter two, it is discussed how this distribution depends on the size of the source and its frequency. In general, a source can efficiently generate far field pressure waves only at wavelengths smaller than one third of its physical length scale. At larger wavelengths, the energy is more concentrated in the near field in which the particle velocity is dominant. Therefore, as there is much biologically relevant information in the lower part of the frequency spectrum (let say 0 to 100 Hz), the ability to sense the particle velocity in this regime is important to many animals. Another influential factor is the range over which the stimulus is detected. Viewing an animal as a source, particle velocity is dominant only at short distances, let say one body length. Therefore, particle velocity detection is less important for larger animals (which can effectively generate low frequency pressure waves) bearing in mind that the length scale of their preys and predators is also usually larger.

1.1.2 Hairs

A "hair" is a defining characteristic of mammals. They are used to regulate the body temperature, for camouflage, protection and, in some cases, as a signal to others. It is also common to talk about hairs on the exoskeleton of arthropods (like insects and spiders or crustaceans). However, in strict scientific terms, these are actually bristles. In mammals and some other animals there are specialized hairs called "Vibrissae" which are usually employed for tactile sensation (e.g. whiskers found in rodents and cats). In this case, the shaft of the "sensory hair" is innervated by one or several sensory cells which end at its base [3, 4].

On the other hand, hair-like structures, which provide flow sensory functions, are ubiquitous in arthropods [5]. These so-called "filiform hairs" consist of hair-like shafts suspended in the exoskeleton and are coupled to the neurons. The minute hair deflections due to flow fluctuations are transduced into electro-chemical neuronal pulses. A Cricket, for example, possesses two abdominal appendages on which there are hundreds of filiform hairs with various structural properties (e.g. length and diameter). The cumulative response of these sensory arrays enables the cricket to detect flow-borne information. Particularly when the fluctuation pattern is recognised as that of an approaching predator, the escape mechanism of the animal is triggered [6].

Vertebrates posses another type of sensory organ which has sensory receptors called "hair cells". Hair cells are found in the inner ear of mammals or the lateral line of fish [7]. The morphology and function of the hair cells is discussed more in the next chapter. A hair cell is a typical sensory cell and is called hair cell because of the tubular extensions on the upper cell surface. Like the filiform hair, the peripheral structure couples the medium motion to these cells, which translate the motion to neuronal pulses. In addition to efficient coupling to the medium (e.g. by impedance matching), these peripheral structures protect the cells from the external environment.

1.2 Engineered Flow Sensors

Is particle velocity detection valuable in engineering? The answer is certainly! It has been mentioned and will be shown in the next chapter that particle velocity is dominant close to the source. Since the fluid behaves as incompressible at this scale, pressure variations are less significant than in far field. Another important feature of particle velocity is its directionality. Pressure is a scalar quantity but velocity is a vector.

Therefore, particle velocity provides information about the direction of propagation, in other words it makes source localisation possible[3]. In addition, combined with pressure sensing, it can provide sound intensity measurement which is used to quantify the generated sound power of a source; an important feature in noise control measurements [8]. Moreover, if the acoustic impedance of the medium is low, it is the particle velocity that dominates and the measurement of pressure may not be possible.

To the author's knowledge, Microflown® [9], a two or three wire thermal flow sensor, is the only commercially available MEMS device which directly measures particle velocity. Microflown® consists of long and thin platinum wires which heat up above 300 °C during operation. Fluid flow changes the temperature distribution around these wires asymmetrically. The electrical resistance of the wires is a function of the temperature. Therefore, temperature changes result in resistance changes which are proportional to the speed of the fluid flow.

Why, despite its proven usefulness, there is only one example of particle velocity measuring devices in engineering[4]? The obvious answer is the ease of pressure measurements in terms of fabrication, characterisation and packaging of a pressure sensor. There are many pressure sensors which measure the deflection of a membrane due to the pressure gradient across it using different methods (e.g. piezoresistive, capacitive, optical) [10, 11]. However, new applications which require in situ measurement of particle velocity emerge with advancements in technology. The pressure gradient has to be measured at distances larger than the characteristic length of the source since at close distances flow has almost incompressible nature and the change in pressure is negligible (see chapter 2). In contrast, particle velocity measurements can be done very close to the source. In addition, the characterisation of sound sources without providing special laboratory environments is a strong driving force for the development of particle velocity sensors [8].

What principle should be used to measure particle velocity? Heat conduction, Doppler effect, pressure difference or, as you may already expect, drag induced motion

[3] One can obtain information about directionality by measuring pressure gradients using arrays of at least two pressure sensors. However, at low frequencies the wavelengths are large (especially in water, e.g. at 10 Hz the wavelength is about 150 m) and, therefore, the distance between the two pressure sensors should be large enough to yield a measurable phase difference. On the other hand, one particle velocity sensor, whatever small, can provide directionality information.

[4] Particle velocity is usually measured indirectly using two pressure microphones (see the previous footnote).

on hair-like structures? And does this choice depend on the medium, i.e. air or water? The pressure difference, having its own merits, may be ruled out for the reasons discussed above for our purpose. Devices based on the Doppler effect are usually big, expensive and difficult to maintain. They are especially limiting when sensory arrays are desired. Heat conduction is limited by the heat capacity of the measuring element (and the medium) and these devices are not energy efficient when continuous operation is needed. Hair-based sensors, on the other hand, are passive, consume little power and are potentially small, robust and cost effective. Although their dynamic range and frequency response are limited, their desired or intended operational range is at low frequencies and low flow velocities.

The remaining questions are: whether nature provides the best engineering solution for this specific situation? And are our engineering interests along the direction in which evolution drives the sensory systems developments?

1.3 CILIA

"CILIA" stands for "Customised Intelligent Life-Inspired Arrays" and is a European funded project by the Future and Emergent Technologies arm of the IST Programme. In this project the morphology and functionality of hair-like mechano-receptors arrays are investigated. The sensory organs in three different media, air, water and fluid-filled compartments coupled to air, were chosen: the filiform hairs of crickets, the lateral line of fish and the bat's ear respectively.

The objectives are 1) to identify the common principles underlying each sensory organ which justify their widespread use in nature, 2) to pinpoint the transduction schemes resulting from distinguished physical structures of the peripheral systems 3) to understand the way the stimulus information is coded in the receptor's neuronal signal, 4) to investigate the effect of the properties of the sensory array in sensory processing and 5) to make the obtained information available for the design of engineered systems.

A multidisciplinary approach is needed to address all the objectives. In a biological context, the respective environments and physical functioning of each organism and the resulting animal behaviour in response to artificial and natural stimuli are studied. In addition, the neuronal architecture is analysed and the processing of stimuli by nervous structures is investigated through modelling. The observed spatiotemporal

neuronal activities are to be used to model the response of the animal. The question is how the information, as coded in the action potentials, is used by the nervous system(s) to detect sources and determine their direction and maybe even the distance to the sources. On the sensory level the information from characterisation of single receptor and array morphology is exploited to model the fluid-structure interactions and properties of the mechanical response of the receptors, both individually and of the entire sensory system. The combined knowledge of peripheral filtering and central processing paves the way for integrated models to describe the collective response.

Inspired by the distinguished functionality of these sensory systems in terms of robustness and sensitivity, Micro-Electro-Mechanical Systems technology has been employed to create artificial flow sensors resembling the studied mechanoreceptor organs. As their biological role model, these flow sensors provide a distributed sensing mechanism from which spatially and temporally rich data is expected.

The partners of the project, alphabetically arranged, were

• Institute of Bio- & Nanosystems – Bioelectronics Forschungszentrum Jülich GmbH	Julich-Germany
• Institut de Recherche sur la Biologie de l'Insecte Faculté des Sciences et Techniques, Université de Tours	Tours-France
• Maersk Mc-Kinney Moller Institute for Production Technology University of Southern Denmark	Odense-Denmark
• School of Physics and Microelectronics Shandong University	Shandong-China
• Active Perception Lab Universiteit Antwerpen	Antwerp-Belgium
• Institut für Zoologie, Abt. für Vergleichende Neurobiologie Universität Bonn	Bonn-Germany
• Centre for Biomimetics University of Reading	Reading-UK
• Transducers Science and Technology group Universiteit Twente	Enschede-Netherlands

The last task, realization of biomimetic mechanosensors, is carried out by the chair of Transducer Science and Technology, University of Twente. Two distinct

implementations of flow sensors are investigated: the hair-based sensors for operation in air and water, which respectively resemble the filiform hairs on the cerci of crickets and neuromasts of fish.

1.4 This Thesis

This thesis describes the attempt to design and fabricate flow sensors based on the function of sensory organs of the lateral line of fish. The driving force is the sensitivity and robustness of these sensory organs and the wide range of engineering applications that can benefit from direct velocity measurement with such accuracy. Three different schemes are proposed and the designs and fabrication procedures which provide the platform for realisation of the functional sensors are described.

Chapter two shortly introduces the morphology and the importance of the lateral line of fish. The physical nature and range of the relevant stimuli and then the concept of Biomimetics is reviewed. Some examples of the use of Micro-Electro-Mechanical Systems (MEMS) technology in biomimetic practice are briefly presented. This is followed by the presentation of the state of the art engineered flow sensors inspired by nature or based on drag induced torque. The description and justification of the approach that is taken concludes the chapter.

Chapter three introduces different designs of aquatic capacitive flow sensors. Detailed analysis is done to extract the design parameters which influence the characteristics of the sensor and can therefore be used to tune the performance. A qualitative comparison between different designs is provided at the end which highlights the merits and drawbacks of each scheme.

Chapter four includes the fabrication procedures of the proposed capacitive flow sensors. Each fabrication step has been characterised and detailed to result in an optimised procedure. The main objective is to devise a robust and high yield process. The general characteristics, drawbacks and complexity of the steps are compared to give an evaluation of the process integrity.

In the next chapter details of SU-8 processing are presented. SU-8 plays an important role in all the schemes and its process requires careful optimisation. This is followed by the fabrication of passive canal embedded hair-like structures from SU-8 on glass wafers. These structures were intended to be used for Particle Image Velocimetry (PIV) measurements. The differences between structural and thermal

properties of glass and silicon results in considerable variation of SU-8 process parameters. These differences were investigated and used to adapt the fabrication process and the design.

Chapter six presents the results from the measurements carried out in air. These results help to understand the mechanical and electrical behaviour of the sensor before its immersion in water. Mechanical characterisation using laser vibrometer as well as electrical measurement are presented. At the time of writing the characterisation of the sensors in water has not been started.

Chapter seven includes the conclusion and outlook. The long mathematical calculations are presented as appendices at the end of the thesis together with detailed fabrication process documents.

1.5 References

[1] T. Shimozawa*, et al.*, "Cricket Wind Receptors: Thermal Noise for the Highest Sensitivity Known," in *Sensors and sensing in biology and engineering*, F. G. Barth*, et al.*, Eds., ed Berlin: Springer-Verlag, 2003, pp. 145-157.

[2] L. C. Osborne, "Signal Processing in a Mechanosensory Array: Dynamics of Cricket Cercal Hairs," Ph.D. Dissertation, Biophysics, University of California at Berkeley, Berkeley, 1996.

[3] P. Myers*, et al.* (2006, June 26, 2010). *Hair*. Available: http://animaldiversity.org

[4] H. G. Cogger*, et al.*, *Encyclopedia of animals : mammals, birds, reptiles, amphibians*: Reader's Digest Association, 1994.

[5] E. Hallberg and B. S. Hansson, "Arthropod sensilla: Morphology and phylogenetic considerations," *Microscopy Research and Technique,* vol. 47, pp. 428-439, 1999.

[6] T. Shimozawa*, et al.*, "Structural scaling and functional design of the cercal wind-receptor hairs of cricket," *Journal of Comparative Physiology a-Sensory Neural and Behavioral Physiology,* vol. 183, pp. 171-186, Aug 1998.

[7] A. N. Popper, "Hair Cell Heterogeneity and Ultrasonic Hearing: Recent Advances in Understanding Fish Hearing," *Philosophical Transactions: Biological Sciences,* vol. 355, pp. 1277-1280, 2000.

[8] J. W. v. Honschoten, "Modelling and optimisation of the Microflown," Ph.D. Dissertation, University of Twente, Enschede, 2004.

[9] H.-E. de Bree*, et al.*, "Novel device measuring acoustical flows," 1995, pp. 536-539.

[10] N. Bilaniuk, "Optical microphone transduction techniques," *Applied Acoustics,* vol. 50, pp. 35-63, 1997.

[11] P. R. Scheeper*, et al.*, "A review of silicon microphones," *Sensors and Actuators A: Physical,* vol. 44, pp. 1-11, 1994.

2
Introduction

This chapter starts with a short introduction of the morphology and the importance of the lateral line of fish. The physical nature and range of stimuli are then reviewed. Afterwards, the concept of biomimetics with some examples using Micro-Electro-Mechanical Systems (MEMS) technology is briefly depicted. It follows by presentation of the state of the art engineered flow sensors inspired by nature or based on drag induced torque. The description of our approach concludes the chapter.

2.1 The Lateral Line of Fish

Aquatic environments have been the cradle of life since its appearance on this planet. Fish, the inhabitants of the vast oceans, have struggled 530 millions years of existence and adapted to their resourceful but venturesome surroundings. The need to perceive and locate prey and to escape from predators or in general to survive in a highly competitive situation has driven the living organisms to develop various sensory organs. Whereas more well-known sensory systems, like the visual system, have played their respective roles in sustaining life, fish and amphibians are additionally gifted with a sensory organ called lateral line.

In 1850, Leydig [1] was the first who observed and described the system of lateral line and its function as water flow detector. But only more than a century later various researchers started to study and publish the actual functions of this system. The lateral line system enables fish to use the velocity profile of the surrounding water to construct a 3D map of their immediate environment on which their ability to school, localise prey or predators, to avoid obstacles and rheotaxes greatly depends [2-7]. In some species like the blind cave fish, which lacks visual capabilities, fish survival predominantly depends upon this system [8].

2.1.1 Structure of the Lateral Line

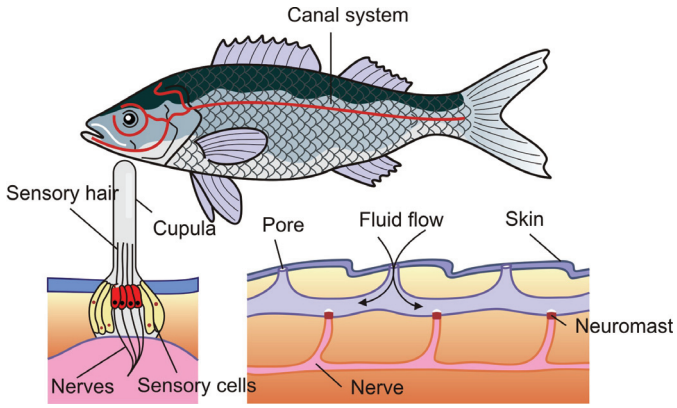

Figure 2.1 *The schematic presentation of lateral line of fish*

The lateral line system, consists of mechanoreceptive hair cells covered by a jelly like cupula which together are referred to as neuromast (see Figure 2.1). Neuromasts are either located on top of the skin at the bottom of a visible pit or groove (superficial neuromasts) or in the lateral line canals along the body (canal

neuromasts) [9]. The displacement of the cupula due to fluid motion couples to the stereovilli of the hair cells and changes the firing rate of the afferent neurons [10]. Using this system, fish are able to perceive cupula displacement as small as a few nanometers which corresponds to a few microns per second fluid velocity [11].

The spatial distribution and morphology of the lateral line organ vary significantly among different species. This diversity is reflected in the distance range of the lateral line system, the extent of the receptive field, frequency response properties and the component of water motion that is encoded [12].

Superficial neuromasts are generally smaller and contain fewer hair cells than canal neuromasts [13]. It is known that superficial neuromasts are sensitive to the fluid flow velocity. On the other hand, canal neuromasts, which are particularly developed in species that swim continuously or live in running or tidal waters, are acceleration sensitive[1] [14, 15]. Canal neuromasts are most commonly distributed on the head and along the trunk of the fish [16].

2.1.2 Hair Cells

Hair cells are the basic biological transducers in auditory and vestibular systems (sense of balance) of all vertebrates. A typical hair cell consists of a body and a bundle of slender hair-like organelles protruding from the apical surface of the body as shown in Figure 2.2. The hair bundle consists of stereocilia arranged in a staircase fashion and a single true cilium, the kinocilium, which is the biggest structure in the bundle.

The deflection of the bundle due to mechanical displacement of the medium opens the mechano-transducer channels at the tip of the structures when the deflection is toward the kinocilium. When these transducer channels open, the overall stiffness of the bundle reduces. Moreover, it triggers the hair cells to release excitatory neurotransmitters at the site of a neural innervation [17]. Moreover, the hair cells are inhibited when the deflection is away from the kinocilium. This makes the hair cells directional sensitive.

The hair cells of fish are morphologically quite similar to those found in the inner ear of higher vertebrates [18]. The specific functionality is determined by the peripheral structures. The function of lateral line, therefore, depends on the mechanics

[1] Canal neuromasts are sensitive to water flow velocity inside the canal. The flow velocity inside a canal, however, depends on external fluid flow acceleration.

of cupulae which, as we will see, are well described by both inertia and viscous forces produced by fluid flow passing it. In case of canal neuromasts, additional filtering imposed by the canal further influences the cupular frequency response.

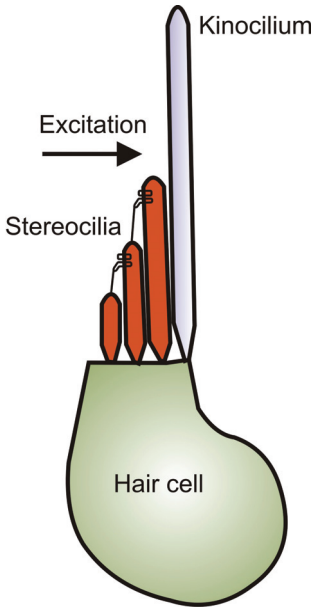

Figure 2.2 *Schematic of a hair cell*

The sense of lateral line system, which has been referred to as feel or touch at a distance, is mainly functional at frequencies from DC up to at most several hundred hertz [9, 11, 19] and is a complement to the inner-ear organ. The combination of dynamic responses of superficial and canal neuromasts (considering the canal filtering properties), in conjunction with the frequency spectra of the amplitude of natural stimuli ensures a fairly constant detectability of the system within the dynamic range of the mechanoreceptor hair cells[2] [15].

2.1.3 The Nature of Stimulus

Water, as other fluids, is an elastic medium. Therefore, any disturbance in water propagates away from its origin as a wave. The movement of the bodies immersed in a fluid exerts force on the fluid particles. This displacement generates a pressure gradient

[2] As it has been stated in [15] the neurophysiological measurements are usually done with a stimulus of constant amplitude regardless of oscillation frequency. The function of lateral line organ, however, should be seen in the context of relevant biological stimuli for which the available energy does depend on frequency. On the other hand, the sensitivity of lateral line has evolved to make sure that the detectability, the product of amplitude of stimulus by the sensitivity, is more or less frequency independent and within the dynamic range of the system.

that causes additional flow of the fluid particles which, in turn, generates a (slightly smaller) pressure gradient. The resulting longitudinal wave propagates from the source at a certain speed. When this wave is composed of frequencies within the hearing range and is of a level sufficiently high to be heard, it is called "sound". Humans can sense (hear) the acoustic waves having frequencies in between 20 Hz to 20 kHz. The inner ear of fish responds to frequencies above several hundred hertz up to several kilo hertz [20] and, in some cases, up to 180 kHz [21, 22]. However, the lateral line, as mentioned before, is a complement to this sensory organ covering the frequency range of DC to up to several hundred hertz. Although, to be exact, lateral line actually has an intermediate function between touch and hearing [23, 24].

A flow source can be represented by a series of multipole sources when its dimensions are small compared to the wavelength of the wave it produces. This is similar to representation of a function by a Fourier series. The prototype of an acoustic monopole is a pulsating sphere. Thus, the monopole moment results from changes in the volume of the source. A dipole is represented by a vibrating rigid sphere which has a constant volume. A dipole moment, therefore, results from displacement of the centre of mass. Higher order moments (quadrupole, octupole and so forth) result from deformations of the source or deviations from a spherical shape. Although the higher moments are mathematically necessary to fully attain the field description, physically their flow field falls with increasing powers of the distance from the source (see below). Therefore, the importance of higher order moments decreases rapidly with increasing distance from the source and in practice biological relevant hydrodynamic fields are often approximated by that of a dipole [15].

In aquatic environments, many biological relevant sources of fluctuation are related to the movement of the whole body rather than the change in the volume. Therefore, monopole type sources are not as ubiquitous as dipole sources. In the absence of monopole sources, the hydrodynamic field is dominated by dipole moments. The velocity potential[3] of a small vibrating sphere of radius a when $k \cdot a \ll 1$ in a compressible, inviscid, irrotational fluid is given by [25]

[3] Somehow a mathematical concept, velocity potential is defined for an irrotational flow (i.e. when the curl of the velocity field is zero) so that its gradient is equal to the velocity field. When the flow is irrotational and incompressible (i.e. the divergence of the velocity field is also zero), it follows that velocity potential satisfies the Laplace equation.

$$\Phi = \frac{a^3}{2r^2} \cdot (1 + j \cdot k \cdot r) \cdot U_0 \cdot \cos(\theta) \cdot e^{j \cdot (\omega \cdot t - k \cdot r)} \tag{2.1}$$

where $U = U_0 \cdot e^{j\omega \cdot t}$ is the vibration velocity, $k = 2\pi/\lambda$ is the wave number, r is the radial distance and θ is the angular coordinate. It is clear that at very small distances, $k \cdot r \ll 1$, this equation reduces to

$$\Phi = \frac{a^3}{2r^2} \cdot U_0 \cdot \cos(\theta) \cdot e^{j \cdot \omega \cdot t} \tag{2.2}$$

which is the resulting velocity potential of a dipole in an incompressible fluid[4]. This shows that the flow near a dipole source, the so called near-field region, exhibits incompressible nature.

The acoustic pressure, using linearised[5] Euler's equation[6] and neglecting the gravitational forces [26], is therefore given by

$$p = -\rho \cdot \frac{\partial \Phi}{\partial t} = \frac{\rho \cdot c \cdot (k \cdot a)^3}{2} \cdot \left(\frac{1}{k \cdot r} - \frac{j}{(k \cdot r)^2} \right) \cdot U_0 \cdot \cos(\theta) \cdot e^{j \cdot (\omega \cdot t - k \cdot r)} \tag{2.3}$$

In addition, the radial and tangential particle velocities can be obtained since by definition

$$\vec{V} = \vec{\nabla} \varphi \tag{2.4}$$

therefore

$$v_r = \frac{\partial \Phi}{\partial r} = \frac{(k \cdot a)^3}{2} \cdot \left(\frac{1}{k \cdot r} - \frac{2 \cdot j}{(k \cdot r)^2} - \frac{2}{(k \cdot r)^3} \right) \cdot U_0 \cdot \cos(\theta) \cdot e^{j \cdot (\omega \cdot t - k \cdot r)} \tag{2.5}$$

and

$$v_\theta = \frac{1}{r} \frac{\partial \Phi}{\partial \theta} = -\frac{(k \cdot a)^3}{2} \cdot \left(\frac{j}{(k \cdot r)^2} + \frac{1}{(k \cdot r)^3} \right) \cdot U_0 \cdot \sin(\theta) \cdot e^{j \cdot (\omega \cdot t - k \cdot r)} \tag{2.6}$$

We shall first examine the pressure given by (2.3). It is clear that for $k \cdot r \gg 1$ the pressure is proportional to k^2 and r^{-1}. This part is identified as the pressure of the propagating wave. On the other hand, when $k \cdot r \ll 1$, the pressure is proportional to k and r^{-2}. Since both parts depend on k, the amplitude of the pressure substantially decreases at lower frequencies.

---

[4] This is clear since only the instantaneous value of velocity appears in this equation. This means a disturbance propagates with an infinite speed which is a consequence of incompressibility.

[5] Considering the amplitude of vibration is small compared to the wave length, which is justified in most cases.

[6] Euler's equation is derived from the conservation of momentum and is basically the approximate Navier-Stokes equation for inviscid fluids.

Now consider the radial particle velocity as given by (2.5). Figure 2.3 shows the normalised amplitude of each of the three terms in (2.5). The first term is proportional to reciprocal of the distance. It depends on k^2, dominates at large distances from the source and, therefore, represents the particle velocity in the propagating wave (compare with the first term of (2.3)). Note that this term has 180° phase shift compared to the source velocity. It is indicated by blue dash-dot lines in Figure 2.3 for 1 and 500 Hz.

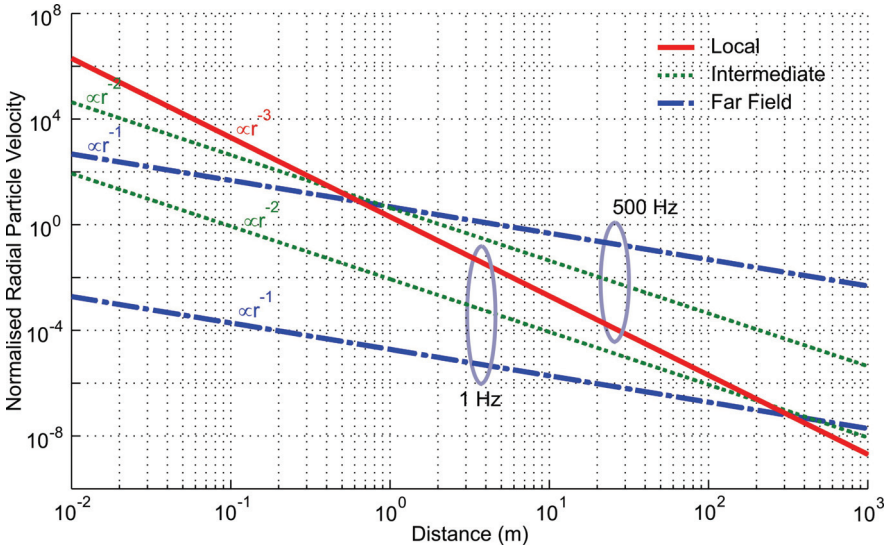

Figure 2.3 *The amplitude of the three components of the radial velocity. All quantities are normalised by* $a^3 \cdot \cos(\theta) \cdot U_0$.

The last term, however, is proportional to r^{-3} and becomes important at close distances to the source especially at lower frequencies (red solid line in the figure). It is in phase with the velocity of the source and independent of the frequency. The region in which this term dominates the total particle velocity is called the near field in comparison to the far field in which the particle velocity of the propagating wave (the first term of (2.5)) overweighs. The flow within this region is normally called the *local flow*. The middle term in (2.5) represents the velocity of the so-called *intermediate flow* (the thin dotted green line). This component is 90° out of phase with the source velocity and is not negligible in the region between far field and near field[7].

[7] Although the equality of the amplitudes of the first and last term in (2.5) has been put as the criteria for far-field and near-field distinction (i.e. $k \cdot r = \sqrt{2}$), the near field is formally defined as the region within which the local or intermediate flows are not negligible.

Similarly, the first term in (2.6) gives the tangential component of velocity of the intermediate flow and the second term that of the local flow. Note that 1) at low frequencies, specially in water, the $k \cdot a \ll 1$ criteria mostly holds, 2) the particle velocity in the propagating wave lacks the tangential component (both terms of (2.6) vanish at large $k \cdot r$) and is only radial, 3) the amplitude of the local flow velocity is independent of the frequency, and 4) as it has been said before, the amplitude of the local pressure scales with k and therefore it is less dominant at low frequencies.

The available stimulus energy for a mechanoreceptor, following (2.3) to (2.6), depends on the size of the source (a), the frequency of the generated wave ($\omega = k \cdot c$) and the distance to the source (r). The larger the size of the animal, the less important is the near field perception. This is because due to their bigger size 1) the distances over which they need to detect the flow is larger than the wavelength of the sound in relevant frequencies, and 2) the minimum frequency above which they can efficiently radiate far field sound is lower ($f_{min} = c/3L$, where L is the typical length scale of the source). In water, however, the speed of sound is roughly five times higher than in air. Therefore, the distance over which the near field particle velocity dominates stretches five times (more than the distance in air for identical source strength and frequency) and the scale of animals which benefit from near field particle velocity is, with the same order, larger. Moreover, although the far field becomes more important at higher frequencies, the propagation loss increases. Consequently, the ability to discern particle velocity is more vital for marine animals especially at low frequencies.

Numerous studies have confirmed that the functionality of the lateral line organ is restricted to low frequencies [27, 28]. The importance of the specialised function of the lateral line organ in detecting the local flow is further illuminated by the frequency independence of the local flow velocity. Consider a quietly gliding fish at constant velocity; at near zero frequency, i.e. small k, the pressure of the propagating wave, given by (2.3), and all frequency dependent terms of (2.5) and (2.6) vanish. Only the last term in each of the velocity equations, which are associated with local flow, preserve. Therefore, at short distances, say few body lengths [29], the ability to perceive low frequency fluctuations can be a matter of survival.

2.2 Biomimetics

The concept of biomimicry, the application of biological methods and systems found in nature to the design of engineering systems, is very old. However only in recent years the growing need for more robust and more sensitive sensors has motivated engineers and scientists to once again look at biological systems [30]. The evolutionary path of nature is to achieve high functionality at minimum cost, both in materials and energy, as are often the engineering objectives.

The achieved advancements in modern technology have specially paved the way for successful attempts to fabricate artificial counterparts from the blueprints of nature. Micro-Electro-Mechanical Systems (MEMS) technology is a capable platform for realization of small, fast, sensitive and cheap sensory systems. It offers numerous advantages over conventional precision engineering, most notably batch fabrication and high spatial resolution. The desired result is an artefact which grants an invaluable tool for further exploitation of the principles learned from nature.

Biomimetic aquatic flow sensors inspired by the lateral line system are useful in underwater robotics for hydrodynamic imaging of complex and noisy environments to provide vital information for surveillance and navigation. The speculative ability to manoeuvre in murky or dark water environments, especially the detection of objects in a short range and a silent environment, has strongly driven the research in this area. The goal is to provide Underwater Autonomous Vehicles (UAV) a passive detection system which operates silently as opposed to an active sonar system [31, 32].

There are many examples of bio-inspired designs in engineering [33]. Flow sensor [34], Gyroscope [35], strain sensor [36], infrared sensor [37, 38], vision [39], Olfactory system [40], Acoustic microphone [41], Flapping Wing Micro Air vehicles (MAV) [42] and robotic systems [43, 44] are few examples of the application of biomimicry in current engineering practice which use MEMS technology as the fabrication platform.

The function of the lateral line for source localization comes from its distinguished array configuration feature. Fabrication of an array consisting of hundreds of similar structures is a cumbersome undertaking using conventional precision fabrication methods. MEMS technology on the other hand provides a platform for the fabrication of dense and repetitive structures. The intrinsic batch

fabrication capability and high spatial resolution can potentially result in high performance and cost effective products.

2.3 Previous Works

Manmade aquatic flow sensors have been built based on many sensing principles including heat conduction[8] [45], Doppler effect[9] [46] and pressure difference[10] [47], but they are still scarcely utilized for underwater applications. Small, robust, cheap and low energy consuming sensors are needed in marine environments for numerous applications [48]. In recent years, however, benefiting from the advancement in technology and the knowledge and inspiration gained from nature, engineers have started to develop biomimetic flow-sensors aiming at a high level of versatility, robustness and sensitivity.

Before we start to review previous works that have been done on this subject, we explain the piezoresistive readout mechanism and cantilever structures that are essential in the following technological overview.

Piezoresistivity [49] is a property of certain materials which change their electrical resistance when being subject to tensile or compressive stresses. The effect is small in metal conductors but easily observable and exploitable in semiconductors such as silicon. It is a function of doping, temperature, crystallographic orientation, etc. Piezoresistive readout is commonly used to measure the deflection of members, such as cantilevers (see below) and membranes. It is possible to deduce the magnitude of force on a cantilever using piezoresistive regions (strain gauges) at the base, where the maximum stress occurs, by measuring resistance changes. These strain gauges are usually arranged in a Wheatstone bridge configuration and the change in resistance is proportional to the strain exerted on them. This relation is formulated as

[8] Hot-wire anemometers measure fluid velocity by detecting temperature changes of heated wires due to heat convection forced by fluid flow. However their function is limited at low flow velocities due to their relative small sensitivity.

[9] Laser Doppler velocimeters point a monochromatic laser beam towards a target and collect the reflected radiation. Due to the Doppler effect, the change in wavelength of the reflected radiation is a function of the relative velocity of the targeted object. They are usually complicated devices and need reflective particles. Moreover, sensors based on acoustic transmission and detection of Doppler phase shift are generally large.

[10] Pressure distribution measurements can be used as an indirect way of flow velocity sensing. However, at low frequencies, especially in water, the pressure gradients are small and thus the information about the main stream is not accurately provided by this method.

$$\frac{\Delta R}{R} \propto \varepsilon \tag{2.7}$$

where R is the electrical resistance of the gauge, ΔR is the change in resistance and ε is the mechanical strain.

A cantilever is a beam that is fixed at one end and free at the other. Cantilevers at the micron-scale are made by micromachining and have a wide range of applications in science and technology such as in AFM (Atomic Force Microscopy) [50], chemical detection sensors [51, 52], RF (Radio Frequency) filters and resonators [53] to name a few. The basic principle of a cantilever-based sensor is to determine the magnitude of a load from the amount of the cantilever deflection. It can be shown [54] that for a cantilever subjected to a transverse load, the maximum strain is at the base (fixed end) and equals to

$$\varepsilon_{\max} = \frac{M \cdot c_1}{E \cdot I} \tag{2.8}$$

in which M is the magnitude of the developed moment at the base, E is the Young's modulus of elasticity, I is the second moment of area and c_1 is the distance from the neutral axis. For cantilevers made of an isotropic and homogeneous material $c_1 = t/2$ in which t is the thickness of the beam.

2.3.1 Sensors Based on Cantilevers

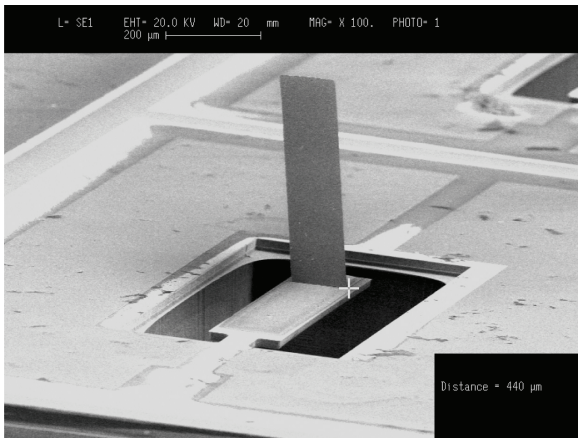

Figure 2.4 *SEM of a single device [55]*

Fan et al. [55] have realized a cantilever-based flow sensor with a piezoresistive readout mechanism. A PDMA[11] process [56] was utilized to obtain 820 μm long out-of-plane cantilevers from in-plane fabricated cantilever beams (see Figure 2.4). The fabrication starts with selectively doping the silicon substrate with boron to form strain gauges. A backside etching process in alkaline (KOH) solution determines the cantilever's thickness. Thereafter, lead wires, a copper sacrificial layer and a thin gold layer are deposited and patterned. Then Permalloy, which is necessary for the PDMA process, is electroplated. Subsequently, the cantilever is realized after an etching process on the front side. The sacrificial layer is removed in a wet etching process and using a magnetic field, the Permalloy structure is raised to a permanent upright position. At the end, in order to insulate the structure and the electrical conductors from water, a thin layer of parylene is deposited. The highest presented relative change of resistance, $\Delta R/R$, is 2.3×10^4 ppm at 1 m/s water flow speed.

The major advantage of this method is the monolithic fabrication process. According to authors, the robustness and compatibility of the device are of concern. The strength of the joint between out-of-plane and in-plane cantilevers is crucial but it was shown that it is possible to strengthen the joint and define the exact bending point by electroplating a thin layer of gold.

In another approach Chen et al. [57] employed the same PDMA principle and reported a polymer-based flow sensor shown in Figure 2.5. Their fabrication consists of successive metal and polymer deposition and patterning. The main difference is in the use of NiCr strain gauges on the base of polyimide film which forms the out-of-plane cantilever (600 to 1500 μm long). Low temperature processing (the highest process temperature reported is 350 °C) allows the use of a variety of substrates including flexible polymer materials. Chen et al. also have claimed that this process is more robust and efficient than using silicon bulk and surface micromachining. However, the strain gauge efficiency is considerably lower [58]. The sensor has been

[11] Plastic Deformation Magnetic Assembly (PDMA) is a technique for three-dimensional assembly of micro structures. Certain parts of the structure can plastically deform by applying external magnetic fields which interact with the magnetic material deposited on the micro structure. The resultant force brings the entire structure to a certain angle at which the developed stress can surpass the elastic limit of material and cause permanent deformation. PDMA is a non-contact, batch process but it is relatively difficult to accurately control the deformation angle of structures.

tested in air flow and the highest reported relative change of resistance, $\Delta R/R$, is 600 ppm at 10 m/s air flow speed.

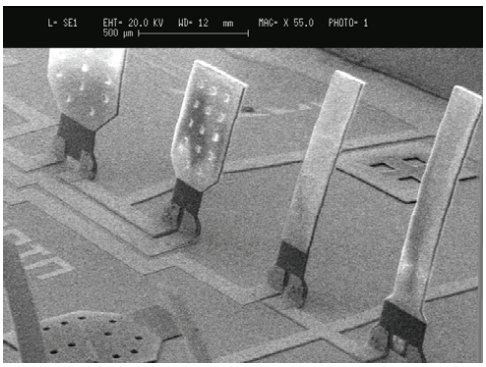

Figure 2.5 *fabricated polymer-based sensor [57]*

Yang et al. [59] have fabricated a cantilever-based flow sensor using SU-8[12] polymer to realize a 500 µm long cylindrical structure at the free end of a cantilever (see the SEM image in Figure 2.6). The reported detection threshold amplitude is 0.1 mm/s at 25 Hz using 2 Hz FFT (Fast Fourier Transform) bandwidth for measurements[13] [60]. The calculated resonance frequency is 1 kHz in water. The readout mechanism is the same as above i.e. piezoresistive. The fabrication process starts using Silicon On Isolator (SOI) wafers. Piezoresistive elements are realized with ion implantation. Subsequently, gold is deposited and patterned to form conductive wires and bond pads. This is followed by two consequent DRIE[14] steps, both on the front and backside of the wafer, to define the cantilever. Subsequently, SU-8 photoresist is spun and patterned to shape the hair-like extension and then the cantilever is released in BHF (Buffered Hydro-Fluoric acid) solution. The devices have been made in pairs oriented perpendicular to each other to provide flow measurement along two orthogonal axes. These sensors have a linear response to AC flow and the hair-like SU-8 structure can be deflected by up to 35° from vertical position without

[12] SU-8 is a photo-sensitive polymer used in MEMS technology. It can be spun with different thicknesses and is often used for fabrication of high aspect ratio structures. For more information about the properties and processing see the next two chapters on design and fabrication of hair-based capacitive sensors.
[13] Detection threshold is defined as the minimum detectable input. It depends on the properties of the sensor, the noise level and the measurement frequency resolution. Using a narrow FFT bandwidth (low measurement resolution) reduces the (Gaussian) noise power incurred in the measurement and, therefore, increases the signal to noise ratio which results in a lower detection threshold. However, it increases the detection time.
[14] Deep Reactive Ion Etching (DRIE) is a process to etch high aspect ratio structures in a silicon substrate.

degradation of performance. Using this sensor, Yang et al. have demonstrated a lateral line system capable of flow source localisation in a 3D domain [61].

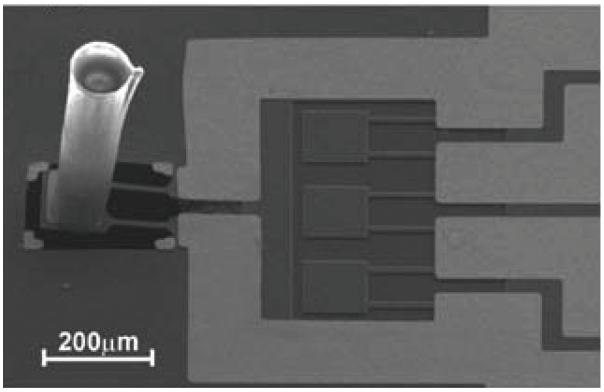

Figure 2.6 *SU-8 cylinder at the tip of a silicon cantilever [59]*

A 20 to 70 times increase in sensitivity[15] at frequencies between 10 to 110 Hz and a decrease in the detection threshold from 100 μm/s to 75 μm/s water flow speed of the above-mentioned sensor has been reported by Peleshanko et al. [62]. A water soluble Polyethylene Glycol (PEG) is dispensed on the SU-8 cylinder (the hair) and its immediate surrounding. Then UV-photo-polymerisation is carried out to cross link the polymer around the hair. After this, the sensor is put into water so that non-cross-linked polymer is dissolved and the cross-linked polymer swells and forms a dome shaped artificial cupula around the hair. This process is shown schematically in Figure 2.7. The increase in sensitivity has been reasoned to be a result of 1) a larger drag force due to a larger effective cross section and 2) the coupling between the flow and the fluid trapped in the hydrogel (water content of the swallowed hydrogel is about 90%). This approach also provides extra protection for the hair sensors. Using a similar principle, McConny et al. [63] have reported 38 times increase in sensitivity and reduction of detection threshold to 2.5 μm/s. In this approach the dispense process was modified to increase the length of the hair and its cross section at the top without changing the mechanical characteristics of the base of the hair (see Figure 2.7 bottom). Although the fabrication process is not monolithic and, therefore, is not suitable for the array fabrication, according to authors, it rivals the fish mechanoreceptors in terms

[15] The sensitivity is defined as the ratio of a change at output to the respective change at input. It is basically the slope of the calibration curve of the sensor.

of sensitivity. It should be noted that the above mentioned values have been obtained using the same narrow (2 Hz) measurement bandwidth[16].

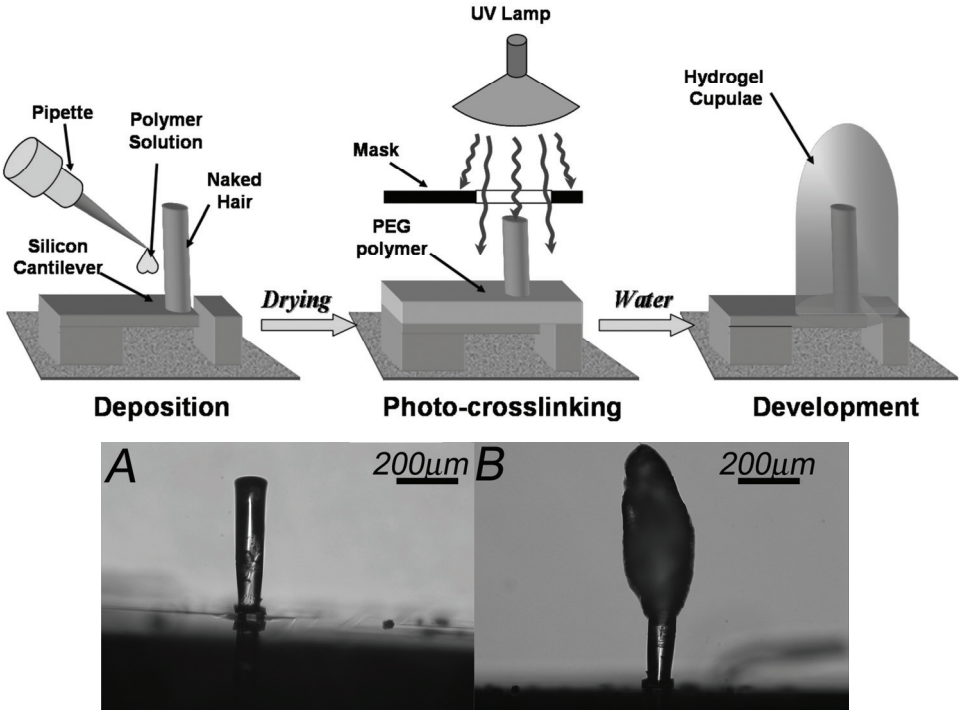

Figure 2.7 *Top: Schematic process steps to form a hydrogel cupula around the SU-8 hair at the tip of silicon cantilever [62] Bottom: Microscopic pictures from a hair without (A) and with (B) hydrogel at the tip [63]*

Another attempt to mimic hair receptors was done by Ozaki et al. [64]. They suggested two types of structure which are shown in Figure 2.8: 1) The first structure is rather simple. It is basically a series of planar cantilevers with piezoresistive strain gauges at the base. After fabrication the substrate is rotated 90° to orient the cantilevers perpendicular to the direction of the fluid flow. The fabrication process is simple and very well developed in MEMS technology. The one dimensional nature of the fabricated array and its low density are two disadvantages of this approach. 2) The second configuration is a cross-shaped structure with a piezoresistive element at the end of each beam which is fixed to the substrate. A long metal wire is attached to the centre of the cross manually. This structure is made on thin (200 µm) silicon substrates which are first oxidized and patterned. Then, Boron is diffused in order to make strain gauges. Anisotropic etching of the substrate from the backside in TMAH (Tetra-

[16] Personal communication with M. McConney.

Methyl-Ammonium-Hydroxide) is used to realize the beams. Afterwards, aluminium interconnects are deposited and finally a Reactive Ion Etching (RIE) process from the front side is used to release the device. Although the fabrication process is simple, the TMAH backside etch process needs a careful consideration to accurately achieve the desired thickness. These structures have been made for and tested in air flow but potentially can be used in water with small modification, mainly insulation of wires to prevent contact with water.

This second configuration has been repeated by Xue et al. [65] and Zhang et al. [66] who have changed the piezo-transducer configuration and fabrication process and included external structures to adapt the sensor to an aquatic environment. The 5 mm long hair is again attached manually (see Figure 2.8). The sensor is connected to a 50 dB low noise preamplifier, immersed in Castor oil and protected using a Polychloroprene rubber dome. The reported sensitivity is -197.7 dB at 400 Hz (0 dB=1 V/μPa)[17].

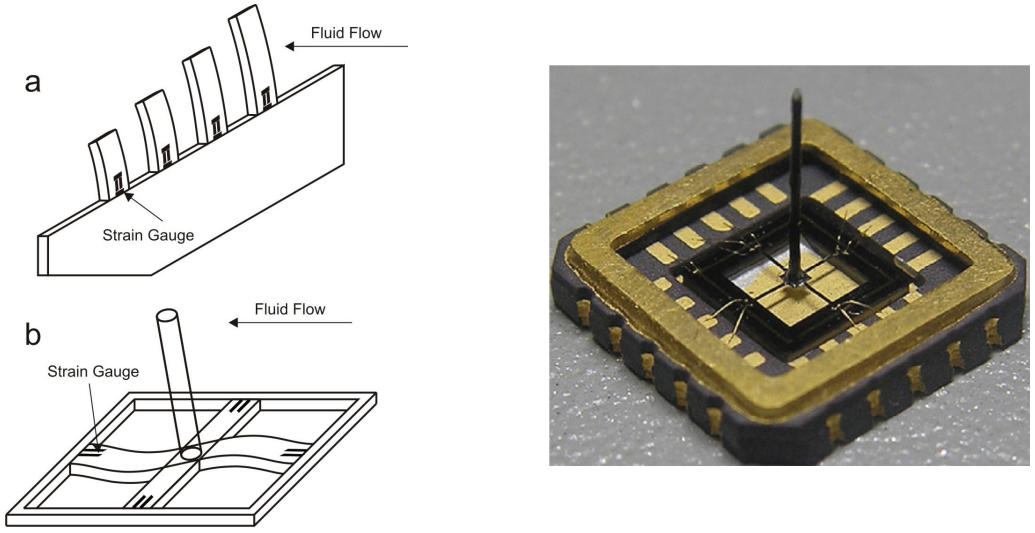

Figure 2.8 *Left: (a) In plane fabricated cantilevers are rotated to face the fluid flow (b) a thin cylindrical wire is mounted at the joint of cross-shaped beams with piezoresistive elements at the base [64] Right: The hydrophone before packaging [65]*

Lee et al. [67] use a piezoelectric polymer film or PVDF (Polyvinylidene Fluoride), which is bonded to the surface of aluminium cantilever beams. The overall size of the device in this approach is bigger (cantilevers are between 22 to 30 mm long) than in the previous ones as macro-fabrication technology has been utilized. Therefore,

[17] This sensitivity probably has been calculated considering the characteristic acoustic impedance of water

their sensitivity and bandwidth are much lower compared to micro-fabricated counterparts.

2.3.2 All Polymer Sensors

Engel et al. [68] have reported another type of hair-based flow sensor, shown in Figure 2.9, using Polyurethane elastomers and Force Sensitive Resistors (FSR). It consists of a hair-like structure (500 μm in diameter and 3 mm long) on top of four FSRs which are in a half bridge configuration and can reveal both magnitude and direction of displacement. When the structure deflects the stress develops at its base and the resistance of the FSRs will change accordingly. The fabrication process starts with deposition and patterning of gold lead wires. Afterwards, a thick photoresist is spun and patterned to form a mould for the FSRs. The actual FSRs are made of Polyurethane that is loaded with an electrically conductive filler. This filler can be Carbon Black (CB) or multiwall carbon nanotubes (MW-CNT). The FSR material is applied to the substrate and sacrificial photo resist is removed. The hairs are made by filling a wax mould with the polymer and then are aligned and attached to the FSR substrate. Subsequently, the wax mould is dissolved in hot water. These structures exhibit a great robustness but they suffer form non-uniformity, viscoelastic creep, size and aspect ratio limitations (because the wax mould is formed by drilling) and cross-axis coupling [68, 69]. Although the latter can be partially overcome using optimized cross-sections.

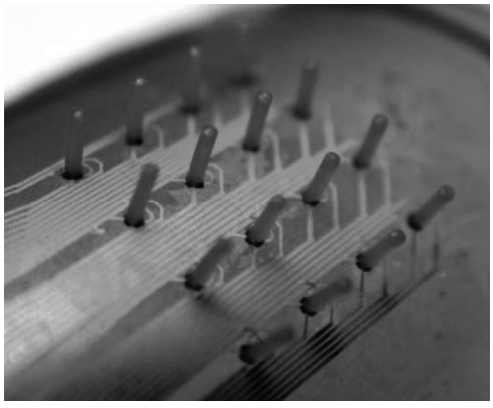

Figure 2.9 *Polyurethane hairs on flexible substrate [68]*

2.4 Our Approach

Aquatic flow sensors have been built based on many sensing principles as has been discussed in previous sections. Piezoresistive sensing has dominated the readout mechanisms of these sensors by far. It has the advantages of being cheap and easy to fabricate. Moreover, the readout circuitry can be rather simple. The development of these sensors has already led to demonstration of artificial lateral line sensor arrays. However, piezoresistors are sensitive to temperature changes while the magnitude of change in resistance due to the stress is comparatively small with respect to the base resistance, i.e. the signal modulation is small. In addition, to decrease the thermal noise the base resistance should be small. When the base resistance decreases, the electrical current supply should increase to yield a strong signal, hence the power consumption increases. An array of piezoresistive sensors consumes a considerable power.

We have taken another approach and exploited a differential capacitive readout mechanism. A capacitor consists of a pair of electrical conductors separated by an insulating material (dielectric). When a voltage difference is applied to the conductors an electric field is established in the dielectric material. Energy is stored in this electric field. The ability of a capacitor to store energy is characterised by its capacitance. An electrical capacitance C is defined as the ratio of the stored electric charge Q induced by establishing the electric potential V between the two electrodes. When these electrodes are parallel plate conductors it can be shown that[18]

$$C = \frac{\varepsilon \cdot A}{d} \tag{2.9}$$

is a physical characteristic of the configuration in which A is the overlapping area of electrodes, d is the distance between them and ε is the electrical permittivity of the medium in between. A change of any of these three quantities is reflected in the magnitude of the capacitance and can be measured with suitable electrical circuits. In short, an alternating voltage is applied to the electrodes. This causes the charges induced by the electric field to reverse their positions continuously. The movement of the charges creates an alternating current which is measured. The amplitude of the current is, naturally, determined by the capacitance. A comprehensive study on the capacitive measurement principle has been given in [70] and [71].

[18] This holds when the effect of the fringing electrical field can be neglected, i.e. when the lateral dimensions of the electrodes are much larger than their separation gap.

A capacitive sensor is a transducer which converts a stimulus to a corresponding change in a certain capacitance. Capacitive sensors are rather cheap and very accurate and have low power consumption. They offer high sensitivity and high signal to noise ratios. The opportunities and advantages of this approach have been demonstrated in numerous applications including fabrication of biomimetic artificial hair based flow sensors (inspired by the cerci of crickets) to operate in air [72]. This latter study functioned as the base for the current design. A basic requirement for using capacitive readout in an aquatic environment is to prevent water from being in contact with the electrodes. This may result in a short circuit or electrolysis if the water has sufficient conductivity. To overcome this difficulty conductors used in aquatic environments have to be insulated. In MEMS technology an option to do so is to deposit or spin a layer of a non-conductive polymer over the chip as in some devices previously reviewed. In addition, a capacitive change is usually due to a change in the distance of the two electrodes. Therefore, the presence of a highly viscous medium in between the electrodes can degrade the performance of the devices considerably[19] [73].

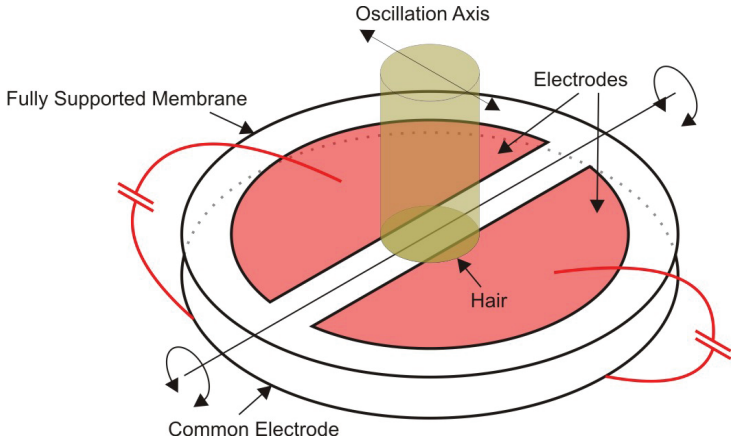

Figure 2.10 *A fully supported membrane with a hair and electrodes on top of a common electrode plate. Note that the electrodes are under the membrane and the fluid runs on top of it. The circular shape of the plates is only a schematic representation.*

To address the requirements of capacitive sensing in aquatic media three different configurations are proposed, analysed and fabricated. The first approach is to use a closed membrane with two electrodes underneath which stretches on top of a narrow gap opposite to a common electrode (see Figure 2.10). This forms two capacitors that can be used in a differential measurement scheme. A high aspect ratio

[19] This effect is called squeeze film damping.

structure, which is called *hair* due to its cylindrical shape, is attached to the top of the membrane and penetrates into the fluid above. The hair deflects as a result of the drag force from the impinging fluid flow. This deflection couples to the membrane and the resulting deformation changes the distance between the capacitors' plates. The fully supported membrane prevents liquid contact with electrodes and eliminates excess squeeze film damping that can result from high-viscosity fluid in between electrodes. The fabrication procedure, as we shall see in chapter four, is however quite complex.

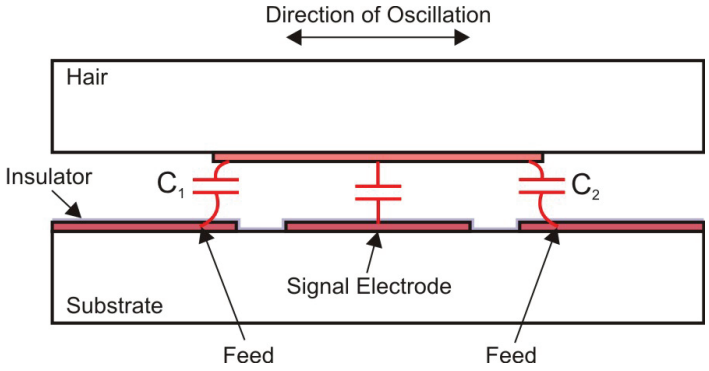

Figure 2.11 *A long hair is hung from the top of canal with floating electrode at the tip. Lateral displacement changes the capacitances. The lateral movement causes negligible squeeze film damping.*

The second approach is planned to realise a canal embedded hair-like capacitive flow sensor. It is inspired by the canal neuromast of fish. The effect of the canal in filtering the outside flow fluctuations results in an acceleration sensitive sensory function as has been stated in section 2.1.1. The sensor (see Figure 2.11) consists of three insulated in plane electrodes which construct two capacitors with another electrode floating opposite to them. The floating electrode is at the tip of a hanging beam which deflects due to fluid induced drag force. The displacement of the floating electrode changes the capacitance. In this way, electrolysis and short circuiting are avoided using insulated bottom electrodes. Since the movement is small and lateral, squeeze film damping should not affect the dynamics of the system considerably. The main part of the fabrication process is realisation of high aspect ratio polymeric beams within a short distance from the substrate.

The last proposal is based on the well-known configuration of shear stress sensors (see Figure 2.12). A laterally moving shuttle which is supported by four flexible beams carries a high aspect ratio hair. The shuttle has fingers which form two sets of parallel capacitors with other fixed fingers on the substrate. The whole structure is

electrically insulated from the medium by a dielectric layer which totally covers the shuttle. The substrate is insulated using a thin polymer which is spun on the surface. The squeeze film damping is negligible due to the small dimensions of the fingers.

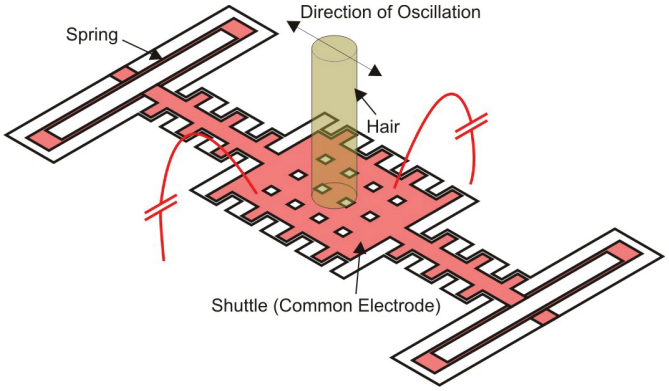

Figure 2.12 *A hair-like structure is added on the shuttle of a shear stress sensor to pickup the fluid drag. Note that the substrate is divided into electrically isolated parts.*

2.5 Summary and Conclusions

Biological sensory systems often display great performance inspiring engineers to develop artificial counterparts. The lateral line system of fish has been widely studied by biologists for its crucial role in fish survival. Moreover lately the robustness, sensitivity and consequently wide range of applications that potentially benefit from the abilities of such a system have attracted the engineering community. Aquatic flow sensors based on the lateral line of fish are useful in underwater robotic applications for hydrodynamic imaging of complex and noisy environments to provide information for e.g. surveillance, navigation and obstacle detection. The speculative ability to manoeuvre in murky or dark water, especially object detection in short range and silent environment has strongly driven the research in this area.

Inspired by the function of neuromast organ of the lateral line system, three different configurations have been proposed for fabrication of an aquatic particle velocity sensor. Our main focus is on the application of Micro-Electro-Mechanical Systems (MEMS) technology, which enables fabrication of sensory structures on length-scales comparable to what can be found in nature. Its intrinsic batch fabrication capability and high spatial resolution facilitate the fabrication of dense arrays of flow sensors and eventually allow mimicking the fish lateral line. For it offers accuracy, high resolution and low power consumption, capacitive sensing is chosen as the readout

mechanism. However, several difficulties arise using the capacitive sensing principle in a conductive medium with high density and viscosity, like water. These are mainly the electrical insulation of the electrodes (to prevent electrolysis and short circuit), added inertia of the movable electrodes and squeeze film damping. The result is usually a rather complicated fabrication process. Moreover, the readout circuitry is also rather complicated.

The proposed configurations address these requirements differently. In the closed membrane scheme the electrodes are separated from the medium and the narrow gap between them is devoid of the high viscosity liquid. The realisation of this structure requires sacrificial layer etch from backside while preserving the area under the membrane which acts as the common electrode. The fabrication process, as we shall see later in chapter four, is quite complex. In the canal embedded sensor configuration, electrical insulation is achieved using a dielectric material on the fixed bottom electrodes. The squeeze film damping is negligible because capacitor plates move parallel to each other. The fabrication process is simpler than that of the closed membrane. However since a polymer, whose characteristics greatly depend on the processing conditions, is used as the structural material reliability is of concern. The last proposed sensor is also insulated and the squeeze film damping is negligible due to small geometrical ratio of individual fingers which form the capacitors. In the presented fabrication procedure in chapter four, the insulation is provided using thermally grown silicon dioxide which results in stress gradient in the flexural beams. This may result in undesirable bending of the structure. The overall fabrication is, however, rather simple.

2.6 References

[1] F. Leydig, "Ueber die Schleimkanäle der Knochenfische," *Arch. Anat. Physiol. Wiss. Med.,* pp. 170–181, 1850.

[2] S. Dijkgraaf, "The functioning and significance of the lateral-line organs," *Biological reviews of the Cambridge Philosophical Society,* vol. 38, pp. 51-105, 1963.

[3] H. Bleckmann, "Role of the lateral line in fish behaviour," in *Behaviour of teleost fishes*, T. J. Pitcher, Ed., 2nd ed London: Chapman & Hall, 1993, pp. 201–246.

[4] B. L. Partridge and T. J. Pitcher, "The sensory basis of fish schools: Relative roles of lateral line and vision," *Journal of Comparative Physiology A: Neuroethology, Sensory, Neural, and Behavioral Physiology,* vol. 135, pp. 315-325, 1980.

[5] E. S. Hassan, "On the discrimination of spatial intervals by the blind cave fish (Anoptichthys jordani)," *Journal of Comparative Physiology A: Neuroethology, Sensory, Neural, and Behavioral Physiology,* vol. 159, pp. 701-710, 1986.

[6] J. C. Montgomery*, et al.*, "The lateral line can mediate rheotaxis in fish," *Nature,* vol. 389, pp. 960-963, 1997.

[7] H. Bleckmann, "Reaction time and stimulus frequency in prey localization in the surface-feeding fishAplocheilus lineatus," *Journal of Comparative Physiology A: Neuroethology, Sensory, Neural, and Behavioral Physiology,* vol. 140, pp. 163-172, 1980.

[8] C. von Campenhausen*, et al.*, "Detection of stationary objects by the blind Cave Fish Anoptichthys jordani (Characidae)," *Journal of Comparative Physiology A: Neuroethology, Sensory, Neural, and Behavioral Physiology,* vol. 143, pp. 369-374, 1981.

[9] J. Montgomery*, et al.*, "Biology of the Mechanosensory Lateral-Line in Fishes," *Reviews in Fish Biology and Fisheries,* vol. 5, pp. 399-416, Dec 1995.

[10] R. Voigt*, et al.*, "Responses of anterior lateral line afferent neurones to water flow," *Journal of Experimental Biology,* vol. 203, pp. 2495-2502, 2000.

[11] S. M. Van Netten, "Hydrodynamic detection by cupulae in a lateral line canal: Functional relations between physics and physiology," *Biological Cybernetics,* vol. 94, pp. 67-85, 2006.

[12] K. Maruska, "Morphology of the Mechanosensory Lateral Line System in Elasmobranch Fishes: Ecological and Behavioral Considerations," *Environmental Biology of Fishes,* vol. 60, pp. 47-75, 2001.

[13] S. Coombs*, et al.*, "Diversity of lateral line systems: evolutionary and functional considerations," in *Sensory Biology of Aquatic Animals*, ed New York: Springer Verlag, 1988, pp. 553-594.

[14] Engelmann*, et al.*, "Lateral line reception in still- and running water," *Journal of Comparative Physiology A: Neuroethology, Sensory, Neural, and Behavioral Physiology,* vol. 188, pp. 513-526, 2002.

[15] A. J. Kalmijn, "Hydrodynamic and Acoustic Field Detection," in *Sensory biology of aquatic animals*, J. Atema*, et al.*, Eds., ed: Springer-Verlag, 1988, pp. 83–130.

[16] B. Curcic-Blake, "Spatial and Temporal Characteristics of Fish Lateral Line Detection," Ph.D. Dissertation, Rijksuniversiteit Groningen, 2006.

[17] T. Dinklo, "Mechano- and electrophysiological studies on cochlear hair cells and superficial lateral line cupulae," Ph.D. Dissertation, Rijksuniversiteit Groningen, 2005.

[18] H. Bleckmann, *Reception of hydrodynamic stimuli in aquatic and semiaquatic animals*: Gustav Fischer Verlag, 1994.

[19] H. Bleckmann*, et al.*, "The Time Course and Frequency Content of Hydrodynamic Events Caused by Moving Fish, Frogs, and Crustaceans," *Journal of Comparative Physiology a-Sensory Neural and Behavioral Physiology,* vol. 168, pp. 749-757, 1991.

[20] D. V. Lychakov and Y. T. Rebane, "Otolith regularities," *Hearing Research,* vol. 143, pp. 83-102, 2000.

[21] D. A. Mann*, et al.*, "Ultrasound detection by clupeiform fishes," *The Journal of the Acoustical Society of America,* vol. 109, pp. 3048-3054, 2001.

[22] D. R. Ketten, "Cetacean Ears," in *Hearing by Whales and Dolphins*, W. W. L. Au*, et al.*, Eds., ed: Springer-Verlag, 2000, pp. 43-108.

[23] S. Coombs and J. C. Montgomery, "The enigmatic lateral line system," in *Comparative Hearing: Fishes and Amphibians*. vol. 11, A. N. Popper and R. R. Fay, Eds., ed New York: Springer-Verlag, 1999, pp. 319-362.

[24] S. Dijkgraaf, "The supposed use of the lateral line as an organ of hearing in fish," *Cellular and Molecular Life Sciences,* vol. 20, pp. 586-587, 1964.

[25] H. Lamb, *The dynamical theory of sound*. London: E. Arnold, 1910.

[26] D. T. Blackstock, *Fundamentals of physical acoustics*: John Wiley & Sons, 2000.

[27] S. Coombs, "Smart skins: Information processing by lateral line flow sensors," *Autonomous Robots,* vol. 11, pp. 255-261, Nov 2001.

[28] M. S. Weeg and A. H. Bass, "Frequency response properties of lateral line superficial neuromasts in a vocal fish, with evidence for acoustic sensitivity," *Journal of Neurophysiology,* vol. 88, pp. 1252-1262, Sep 2002.

[29] E. J. Denton and J. Gray, "Mechanical factors in the excitation of clupeid lateral lines," *Proceedings of the Royal Society of London. Series B. Biological sciences,* vol. 218, pp. 1-26, 1983.

[30] J. F. V. Vincent, "Stealing ideas from nature," in *Deployable Structures*, S. Pellegrino, Ed., ed Wien: Springer, 2001, pp. 51-58.

[31] A. A. Winder, "II. Sonar System Technology," *Sonics and Ultrasonics, IEEE Transactions on,* vol. 22, pp. 291-332, 1975.

[32] Y. C. Yang*, et al.*, "Distant touch hydrodynamic imaging with an artificial lateral line," *Proceedings of the National Academy of Sciences of the United States of America,* vol. 103, pp. 18891-18895, Dec 2006.

[33] J. K. Stroble*, et al.*, "An overview of biomimetic sensor technology," *Sensor Review,* vol. 29, pp. 112-119, 2009.

[34] M. A. Dijkstra*, et al.*, "Artificial sensory hairs based on the flow sensitive receptor hairs of crickets," *Journal of Micromechanics and Microengineering,* vol. 15, 2005.

[35] D. H. B. Wicaksono*, et al.*, "Design and Modelling of a Bio-inspired MEMS Gyroscope," in: *Proceedings of the International Conference on Electrical Engineering and Informatics*, Institut Teknologi Bandung, Indonesia, 2007, pp. 226-229.

[36] A. Skordos*, et al.*, "A novel strain sensor based on the campaniform sensillum of insects," *Philosophical Transactions of the Royal Society of London. Series A: Mathematical, Physical and Engineering Sciences,* vol. 360, pp. 239-253, February 15, 2002 2002.

[37] M. E. McConney*, et al.*, "Bioinspired material approaches to sensing," *Advanced Functional Materials,* vol. 19, pp. 2527-2544, 2009.

[38] M. E. McNie*, et al.*, "Bio-inspired MEMS Resonant Thermal Detector," in: *Proceedings of the Institution of Engineering and Technology Seminar on MEMS Sensors and Actuators*, 2006, pp. 83-90.

[39] P. Tawdross and A. König, "Feasibility study of a novel bio-inspired location sensor concept for indoor location based services in ambient intelligence applications," presented at the 3rd International Workshop on Intelligent Solutions in Embedded Systems (WISES), Hamburg, 2005.

[40] H. T. Nagle*, et al.*, "The how and why of electronic noses," *IEEE Spectrum,* vol. 35, pp. 22-31, 1998.

[41] L. J. Currano*, et al.*, "Microscale implementation of a bio-inspired acoustic localization device," 2009.

[42] T. N. Pornsin-Sirirak*, et al.*, "Titanium-alloy MEMS wing technology for a micro aerial vehicle application," *Sensors and Actuators, A: Physical,* vol. 89, pp. 95-103, 2001.

[43] P. Dario*, et al.*, "Design, fabrication and applications of biomimetic sensors in biorobotics," in: *Proceedings of the IEEE International Conference on Information Acquisition*, 2005, p. 4 pp.

[44] K. Suzuki*, et al.*, "Creation of an insect-based microrobot with an external skeleton and elastic joints," in: *Proceedings of the IEEE Micro Electro Mechanical Systems (MEMS)*, 1992, pp. 190-195.

[45] J. Chen*, et al.*, "Two-dimensional micromachined flow sensor array for fluid mechanics studies," *Journal of Aerospace Engineering,* vol. 16, pp. 85-97, 2003.

[46] H. W. Jentink*, et al.*, "A compact differential laser Doppler velocimeter using a semiconductor laser," *Journal of Physics E: Scientific Instruments,* vol. 20, pp. 1281-1283, 1987.

[47] V. I. Fernandez*, et al.*, "Lateral line inspired MEMS-array pressure sensing for passive underwater navigation," in: *Proceedings of the International Symposium on Unmanned Untethered Submersible Technology*, 2007.

[48] M. R. Arshad, "Recent advancement in sensor technology for underwater applications," *Indian Journal of Marine Sciences,* vol. 38, pp. 267-273, 2009.

[49] C. S. Smith, "Piezoresistance Effect in Germanium and Silicon," *Physical Review,* vol. 94, pp. 42-49, 1954.

[50] F. J. Giessibl, "Advances in atomic force microscopy," *Reviews of Modern Physics,* vol. 75, p. 949, 2003.

[51] H. P. Lang*, et al.*, "An artificial nose based on a micromechanical cantilever array," *Analytica Chimica Acta,* vol. 393, pp. 59-65, 1999.

[52] N. V. Lavrik, *et al.*, "Cantilever transducers as a platform for chemical and biological sensors," *Review of Scientific Instruments,* vol. 75, pp. 2229-2253, 2004.

[53] G. M. Rebeiz, *RF MEMS: Theory, Design, and Technology*: John Wiley & Sons, 2003.

[54] J. M. Gere, *Mechanics of materials*, 4th ed. ed. Boston :: PWS Pub Co., 1997.

[55] Z. Fan, *et al.*, "Design and fabrication of artificial lateral line flow sensors," *Journal of Micromechanics and Microengineering,* vol. 12, pp. 655-661, 2002.

[56] J. Zou, *et al.*, "Plastic deformation magnetic assembly (PDMA) of out-of-plane microstructures: Technology and application," *Journal of Microelectromechanical Systems,* vol. 10, pp. 302-309, 2001.

[57] J. Chen, *et al.*, "Development of polymer-based artificial haircell using surface micromachining and 3D assembly," in: *Proceedings of the 12th IEEE International Conference on Solid-State Sensors, Actuators and Microsystems (TRANSDUCERS)*, 2003, pp. 1035-1038.

[58] C. Liu, "Micromachined biomimetic artificial haircell sensors," *Bioinspiration & Biomimetics,* vol. 2, p. S162, 2007.

[59] Y. Yang, *et al.*, "From artificial hair cell sensor to artificial lateral line system: Development and application," in: *Proceedings of the IEEE International Conference on Micro Electro Mechanical Systems (MEMS)*, 2007, pp. 577-580.

[60] N. N. Chen, *et al.*, "Design and characterization of artificial haircell sensor for flow sensing with ultrahigh velocity and angular sensitivity," *Journal of Microelectromechanical Systems,* vol. 16, pp. 999-1014, Oct 2007.

[61] Y. Yang, *et al.*, "Artificial lateral line with biomimetic neuromasts to emulate fish sensing," *Bioinspiration and Biomimetics,* vol. 5, 2010.

[62] S. Peleshanko, *et al.*, "Hydrogel-encapsulated microfabricated haircells mimicking fish cupula neuromast," *Advanced Materials,* vol. 19, pp. 2903-2909, 2007.

[63] M. E. McConney, *et al.*, "Biologically inspired design of hydrogel-capped hair sensors for enhanced underwater flow detection," *Soft Matter,* vol. 5, pp. 292-295, 2009.

[64] Y. Ozaki, *et al.*, "Air flow sensor modeled on wind receptor hairs of insects," in: *Proceedings of the 13th IEEE International Conference on Micro Electro Mechanical Systems (MEMS)*, 2000, pp. 531-536.

[65] C. Xue*, et al.*, "Design, fabrication, and preliminary characterization of a novel MEMS bionic vector hydrophone," *Microelectronics Journal,* vol. 38, pp. 1021-1026, 2007.

[66] B. Zhang*, et al.*, "Modeling and characterization of a micromachined artificial hair cell vector hydrophone," *Microsystem Technologies,* vol. 14, pp. 821-828, 2008.

[67] Y. S. Lee*, et al.*, "Biologically inspired smart sensor for acoustic emission detection," *Key Engineering Materials,* vol. 321-323 I, pp. 204-207, 2006.

[68] J. M. Engel*, et al.*, "Polyurethane rubber all-polymer artificial hair cell sensor," *Journal of Microelectromechanical Systems,* vol. 15, pp. 729-736, 2006.

[69] C. Liu, "Artificial Hair Cell Sensors For Flow, Vibration, And Force Imaging," in *IEEE Sensors Council Newsletter*, ed, 2005.

[70] J. W. d. Jong, "Smart capacitive sensors," Ph.D. Dissertation, Delft Technical University, Delft, 1994.

[71] L. K. Baxter, *Capacitive sensors: Design and application*: Wiley-IEEE Press, 1997.

[72] G. J. M. Krijnen*, et al.*, "Biomimetic micromechanical adaptive flow-sensor arrays," in: *Proceedings of SPIE - The International Society for Optical Engineering*, 2007.

[73] J. J. Blech, "On Isothermal Squeeze Films," *Journal of Lubrication Technology-Transactions of the Asme,* vol. 105, pp. 615-620, 1983.

3
Modelling and Design

This chapter describes three capacitive flow sensor designs. Detailed analyses are performed to identify the design parameters that influence the sensor characteristics and, thus, which can be used to tune the sensor performance. A qualitative comparison between different designs is provided at the end, highlighting the merits and drawbacks of each scheme.

3.1 Introduction

In the following sections of this chapter first a brief introduction to the fluid properties, with emphasis on water, is given. Subsequently, three hair-based artificial flow-sensor designs are proposed and their practical constrains are introduced. Wherever possible, detailed analyses of the diverse aspects of the sensors are provided. These analyses lead to identification of the most important design parameters.

The analysis of each sensor design is threefold:

- Fluid-structure interactions, which play an important role in any flow sensor, are investigated. These kinds of interactions are fairly complex and FEM (Finite Element Method) are usually used to predict the precise behaviour. On the other hand, approximate analytical approaches provide valuable insights and can be used as first order design tools.
- Static and dynamic mechanical behaviour of the structure. The dynamic model of the sensor is needed, amongst others, to characterise the frequency response. The mechanical sensitivity of the sensor configuration should be maximized through careful design, geometrical optimization and material selection. This, of course, needs to be done while respecting technological limitations and being aware of the various trade-offs that need to be made.
- Electrical readout mechanism. The modulation of electrical signals corresponding to changes of the fluid velocity should be elaborated. As the mechanical sensitivity, electrical sensitivity of the device should be maximized. The influence of geometry and configuration of readout electrodes as well as parasitic impedances is outlined. The structures are designed to optimize the Signal to Noise Ratio (SNR) and to be insensitive to pressure variations.

3.2 Fluid

Fluid is defined as a material which deforms continuously when subjected to shear stresses of any magnitude [1]. In this section, the relevant mechanical and electrical parameters of fluids which are used in the analysis of hair-based flow sensors are reviewed in brief. Naturally the emphasis is on liquids. Density, bulk modulus,

viscosity, surface tension and vapour pressure are the most important parameters influencing the mechanical behaviour of liquids.

Mass density is the ratio of mass to volume of a material. Compressibility of a fluid is related to the magnitude of change in the density or equally to the magnitude of change in the volume of a given mass of the fluid. This is quantitatively best described by the bulk modulus as

$$E_v = -V \cdot \frac{dp}{dV} = \rho \cdot \frac{dp}{d\rho} \tag{3.1}$$

where V is the volume, ρ is the density and p is the pressure. A high bulk modulus suggests a nearly incompressible fluid, i.e. a fluid of which the density is fairly constant. Liquids are usually considered to be incompressible.

Viscosity is a measure of "stickiness" or "fluidity" of a fluid. It is defined as the constant of proportionality which equates the shear stress with the rate of shearing strain or equally the gradient of fluid velocity. In Newtonian fluids this relation is linear. Viscosity coefficients are defined in two different ways:

- Dynamic (absolute) viscosity, which has been discussed above and is usually shown by the Greek letter μ and is expressed in SI unit by N.s/m^2 or Pa.s
- Kinematic viscosity, which is the dynamic viscosity divided by the density. It is usually shown by the Greek letter ν and is expressed in SI units by m^2/s

Viscosity (dynamic or kinematic) is a strong function of temperature. The relation is described by two empirical equations for gases and liquids separately. For gases the Sutherland's equation is

$$\mu = \frac{D \cdot T^{3/2}}{T + E} \tag{3.2}$$

where D and E are empirical constants and T is the absolute temperature. For liquids the Andrade's equation is

$$\mu = A \cdot \exp\left(\frac{B}{T}\right) \tag{3.3}$$

where A and B are constant. The static pressure inside a liquid at rest linearly increases with depth. The familiar relation is

$$p = p_0 + \rho \cdot g \cdot h \tag{3.4}$$

where p_0 is the reference pressure (usually ambient pressure on the surface), g is the gravitational acceleration and h is the depth of the liquid measured from the free

surface. The design of aquatic flow sensors naturally depends on the above mentioned properties of water.

3.2.1 Mechanical properties of water

The mass density of water is a weak function of temperature. However, the relation is neither linear nor monotonic with the highest density (999.9720 kg/m^3) at 4 °C. In addition, the degree of salinity has an appreciable effect on the density; the higher the salinity the higher the density. Hereafter the density of water is considered to be 1000 kg/m^3. In addition, since its bulk modulus of elasticity is around 2.15×10^9 Pa, water is considered incompressible in most of the cases treated in this thesis. The dynamic viscosity of water at 4 and 20 °C is 1.547×10^{-3} Pa.s and 1.002×10^{-3} Pa.s respectively. This results in 1.547×10^{-6} and 1.004×10^{-6} m^2/s for kinematic viscosity. The static pressure in water increases by about 10 kPa for each meter in depth. This is important when a pressure difference is acting on a closed submerged structure; the structure may collapse due to the high static pressure.

3.2.2 Electrical properties of water

Pure water, when having no ions, is an excellent insulator. But even "deionized" water is not totally free of ions (due to self-ionization of water[1]) and, therefore, is a weak electrical conductor. However its conductivity increases significantly by dissolved ionic materials like salt. The electrical conductivity of deionized water is in the order of 10^{-6} to 10^{-4} S/m which increases to about 3.27 S/m for sea water[2] [2]. The conductivity of an aqueous electrolyte solution depends on temperature; usually the higher the temperature, the higher the conductivity[3] [3]. Moreover, it also depends on the frequency [4, 5].

It is known that the dielectric constant of many materials decreases from a static value, ε_s, at low frequencies to a limiting value, ε_∞, at higher frequencies. However usually it is only when entering into the GHz range when appreciable changes occur.

[1] Self-ionization is a process in which two water molecules form a H_3O^+ and an OH^-. This process occurs naturally in pure water and depends on pressure and temperature. At standard pressure and temperature the self-ionization constant of water is 10^{-14}.

[2] The conductivity of sea water changes with salinity and temperature. The presented value is the mean conductivity of oceans excluding the shallow seas.

[3] The electrical conductivity of water increases with temperature up to about 230°C due mainly to its increased ionization. Above this temperature the density is much reduced and this reduces the ability for ionization.

As the carrier frequency of the readout signal of our capacitive sensors is only about 1 MHz (see section 3.3.5), the dielectric constant of water can be treated as a constant given by the low frequency limit.

Another factor that influences the dielectric constant of water is its temperature. The dielectric constant of pure water changes from about 88 at 0 °C to about 55 at 100 °C. The relative dielectric constant of pure water at 20 °C is considered to be 80.22. For more information on the dielectric constant of water and ionic solutions see [6].

Electrolysis is decomposition of a material by passing electrical current through it. The electrolysis of water is the oxidation and reduction of its ions at the anode and cathode according to the following equations

$$\begin{aligned} &(Anode) \quad 4OH^- \rightarrow O_2 + 2H_2O + 4e^- \\ &(Cathode) \quad 2H_2O + 2e^- \rightarrow H_2 + 2OH^- \end{aligned} \tag{3.5}$$

The necessary electrode potential for oxidation (of pure water, PH 7) is -0.40 V and for reduction 0.83 V. Therefore, the theoretical (reversible) potential of the electrolysis cell is 1.23 V. This means that having a voltage difference above this value will result in electrolysis of water. In practice, due to the ohmic loss and polarization effects of electrolytes [7], usually a voltage higher than 1.47 V is needed.

On the other hand, the presence of an electrolyte can change one or both of the above equations depending on the standard electrode potential of its ions. Using conventional electrodes and under normal conditions the electrolysis of sea water produces hydrogen at the cathode and chlorine at the anode. The Nernst equation [7] gives the electrode potential for a specific temperature and concentration of ions. In industrial sea water electrolysis the applied voltage is above 1.8 V.

3.3 Sensors with Closed Membrane

3.3.1 Design description

As has been said before, there are two main concerns about using a capacitive readout mechanism in an aquatic medium. First, the electrodes should be insulated from the fluid to prevent short-circuiting and electrolysis. Second, usually it is the relative movement of electrodes with respect to each other that causes a change in the gap in between leading to a corresponding modulation of an electrical signal. As the gap between electrodes becomes very small, the flow of the fluid in between the electrodes dissipates some of the energy harvested by the sensor structure. Therefore, a

high viscosity fluid in between the electrodes will have an adverse effect on the mechanical response of the system. The smaller the gap between the two counter electrodes the larger this effect is (squeeze film damping) and thus it should be avoided.

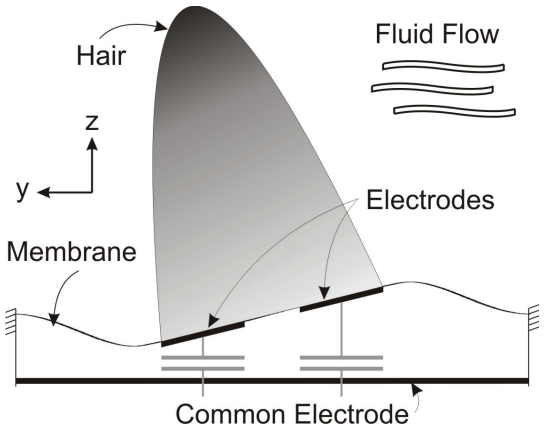

Figure 3.1 *The schematic view of the proposed design for capacitive artificial neuromast*

Considering all constraints and opportunities described in the previous chapter, a plausible design for a differential capacitive hair sensor is proposed in Figure 3.1. A fully supported flexible membrane with two electrodes underneath supports a cilium[4] in the middle. A common electrode exists at a distance beneath the membrane and forms two capacitors which can be used in a differential measurement scheme. The cilium deflects as a result of the drag force from the impinging fluid flow. This deflection mirrors in the flexible membrane to which the cilium is firmly attached. This deflection changes the distance between each of the electrodes and the common electrode or, in other words, the gap between the capacitor plates. One gap increases while the other one decreases. When this change is measured, the amount of cilium rotation and membrane deflection, hence the magnitude of the drag torque can be deduced. The fully supported membrane prevents liquid contact with electrodes and eliminates excess squeeze film damping that can result from high-viscosity fluid in between electrodes.

[4] We use the word "cilium" here to refer to a high aspect ratio hair-like projection which resembles the shape of the sensory hairs. It does not refer to the function of a cilium as a biological structure.

In order to understand the basic design parameters and optimize them, a relation between capacitor change and the drag torque on the cilium is needed. For this purpose, the problem is divided into three parts which are discussed in the following sections.

3.3.2 Fluid Solid interaction

3.3.2.1 Drag force

In this section, following the analysis that has been done for filiform hairs of crickets [8, 9], we calculate the drag force on the hair structure. For this purpose, it is necessary to obtain the fluid flow profile along the length of the hair structure. Considering an infinite flat substrate and the no-slip condition, the velocity profile of a flow moving in parallel to the substrate is given by

$$\vec{U}_f(z,t) = U_z \cdot e^{j(\omega \cdot t + \zeta_z)} \cdot \hat{e}_y \tag{3.6}$$

where

$$\begin{aligned} U_z &= U_0 \cdot \left(1 + e^{-2z/\delta} - 2e^{-z/\delta} \cdot \cos(z/\delta)\right)^{1/2} \\ \zeta_z &= \tan^{-1}\left(\left(e^{-z/\delta} \cdot \sin(z/\delta)\right) / \left(1 - e^{-z/\delta} \cdot \cos(z/\delta)\right)\right) \end{aligned} \tag{3.7}$$

in which U_0 is the far field (or free stream) velocity amplitude, ω is the angular frequency, t is the time, $\hat{e}_y$ is the unit vector in the y direction, z is the distance from the substrate as indicated in Figure 3.1 and

$$\delta = \sqrt{\frac{2\mu}{\omega \cdot \rho_L}} \tag{3.8}$$

is proportional to the boundary layer thickness for which μ is the dynamic viscosity and ρ_L is the density of the fluid. The flow profile in an aquatic medium is shown in Figure 3.2 for various frequencies. A more comprehensive study of boundary layers has been given in [10] and in the context of filiform hairs in [11-13].

Humphrey et al. [8] have shown that the boundary layer around a cylinder can be estimated by that of a flat substrate when $f \cdot D^2/\nu > 20/\pi$, where f is the frequency of the oscillatory flow, D is the diameter of the cylinder and ν is the kinematic viscosity of the fluid. Therefore, in water the flat substrate approximation is valid even for substrates with fairly high curvature [14].

The hair structure can be modelled as a rigid cylinder connected to a pivot at the base. Stokes [15] investigated the drag force of a fluid on an infinitely long rigid

cylinder in a harmonic laminar flow and showed that the drag force per unit length of the cylinder is obtained from

$$F(z,t) = Z_s \cdot U_r \tag{3.9}$$

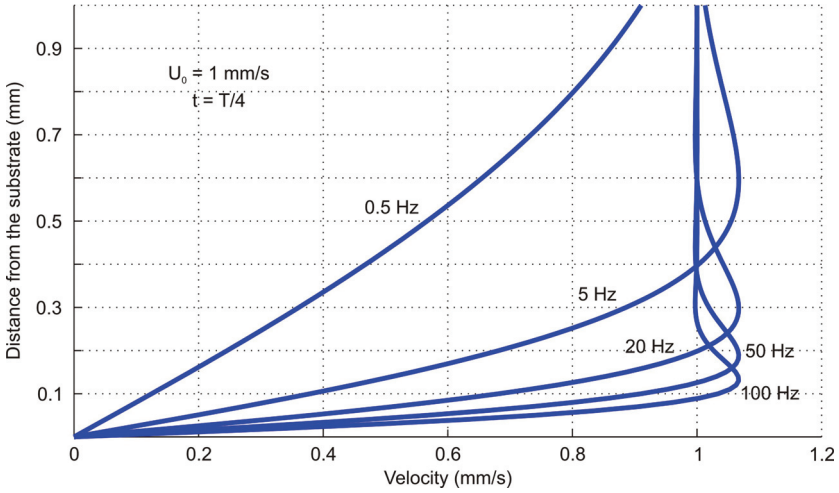

Figure 3.2 *Oscillatory flow velocity profile over an infinite substrate for various frequencies. The plot is presented at one forth of the period of the indicated frequencies*

in which U_r is the phasor of the relative velocity of the fluid and $Z_s = Z_r + j\,\omega \cdot Z_i$ is the complex Stokes' mechanical impedance. The real part of the impedance is a result of frictional drag due to non-zero viscosity of the fluid. The imaginary part, which results from the time derivative of the fluid velocity, i.e. acceleration, represents the inertia effects and pressure drag. Since these coefficients are derived for an infinite cylinder in an infinite mass of the fluid they do not depend on the spatial coordinates. In our case we shall neglect the end effects and retain the coefficients derived for the infinite case. In other words, we assume that the flow remains two dimensional along the length of the cylinder. The relative velocity, which is the fluid velocity minus the velocity of the cylinder, is written as

$$U_r = U_f - j\,\omega \cdot z \cdot \Phi_h \tag{3.10}$$

in which U_f is given by (3.6) and Φ_h represents the angular deflection amplitude of the cylinder. Therefore, the resultant torque is obtained by direct integration as

$$M = \int_0^{L_h} F(z,t) \cdot z \cdot dz = Z_s \cdot \int_0^{L_h} U_f \cdot z \cdot dz - j\,\omega \cdot Z_s \cdot \int_0^{L_h} \Phi_h \cdot z^2 \cdot dz \tag{3.11}$$

where L_h is the length of the cylinder. The first term on the right hand side of (3.11), hereafter called M_f, shows the drag force on a stationary rigid cylinder due to the fluid

flow. The second term on the right hand side of (3.11) denotes the torque due to the movement of the cylinder. The role of this term is better understood in connection with the dynamic response of the system and will be discussed in section 3.3.4.

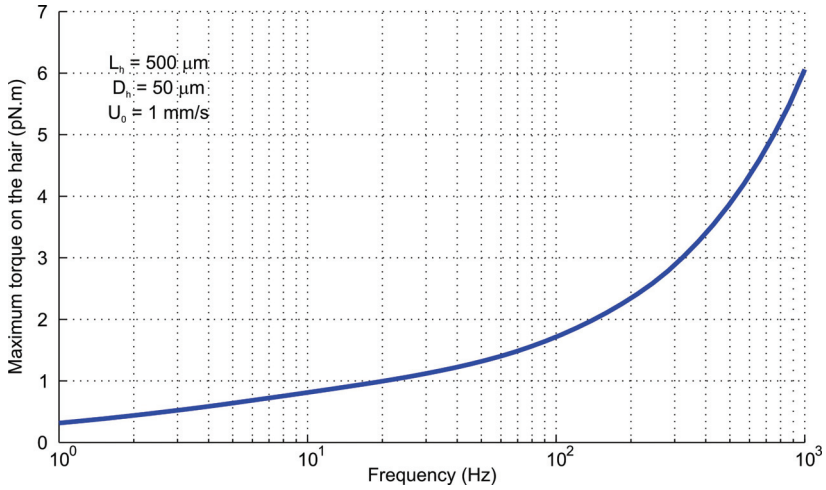

Figure 3.3 *The torque on the hair structure at different frequencies.*

Figure 3.3 shows the amplitude of the harmonic torque, M_f, on a 500 µm long and 50 µm wide cylinder as a function of frequency for a far field amplitude of 1 mm/s. The value of Z_s is given by [8, 9] following Stokes [15] as

$$Z_s = \left(4\pi \cdot \mu \cdot G\right) + j\,\omega \cdot \left(\pi \cdot \rho_L \cdot R_h^2 - \frac{\pi^2 \cdot \mu \cdot G}{\omega \cdot g}\right) \tag{3.12}$$

where R_h is the radius of the cylinder (i.e. the hair structure) and

$$G = \frac{-g}{g^2 + \left(\frac{\pi}{4}\right)^2} \tag{3.13}$$

$$g = 0.577 + \ln\left(\frac{R_h}{\sqrt{2}\,\delta}\right) \tag{3.14}$$

It should be noted that for the Stokes' theory to be applied three conditions must be satisfied simultaneously [14]: $L_h/2R_h \gg 1$, $u_r \cdot R_h/\nu \ll 1$ and $R_h \cdot \beta/\sqrt{2} \ll 1$ where u_r is the relative velocity of the cylinder. The first condition, considering the aspect ratio of 20, is readily satisfied. The second condition, states that the Reynolds number should be vary small. Since the velocity amplitude of interest is in the range of mm/s, this condition is also satisfied. The last criterion, however, implies that the Stokes's theory is only valid when inertia effects are negligible, hence at low frequencies. Moreover, at higher frequencies the Strouhal number defined as

$$St = \frac{\omega \cdot \left(2 R_h\right)}{U_0} \tag{3.15}$$

increases and the effect of the curvature of the cylinder is no longer negligible [16]. It has been shown (see Figure 8 in [8]) that the proper theories at higher frequencies are that of Wang [16] or that of Holtsmark [17] depending on the magnitude of

$$Re \cdot St = \frac{\omega \cdot \left(4 R_h^2\right)}{\nu} \tag{3.16}$$

As it has been shown in Appendix V, the use of Stokes' theorem when (3.16) is not much less than unity yields a serious underestimation of the drag force.

Is the assumption of a rigid cylinder valid? The hair-like cylinder is regarded rigid when its stiffness is much higher that the bending stiffness of its base[5]. The latter is given in the next section by (3.36). The stiffness of the cylinder can be calculated assuming a resultant force

$$F_t = \int_0^{L_h} F\left(z,t\right) \cdot dz \tag{3.17}$$

which acts at the distance z_t from the base of the cylinder on it. In the worst case, this force acts at the tip of the cylinder. This leads to a stiffness equal to $3E \cdot I / L_h^3$ which is, considering a circular hair of 25 μm diameter and 1 mm length, much larger than the stiffness of a 1 μm thick membrane obtained from (3.36). Therefore, the hair can be considered rigid. The actual distance is computed using the moment equality and (3.11) as

$$M = \int_0^{L_h} F(z,t) \cdot z \cdot dz = F_t \cdot z_t \tag{3.18}$$

Figure 3.4 shows the position of the resultant force on the cylinder. This position is a very weak function of the frequency and changes almost linearly with hair length. It can be seen that the position is between 1/2 and 2/3 of the hair length. The minimum stiffness of the cylinder is, therefore,

$$K_{cylinder-min} \approx 10 \frac{E \cdot I}{L_h^3} \tag{3.19}$$

[5] It is better to state this in terms of eigen frequencies. The hair-like cylinder is regarded rigid when its eigen frequencies are well above those of the membrane (considering the rigid centre part).

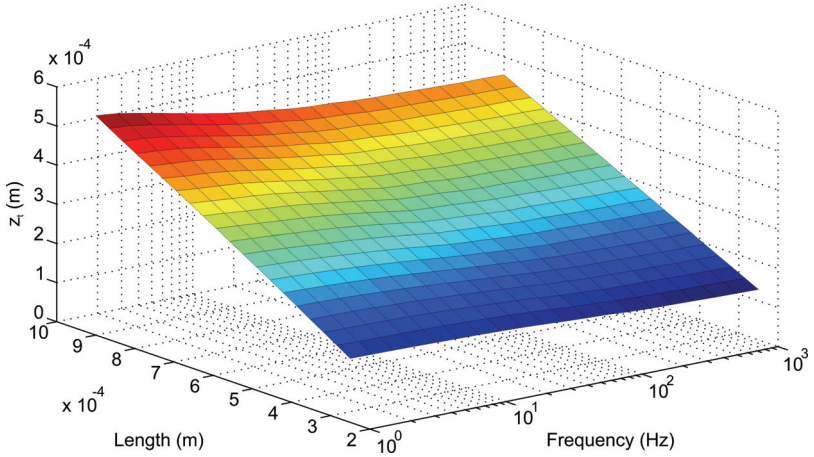

Figure 3.4 *The position of the resultant force, z_r, on the cylinder in different hair lengths and frequencies*

3.3.3 Mechanical structure

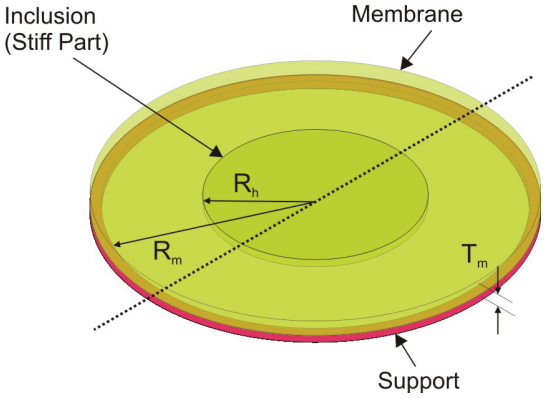

Figure 3.5 *Schematic of a fully supported membrane with a stiff inclusion in the middle*

The design of the sensor is based on a fully supported membrane (see Figure 3.5 above) for the reasons that have been discussed before. Since the deflection of the membrane determines the change in the capacitance, it is important to optimize the membrane structure to obtain the maximum possible displacement.

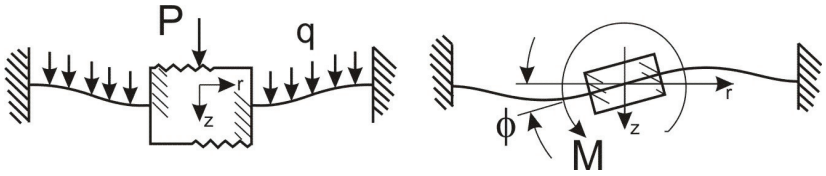

Figure 3.6 *The schematic view of the deflection modes of the membrane*

The membrane can deflect in two ways as shown in Figure 3.6. At the left of the figure the static downward deflection is shown which is caused by a pressure

difference across the membrane and the weight of the structure on the membrane. At the right the anti-symmetric deflection of the membrane due to a torque, generated by the force on the hair, is depicted. We shall, considering small displacements, treat these two modes separately and use the principle of superposition to obtain the total deformation of the structure.

The vibration of plates with uniform thickness neglecting the shear deformation and rotary inertia is governed by [18]

$$D \cdot \nabla^4 w + \rho_m \cdot T_m \cdot \frac{\partial^2 w}{\partial t^2} = f\left(r, \theta, t\right) \tag{3.20}$$

Where ρ_m is the density and T_m is the thickness of the plate, ∇^2 is the Laplace operator,

$$\nabla^2 = \frac{\partial^2}{\partial r^2} + \frac{1}{r} \cdot \frac{\partial}{\partial r} + \frac{1}{r^2} \cdot \frac{\partial^2}{\partial \theta^2} \tag{3.21}$$

f is the density of the distributed transverse force, w is the deflection, r and θ are coordinates in a polar system and

$$D = \frac{E \cdot T_m^{\,3}}{12 \cdot \left(1 - \nu^2\right)} \tag{3.22}$$

is the flexural rigidity of the membrane. Here E is the Young's modulus and ν is the Poisson's ratio of the plate. Let us first determine the natural resonance frequencies of a fully supported circular plate. The dispersion relation, using the method of separation of variables, is obtained as

$$\omega_{pq}^2 = \frac{D \cdot k_{pq}^4}{\rho_m \cdot T_m \cdot R_m^4} \tag{3.23}$$

where R_m denotes the radius of the membrane and k_{pq} is the q^{th} root of

$$\frac{J_{p+1}\left(k_{pq}\right)}{J_p\left(k_{pq}\right)} + \frac{I_{p+1}\left(k_{pq}\right)}{I_p\left(k_{pq}\right)} = 0 \tag{3.24}$$

Here J_p and I_p are, respectively, the Bessel function and modified Bessel function of the first kind and of p^{th} order. Furthermore, p and q are the number of nodal diameters and circles respectively. The first resonance frequency, ω_{01}, of a clamped circular plate is, therefore,[6]

[6] Sometimes the nodal circle at the edge of the membrane is not taken into account and the first resonance is denoted by ω_{00}.

$$\omega_{01} = \frac{10.21}{R_m^2} \cdot \sqrt{\frac{D}{\rho_m \cdot T_m}} \tag{3.25}$$

For a 1 μm thick SU-8 membrane with 50 μm radius (see section 3.3.7.1) (3.25) amounts to 2.3 MHz. It should be noted that the classical theory of vibration of the plates (also known as Kirchhoff's theory) overestimates the resonance frequency by neglecting the effects of the shear deformation and rotary inertia [19, 20]. The thicker the plate the more serious is the overestimation. FEA shows that the first resonance is approximately 0.36 MHz, more than a factor of six lower. The resonance frequency of the actual structure, with the stiff inclusion, is about 0.63 MHz. To this end, because of the high first resonance frequency, the dynamic response of the membrane can be approximated by its static behaviour at the frequency range of interest. Therefore, (3.20) is simplified to govern the static deflection of a circular membrane as

$$D \cdot \nabla^4 w = f(r, \theta) \tag{3.26}$$

3.3.3.1 On the static downward deflection of a fully supported membrane

For the static downward deflection, shown at the left side of Figure 3.6, the boundary conditions are given as

$$w\big|_{r=R_m} = \left.\frac{\partial w}{\partial r}\right|_{r=R_m} = \left.\frac{\partial w}{\partial r}\right|_{r=R_h} = 0 \tag{3.27}$$

The forth boundary condition is the value of the shear stress at $r = R_h$. The complete solution is presented in Appendix I. When the weight of the structure is negligible the static downward deflection is obtained from

$$w(\rho) = \frac{P \cdot R_m^4}{64\,D} \cdot \left(2\zeta^2 \cdot \left(1 - \rho^2 + 2\ln(\rho)\right) + \left(1 - \rho^2\right)^2\right) \tag{3.28}$$

in which ρ is the normalised radial distance from the centre of the membrane given by

$$\rho = \frac{r}{R_m} \tag{3.29}$$

and

$$\zeta = \frac{R_h}{R_m} \tag{3.30}$$

This leads to a simple expression for the stiffness of the membrane for downward displacement evaluated at $\rho = \zeta$ as

$$K_s = \frac{64\,D}{R_m^4} \cdot \frac{1}{\left(1-\zeta^2 \cdot \left(\zeta^2 - 4\ln(\zeta)\right)\right)} \tag{3.31}$$

3.3.3.2 On the anti-symmetric static deflection of the fully clamped membrane

It has also been shown [21] that the solution to the governing equation for the deflection of the membrane for anti-symmetric case is

$$w = \frac{q \cdot {R_m}^4}{192\,D} \cdot \left(\rho^5 + A \cdot \rho + B \cdot \rho^3 + C \cdot \rho^{-1} + H \cdot \rho \cdot \ln(\rho)\right) \cdot \cos(\theta) \tag{3.32}$$

For the case of a fully clamped membrane, the boundary conditions are set as

$$\begin{aligned} w\big|_{\rho=1} &= \left.\frac{\partial w}{\partial r}\right|_{\rho=1} = 0 \\ w\big|_{\rho=\zeta} &= R_h \cdot \varphi \cdot \cos(\theta) \\ \left.\frac{\partial w}{\partial r}\right|_{\rho=\zeta} &\approx \frac{w\big|_{\rho=\zeta}}{R_h} \end{aligned} \tag{3.33}$$

in which φ has been shown in Figure 3.6. Using the boundary conditions, the membrane's deflection is calculated as

$$w(\rho,\theta) = \frac{M}{8\pi \cdot D} \cdot \frac{R_m \cdot \left(\rho^2 \cdot \left(1-\zeta^2-\rho^2+2\ln(\rho)+2\ln(\rho)\cdot\zeta^2\right)+\zeta^2\right)\cdot\cos(\theta)}{\rho \cdot \left(1+\zeta^2\right)} \tag{3.34}$$

in which M is the moment produced by the drag force on the hair. The complete solution is presented in Appendix I.

To derive the stiffness of the membrane for anti-symmetric deflection we should write φ as a function of applied torque as

$$\varphi = \frac{M}{K_\varphi} = \frac{w\big|_{\rho=\zeta}}{R_h \cdot \cos(\theta)} \tag{3.35}$$

which results in

$$K_\varphi = \frac{-4\,\pi \cdot D \cdot \left(1+\zeta^2\right)}{\left(1-\zeta^2\right)+\left(1+\zeta^2\right)\cdot\ln(\zeta)} \tag{3.36}$$

Figure 3.7 shows the torsional stiffness of the membrane as a function of ζ. Figure 3.8 shows the deflection of the membrane considering a 2 pN·m torque and a 500 Pa pressure difference across the membrane. It shows both the downward displacement due to the static pressure difference and the anti-symmetric deflection

due to the external torque. The plot shows the membrane profile between the hair and the clamped edge along a diameter parallel to the fluid flow, i.e. $\theta=0$.

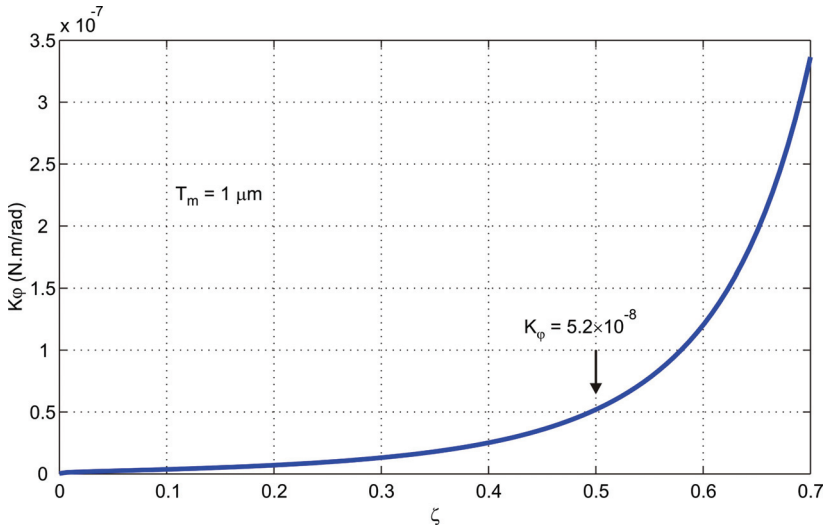

Figure 3.7 *The torsional stiffness as a function of ζ*

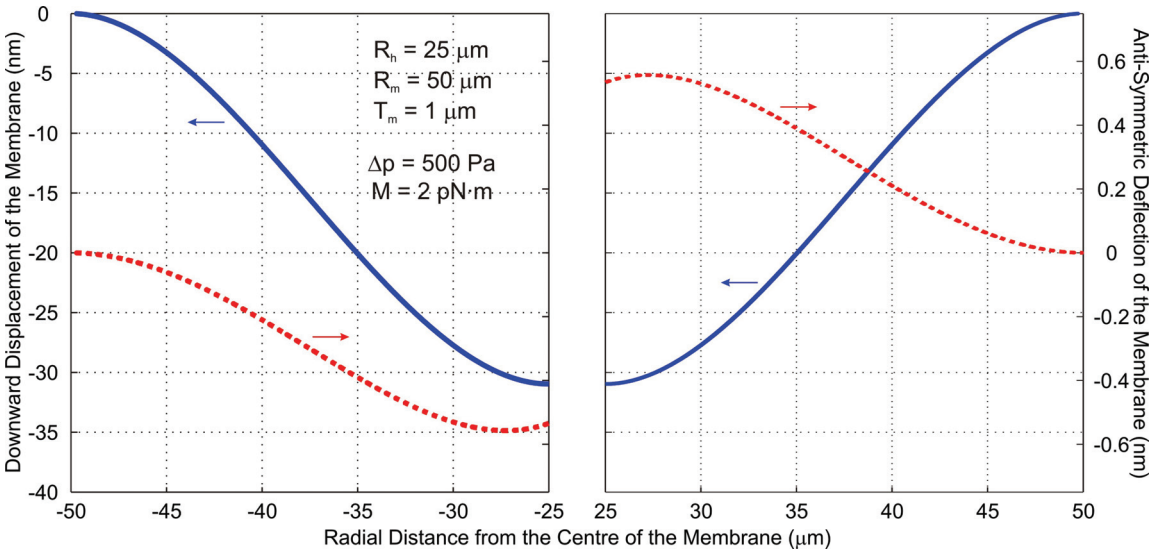

Figure 3.8 *The static downward displacement (left axis, solid line) due to 500 Pa pressure difference and the static anti-symmetric deflection (right axis, dashed line) due to 2 pN·m torque of a 1 μm thick SU-8 membrane. The distance between the two parts represents the hair diameter.*

3.3.3.3 Discussion

Before we end this section we should address some of the practical issues. First, in previous analysis we have assumed that the deformation of the membrane in the range of interest is small compare to its thickness. Therefore, the strain of the middle

plane of the plate can be neglected. In this case, the classical theory of thin plates can be used and the two modes of deflection can be treated separately. However, as the pressure difference across the membrane increases and the downward displacement becomes comparable to the membrane thickness, the membrane stiffens. This will affect the anti-symmetric bending. Naturally, the problem is more pronounced in case of thinner membranes. The nonlinear stiffening of the membrane can be avoided by adjusting the back pressure to avoid downward displacement (see section 3.3.4.1).

The other issue is the presence of initial tensile stress in the membrane. As discussed in section 3.3.7.1, and as we will see in the next chapter which deals with the fabrication, the membrane is made from SU-8. This polymer can develop a tensile stress after curing on a substrate. The governing equations for the membrane deflection should be changed accordingly to consider this fact. That is, if σ represents the uniform residual biaxial plane stress,

$$D \cdot \nabla^4 w - \sigma \cdot T_m \cdot \nabla^2 w = q(r,\theta) \tag{3.37}$$

To estimate the stiffening of the membrane due to residual stress one can use the change in the natural frequency of the desired mode. The natural frequencies of a circular plate with tension are given by [22] (compare with (3.25))

$$\omega_n = \frac{\alpha \cdot \beta}{R_m^2} \cdot \sqrt{\frac{D}{\rho_m \cdot T_m}} \tag{3.38}$$

For a fully clamped plate, α and β are obtained using

$$\begin{aligned} &\alpha \cdot \frac{J_{n+1}(\alpha)}{J_n(\alpha)} + \beta \cdot \frac{I_{n+1}(\beta)}{I_n(\beta)} = 0 \\ &\beta^2 - \alpha^2 = \frac{\sigma \cdot T_m \cdot R_m^2}{D} \end{aligned} \tag{3.39}$$

where J_n is the Bessel function of the first kind and order n and I_n is the modified Bessel function of the first kind and order n. The numerical evaluation of (3.39) for membranes with maximum residual stress ($\sigma_{\max} = 34$ MPa) and stress free membrane shows that $\omega_{max-stress} \approx 2.96\,\omega_{stress-free}$ from which we can conclude that $K_{max} \approx 8.8\,K_{min}$.

In addition, there is a thin aluminium layer that forms the electrodes and the lead wires connected to them at the bottom of the membrane (see section 3.3.5). This layer will increase the stiffness of the membrane. Although, again FEM analysis is needed in order to precisely account for their effect, an approximate evaluation can be done. It basically means that the actual structure is replaced by a single layer with an

effective flexural rigidity such that the stiffness of this artificial layer equals the stiffness of the actual compound layer. To estimate the effective flexural rigidity, one can consider the absolute worse case, which is when the membrane is fully covered by the aluminium. Considering the origin at the interface of the layers, the effective flexural rigidity of this bimorph membrane is derived as a function of z_n, the position of the neutral plane, from

$$D_{eff} = \int_{-T_{Al}}^{0} \frac{E_{Al} \cdot (z - z_n)^2}{1 - \nu_{Al}^2} + \int_{0}^{T_{SU8}} \frac{E_{SU8} \cdot (z - z_n)^2}{1 - \nu_{SU8}^2} \tag{3.40}$$

for which E_{Al} , ν_{Al} and T_{Al} are the Young's modules, Poisson's ratio and thickness of the aluminium layer respectively and E_{SU8} , ν_{SU8} and T_{SU8} are those of the SU-8 membrane. Figure 3.9 shows the flexural rigidity as a function of the neutral plane position. For equilibrium reasons the position of the neutral plane coincides with the minimum of the overall flexural rigidity. Using this approximation it can be seen that a 100 nm thick aluminium layer increases the flexural rigidity of a 1 μm thick SU-8 membrane by a factor of 3.3. The simulation results (see Figure 3.17) show that the actual increase in flexural rigidity, for the configuration with stiff centre, is about half of this value.

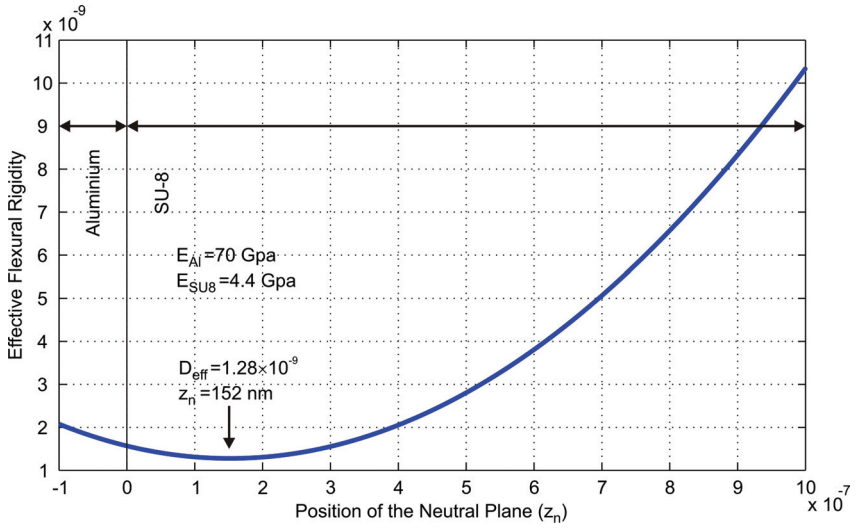

Figure 3.9 *Flexural Rigidity as a function of position of the neutral plane*

Finally, although the analysis and following design are based on circular shaped membranes, it can be shown that an elliptical membrane with its major axis along the desired direction of measurement (flow direction) exhibits bigger rotations. For a

clamped elliptical plate bent by a linearly varying pressure $q = q_0 \cdot x$ it has been shown [21] that

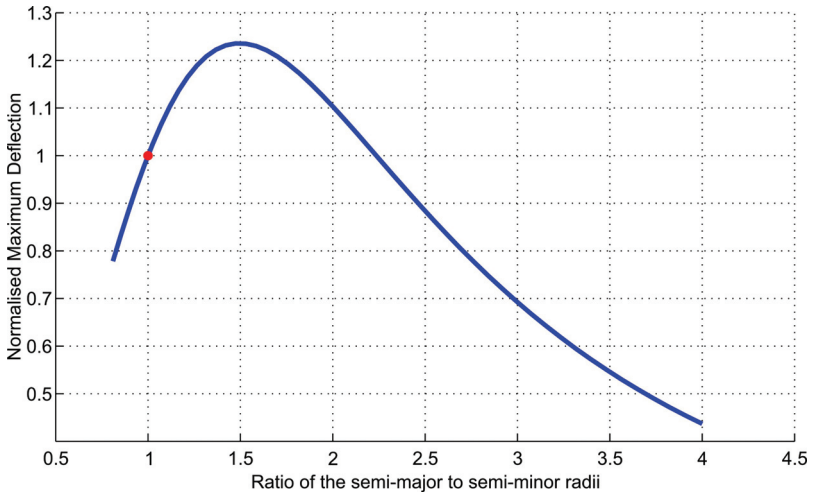

Figure 3.10 *Normalised maximum deflection of an elliptical membrane as a function of the ratio of semi-major radius to semi-minor radius. The red dot shows a circular membrane.*

$$w(x,y) = \frac{q_0 \cdot x}{24\,D} \cdot \frac{\left(1 - \frac{x^2}{a^2} - \frac{y^2}{b^2}\right)^2}{\frac{5}{a^4} + \frac{1}{b^4} + \frac{2}{a^2 \cdot b^2}} \tag{3.41}$$

where a and b are the semi-major and semi-minor axes respectively. When the total area of the plate is kept constant, the ratio of this expression to that of a clamped plain circular membrane carrying the same load (which can be obtained by substituting $b = a$ in (3.41)) is shown in Figure 3.10. It can be seen that the maximum deflection increases by a factor of about 1.24 when the semi-major radius is 1.5 times the semi-minor. Therefore, one can expect an improvement of the same order in plates with a stiff inclusion as in present case. However the exact measure is obtained using FEA (Finite Element Analysis) [23].

3.3.4 The dynamic mechanical model

The dynamic behaviour of the system, as shown in Figure 3.11, is approximated by that of a second order system. The governing equation is, therefore, written as

$$I \cdot \frac{\partial^2 \varphi_h}{\partial t^2} + R \cdot \frac{\partial \varphi_h}{\partial t} + K_\varphi \cdot \varphi_h = M \tag{3.42}$$

in which φ_h is the angular deflection of the hair structure, I is the moment of inertia, R is the damping factor, K_φ is the torsional resistance and M is the torque that is generated by the fluid drag force on the hair structure. The drag torque has been given by (3.11) and is repeated here for convenience

$$M = \int_0^{L_h} F(z,t)\cdot z\cdot dz = Z_s \cdot \int_0^{L_h} U_f \cdot z\cdot dz - j\,\omega\cdot Z_s \cdot \int_0^{L_h} \Phi_h \cdot z^2 \cdot dz$$

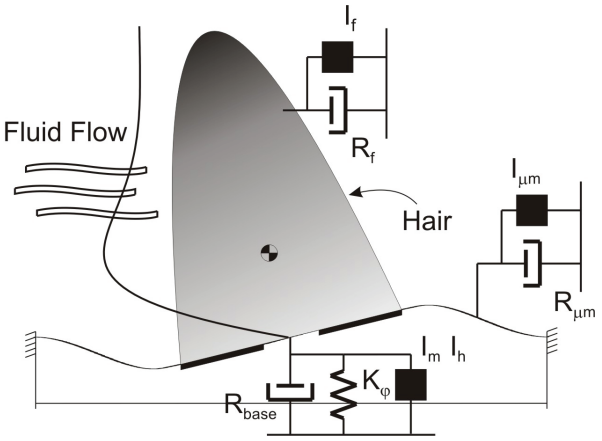

Figure 3.11 *Mechanical model of the structure*

When the bending of the cylinder is negligible, i.e. Φ_h is constant, the drag torque due to the movement of the cylinder, i.e. the second term at the right hand side of (3.11), is readily computed as

$$j\,\omega\cdot Z_s \cdot \int_0^{L_h} \Phi_h \cdot z^2 \cdot dz = \frac{L_h^3}{3}\left(j\,\omega\cdot\Phi_h\cdot Z_r - \omega^2\cdot\Phi_h\cdot Z_i\right) = j\,\omega\cdot\Phi_h\cdot R_f - \omega^2\cdot\Phi_h\cdot I_f \quad (3.43)$$

Taking this term to the left hand side of and expanding the coefficients to highlight all the individual contributions of various physical origin, (3.42) is rewritten as

$$\left(I_h + I_m + I_{\mu m} + I_f\right)\cdot\frac{\partial^2\varphi_h}{\partial t^2} + \left(R_{base} + R_{\mu m} + R_f\right)\cdot\frac{\partial\varphi_h}{\partial t} + K_\varphi\cdot\varphi_h = M_f \quad (3.44)$$

where M_f is the drag force of fluid on a stationary cylinder, i.e. the first term of the right hand side of the (3.11), as introduced at section 3.3.2.1. Note that this is only valid for harmonic flow and hair movement. Now, let us consider each of the coefficients separately. The torsional stiffness at the base of the hair structure is denoted by K_φ. This coefficient has been discussed at section 3.3.3.2 and is given by (3.36). The effective geometrical parameters in this coefficient are the ζ ratio, given by

(3.30), and the thickness of the membrane. The stiffness of the membrane increases with the third power of the thickness and its dependency on ζ is shown in Figure 3.7.

The first inertia coefficient, I_h, denotes the moment of inertia of the hair. For a cylindrical hair it is given by

$$I_h = m_h \cdot (\tfrac{1}{3} L_h^{\,2} + \tfrac{1}{4} R_h^{\,2}) \tag{3.45}$$

where, m_h, L_h and R_h are the mass, length and radius of the hair respectively. I_m is the rotary inertia of the membrane. An overestimation of this term is obtained, considering a rigid circular plate with free boundaries, as

$$I_m = m_m \cdot (\tfrac{1}{12} T_m^{\,2} + \tfrac{1}{4} R_m^{\,2}) \tag{3.46}$$

Here, m_m is the mass, T_m is the thickness and R_m is the radius of the membrane. The actual inertia is smaller than this value since the edge of the membrane is restricted and the movement of all the structural elements is less. Since the value of the inertia obtained using (3.46) is also small compare to other terms contributing in the total moment of inertia, this term can be effectively neglected[7].

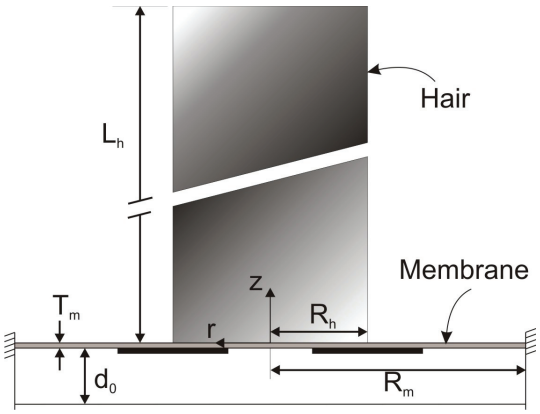

Figure 3.12 *The dimensions of the structure*

The effect of the contact of the membrane on one side with a high density fluid (i.e. water) appears as an added virtual mass [24] of the membrane which is denoted by $I_{\mu m}$. This term is related to the inertia of the membrane as

$$I_{\mu m} = \eta_{pq} \cdot I_m \tag{3.47}$$

[7] The rotary inertia of the membrane can be, more precisely, taken into account in the governing equation for vibration of the membrane, i.e. (3.20). However, again its effect appears only at high frequencies or large amplitude deflection.

where η_{pq} is the ratio of the induced surface kinetic energy of the liquid and that of the membrane and p and q denote the number of nodal diameters and circles respectively. It has been shown [25] that for a circular membrane

$$\eta_{pq} = \Gamma_{pq} \cdot \frac{\rho_L}{\rho_m} \cdot \frac{R_m}{T_m} \tag{3.48}$$

in again ρ_m is the density of the membrane material and ρ_L is the density of the fluid. Γpq is the non-dimensional added virtual mass incremental factor and is given in [24] and [25] for a number of different boundary conditions including a plain[8] fully supported membrane. For a clamped circular plate with Poisson's ratio of 0.3, Γ_{11} is approximately 0.3 which leads to $\eta_{11} \approx 12.5$. Although this is a substantial increase of the inertia, the collective effect is still negligible compare to the inertia of the hair and added inertia of the fluid (see Table 3-I).

The last part, I_ρ, is the result of the fluid displacement due to the relative movement of the hair structure. Using Stokes's theorem, this term is further divided into two parts as [8] (see (3.12))

$$I_\rho = \frac{\pi \rho_L \cdot R_h^2 \cdot L_h^3}{3} \tag{3.49}$$

$$I_\mu = -\frac{\pi^2 \mu \cdot G \cdot L_h^3}{3\omega \cdot g} \tag{3.50}$$

in which G is defined by (3.13). This highlights the distinct contributions of the density, I_ρ, and viscosity, I_μ, of the fluid as the added inertia.

Table 3-I *Comparison of the magnitude of different mechanisms which contribute to the moment of inertia of the system*

L_h (μm)	I_h	I_m	I_ρ	I_μ		
				10 Hz	100 Hz	200 Hz
500	9.84×10^{-17}	5.89×10^{-21}	8.18×10^{-17}	1.63×10^{-15}	4.85×10^{-16}	3.58×10^{-16}
900	5.73×10^{-16}	5.89×10^{-21}	4.77×10^{-16}	9.51×10^{-15}	2.83×10^{-15}	2.09×10^{-15}

The damping factor, R, has similarly been split into three parts. It consists of: First, R_{base} which is a damping coefficient due to the viscoelastic dissipation of energy at the base of the hair structure. It is partly a result of squeeze film damping under the

[8] The given added virtual incremental factor in the above mentioned references is for a plain circular membrane (i.e. without an inclusion in the middle as in the present case). However considering that a plain circular membrane is more flexible, the amount of energy transferred to the bulk of the fluid is higher. This translates to overestimations of added virtual mass incremental factor, Γ.

membrane which is derived and discussed in section 3.3.4.1. Another part of the damping at the base of the structure is due to the intrinsic structural damping of the material of the membrane. This damping linearly depends on the frequency and should be determined experimentally (see section 3.3.4.2 for more discussion). However, it can be derived that at low frequencies of interest, both of these effects are negligible. Second, R_{μ_m} which is a viscous damping coefficient due to the fluid-membrane interaction. For the first vibration mode having a nodal diameter (corresponds to Γ_{11}) this coefficient has been given by Lamb [25] for a plain, fully supported membrane as (c is the speed of sound in water ~1440 m/s)

$$R_{\mu m} = \frac{5}{576} \cdot \omega^4 \cdot R_m^4 \cdot \frac{\rho_L}{\rho_m} \cdot \frac{c}{T_m} \tag{3.51}$$

And finally R_f, a viscous damping coefficient due to the fluid-hair structure interaction. It is a result of non-zero viscosity of the fluid which results in frictional forces on the hair structure. Using the Stokes' theorem, it can be computed as [26]

$$R_f = R_{\mu h} = \frac{4}{3} \pi \cdot \mu \cdot G \cdot L_h^3 \tag{3.52}$$

In the next three sections we shall focus on these damping mechanisms, their relative importance and their effect on the dynamic response of the system.

3.3.4.1 Squeeze film damping

When an object moves inside a fluid, two forces act upon it: the inertial forces, which result from the displacement of the body of fluid, and the viscous forces due to the non-zero viscosity of the fluid. At large Reynolds numbers, i.e. large geometrical scales or high velocities, the viscous forces are negligible compared to inertia forces and other frictional forces. However, as the dimension of a system decreases the viscosity gains more significance. One particular case of interest arises when a solid object moves very close to a surface. This movement squeezes or stretches any intermediate fluid. The associate dissipation of kinetic energy which transfers to the fluid in this case is called squeeze film damping. In MEMS technology, such effects due to lateral and transversal movements have been studied thoroughly [27, 28].

In the present case, the movement of the two closely spaced electrodes result in squeeze film damping. An overestimation of this damping effect is obtained considering a sealed chamber under the membrane. To this end, the linearized isothermal Reynolds equation [29] is used to predict the effect of air pressure under the

membrane. The complete derivation of the resistive torque due to the squeeze film damping is given in Appendix II.

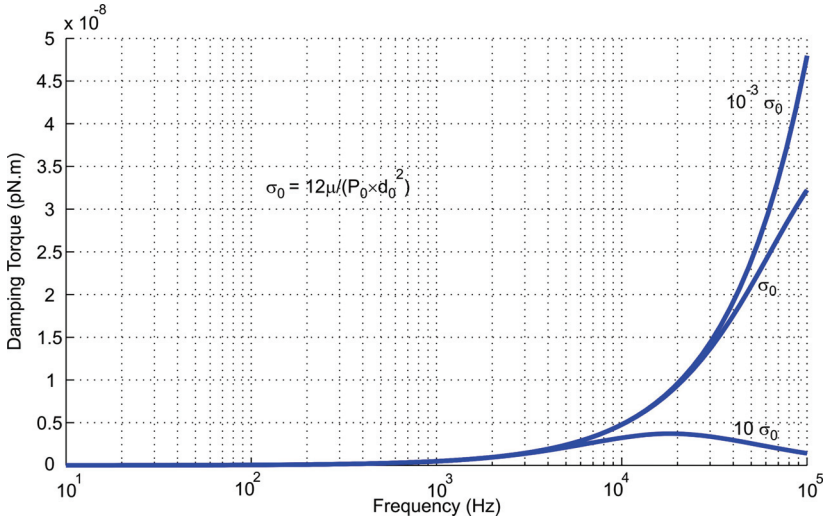

Figure 3.13 *Squeeze film damping torque generated by the air in the closed chamber under the membrane*

Figure 3.13 shows the resulting damping torque on the membrane at three different damping number, σ_0. It can be seen that at low frequencies of interest, the squeeze film damping is basically independent of the air pressure under the membrane, P_0. This is consistent with [30] and highlights one of the important features of the current design. The static downward deflection of the membrane (see section 3.3.3.1) can be tuned by adjusting the air pressure at the backside of the sensor. Therefore, the nonlinear effects that impose limitations on the dynamics behaviour of the sensor can be alleviated while the resulting damping is fairly constant.

3.3.4.2 Intrinsic material damping

The viscoelastic behaviour of a material can be modelled using the Kelvin-Voigt model [31]. To this end, the dynamic modulus is defined as

$$E^*(\omega) = E + j \cdot \eta \cdot \omega \tag{3.53}$$

in which the first term on the right hand side represents the energy storage or the spring function in the material. The second term represents the damping and is called loss modulus. The intrinsic quality factor of the material is defined as the ratio of the first term to the second term in (3.53). The inverse of the intrinsic quality factor is sometimes called the "loss factor".

Since the properties of SU-8 (the material used for the membrane) greatly depend on the processing procedure, experimental results are needed to obtain the exact value of the intrinsic damping. The experimental data on SU-8 cantilevers show that its intrinsic quality factor, Q_i, is lower than that of other structural materials [32-35]. Using the frequency dependent expressions of a second order system, intrinsic damping coefficient, R_i, can be computed as

$$R_i = \frac{\omega_n \cdot I}{Q_i(\omega)} = \frac{\sqrt{K_\varphi \cdot I}}{Q_i(\omega)} \tag{3.54}$$

Considering the Young's modulus of SU-8 is equal to 4.4 GPa and the reported value of loss modulus is 0.17 GPa [34] at 120 Hz[9], the intrinsic quality factor equals to $Q_i(\omega) \approx 3100/\omega$. However, SU-8 properties strongly depend on processing conditions and further systematic experiments are needed to support the analysis.

3.3.4.3 Discussion

A close investigation of the above mentioned contributions considering the geometrical characteristics of the structure and frequency range of interest shows that the viscous damping, R_f, dominates the damping specially at low frequencies. The magnitude of different damping coefficients at three frequencies for a 1 μm thick membrane are given in Table 3-II.

Table 3-II *Magnitude of different damping mechanisms on the structure*

Frequency (Hz)	$R_{squeeze}$	R_i		R_f		$R_{\mu m}$
		L_h = 500 μm	L_h = 900 μm	L_h = 500 μm	L_h = 900 μm	
10	7.05×10^{-22}	3.13×10^{-14}	7.56×10^{-14}	2.54×10^{-13}	1.48×10^{-12}	2.78×10^{-36}
100	6.85×10^{-22}	1.90×10^{-13}	4.58×10^{-13}	4.48×10^{-13}	2.61×10^{-12}	2.78×10^{-32}
200	6.42×10^{-22}	3.41×10^{-13}	8.24×10^{-13}	5.53×10^{-13}	3.23×10^{-12}	4.45×10^{-31}

The internal damping coefficient scales linearly with frequency and, therefore, quickly overrides the viscous damping at higher frequencies and limits the dynamic response of the system. In addition, as mentioned before, the squeeze film damping and viscous damping of the membrane are negligible in low frequency range. Figure 3.14 shows the amplitude of the rotation angle of the membrane for different hair

[9] Personal communication with Dr. A. T. Al-Halhouli, Technische Universität Braunschweig, Institute for Microtechnology.

lengths and diameters. It is clear that typically the quality factor of the system is around unity. The resonance frequency, and therefore the bandwidth, varies considerably by changing the hair diameter or length. It is of course clear that a thinner hair results in a more flexible membrane, hence a lower resonance frequency. However, we shall see in section 3.3.6 that the low frequency sensitivity drops at certain point when the hair diameter becomes increasingly small. This is due to the decrease of the flow induced drag torque on the hair.

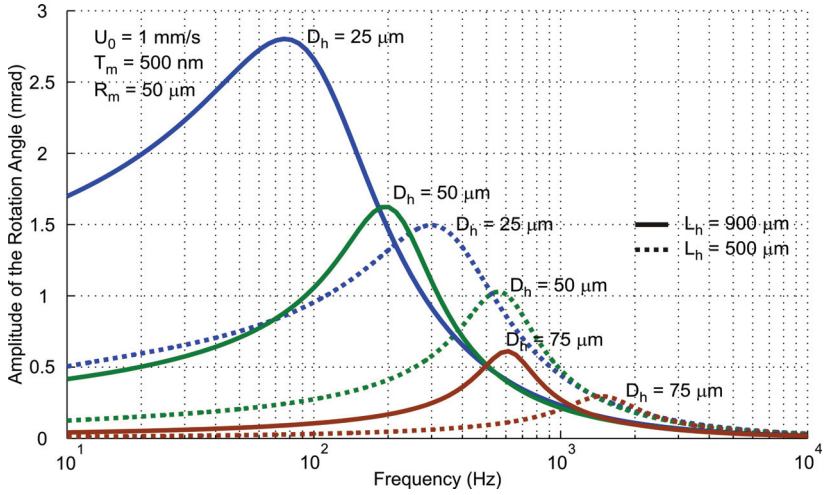

Figure 3.14 *Deflection amplitude as a function of frequency*

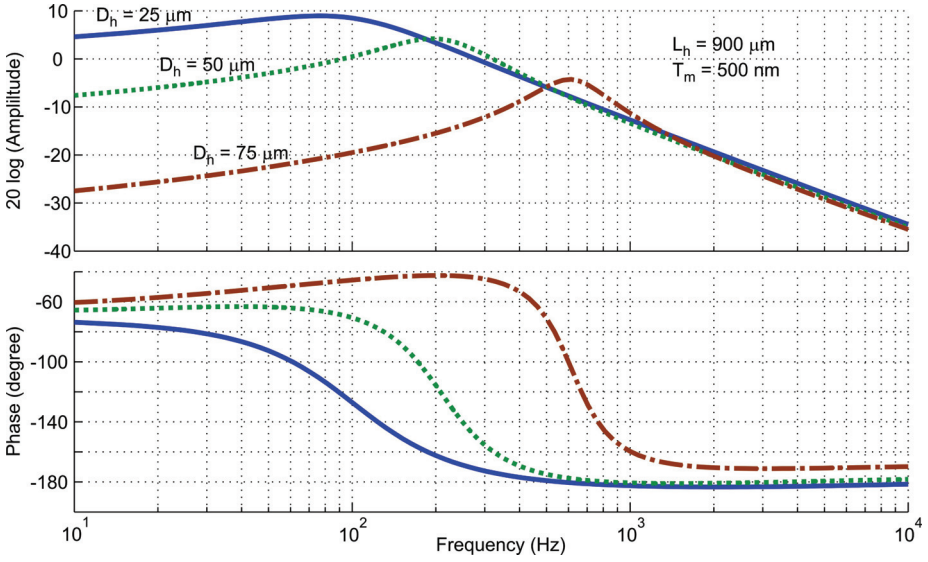

Figure 3.15 *Bode plot diagram of the frequency response of the system*

Figure 3.15 shows the Bode plot of the system. Considering the far field flow velocity as the input and rotation angle as the output, the general characteristic is that of a second order system with an additional low frequency zero. Mathematically, this zero results from the complex Stokes' mechanical impedance. The damping coefficients of the second order system obtained from the Bode plots are approximately 0.8, 0.4 and 0.25 for the hair diameters of 25, 50 and 75 μm respectively.

Naturally, the system with the fastest time response, i.e. the one with a smaller settling time[10], is preferred. When the system stays underdamped, the settling time is proportional to the inverse of the product of damping coefficient and resonance frequency. As a result, although it exhibits some overshoot, the sensor having a hair with a larger diameter has a faster response. On the other hand, a sensor having a hair with a smaller diameter has a higher sensitivity and is more close to a critically damped system. Therefore, it demonstrates the fastest response among the systems having the same bandwidth.

3.3.5 Electrical readout

The electrical ports of the device are two electrodes underneath the membrane. The change of their respective distances to the common electrode will modulate an electrical signal corresponding with the hair-rotation. The two possible configurations are shown in Figure 3.16. In order to derive an analytical estimate for the capacitance change to get some insight, one needs to approximate the membrane deflection. The capacitance depends on the area of the membrane that is covered with electrodes and on their exact shapes. A more accurate measure can be obtained using FEM analysis.

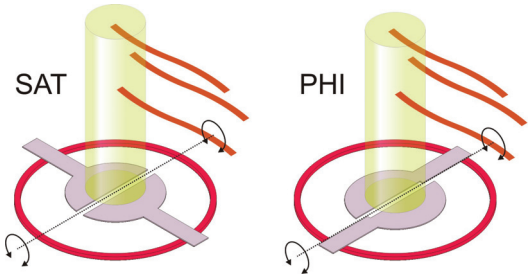

Figure 3.16 *Two configurations for electrodes. Left: in SAT configuration the wiring is perpendicular to the axis of rotation. Right: in PHI configuration the wiring is along the axis of rotation*

[10] Settling time of a system is defines as the time elapsed from the application of an input signal up to the point when the output reaches and stays within a specific error band, let say 2%, of the final value.

For the configurations shown (considering only the electrode part), using the parallel plate approximation, at the initial state (no deflection) the capacitance of each side is

$$C_i = \frac{\varepsilon \cdot \pi \cdot R_e^2}{2 \cdot d_0} \tag{3.55}$$

where ε is the electrical permittivity, R_e is the radius of the electrode and d_0 is the gap between counter electrodes. Now, to calculate the capacitance while the membrane is deflected, we need to evaluate

$$C_f = \iint \frac{\varepsilon \cdot r \cdot d\theta \cdot dr}{d_0 \pm w(r,\theta)} \tag{3.56}$$

in which w is derived form (3.34).

The size and position of lead wires that are connected to electrodes has an appreciable effect on membrane stiffness and, hence, on the deflection and associated capacitance change. For the optimization of the design, FEA (Finite Element Analysis) needs to be done for the two proposed structures (shown in Figure 3.16). In the *SAT* configuration lead wires are perpendicular to axis of rotation and the stiffness of the membrane is higher but the lead wires contribute to the capacitance. On the other hand in the *PHI* configuration the wires are along the rotation axis; the membrane is more flexible and has a larger deflection. Figure 3.17 shows the simulation results for both configurations. The overall stiffness of the membrane with electrodes has increased about 1.5 times.

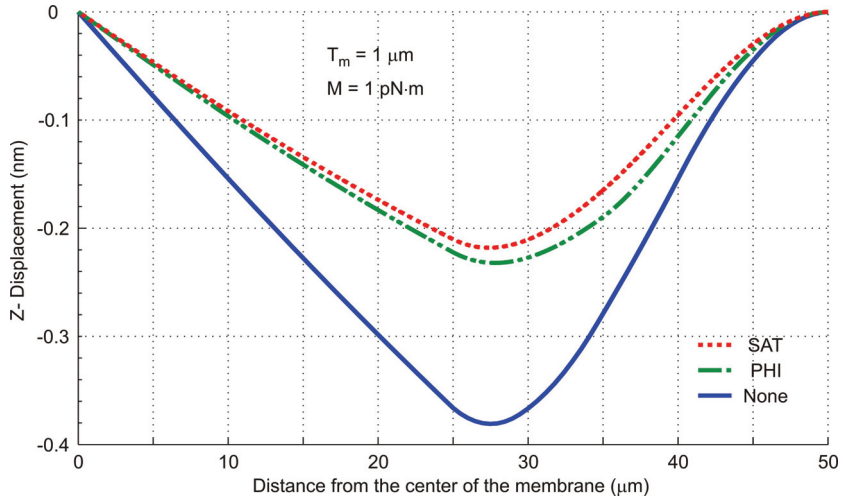

Figure 3.17 *The anti-symmetric deflection of the membrane with different electrode configurations (evaluated along the radius of the membrane parallel to the fluid flow, i.e. at θ=0)*

What is the best geometry of electrodes? The centre part of the membrane, where the hair is situated, is practically rigid. Therefore, addition of an aluminium layer does not change the overall stiffness. On the other hand, as the parts of the membrane close to the fixed edge do not undergo a large movement, the presence of aluminium layer is not beneficial for the overall electrical sensitivity. Therefore, the electrodes should cover the area under the hair but not close to the edge of the membrane. The effect of the area coverage of the electrodes is two fold. The smaller the covered area, the lower is the stiffness and hence the larger the displacement. However, at the same time, the smaller is the capacitance. The optimum geometry of the membrane needs to be determined using FEA. The results have been presented at [23].

3.3.5.1 Electrical circuit

A rough electrical model of the system and readout circuitry is depicted below.

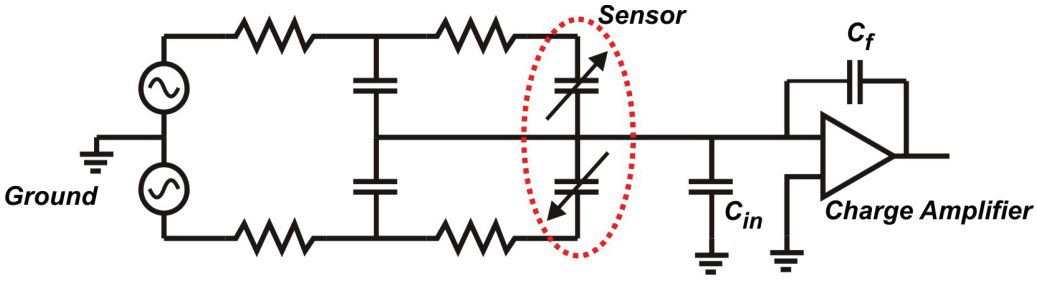

Figure 3.18 *Schematic of the electrical circuit model of the sensor*

Considering the change in the capacitances as a function of the applied moment, M, as

$$\begin{aligned} C_+ &= C_0 + \delta C(M) \\ C_- &= C_0 - \delta C(M) \end{aligned} \tag{3.57}$$

where

$$\delta C \approx \left.\frac{\partial C}{\partial M}\right|_{M=0} \cdot M \tag{3.58}$$

the feed current of the charge amplifier is

$$\begin{aligned} i_c &= \left((C_+ - C_-) \cdot \frac{\partial u_+}{\partial t} + u_+ \cdot \frac{\partial (C_+ - C_-)}{\partial t} \right) \\ &\approx 2 \left.\frac{\partial C}{\partial M}\right|_{M=0} \cdot \left(M \cdot \frac{\partial u_+}{\partial t} + u_+ \cdot \frac{\partial M}{\partial t} \right) \end{aligned} \tag{3.59}$$

where

$$u_+ = A \cdot \cos(\omega \cdot t)$$
$$u_- = -u_+ = -A \cdot \cos(\omega \cdot t) \tag{3.60}$$

The second term on the right hand side of the last equality is negligible at low flow frequencies, especially when considering that the electrical frequency is about 1 MHz. Therefore, the total current for n parallel sensors is

$$i_t \approx 2n \cdot M \cdot \left.\frac{\partial C}{\partial M}\right|_{M=0} \cdot \frac{\partial u_+}{\partial t} \tag{3.61}$$

The output voltage of the charge amplifier is, therefore,

$$u_{out} \approx 2n \cdot M \cdot \left.\frac{\partial C}{\partial M}\right|_{M=0} \cdot \frac{u_+}{C_f} \tag{3.62}$$

where C_f is the feedback capacitor. Using the relation given in Table 3-V (PHI configuration, 500 nm thick membrane), for $C_f = 2.2pF$ [11], an array of 500 sensors and a torque of 2 pN·m we obtain

$$u_{out} \approx 1.3u_+ \times 10^{-3} \tag{3.63}$$

3.3.6 Sensitivity

To estimate the overall sensitivity of the sensor, $\Delta C/\Delta U_0$, we use the previous analysis to evaluate approximate sensitivity using Taylor's expansion as (factor 2 accounts for the two halves of the membrane)

$$\frac{\Delta C}{\Delta U_0} \approx 2 \left.\frac{\partial C}{\partial d}\right|_{d=d_0} \cdot \left.\frac{\partial d}{\partial \varphi}\right|_{\varphi=0} \cdot \left.\frac{\partial \varphi}{\partial M}\right|_{M=0} \cdot \left.\frac{\partial M}{\partial U_0}\right|_{U_0=0} \tag{3.64}$$

Let us consider each term of the right hand side of (3.64) separately. The first term represents the electrical sensitivity and is easily obtained using parallel plate approximation as

$$\left.\frac{\partial C}{\partial d}\right|_{d=d_0} \approx \left.\frac{\partial}{\partial d}\left(\frac{\varepsilon_0 \cdot A_e}{d}\right)\right|_{d=d_0} = \frac{C_i}{d_0} \tag{3.65}$$

where ε_0 is the dielectric permittivity of air in between the electrodes, A_e and d are the surface area and the distance of the electrodes, d_0 is the initial gap and C_i is the initial capacitance (see section 3.3.5).

[11] Although a smaller feedback capacitance increases the gain, it may result in saturation of the charge amplifier or the next stage and decreases the bandwidth. In addition, when it is too small the input capacitance of the opamp gains more importance and determines the Signal to Noise Ratio (SNR).

The remaining terms collectively represent the mechanical sensitivity. When the change in capacitance, ΔC, is approximated as a linear function of the deflection angle [23], the second term of (3.64) is the mean deflection of the membrane defined as

$$\left.\frac{\partial d}{\partial \varphi}\right|_{\varphi=0} \approx \frac{\int_0^{R_m}\int_{-\pi/2}^{\pi/2} w \cdot r \cdot dr \cdot d\theta}{\pi R_m^2/2} \tag{3.66}$$

in which w is the displacement of the membrane (see section 3.3.3). One should note that although the electrode area is smaller than the area of the membrane, the overestimation is not large. This is due to the very small displacement of the membrane where there is no electrode, i.e. at the edge of the membrane and close to the rotation axis. The third term of (3.64) is basically the rotational stiffness of the membrane, K_φ, which has been given by (3.36). Combining these three terms, we can obtain $\Delta C/\Delta M$ which is shown in Figure 3.19 as a function of $\zeta = R_h/R_m$.

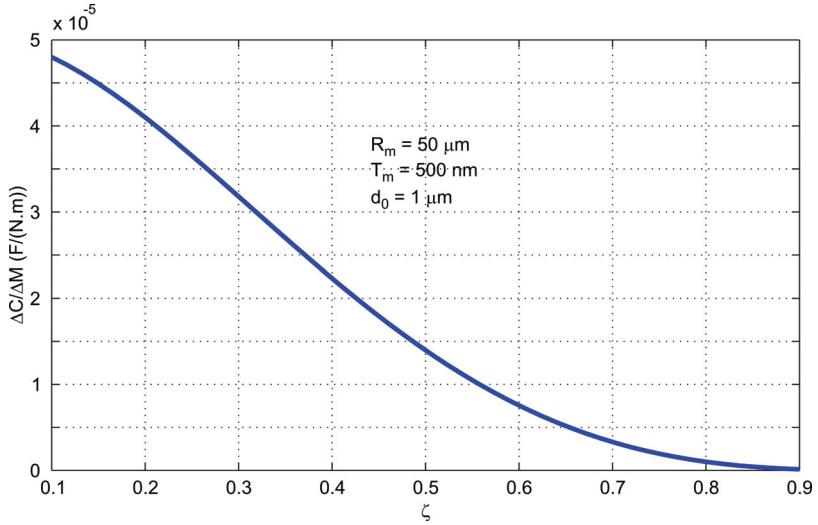

Figure 3.19 *The change in capacitance (one side) per unit torque*

The relation between the torque and the far field velocity amplitude, though frequency dependant, is linear. This can be seen from (3.11) and (3.6). Therefore, the last term on the right hand side of (3.64) is a frequency dependant factor. In section 3.3.7.2, to evaluate the sensitivity of the sensor for a proposed geometry we evaluate this relation.

3.3.7 The design

In this part we use the results of the analyses done in previous sections to introduce the design parameters and investigate the dependence of the sensor performance on them. This provides us with insight on how various parameters influence the static and dynamic behaviour of the system and results in the ability to tune the characteristics of the sensor to specific performance within the technological restrictions.

It has been said that the mechanical sensitivity, S_m, contains three distinct terms and is frequency dependant. However, it is the low frequency sensitivity that is important in the current application. The three terms come from the drag pickup mechanism, membrane flexibility and the resulting displacement as

$$S_m = \frac{\partial d}{\partial \varphi} \cdot \frac{\partial \varphi}{\partial M} \cdot \frac{\partial M}{\partial U_0} \tag{3.67}$$

Using the relations that have been developed in the pervious sections, it can be seen that approximately

$$\begin{aligned} &\partial M / \partial U_0 \propto L_h^2 \cdot R_h^{1/2} \\ &\partial \varphi / \partial M = E^{-1} \cdot T_m^{-3} \cdot \zeta^p \\ &\partial d / \partial \varphi \propto R_m \cdot \zeta^q \end{aligned} \tag{3.68}$$

where p and q are fitting parameters. Therefore, to increase the low frequency mechanical sensitivity

- a more compliant material should be used as the membrane. For a discussion about the material used for the membrane see section 3.3.7.1.
- the thickness of the membrane should be minimised. However, realisation of a defect free, thin membrane is technologically limited. For a discussion about the minimum achievable thickness of the membrane see section 3.3.7.1 and the chapter five on SU-8 processing.
- a larger membrane should be used. For a constant ζ, a larger membrane results in an increase of the mean deflection of the electrodes. This translates directly in a higher sensitivity.
- a thinner hair is needed. Although a thicker hair experiences more drag, its effect on membrane stiffness is dominant and, hence, it reduces the sensitivity.

- the length of the hair should be maximised. Technologically this is limited by the maximum achievable aspect ratio of the hair structure (which is the L_h to $D_h=2\cdot R_h$ ratio). This is limited to a maximum value of about 20. Therefore, when the diameter of the hair structure is 50 μm (see below) the maximum length is about 1 mm.

In practice, the relation between the corresponding terms in (3.68) and ζ is more complex. Therefore, the dependency of S_m on ζ cannot be described by one fitting factor ($p\times q$). It can be observed that S_m depends on $R_m^{p'}$ and $R_h^{-q'}$ where p' and q' are both positive and larger than one but they are not constant.

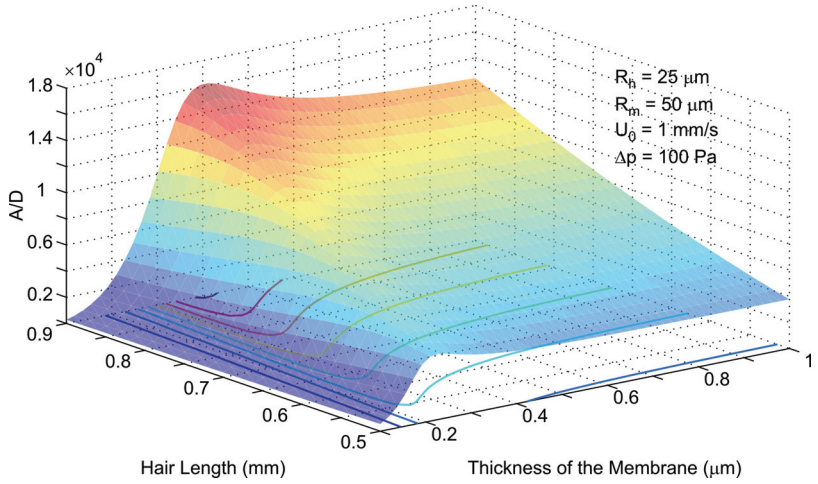

Figure 3.20 *A/D ratio as a function of the length of the hair and the thickness of the membrane at 100 Hz for R_h=25 μm, R_m=50 μm, U_0=1 mm/s and Δp=100 Pa across the membrane.*

The first three points mentioned above suggest that a thin, large and compliant membrane is favourable. However, one should note that such membrane experiences more downward deflection which may result in membrane stiffening as discussed before (see section 3.3.3.3). Although this effect can be compensated for by increasing the air pressure at the back of the membrane (see section 3.3.4.1), we shall introduce a parameter, hereafter called the A/D ratio, to quantify this effect. The A/D ratio is defined as the ratio between maximum displacement due to steady anti-symmetric deflection and that of static downward deflection. Note that the A/D ratio is a function of the frequency because the drag torque on the hair, hence the magnitude of the anti-symmetric deflection, depends on the frequency of the oscillatory flow. This ratio is shown in Figure 3.20 for a far field velocity of 1 mm/s and a pressure difference of 100 Pa across the membrane at 100 Hz. It weakly depends on the

thickness of the membrane with a maximum between 200 to 400 nm. Consequently, the thickness of the membrane should be in this range. In addition, it is clear from Figure 3.20 that the A/D ratio has a direct linear relation with the length of the hair structure for the membranes thicker than 200 nm. This emphasises the need for longer hairs.

Figure 3.21 shows the A/D ratio as a function of the radius of the hair structure and the radius of the membrane. When the radius of the membrane is very small the ratio increases but the flexibility ($1/K_{\varphi}$) decreases very rapidly which will seriously hamper the deflection of the membrane. On the other hand, large membranes exhibit low A/D ratio and are more difficult to fabricate. Therefore, at first the membrane radius is set to be between 50 to 60 μm.

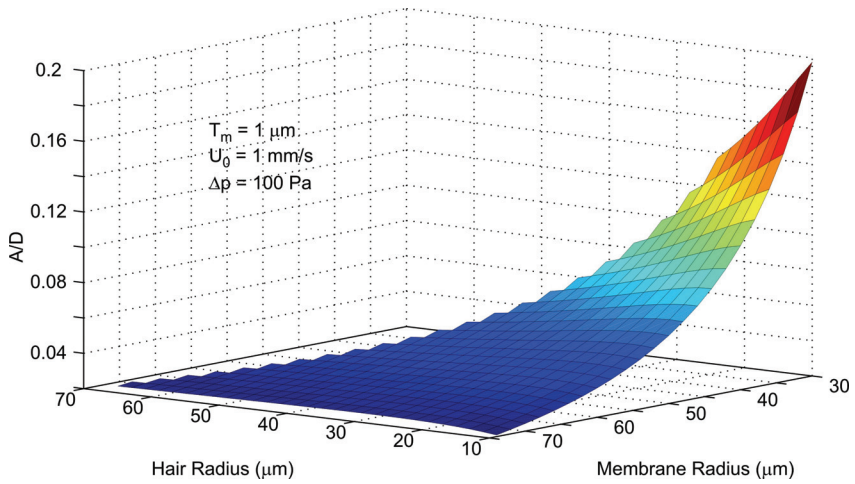

Figure 3.21 *A/D ratio as a function of the membrane radius and the hair radius at 100 Hz for T_m=1 μm, U0=1 mm/s and Δp=100 Pa across the membrane.*

As the last two points in the above mentioned list suggest a thin and long hair is favourable. Considering the radius of the membrane to be set, to decrease ζ the hair diameter should be reduced. However, in that case the drag force on a hair decreases as well and the fabrication of it becomes more difficult. Decrease of the hair diameter also results in a smaller moment of inertia but this will have a little effect on the dynamics of the system as the main contribution to the moment of inertia comes from the added mass due to the viscosity of the fluid (see Table 3-I). Figure 3.22 is a contour plot of the deflection amplitude of a sensor having a 500 nm thick circular membrane with a radius of 50 μm for different ζ ratios (hair radius is specified) considering all

above mentioned contributions. The figure is plotted for the two convenient and maximum technologically possible aspect ratios. It can be seen that the maximum deflection is obtained for hair diameter around 40 to 50 μm.

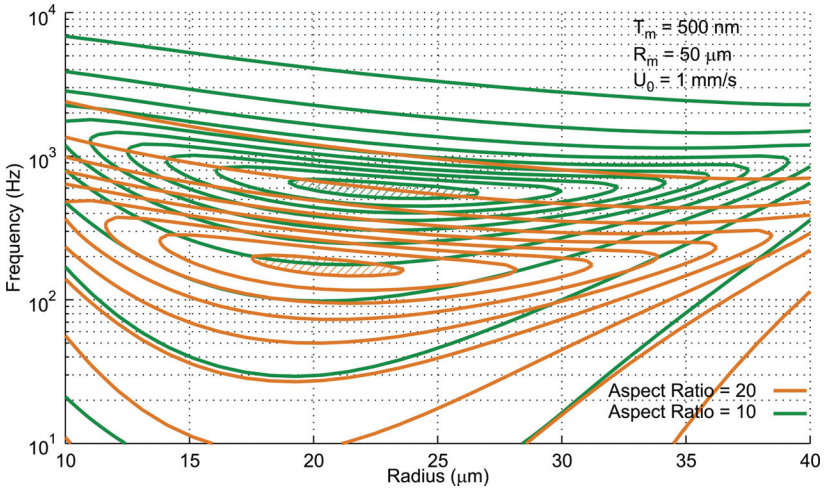

Figure 3.22 *Membrane deflection as a result of the fluid drag force for different hair radii considering a constant aspect ratio. The graph is plotted for two different aspect ratios, convenient and maximum.*

3.3.7.1 Material Selection

The silicon substrate on which the structure is build should be highly conductive or needs to be selectively doped to form the common electrode. The latter case needs more processing and adds an aligning step. Therefore, a highly conductive silicon wafer is chosen as a substrate. Later in the fabrication procedure it is described that the substrate should be double side polished as well to ease etching requirements.

Electrodes are made from aluminium. Aluminium has a good electrical conductivity and relatively low Young's modulus. It can also be deposited (sputtered) on the substrate at low temperatures yielding a low stress thin film. Moreover, the adhesion of aluminium to SU-8, which is an essential requirement in the design, is fairly good (see Table 3-III below).

SU-8

SU-8 is a negative tone, epoxy based, near UV (Ultra-Violet) photoresist [36]. This photoresist is used to realize chemically, thermally and mechanically stable structures at various aspect ratios. There is a series of standard SU-8 resists with varying viscosities. This provides the possibility to obtain a wide range of thicknesses (between 0.5 to 650 μm [37]) in a one time spin process. It can be exposed as normal

photoresists with standard contact lithography equipment as well as with e-beam or x-ray radiation. Consequently it is widely used in microfabrication. This includes lab-on-a-chip [38], Micro-optics [39-41] and various sensor applications [42-44] to name a few.

A normal process scheme is to spin coat, softbake, expose, Post Exposure Bake (PEB) and develop. Each step is described in detail in the next chapter as a part of the fabrication process.

Table 3-III *Mechanical and electrical characteristics of SU-8 and Parylene-C*

Property	**SU-8**	**Parylene**
Modulus of elasticity (E) (GPa)	4.02 [45]	4.75 [46]
	4.95 ± 0.42 [47]	
Poisson's ratio (ν)	0.22	0.4 [48]
Film stress (MPa)	16~19 [49]	~0
Maximum stress (MPa)	34 [47]	34
Bond strength (MPa)	20.7 ± 4.6 (on Si) [50]	
	12.1 ± 2.8 (on Al) [50]	
Coefficient of thermal expansion (α) (ppm/K)	52 ± 5.1 [49]	35
Thermal conductivity (W/mK)	0.2	0.082
Density (ρ) (kg/m³)	1200	1289
Relative dielectric constant (ε_r)	4 [51]	3.15 at 60 Hz, 2.95 at 1 MHz
Water absorption at 24 hour (% wt)		0.06
Biocompatibility	Good [52]	Very Good [53, 54]
Hydrophobicity	Hydrophobic	Hydrophobic [55]

The mechanical and electrical properties of this resist are given in Table 3-III. However it should be noted that the characteristics of SU-8 vary significantly with varying processing conditions. Moreover, SU-8 has a very good chemical resistance. Its adhesion to silicon substrates and aluminium (which will be used as electrode material) is pretty good (see Table 3-III). It has a good biocompatibility and is sometimes used to culture cells. Therefore, in brief, the points of interest are

- Using the broadband UV sources of standard lithography equipment, it is possible to reach aspect ratios as high as 20.
- It can be spun with varying thickness
    - About 500 nm for the membrane
    - About 500 μm for the hair structure (one-time spin)

- It is a good insulator which can cover the electrodes
- It has a low modulus of elasticity which is desirable for the membrane
- Using it for the membrane and hair structure provides good connection between them and alleviates adhesion problems.
- It is cost effective

On the other hand

- It can produce a large stress when a thick layer is used
- It has a very big coefficient of thermal expansion which can further produce some stress

The above mentioned properties designate SU-8 as a suitable material for fabrication of the membrane and the hair structure.

Parylene-C, PDMS and PMMA

In addition to SU-8, it is possible to use Parylene-C [56] to form flexible membranes. Parylene-C is transparent in the visible region, has a good thermal endurance and is chemically and biologically inert. Moreover, it is deposited at room temperature which means the layer has no initial thermal stress although the subsequent thermal steps may cause residual stress in Parylene-C thin films [48]. It is usually used for conformal coatings to protect fabricated devices but also as structural material for realisation of sensors [57] and actuators [58]. Table 3-III summarises some important properties of Parylene-C.

Other common polymers in MEMS technology which offer low Young's modulus are PDMS (Polydimethylsiloxane) and PMMA (polymethylmethacrylate). PDMS has a very low Young's modulus around 0.6 GPa, a high Poisson's ratio around 0.5, a high thermal expansion coefficient of 9×10^{-4} K^{-1} and a density of approximately 960 Kg/m^3. It is not photosensitive and is used in soft lithography [59] although, some photo-definable versions have been reported [60, 61]. Moreover, it is very difficult to realise thin layers of this polymer. This fact and the high thermal expansion coefficient are the main stumbling blocks for the use of this polymer as the membrane. In addition, the high aspect ratio hair structures still should be made of SU-8. However, SU-8 and PDMS exhibit a poor adhesion without surface modification [62].

PMMA is a positive resist used in e-beam, x-ray or deep UV lithography processes for high resolution imaging. It can be spun on the substrate to form thin

(<100 nm) or thick (>1 mm) layers. It has Young's modulus equal to 5 GPa, Poisson's ratio 0.34 to 0.4 and thermal expansion coefficient in the order of 2×10^{-4} K^{-1}. PMMA exhibits low sensitivity toward UV exposure and requires high doses at 248 nm. In addition, the thermal expansion coefficient is more than 4 times higher than SU-8. Therefore, it is not preferred over SU-8 or Parylene for the application in hand.

3.3.7.2 Evaluation

Considering the above analysis, structural parameters of the sensor are set as shown in Table 3-IV. The membrane and hair are made of SU-8 polymer (see the previous section) because of its compatibility with micro-fabrication technology and favourable mechanical characteristics, namely its low Young's Modulus. In addition, the mechanical properties of water are given.

Table 3-IV *Parameters of the mechanical system*

Parameter	Symbol	Value	Unit
Radius of the membrane	R_m	50×10^{-6}	m
Thickness of the membrane	T_m	500×10^{-9}	m
Radius of the hair	R_h	25×10^{-6}	m
Length of the hair	L_h	500×10^{-6}	m
Gap between counter electrodes	d_0	1×10^{-6}	m
Density of SU-8	ρ_{SU8}	1200	kg/m^3
Young's Modulus of SU-8	E_{SU8}	4.4×10^9	Pa
Poisson's ratio of SU-8	ν_{SU8}	0.22	
Density of water	ρ_f	1000	kg/m^3
Dynamic viscosity of water	μ	1.002×10^{-3}	Pa·s

The relation between the torque and the far field velocity is shown in Figure 3.23 from which the last term of (3.64) can be calculated. Note that this term is frequency dependant and, therefore, the sensitivity of the sensor varies with frequency. At higher frequencies the boundary layer is thinner and for specific far field velocity amplitude the drag torque on the hair, hence the sensitivity, is larger.

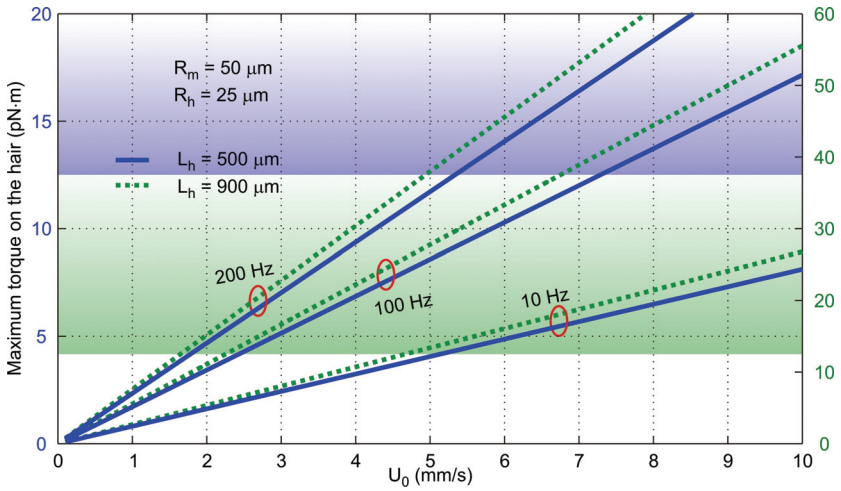

Figure 3.23 *Drag torque as a function of far field velocity amplitude at various frequencies*

When the minimum detectable relative change of capacitance, $\Delta C/C$, is 1% and considering the parasitic capacitances are 10 times larger than the initial capacitance, the minimum detectable torque using a 500 nm thick membrane is about 137 pN·m. However, when the parasitic and initial capacitances were in the same order, the minimum detectable torque would reduce to 12.5 pN·m. The detection threshold of the sensor in the later case is, therefore, 2.2 mm/s at 100 Hz for the hairs of 900 µm long. The shaded areas in Figure 3.23 show the detectable range of the torque for each axis. This detection threshold lies about 1000 times higher than that of the fish [63].

Table 3-V *Characteristics of the sensor*

	L_h = 500 µm		**L_h = 900 µm**	
T_m (µm)	1.0	0.5	1.0	0.5
Static ΔC/M (F/N·m) (One Side)	1.75×10^{-6}	1.40×10^{-5}	see the note below	see the note below
Simulated Static ΔC/M (F/N·m) (One Side)	2.005×10^{-6} (PHI) 1.930×10^{-6} (SAT)	1.482×10^{-5} (PHI) 1.367×10^{-5} (SAT)	see the note below	see the note below
Sensitivity (at 100 Hz) (aF/mm/s)	6	48	19	154
Detection threshold (at 100 Hz) (mm/s) $C_p=C_i$	59.25	7.25	18	2.2
Detection threshold (at 100 Hz) (mm/s) $C_p=10\cdot C_i$	320	40	100	12.5

The static change in capacitance per unit torque does not depend on the length of the hair. Therefore, these values are the same as those given in the left columns for 500 micometer hair length.

The mechanical sensitivity of the sensor is shown in Figure 3.24 and compared with that of fish [63]. It is seen that using the proposed geometry and materials, the sensitivity of the sensor is around two orders of magnitude below its natural

counterpart. In order to achieve a higher sensitivity, as discussed above, the drag pickup mechanism should be further improved and a thinner, larger and hence more flexible membrane should be employed. Furthermore, the overall performance is affected by the electrical sensitivity which is determined by the parasitic capacitances and the minimum detectable relative change of capacitance, $\Delta C/C$, both of which should be reduced by improvement of the readout circuit or possibly by integration of it with the sensor.

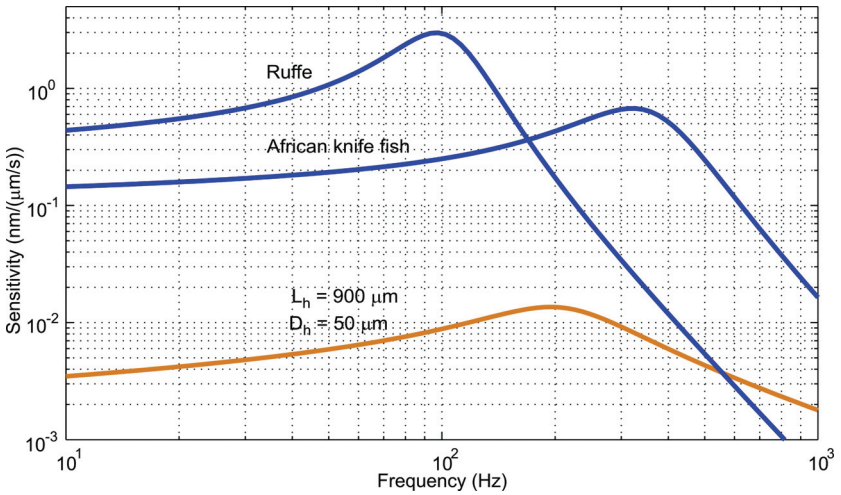

Figure 3.24 *Comparison of the mechanical sensitivities of the capacitive sensor and fish neuromast*

3.3.7.3 Optimisation

The performance of the sensor has (at least) two dimensions: the sensitivity and the bandwidth. The mechanical sensitivity has been discussed in detail at the first part of this section. The bandwidth is equal to the cut-off frequency, f_c. It is the frequency in which the sensitivity falls below the sensitivity at low frequencies. However, it is difficult to derive an analytical expression for it since the coefficients of the transfer function of the system depend on the frequency. Qualitatively, one can expect that a stiffer system or a system with lower moment of inertia has a higher resonance, hence, cut-off frequency. Therefore, in our case, considering K_φ and the moment of inertia, the resonance frequency has a direct relation with the Young's modulus and thickness of the membrane and the diameter of the hair. Moreover, it is inversely related to the length of the hair and the diameter of the membrane. It should be noted that the quality factor of the system also influences the cut-off frequency.

For the evaluation of the performance of the sensor we can also define a dimensionless Figure of Merit (*FoM*) as

$$FoM = Bandwidth \times Mechanical\ Sensitivity$$

Table 3-VI shows the calculated low frequency mechanical sensitivity, resonance and cut-off frequency and *FoM* for different geometries and compares them with that of fish. The current sensor geometry is R_m=*50* μm, T_m=*500* nm, D_b=*50* μm and L_b=*900* μm.

Table 3-VI *Comparison between fish and artificial sensor, current and optimised*

	Ruffe	**African Knife**	**Current**	**Optimised 1**	**Optimised 2**
Low frequency mechanical sensitivity (S_m) (nm/μm/s)	0.3	0.12	1.8×10^{-3}	1×10^{-2}	2.7×10^{-2}
Resonance frequency (Hz)	102	350	195	63	41
Cut-off frequency (Hz)	177	600	986	244	182
FoM	5.4×10^{-2}	7.4×10^{-2}	1.8×10^{-3}	2.5×10^{-3}	5×10^{-3}

The dimensions of the "optimised 1" sensor are R_m=*100* μm, T_m=*500* nm, D_b=*70* μm and L_b=*1000* μm and those of "optimised 2" sensor are R_m=*130* μm, T_m=*300* nm, D_b=*150* μm and L_b=*1000* μm. The sensors were chosen to have cut-off frequency around 200 Hz. The low frequency sensitivity of the optimised sensor is one order of magnitude better than the current sensor but less than that of fish by the same amount. The *FoM* is about an order of magnitude lower than fish.

Figure 3.25 shows the ratio of the above mentioned quantities when one of the dimensions of the sensor changes to that of the current design. It can be seen that an increase in the low frequency sensitivity is always accompanied by a decrease in the cut-off frequency. The former increases as the radius of the membrane or the length of the hair increase. However, overall *FoM* is fairly constant. It slightly increases as the hair diameter increases and decreases when a longer hair is used.

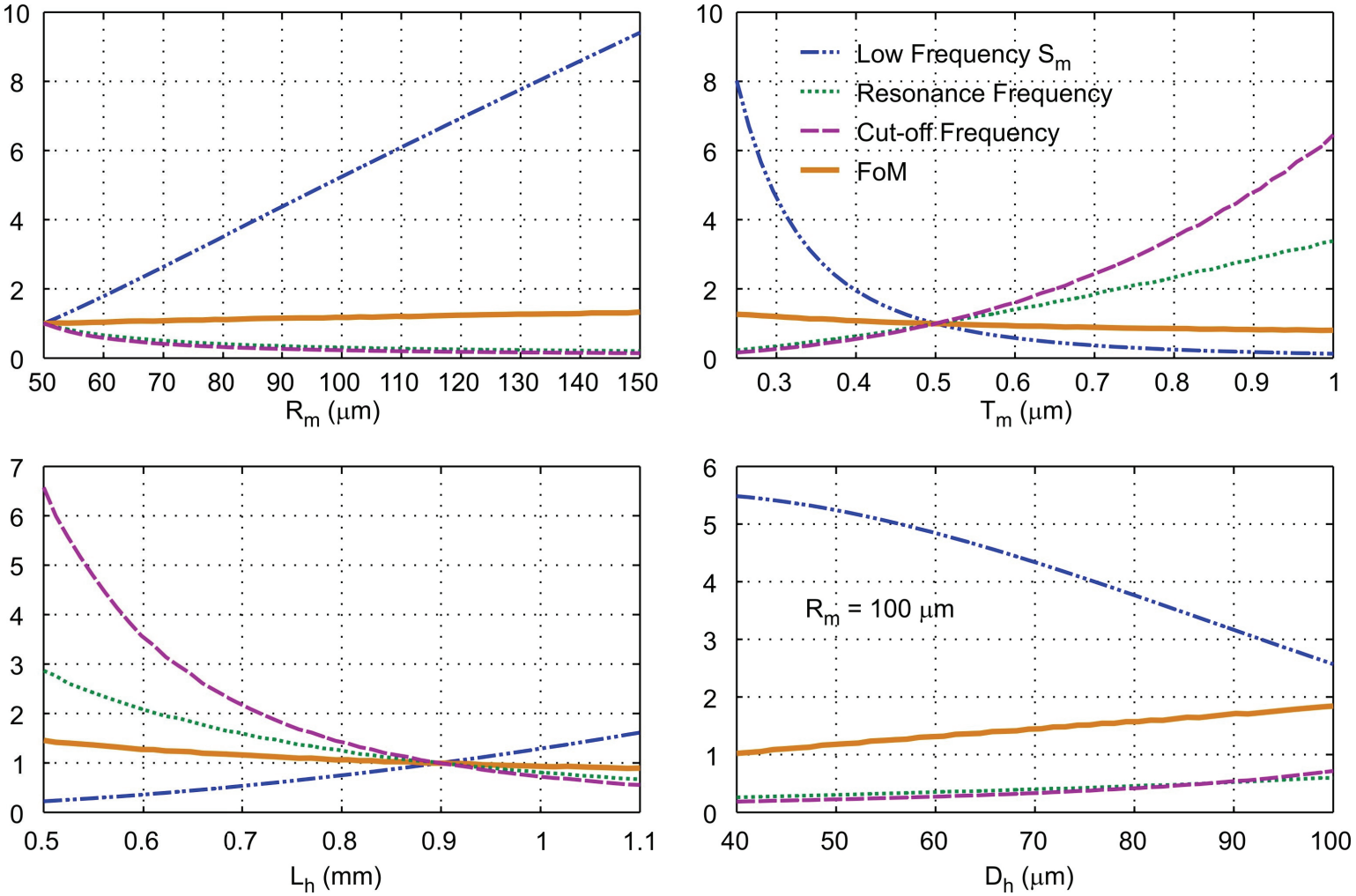

Figure 3.25 *The ratio of the low frequency mechanical sensitivity, resonance and cut-off frequency and FoM for different geometries to those of the current sensor*

Although in the definition of *FoM* we did not take it into account, it is clear that the electrical sensitivity should also be maximised. Referring back to (3.65) it can be seen that $\partial C/\partial d \propto R_m^2/d_0^2$. This suggests that a bigger membrane brings forth even more advantages. In addition, the gap between the electrodes plays an important rule in the electrical sensitivity, hence in the overall performance of the system. The narrower the gap, the higher is the sensitivity but the more difficult the fabrication procedure. Note that $\Delta C/C$ does not change when the radius of the membrane changes and it is inversely proportional to the gap between the electrodes.

Now, let us now refer back to Figure 3.22. It has been discussed that to obtain a more flexible membrane the radius of the hair should be minimised but, at the same time, the drag force on a thinner hair decreases. Therefore, the optimum hair radius has been evaluated to be between 20 to 25 μm. In order to decoupled ζ and L_h, the hair can be made of two separate segments as shown in Figure 3.26. The thicker top segment provides a wider area and the fluid exerts a greater drag force on it while a thinner segment at the bottom is used to tune the flexibility of the membrane. In this way ζ and L_h can be tuned separately without having adverse effects on each other through the limited aspect ratio of the hair structure.

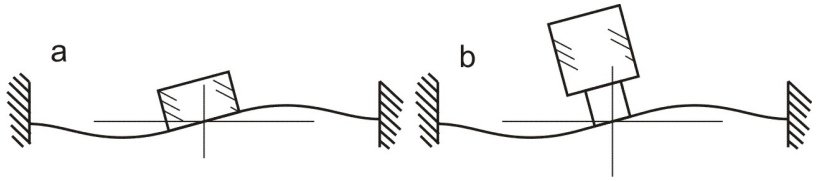

Figure 3.26 *The optimization of the shape of the hair structure, a) the normal shape b) the mace shape*

However, when the aspect ratio of the lower segment increases its rigidity decreases. Therefore, to avoid any detrimental effect on the mechanical energy transfer into the flexible membrane, the hair structure should be several orders of magnitude stiffer than the membrane. Considering an absolutely rigid upper part, the stiffness of a two segmented hair structure, as experienced at the tip of the hair, is approximated by

$$K_s = 12\frac{E_s \cdot I_s}{L_s \cdot \left(4L_s^2 + 9L_h \cdot L_s + 6L_h^2\right)} \tag{3.69}$$

in which K_s, L_s, E_s and I_s are the stiffness, length, Young's modulus and moment of inertia of the lower segment (stem) respectively and L_h is the length of the upper segment of the structure. Considering the typical geometry and parameters of interest, the K_φ/K_s ratio with reference to (3.36) is on the order of 10^{-7}. This small ratio shows

that a two segmented hair, like a normal hair, can be considered rigid with respect to the underneath membrane. Therefore, the energy transfer from oscillatory fluid to the membrane is not affected.

Figure 3.27 shows the increase in the maximum deflection angle of a membrane having 50 μm radius considering an upper segment with a fixed geometry. It shows that the overall displacement of the membrane improves approximately 35 times when the radius of the stem reduces from 25 to 5 μm. A longer stem part passes deeper into the boundary layer (see Figure 3.2) and, therefore, increases the fluid force on the upper part. This, however, has more importance at lower frequencies.

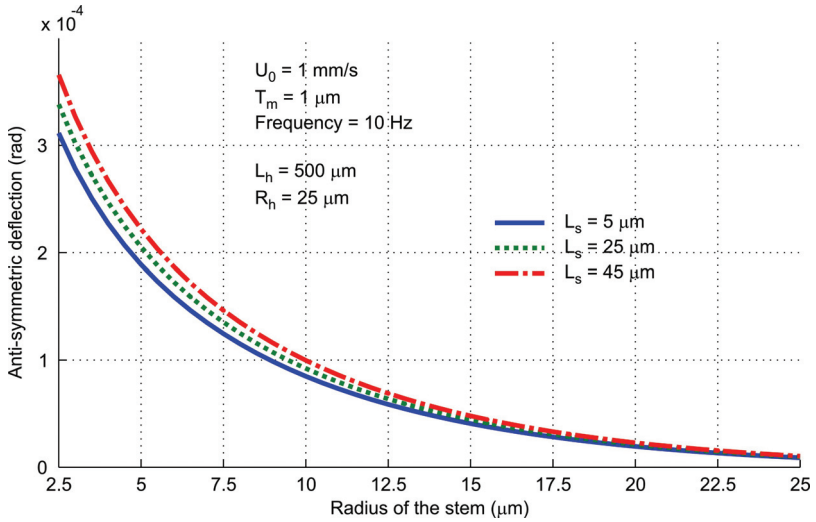

Figure 3.27 *Change of the maximum deflection angle of the membrane by reducing the radius of the stem*

3.4 Canal Embedded Sensors

In this part, the design of canal embedded hair-based flow sensors inspired by the canal neuromasts of fish is presented. The design and fabrication procedures allow for variations of functional characteristics of individual sensors within an array and within a canal. The proposed sensor design consists of three electrodes: one floating electrode on the tip of a hanging hair and two counter-electrodes parallel with the floating electrode (see Figure 3.28). This structure forms a differential capacitive sensor. Although the floating electrode is in contact with the liquid medium, the two other (differential electrodes) are insulated. This prevents short circuits and electrolysis which are among the main concerns in aquatic environments. The simultaneous

fabrication of the sensory structures and the embedding canal is an important feature of this process.

3.4.1 Design

A schematic of the hair structure is shown in Figure 3.28. The structure has two parts: A thin supporting beam which is connected to the top of the channel (hereafter called stem) and a wider area (hereafter called hair) upon which the fluid drag force acts but is essentially rigid. There is a floating electrode on the tip of the hair which forms two capacitors with the fixed electrodes underneath. Deflection of the hair due to the fluid drag force causes a change in the distance between the capacitor plates and in the overlap area of the plates, which reflects in a variation of the magnitude of the capacitance that can be detected. This deflection can be measured differentially to obtain the fluid velocity.

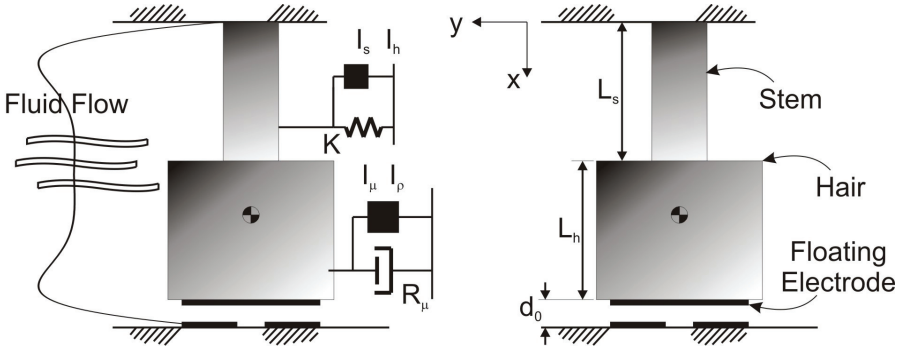

Figure 3.28 *The schematic of the canal embedded flow sensor (not to scale). The flow profile is indicated at the left side of the figure.*

The resonance frequency and sensitivity of hairs depends on the stiffness of the support. The stiffness of a cylindrical supporting structure, as proposed in this work, strongly depends on its length and diameter, of which the latter can be varied within a large margin in the design. Moreover, the procedure is suitable for fabrication of sensory arrays.

The base of the structure, i.e. the top of the canal, is considered to be rigid. Therefore, to increase the flexibility of the hair while maintaining the necessary area for the floating electrode, as shown in Figure 3.28, a segmented structure is needed. When the force on the larger part is considered uniform and the force on the support is neglected, the stiffness of the structure, as experienced at the tip of the hair, is approximated by

$$S = 12\frac{E_s \cdot I_s}{L_s \cdot \left(4L_s^2 + 9L_h \cdot L_s + 6L_h^2\right)} \tag{3.70}$$

where E_s, I_s and L_s are the Young's modulus of elasticity, the moment of inertia and the length of the supporting segment and L_h is the length of the hair. When the total force on the wider part is denoted by F_t, using simple geometrical calculations it can be seen that to prevent the side of the wider part to touch the substrate

$$F_t \cdot L_s^2 \cdot \left(\frac{L_h}{2L_s} + 0.5\right) \Big/ E_s \cdot I_s < \frac{R_h}{L_h} \tag{3.71}$$

which is satisfied considering the drag force in our range of interest.

The design process can be divided into two parts. First, the flow profile in a canal should be calculated. The force on a cylindrical structure in a canal is determined using the same procedure as outlined in section 3.3.2 for superficial structures. Second, the hair deflection due to the fluid drag force, which determines the relative change in the capacitance, should be evaluated.

To derive the flow velocity the canal can be approximated by two opposing infinite flat substrates and be treated as has been discussed in section 3.3.2.1. When the boundary layer thickness is less than half the height of the canal the flow profile is found from a combination of the effects of the two substrates. When the height of the canal is 1 mm, this condition is readily satisfied for frequencies above 25 Hz. Further, the problem of determining the velocity profile of an oscillatory flow in a tube with circular cross section has been solved analytically for laminar flow [64]. The solution can be expressed in the form of Bessel functions with imaginary arguments as

$$U_C = \frac{-j \cdot A_0 \cdot e^{j \cdot \omega \cdot t}}{\omega} \cdot \left(1 - \frac{J_0\left(\sqrt{-2j} \cdot r/\delta\right)}{J_0\left(\sqrt{-2j} \cdot R/\delta\right)}\right) \tag{3.72}$$

where R is the radius of the tube, r is the distance to the centre line, δ is proportional to the boundary layer thickness (for definition see section 3.3.2.1) and A_0 is the amplitude of fluid acceleration outside the tube. Note that the velocity is the real part of the right hand side of (3.72). Figure 3.29 shows the velocity profile of an oscillating flow in a circular tube with 1 mm diameter. As can be seen, at higher frequencies the thickness of the boundary layer decreases and the velocity at the centre line approaches the far field velocity. At low frequencies, however, the boundary layers merge and form a parabolic flow profile.

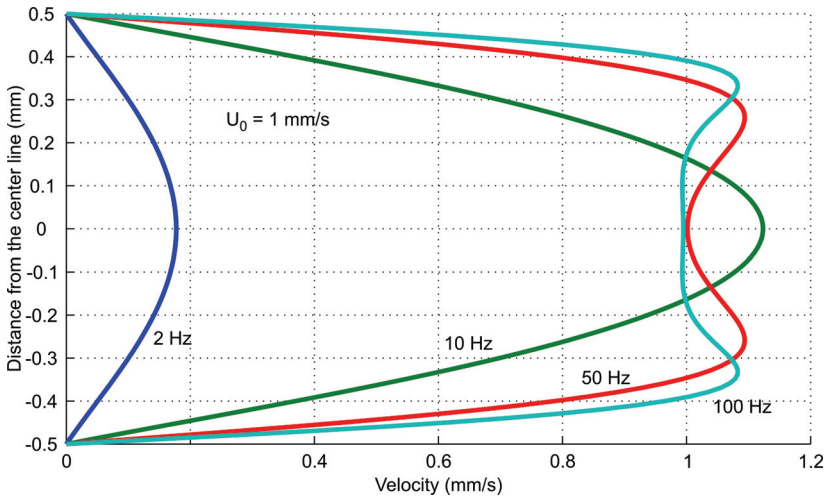

Figure 3.29 *The maximum velocity profile of water in a circular canal. The diameter of the cross section is 1 mm.*

In fish, equidistant pores in the canal couple external fluid flow to the flow inside the canal. Since it is possible to integrate the fabrication of these pores with the rest of the structure, we shall examine their effect on the internal fluid flow. However when the dimensionless product of Reynolds and Strouhal numbers for the canal

$$Re \cdot St = \frac{\omega \cdot D_h^2}{\nu} \tag{3.73}$$

is very small (i.e. $\ll 16$), the fluid velocity near the centre line of the tube can be approximated by [65]

$$U_C \approx \frac{A_0 \cdot (Re \cdot St)}{4\omega} \cdot \cos(\omega \cdot t) \tag{3.74}$$

and when it is very large (i.e. $\gg 16$) by

$$U_0 \approx \frac{A_0}{\omega} \cdot \sin(\omega \cdot t) \tag{3.75}$$

In these equations ω is the frequency of oscillation, ν is the kinematic viscosity and D_h is the diameter of the canal. A_0, the amplitude of fluid acceleration, is related to the pressure gradient in the tube as

$$\frac{dP}{dx} = -\rho \cdot A_0 \cdot e^{j\omega \cdot t} \tag{3.76}$$

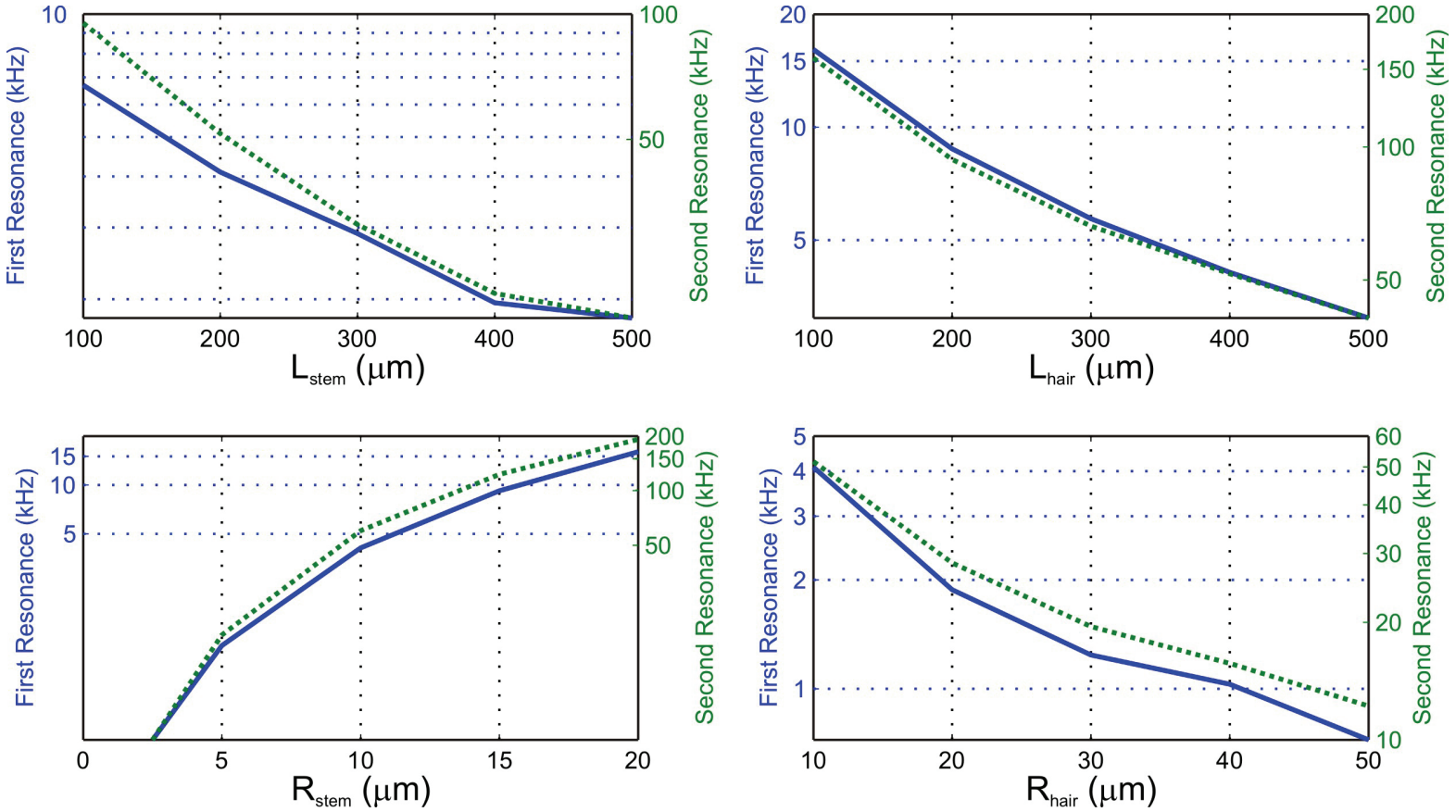

Figure 3.30 *The change of first and second resonance frequency of the structure with varying geometrical characteristics: Top Left:* R_s*=5 μm,* R_h*=10 μm,* L_h*=400 μm; Top Right:* R_s*=5 μm,* R_h*=10 μm,* L_s*=200 μm; Bottom Left:* L_s*=200 μm,* L_h*=400 μm,* R_h*=40 μm; Bottom Right:* L_s*=200 μm,* L_h*=400 μm,* R_s*=5 μm.*

which upon considering an oscillatory pressure, a linear pressure drop and a tube of length L leads to $A_0 = \Delta P/(\rho \cdot L)$. In the range of interest for the problem at hand, the centreline velocity of a canal is given by (3.75) for frequencies above 25 Hz. The above mentioned relations are used to compute the necessary pressure threshold from the minimum detectable velocity of the fluid at the centreline.

The dynamic behaviour of the system should be examined as well. The governing equation for vibration of an Euler-Bernoulli beam (neglecting the shear deformation and rotary inertia) is

$$EI \cdot \frac{\partial^4 w}{\partial x^4} + \rho \cdot A \cdot \frac{\partial^2 w}{\partial t^2} + \eta \cdot \frac{\partial w}{\partial t} = f(x,t) \tag{3.77}$$

where E is the Young's modulus, I is the moment of inertia, $A = \pi R_s^2$ is the constant cross sectional area, ρ is the mass density, η is the structural damping coefficient and f is the distributed drag force, i.e. force per unit length of the structure. The procedure to derive the natural resonance frequencies and mode shapes from the homogenous, undamped equation is presented in Appendix IV. Figure 3.30 indicates the (simulated) first and second natural frequencies for varying geometrical properties and the corresponding mode shapes are shown in Figure 3.31. It can be seen that the length of the hair and the diameter of the stem have very strong effects on the flexibility of the system.

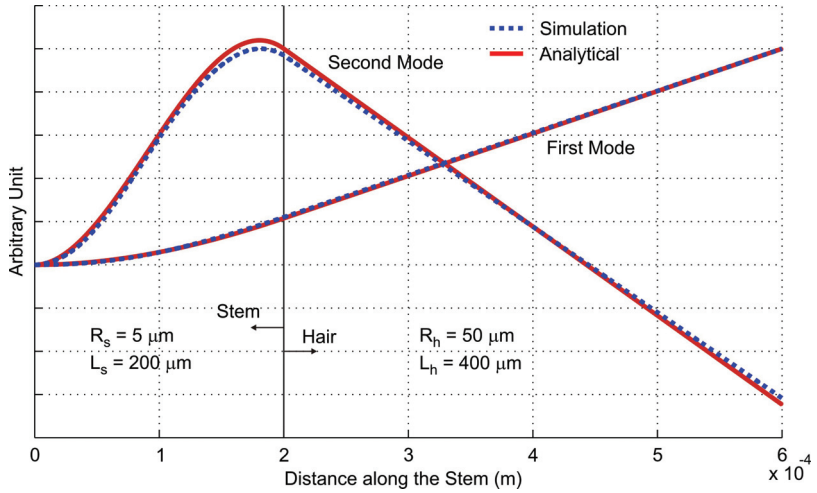

Figure 3.31 *Comparison between analytical and simulation of the first and second mode shapes*

Having the resonance frequencies and mode shapes, the actual deflection of a beam is derived using modal analysis. We shall seek a solution of the form

$$w(x,t) = \sum_i q_i(t) \cdot X_i(x) \tag{3.78}$$

in which X_i is the i^{th} mode shape of the homogenous, undamped equation and q_i is the generalised coordinate. The full derivation of the weighting factors is also to be found in Appendix IV. Figure 3.32 shows the approximate frequency response of a sensor with the given dimension. It exhibits a resonance frequency around 400 Hz and a quality factor of about 0.75. The mechanical sensitivities at 10 and 100 Hz are 38 and 180 nm/mm/s respectively. The intrinsic damping of the structure has been neglected in computation of the frequency response curve.

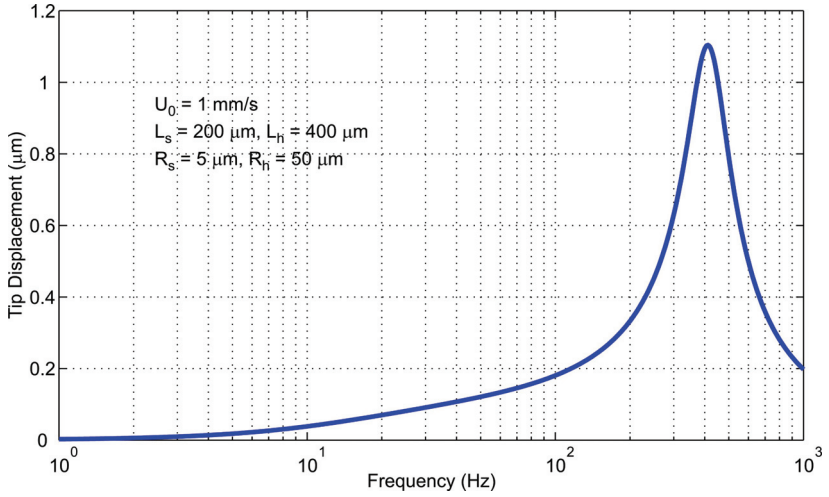

Figure 3.32 *The frequency response of the hair structure in a circular canal*

The structure of the electrodes is shown in Figure 3.33. We choose the initial capacitance to be between 0.1 pF and 1 pF[12]. Neglecting the fringing field, the proposed geometry leads to 0.42 pF initial capacitance (one side; the dielectric permittivity of water is chosen 80 and the gap between counter electrodes is 1 μm). This means that maximum 3 hairs need to be connected in parallel to satisfy the initial static capacitance criteria.

In addition, considering that the minimum detectable relative change in the capacitance, $\Delta C/C$, is 0.01[13], the displacement should satisfy $|\delta w| > 0.01 w_{overlap}$ (δw is the horizontal displacement at the tip of the hair and $w_{overlap}$ is the initial overlap width of an

[12] In order to have a reasonable signal to noise ratio and a predictable performance, the total initial capacitance of the sensors connected in parallel should be comparable to the parasitic capacitances.
[13] Just a rule of thumb to make sure that the out-of-phase input voltages for differential read-out circuitry can be balanced within the limited accuracy of the available sources.

electrode pair, i.e. 2 μm for this design). Using the above configuration, the displacement at the tip of the hair should be above 20 nm. The asymmetric pattern of the electrodes plays an important rule in determining the relative capacitance change.

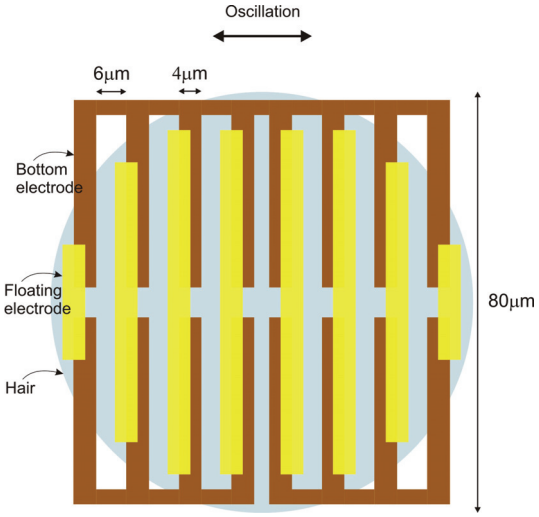

Figure 3.33 *Schematic drawing of the electrode configuration*

Note that neglecting fringing fields results in a serious underestimation of the capacitance as the dimensions of the gap and the overlap width of the electrodes are comparable. Moreover, the high relative electrical permittivity of water increases the capacitance which is a beneficial effect against parasitics. The values given above are for the first order approximation of the capacitance. The exact values should be obtained using FEM. Figure 3.34 shows the simulated configuration using COMSOL Multiphysics® 3.5a. The evaluation of the total capacitance results in 0.71 pF, compared to 0.42 for the situation without fringe fields. The required horizontal displacement of the floating electrode for 1% relative capacitance change, $\Delta C/C$, is about 30 nm which is 1.5 times larger than what has been calculated with simple equations. This results in an overall sensitivity of about 43 fF/mm/s.

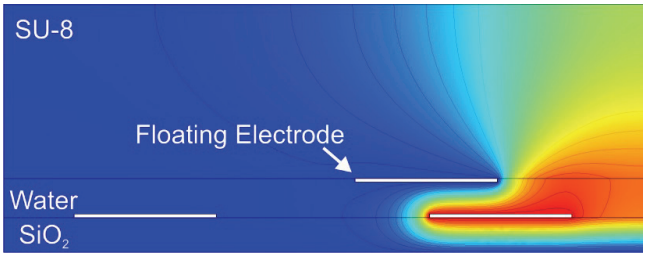

Figure 3.34 *The simulated configuration for electrical capacitance estimations*

3.5 BooT[14] (Laterally Moving Sensor)

Shear force sensors using micro-fabrication technology are well known. There are many examples using piezoresistive or capacitive readout mechanisms with largely varying specifications [66-71]. There also have been some attempts for realisation of shear stress sensors to operate in liquids [72-74]. In this part, another design for hair-based flow sensors resembling shear-stress sensors is presented.

3.5.1 Design

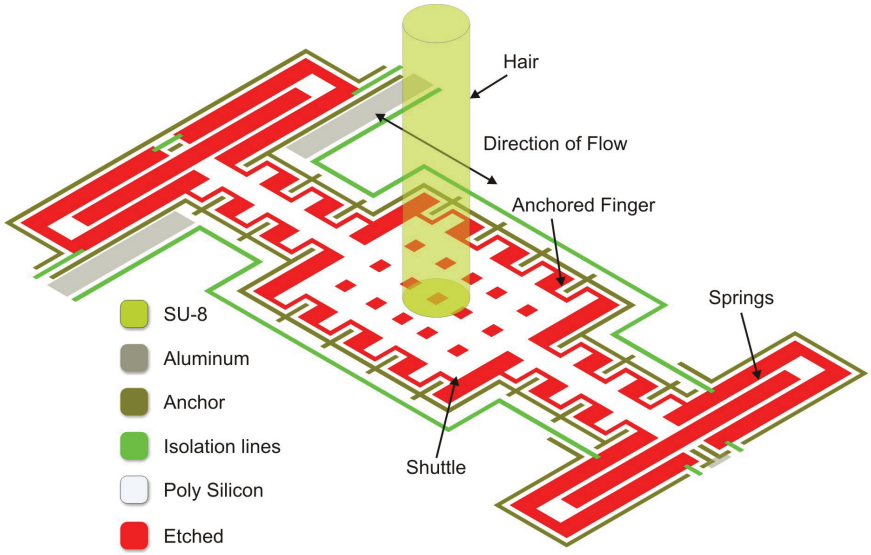

Figure 3.35 *Schematic of BooT*

The schematic of the sensor is presented in Figure 3.35. It consists of a laterally moving comb-drive structure with a cylindrical hair attached to the shuttle. The fluid drag force causes horizontal displacement of the shuttle which is kept in equilibrium with the spring forces. The shuttle structure, including the fingers, is covered with a dielectric material to prevent contact with liquid. The configuration of the fingers is chosen to allow for a differential readout scheme. To this end, for a movement parallel to the direction of flow, say in the positive direction, due to the change of the gap in between the electrodes the capacitance on one side increases whereas the capacitance at the other side decreases. For displacement in the negative direction the capacitance changes are reversed. The stationary fingers are anchored to the substrate to prevent deflection by drag forces.

[14] BooT is the Dutch translation for "boat". It is also said that "Ik heb een boot,…"

The springs, which connect the shuttle to the substrate, can have simple (clamped-clamped beam) or folded (see the schematic in Figure 3.35) configurations. The simple shape is modelled as shown in Figure 3.36. In the linear limit, i.e. when the displacement is much smaller than the beam width, the resulting lateral displacement in this configuration is

$$\upsilon(L_s) = \frac{F \cdot L_s^3}{12\,EI} \tag{3.79}$$

where υ is the lateral displacement, F is the lateral force, L is the length of the spring, E is the Young's modulus and I is the area moment of inertia of the spring's cross section.

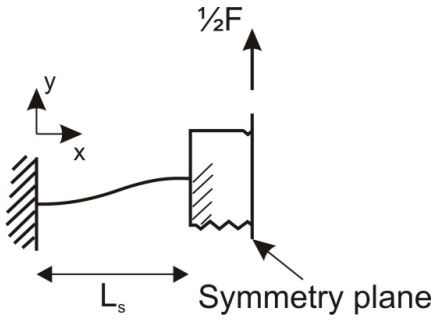

Figure 3.36 *The schematic model of the simple springs*

Therefore, the spring constant for each pair of simple springs is

$$K_{simple} = \frac{2\,E \cdot T_s \cdot W_s^3}{L_s^3} \tag{3.80}$$

in which W_s and T_s are the width and thickness[15] of the springs respectively. Simple springs are less sensitive to stress gradients but show spring stiffening due to residual axial stress [75].

Folded springs, on the other hand, are used to increase the compliance while keeping the spring length perpendicular to the shuttle displacement constant. When the springs are folded once, the spring constant is half of the simple springs. However, folded springs are subject to out of plane bending due to residual stress gradients.

The sensor configuration can be rearranged to induce parallel movement between the capacitor's plates (the fingers). A parallel design has the advantage that the output signal is linear because the induced displacement changes the overlap area of

[15] Note that the thickness, T_s, actually is the thickness of the electrode layer or equally the "height of the fingers".

the fingers. In the perpendicular design the output signal is nonlinear but the sensitivity (i.e. the relative capacitance change per unit displacement) can be higher. Since the induced displacement in the range of flows we are interested in is very small, the nonlinearity is not a limiting factor and, hence, the sensors are designed in the perpendicular configuration.

Considering the parasitic capacitance of the discrete peripheral readout electronics and the integration capacitor of the charge amplifier, the total initial capacitance needs to be between 0.1 and 1 pF, as in the previous schemes. Therefore, given the gap between the fingers, d_0, the thickness of the fingers, T and their overlap length, $L_{overlap}$, the initial capacitance of n pairs of fingers is given by

$$C_i = 2n \cdot \frac{\varepsilon_0 \cdot \varepsilon_r \cdot \left(L_{overlap} \cdot T\right)}{d_0} \tag{3.81}$$

which is used to calculate the required number of fingers. However, because of the dielectric medium (water) with high permittivity and comparable dimensions of the gap between the fingers and their thickness, the classical parallel plate approximation underestimates the capacitance by neglecting the fringing fields. For the geometrical parameters given in Table 3-VII, a more accurate calculation [76] shows that the actual capacitance is about 2.5 times larger than the value given by (3.81).

The minimum required relative change in capacitance $\Delta C/C$, is set to 1%. The differential capacitance change, neglecting the fringing field, is given by

$$\Delta C \approx 2n \cdot \varepsilon_0 \cdot \varepsilon_r \cdot \left(L_{overlap} \cdot T\right)\left(\frac{\alpha^2 - 1}{\alpha^2 \cdot d_0^2}\right) \cdot \upsilon\left(L_s\right) \tag{3.82}$$

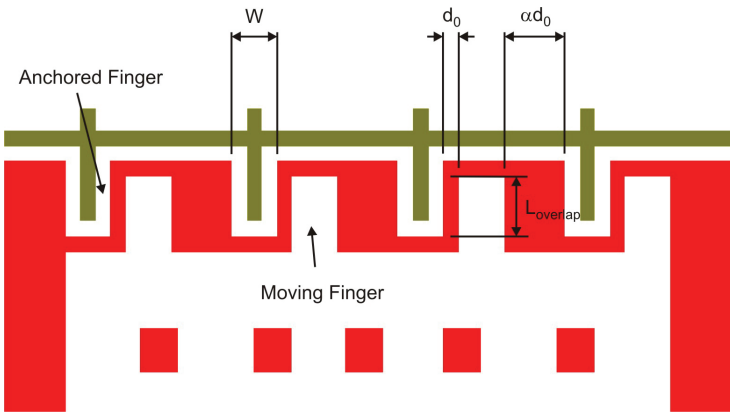

Figure 3.37 *Dimensions of the comb structure*

in which α is the gap incremental factor as shown in Figure 3.37. This requires that the lateral movement of the shuttle, $v(L_s)$, to be more than 22 nm (considering C_p=C_i). Therefore, by setting the geometrical parameters of the springs, the minimum detectable velocity can be obtained from (3.79). The design parameters and the resultant specifications are summarised in Table 3-VII below. The diameter of the hairs can be tuned to give the necessary bandwidth and sensitivity.

Table 3-VII. *The geometrical parameters of the laterally moving flow sensor*

Parameter	Symbol	Value	Unit
Length of the springs	L_s	4×150	µm
Width of the springs	W_s	2	µm
Thickness of springs	T_s	2	µm
Number of spring pairs	m	2	
Overlap length of fingers	$L_{overlap}$	8	µm
Width of fingers	W	6	µm
Thickness of fingers	T	2	µm
(Minimum) Number of fingers	n	10	
Relative dielectric permittivity of water	ε_r	80	
Young's modulus (polysilicon)	E	160	GPa
Sensitivity (at 100 Hz)		2.74	fF/mm/s
Detection threshold (at 100 Hz) C_p=C_i		0.8	mm/s

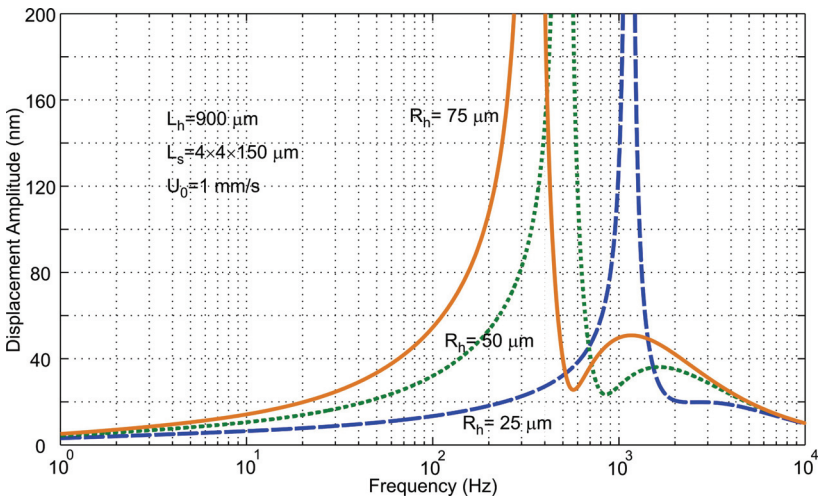

Figure 3.38 *Frequency response of the BooT structure having a hair with different diameters*

Figure 3.38 shows the frequency response of the system having the geometrical properties presented in Table 3-VII with different hair diameter. Considering the small lateral dimensions of the fingers, the squeeze film damping has been neglected. In addition, the shear force on the shuttle has also been neglected. However, the effect of the fluid added inertia and damping on the fingers has been taken into account. Note that the springs are much more flexible than the hair. Therefore, the hair structure is considered absolutely rigid.

The strong resonance of the sensor, compare to the closed membrane scheme, is due to its lower damping coefficient. The hair undergoes a translational rather than a rotational movement in the fluid. As a result, the damping coefficient depends directly on the length rather than its cube (see (3.52)).

The force on hair has a linear relation with the amplitude of the far field velocity. Therefore, the (frequency dependant) sensitivity is easily computed from the displacement graph in Figure 3.38 and (3.82). At 100 Hz, the calculated sensitivity of the device is 2.74 fF/mm/s and increases rapidly when approaching the resonance frequency. The detection threshold at this frequency is 0.8 mm/s.

In this scheme, the stiffness of the sensor is decoupled from the hair geometry but the thickness of springs and fingers are the same. Although thicker fingers improve the electrical sensitivity, a thicker spring is stiffer and results in a higher resonance frequency. Consequently, the low frequency sensitivity of the device is almost independent of the thickness of the springs and fingers. Clearly, a thinner spring results in a lower bandwidth and higher mechanical sensitivity. However, they are more sensitive to stress gradient and more difficult to fabricate.

3.6 Conclusion

In this chapter three designs for capacitive aquatic flow sensors inspired by fish neuromast have been presented. Various aspects of each of the designs have been analysed in detail to provide sufficient knowledge of the parameters that strongly influence the performance of the sensor. These parameters are then tailored to obtain desired characteristics.

At first, a closed membrane configuration has been proposed. The electrodes are attached underneath the membrane and are, therefore, insulated from the liquid medium on the surface. This excludes any chance of electrolysis and reduces the

squeeze film damping effect. The drawback of the design is the complex nature of the structure which results in a rather complicated fabrication scheme (as we shall see in the next chapter). For example the variation in the residual stress of the membrane according to the fabrication process, appreciably changes the dynamic behaviour of the system. The large value of the parasitic capacitances of the discrete readout circuitry demands parallel connection of a large number of individual sensors to obtain a sufficiently large capacitance. Important design parameters have been identified and are summarised in Table 3-VIII below.

Table 3-VIII. *Qualitative comparison between presented designs*

Parameter	**Membrane**	**Canal**	**BooT**
Parallel Tuning Parameters	R_h, R_m	R_h, R_s	R_h, L_s, $L_{overlap}$
Wafer scale Tuning Parameters	d_0, L_h, T_m	L_s, L_h, d_0	T_s, L_h
Squeeze Film Damping	Excluded	d_0, D_h	d_0, T_s, $L_{overlap}$
Drawback	Stiffness	Small Gap	Bending
Water in contact with electrodes	No	One Insulated	Insulated
Sensitivity (at 100 Hz) (fF/mm/s)	0.15	43	2.74
Detection threshold (at 100 Hz) (mm/s) C_p=C_i	2.2	0.3	0.8
Superficial or canal performance	Superficial	Canal	Superficial
Overall complexity of the design	High	Moderate	Low

For realisation of canal embedded structures another scheme has been presented. The configuration helps to attain a simpler, more rigorously to model design and reduces the number of sensors needed to be connected in parallel. It also improves the sensitivity and the detection threshold. Rather than using the previous structure in a channel in this design structures are built directly in a canal. The disadvantage is the requirement for a small gap between the electrodes compared to the length of the hanging hair which makes the structure susceptible to stiction and strain.

Laterally moving flow sensors (BooT) based on the design of existing shear stress sensors have been presented next. The fabrication and design of shear stress sensors are well established and documented in literature. To avoid undesirable deflection due to fluid drag force, the configuration has been changed to anchor the fixed fingers to the substrate. A SU-8 hair structure is made on the shuttle to transmit the fluid flow movements to the horizontal force to deflect the springs. The structure should be very flexible in the horizontal direction while having a large rotational

stiffness. There is always an out-of-plane rotation due to the generated torque on the hair. The asymmetry in the place of the hair does not affect the lateral movement.

The first (closed membrane) and last (Boot) presented designs incorporate a differential capacitive readout scheme to benefit from the advantages described before. All designs have electrodes insulated from the aquatic medium. In the last two designs, however, the liquid is present between the electrodes. Despite this fact, the squeeze film damping is not expected to impose a major drawback at low frequencies and low displacements as in our range of interest.

Note that the detection threshold presented in Table 3-VIII have been calculated using a very crude estimation for the minimum relative change in the capacitance, i.e. $\Delta C/C=0.01$. In reality this can be an order of magnitude lower which lowers the detection threshold with the same order. In addition, the optimised closed membrane sensor exhibits an order of magnitude higher mechanical sensitivity which translates to a higher sensitivity and lower detection threshold with the same order and, therefore, making it comparable to BooT. In the next chapter the fabrication processes of these sensors are discussed. It is the combination of the fabrication procedure and the analytical evaluation, which has been done in this chapter, that determines the overall complexity of a system.

3.7 References

[1] B. R. Munson, *et al.*, *Fundamentals of fluid mechanics*, 5th ed. New York: Wiley, 2006.

[2] S. E. Bullard. (2008, *Physical properties of sea water*. Available: http://www.kayelaby.npl.co.uk/general_physics/2_7/2_7_9.html

[3] A. L. Horvath, *Handbook of aqueous electrolyte solutions: physical properties, estimation, and correlation methods*. Chichester: Ellis Horwood, 1985.

[4] T. Yamaguchi, *et al.*, "A theoretical study on the frequency-dependent electric conductivity of electrolyte solutions. II. Effect of hydrodynamic interaction," *The Journal of Chemical Physics,* vol. 130, pp. 094506-11, 2009.

[5] T. Yamaguchi, *et al.*, "A theoretical study on the frequency-dependent electric conductivity of electrolyte solutions," *The Journal of Chemical Physics,* vol. 127, pp. 234501-9, 2007.

[6] J. B. Hasted, *et al.*, "Dielectric Properties of Aqueous Ionic Solutions. Parts I and II," *The Journal of Chemical Physics,* vol. 16, pp. 1-21, 1948.

[7] J. Koryta, *et al.*, *Principles of Electrochemistry*, 2 ed. vol. 71. Chichester: John Wiley and Sons Ltd., 1993.

[8] J. A. C. Humphrey, *et al.*, "Dynamics of Arthropod Filiform Hairs. I. Mathematical Modelling of the Hair and Air Motions," *Philosophical Transactions: Biological Sciences,* vol. 340, pp. 423-444, 1993.

[9] T. Shimozawa, *et al.*, "Structural scaling and functional design of the cercal wind-receptor hairs of cricket," *Journal of Comparative Physiology a-Sensory Neural and Behavioral Physiology,* vol. 183, pp. 171-186, Aug 1998.

[10] H. Schlichting and K. Gersten, *Boundary-layer theory*, 8th ed. Berlin: Springer Verlag, 2000.

[11] B. T. Dickinson, "Hair receptor sensitivity to changes in laminar boundary layer shape," *Bioinspiration & Biomimetics,* vol. 5, p. 016002, 2010.

[12] T. Steinmann, *et al.*, "Air-flow sensitive hairs: boundary layers in oscillatory flows around arthropod appendages," *Journal of Experimental Biology,* vol. 209, pp. 4398-4408, Nov 2006.

[13] J. J. Heys, *et al.*, "Modeling arthropod filiform hair motion using the penalty immersed boundary method," *Journal of biomechanics,* vol. 41, pp. 977-984, 2008.

[14] R. Devarakonda*, et al.*, "Dynamics of Arthropod Filiform Hairs. IV. Hair Motion in Air and Water," *Philosophical Transactions: Biological Sciences,* vol. 351, pp. 933-946, 1996.

[15] G. G. Stokes, "On the effect of the internal friction of fluids on the motion of pendulums," *Transactions of the Cambridge Philosophical Society,* vol. 9, pp. 8-106, 1851.

[16] C.-Y. Wang, "On high-frequency oscillatory viscous flows," *Journal of Fluid Mechanics Digital Archive,* vol. 32, pp. 55-68, 1968.

[17] J. Holtsmark*, et al.*, "Boundary Layer Flow Near a Cylindrical Obstacle in an Oscillating, Incompressible Fluid," *The Journal of the Acoustical Society of America,* vol. 26, pp. 26-39, 1954.

[18] G. N. Weisensel, "Natural frequency information for circular and annular plates," *Journal of Sound and Vibration,* vol. 133, pp. 129-137, 1989.

[19] L.-s. Ma and T.-j. Wang, "Analytical relations between eigenvalues of circular plate based on various plate theories," *Applied Mathematics and Mechanics,* vol. 27, pp. 279-286, 2006.

[20] J. N. Reddy and C. M. Wang, "An overview of the relationships between solutions of the classical and shear deformation plate theories," *Composites Science and Technology,* vol. 60, pp. 2327-2335, 2000.

[21] S. Timoshenko and S. Woinowsky-Krieger, *Theory of Plates and Shells*, 2 ed.: McGraw-Hill, 1959.

[22] T. Wah, "Vibration of Circular Plates," *The Journal of the Acoustical Society of America,* vol. 34, pp. 275-281, 1962.

[23] B. Verlaat, "Optimization of hair-based flow sensors in an aquatic environment," Master, University of Twente, Enschede, 2010.

[24] M. Amabili and M. K. Kwak, "Free vibrations of circular plates coupled with liquids: Revising the lamb problem," *Journal of Fluids and Structures,* vol. 10, pp. 743-761, Oct 1996.

[25] H. Lamb, "On the Vibrations of an Elastic Plate in Contact with Water," *Proceedings of the Royal Society of London. Series A, Containing Papers of a Mathematical and Physical Character,* vol. 98, pp. 205-216, 1920.

[26] J. A. C. Humphrey and F. G. Barth, "Medium Flow-Sensing Hairs: Biomechanics and Models," in *Advances in Insect Physiology*. vol. Volume 34, J. Casas and S. J. Simpson, Eds., ed: Academic Press, 2007, pp. 1-80.

[27] M. H. Bao and H. Yang, "Squeeze film air damping in MEMS," *Sensors and Actuators a-Physical,* vol. 136, pp. 3-27, May 2007.

[28] R. Pratap*, et al.*, "Squeeze Film Effects in MEMS Devices," *Journal of the Indian Institute of Science,* vol. 87, pp. 75-94, 2007.

[29] W. S. Griffin*, et al.*, "A study of fluid squeeze film damping," *Journal of Basic Engineering,* pp. 451-456, 1966.

[30] F. Pan*, et al.*, "Squeeze film damping effect on the dynamic response of a MEMS torsion mirror," *Journal of Micromechanics and Microengineering,* vol. 8, pp. 200-208, Sep 1998.

[31] A. C. Eringen, *Mechanics of continua*, 2nd ed. Huntington, NY: Robert E. Krieger Publishing Co., 1980.

[32] S. Schmid*, et al.*, "Electrostatically actuated nonconductive polymer microresonators in gaseous and aqueous environment," *Sensors and Actuators, A: Physical,* vol. 145-146, pp. 442-448, 2008.

[33] T. Dargent and et al., "Micromachining of an SU-8 flapping-wing flying micro-electro-mechanical system," *Journal of Micromechanics and Microengineering,* vol. 19, p. 085028, 2009.

[34] A. T. Al-Halhouli*, et al.*, "Nanoindentation testing of SU-8 photoresist mechanical properties," *Microelectronic Engineering,* vol. 85, pp. 942-944, 2008.

[35] M. Calleja*, et al.*, "Polymeric Cantilever Arrays for Biosensing Applications," *Sensor Letters,* vol. 1, pp. 20-24, 2003.

[36] K. Y. Lee*, et al.*, "Micromachining applications of a high resolution ultrathick photoresist," *Journal of Vacuum Science and Technology B: Microelectronics and Nanometer Structures,* vol. 13, pp. 3012-3016, 1995.

[37] Microchem. *SU-8 Data Sheets.* Available: http://www.microchem.com/products/su_eight.htm

[38] P. Abgrall*, et al.*, "SU-8 as a structural material for labs-on-chips and microelectromechanical systems," *Electrophoresis,* vol. 28, pp. 4539-4551, Dec 2007.

[39] J. Hsieh*, et al.*, "Realization and characterization of SU-8 micro cylindrical lenses for in-plane micro optical systems," *Microsystem Technologies-Micro-and Nanosystems-Information Storage and Processing Systems,* vol. 11, pp. 429-437, May 2005.

[40] Z. Ling and K. Lian, "SU-8 3D microoptic components fabricated by inclined UV lithography in water," *Microsystem Technologies-Micro-and Nanosystems-Information Storage and Processing Systems,* vol. 13, pp. 245-251, Feb 2007.

[41] A. Llobera*, et al.*, "SU-8 optical accelerometers," *Journal of Microelectromechanical Systems,* vol. 16, pp. 111-121, 2007.

[42] A. Johansson*, et al.*, "Polymeric cantilever-based biosensors with integrated readout," *Applied Physics Letters,* vol. 89, Oct 2006.

[43] S. Mouaziz*, et al.*, "Polymer-based cantilevers with integrated electrodes," *Journal of Microelectromechanical Systems,* vol. 15, pp. 890-895, Aug 2006.

[44] J. Thaysen*, et al.*, "SU-8 based piezoresistive mechanical sensor," in: *Micro Electro Mechanical Systems, 2002. The Fifteenth IEEE International Conference on*, 2002, pp. 320-323.

[45] H. Lorenz*, et al.*, "SU-8: A low-cost negative resist for MEMS," *Journal of Micromechanics and Microengineering,* vol. 7, pp. 121-124, 1997.

[46] S. Victor Chi-Yuan*, et al.*, "Yield strength of thin-film parylene-c," in: *Design, Test, Integration and Packaging of MEMS/MOEMS 2003. Symposium on*, 2003, pp. 394-398.

[47] L. Dellmann*, et al.*, "Fabrication proces of high aspect ratio elastic structures for piezoelectric motor applications," 1997, pp. 641-644.

[48] T. A. Harder*, et al.*, "Residual stress in thin-film parylene-c," in: *Micro Electro Mechanical Systems, 2002. The Fifteenth IEEE International Conference on*, 2002, pp. 435-438.

[49] H. Lorenz*, et al.*, "Mechanical characterization of a new high-aspect-ratio near UV-photoresist," *Microelectronic Engineering,* vol. 42, pp. 371-374, 1998 1998.

[50] M. Nordstrom*, et al.*, "Investigation of the bond strength between the photo-sensitive polymer SU-8 and gold," *Microelectronic Engineering,* vol. 78-79, pp. 152-157, Mar 2005.

[51] J. R. Thorpe*, et al.*, "High frequency transmission line using micromachined polymer dielectric," *Electronics Letters,* vol. 34, pp. 1237-1238, 1998.

[52] G. Kotzar*, et al.*, "Evaluation of MEMS materials of construction for implantable medical devices," *Biomaterials,* vol. 23, pp. 2737-2750, 2002.

[53] T. Y. Chang*, et al.*, "Cell and Protein Compatibility of Parylene-C Surfaces," *Langmuir,* vol. 23, pp. 11718-11725, 2007.

[54] J. S. Song*, et al.*, "Improved biocompatibility of parylene-C films prepared by chemical vapor deposition and the subsequent plasma treatment," *Journal of Applied Polymer Science,* vol. 112, pp. 3677-3685, 2009.

[55] S. Selvarasah, *et al.*, "A reusable high aspect ratio parylene-C shadow mask technology for diverse micropatterning applications," *Sensors and Actuators A: Physical,* vol. 145-146, pp. 306-315, 2008.

[56] E. Meng, *et al.*, "Plasma removal of Parylene C," *Journal of Micromechanics and Microengineering,* vol. 18, p. 045004, 2008.

[57] P. J. Chen, *et al.*, "Microfabricated implantable parylene-based wireless passive intraocular pressure sensors," *Journal of Microelectromechanical Systems,* vol. 17, pp. 1342-1351, 2008.

[58] X.-Q. Wang, *et al.*, "Parylene micro check valve," 1999, pp. 177-182.

[59] Y. Xia and G. M. Whitesides, "Soft Lithography," *Angewandte Chemie International Edition,* vol. 37, pp. 550-575, 1998.

[60] K. Tsougeni, *et al.*, "Photosensitive poly(dimethylsiloxane) materials for microfluidic applications," *Microelectronic Engineering,* vol. 84, pp. 1104-1108, 2007.

[61] A. A. S. Bhagat, *et al.*, "Photodefinable polydimethylsiloxane (PDMS) for rapid lab-on-a-chip prototyping," *Lab on a Chip,* vol. 7, pp. 1192-1197, 2007.

[62] S. Talaei, *et al.*, "Hybrid microfluidic cartridge formed by irreversible bonding of SU-8 and PDMS for multi-layer flow applications," *Procedia Chemistry,* vol. 1, pp. 381-384, 2009.

[63] S. M. Van Netten, "Hydrodynamic detection by cupulae in a lateral line canal: Functional relations between physics and physiology," *Biological Cybernetics,* vol. 94, pp. 67-85, 2006.

[64] H. T. Schlichting and K. Gersten, *Boundary Layer Theory*, 8 ed. Berlin: Springer-Verlag, 1970.

[65] J. A. C. Humphrey, "Drag force acting on a neuromast in the fish lateral line trunk canal. II. Analytical modelling of parameter dependencies," *Journal of the Royal Society Interface,* vol. 6, pp. 641-653, 2009.

[66] L. Lennart and G.-e.-H. Mohamed, "MEMS-based pressure and shear stress sensors for turbulent flows," *Measurement Science and Technology,* vol. 10, p. 665, 1999.

[67] A. O'Grady, *et al.*, "A MEMS sensor for mean shear stress measurements in high-speed turbulent flows with backside interconnects," 2009, pp. 272-275.

[68] T. Pan, *et al.*, "Microfabricated shear stress sensors, part 1: Design and fabrication," *AIAA Journal,* vol. 37, pp. 66-72, 1999.

[69] M. A. Schmidt*, et al.*, "Design And Calibration Of A Microfabricated Floating-Element Shear-Stress Sensor," *IEEE Transactions on Electron Devices,* vol. 35, pp. 750-757, 1988.

[70] A. Padmanabhan*, et al.*, "Micromachined sensors for static and dynamic shear-stress measurements in aerodynamic flows," 1997, pp. 137-140.

[71] A. V. Desai and M. A. Haque, "Design and fabrication of a direction sensitive MEMS shear stress sensor with high spatial and temporal resolution," *Journal of Micromechanics and Microengineering,* vol. 14, pp. 1718-1725, 2004.

[72] K. Y. Ng*, et al.*, "A liquid shear-stress sensor fabricated using wafer bonding technology," in: *Solid-State Sensors and Actuators, 1991. Digest of Technical Papers, TRANSDUCERS '91., 1991 International Conference on*, 1991, pp. 931-934.

[73] X. Yong*, et al.*, "Underwater flexible shear-stress sensor skins," in: *Micro Electro Mechanical Systems, 2004. 17th IEEE International Conference on. (MEMS)*, 2004, pp. 833-836.

[74] X. Yong*, et al.*, "Underwater shear-stress sensor," in: *Micro Electro Mechanical Systems, 2002. The Fifteenth IEEE International Conference on*, 2002, pp. 340-343.

[75] N. Tiliakos*, et al.*, "A MEMS-based shear stress sensor for high temperature applications," 2007, pp. 1477-1478.

[76] H. Nishiyama and M. Nakamura, "Form and capacitance of parallel-plate capacitors," *Components, Packaging, and Manufacturing Technology, Part A, IEEE Transactions on,* vol. 17, pp. 477-484, 1994.

4
Fabrication

In this chapter three fabrication procedures of differential capacitive flow sensors, as described in previous chapter, are presented. Each fabrication step has been characterised and detailed to result in an optimised procedure. The main objective is to devise a robust and high yield process. At the end a short comparison between these approaches is given.

4.1 Introduction

Micro-Electro-Mechanical Systems (MEMS) technology [1] is a capable platform for realization of microscale, fast, sensitive and cheap sensory systems. It offers numerous advantages over conventional precision technology, most notably cost-effective batch fabrication and high spatial resolution.

The biomimetic approach is a speculative practice to implement a function found in nature in modern technological design and fabrication processes. The evolutionary path of nature is to achieve high functionality at minimum cost, both in materials and energy, as are often engineering objectives. MEMS technology provides a unique potential for the realization of complex systems at geometric scales comparable to those found in nature. The desired result is an artificial counterpart which grants an invaluable tool for further exploration and exploitation of the principles found in nature.

Here the fabrication process for the realization of artificial capacitive hair-sensors and, ultimately, lateral line systems is presented. The advantages of capacitive sensors have previously been demonstrated by artificial hair-based flow sensors inspired by the mechanosensitive hairs found on the cerci of crickets [2]. In the current approaches we specifically address the requirements for operation in aquatic environments while maintaining the capacitive readout mechanism of the sensors. This chapter consists of three major sections each of which focuses on the fabrication procedure of a different design presented in chapter three.

4.2 Sensors with Closed Membrane

This part focuses on the fabrication procedure of hair-like structures supported by a fully clamped membrane. The membranes have been realised by sacrificial layer etching from the backside of the wafer. This approach is more widely applicable as it can be used for the fabrication of structures that need sealed membranes for proper operation in general.

An array of densely packed fully supported membranes with integrated electrodes underneath is fabricated. The gap between the membrane and substrate determines the electrode separation and can be tuned. The SU-8 cylinder on top of the membrane resembles the neuromast of lateral line system of fish. The design parameters, namely the size, shape and thickness of the membrane, the diameter and

length of the hair and shape of the electrodes and their optimal values have been discussed previously. As it has been stated, the insulation of the electrodes from fluid and the reduction of squeeze film damping effect are the main objectives which lead to the specific proposed configuration.

4.2.1 Design Description

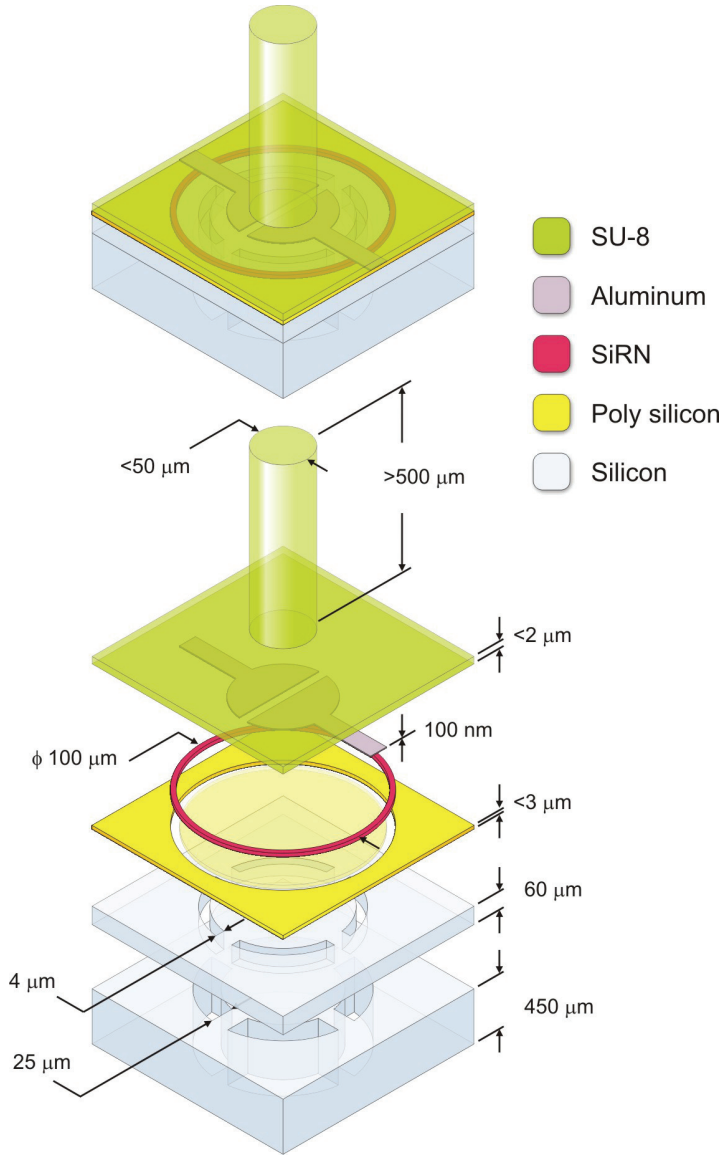

Figure 4.1 *The Exploded schematic view of the proposed sensor. Drawing is not in scale.*

A 3D exploded view of the sensor is shown in Figure 4.1. The fluid exerts a drag force on the hair which consequently produces a moment on the membrane. Since electrodes are attached to the membrane, they follow the anti-symmetric deflection of the membrane. The distance of one electrode with respect to substrate increases whereas the other one decreases. This capacitance change is measured differentially and indicates the magnitude of the force, hence the fluid velocity. A highly doped silicon wafer is used as the substrate which functions as common electrode for the variable capacitors. A polysilicon layer, the thickness of which can be tuned to the gap-height requirements, is used as the spacer between counter electrodes. A rim of Silicon Rich silicon Nitride (SiRN) delineates the border of the membrane and acts as a barrier during later sacrificial polysilicon layer etching in order to free the membrane. Aluminium electrodes form the two variable capacitors with the substrate. These electrodes get attached to the bottom of a subsequently deposited SU-8 layer which serves as the membrane. The lead wires run over the polysilicon layer to the bond pads. The hair structure is made of SU-8 as well. The sacrificial layer etch is done through ports that are etched in the front and backsides of the wafer. The two separate parts of the substrate shown in the schematic of Figure 4.1 are to distinguish the extends of these etch processes.

The structure ensures that the design objectives are met as the fluid is kept separated from the capacitors' plates by the topside membrane. The backside of the device is protected with proper packaging. The pressure of the enclosure can be set to ensure low downward deflection of the membrane as the fluid pressure on the top changes (i.e. as the working depth changes). The resulting squeeze film damping effect (see chapter three) is negligible in the flow amplitude and frequency range of interest.

The thickness of the membrane is a determining factor in its performance and solely depends on the limitations of the SU-8 processing. The membrane can be replaced with other flexible materials like PMMA or Parylene-C which have lower Young's modulus. These alternative approaches are briefly discussed in the next chapter. The fabrication process is described in the next section followed by the results and discussion.

4.2.2 Fabrication Procedure

To fabricate the sensor we start with DSP (Double Side Polished), low resistance silicon wafers. They should be low resistance since they act as the common electrode in the sensor configuration and DSP because the backside etch process should be uniform and optimized (as we will see shortly). However, this is hard to achieve if started from a rough surface. The nominal resistivity of the wafers used is 0.01 to 0.05 Ω·cm. In addition, the thickness of each wafer should be measured carefully before processing. This information is needed to tune the etch depth in steps *a* and *d* respectively (see below).

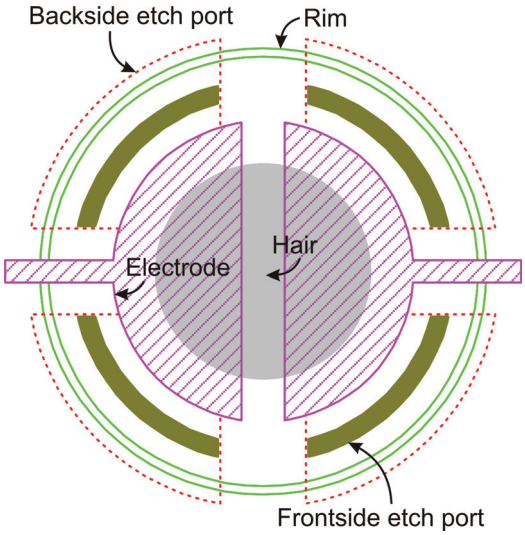

Figure 4.2 *The mask layout of a single sensor*

Figure 4.2 shows the mask layout of the design for a single hair with the various colours indicating the masks as used in the corresponding processing steps. The figure shows the alignment of each part with respect to the others. Figure 4.3 shows the fabrication scheme. A standard DRIE (Deep Reactive Ion Etching) process etches 60 μm deep, 4 μm wide trenches on the frontside of the wafer (*step a*). Since these trenches are used to access the sacrificial layer from the backside and etch it, they are called "etch ports". The dimensions have been chosen to minimize the area consumption (common electrode area) and the necessary backside etch depth. The latter is due to the fact that the diffusion of etch species through these "etch ports" should not be hindered significantly during the later sacrificial layer etch process (*step j*).

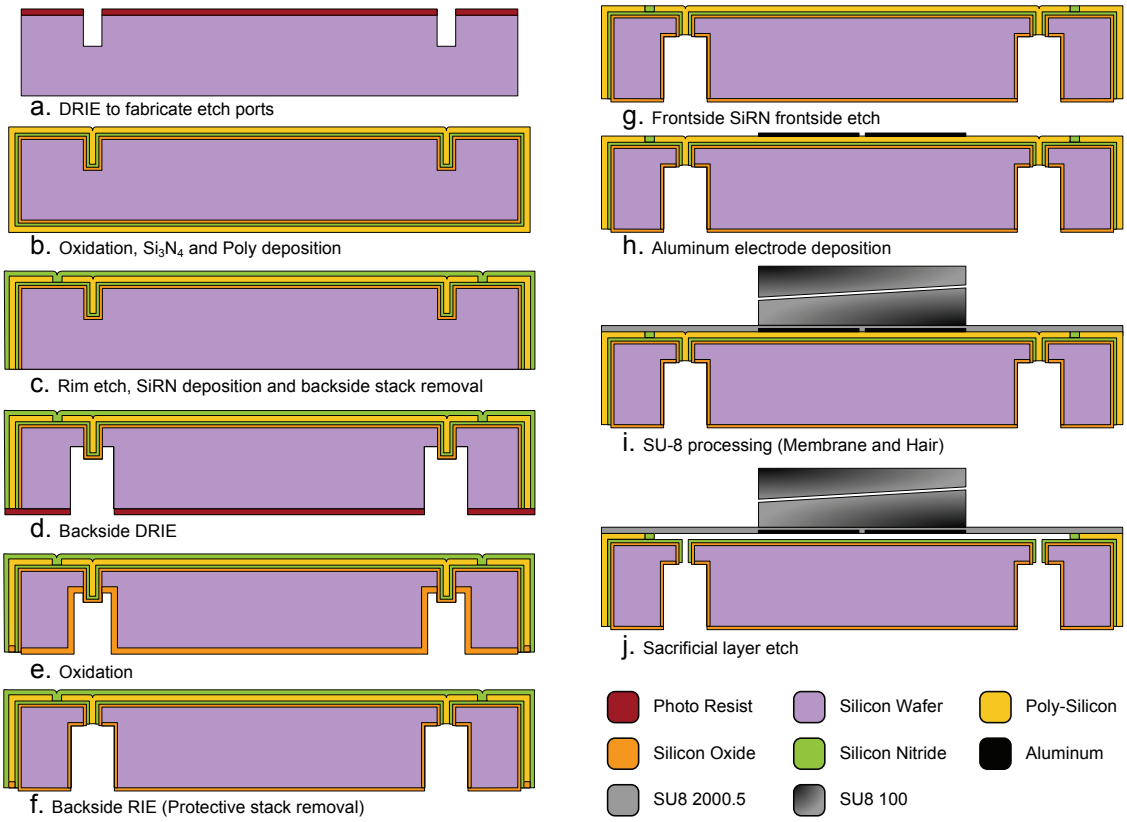

Figure 4.3 *Outline of the fabrication process steps*

An Adixen AMS100-SE DRIE etcher is used for the process. As the mask, conventional positive tone resist Olin 907/17 is spun on the wafer to form a 1.7 µm thick layer. Although it results in a dark mask, it is more convenient to use positive resist. However, this is not problematic since no alignment is necessary for the first step. The hard-bake process is omitted because spatial resolution degrades due to the reflow of the resist.

A short (30 minutes) dry oxidation at 800 °C and consequently HF 50% dip is done after photoresist removal and cleaning of the wafers to remove deposited Fluorocarbon on the side walls of the "etch ports".

The next step (*step b*) is to grow 100 nm oxide and to deposit 40 nm stoichiometric silicon nitride (Si_3N_4)[1]. We will point out the roles of these layers

[1] Stoichiometric nitride has less oxidation rate compare to SiRN and provides a better protection against oxidation of the sacrificial polysilicon layer. This need becomes clearer in the explanation of step e later on in this section.

shortly. The oxidation is done using a dry or wet oxidation method. The growth rate should be determined before each run. The uniformity of the layer and the thickness is better controlled using dry oxidation but the resultant stress is lower in wet oxidation [3]. Figure 4.4 shows the typical growth rate and wafer level non-uniformity of the wet grown oxide. Note that the curve is almost linear in this regime[2]. The orange line shows the theoretical values using Deal-Grove's model [4].

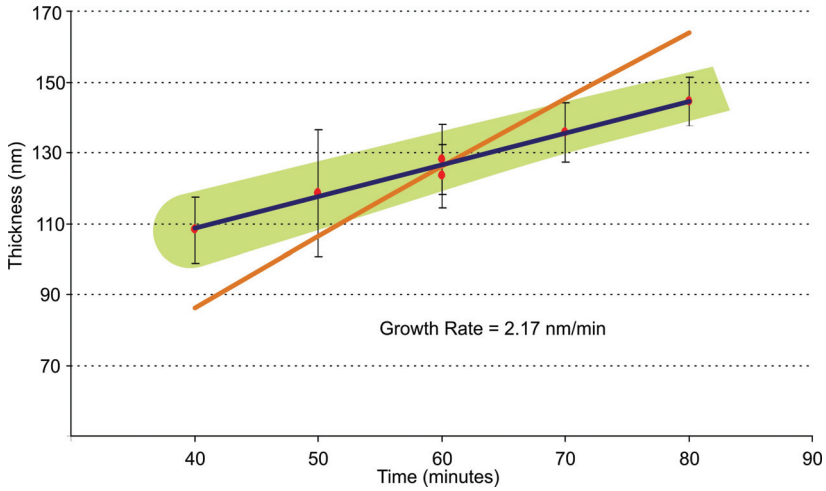

Figure 4.4 *Wet Oxidation rate at 900 °C. The orange line shows the theoretical values.*

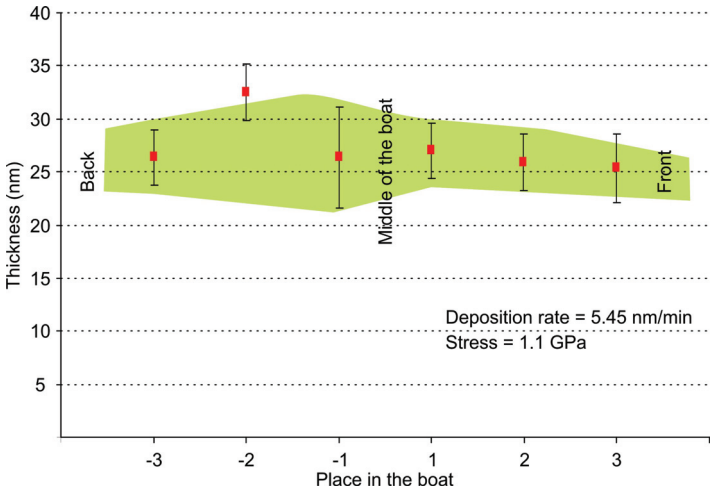

Figure 4.5 *Uniformity Distribution and deposition rate of Si_3N_4*

[2] When the oxide is thin, the growth rate depends on the reaction at the Si/SiO_2 interface rather than the diffusion of the oxygen radicals through the oxide layer.

The stoichiometric nitride is deposited using Low Pressure Chemical Vapour deposition (LPCVD) method at 800 °C and 200 mTorr chamber pressure with 22 and 100 sccm flow of Dichlorosilane (SiH_2Cl_2) and Ammonia (NH_3) respectively. The uniformity and deposition rate are shown in Figure 4.5.

Following Si_3N_4 deposition, a 3 µm thick polysilicon layer is deposited by LPCVD. This layer acts both as sacrificial layer (under the membrane area) and as a base for metal interconnects (everywhere else). It should be thick enough to fill the "etch ports" and smooth enough not to degrade the metal interconnects' electrical resistance. The deposition is done at 590 °C using 50 sccm flow of Silane (SiH_4) at 250 mTorr pressure. The distribution of non-uniformity for 1.5 to 1.7 µm thick layers is shown in Figure 4.6. The blue markers show a single crystalline silicon substrate and the red ones show the result for oxidized silicon substrates. There is no visible difference between the two substrates. It should be noted that for a 3 µm thick polysilicon layer the deposition time is around 14 hours and, therefore, the wafers stay in the tube over night and the process continues the day after. However, this does not have an appreciable effect on the deposited layers.

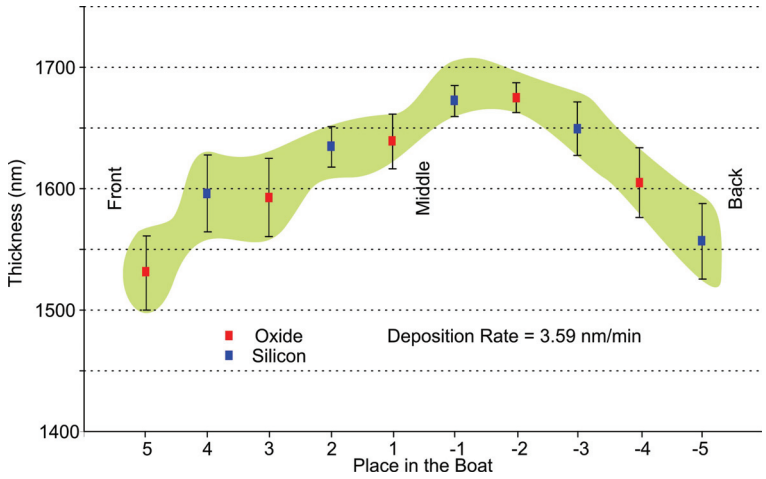

Figure 4.6 *Deposited thickness (symbols), wafer-scale non-uniformity (green band) and boat-position dependence of LPCVD polysilicon*

The polysilicon layer is annealed at 1100 °C for an hour to lower the stress and prevent morphological changes in the layer during later high temperature processes.

Subsequently 2 µm narrow trenches (limited by lithography) are etched into the polysilicon layer to define the membrane shape (*step c*). These rims separate sacrificial parts from the rest of the polysilicon layer after they are filled with SiRN (Silicon Rich

Nitride) in the next deposition step[3]. Again, an Adixen AMS100-SE DRIE etcher is used to precisely control the etch depth. The resulting etch rate is shown in Figure 4.7. The etch process is done without native oxide removal from the surface. For good adhesion of the deposited SiRN layer, it is necessary to perform a Fluorocarbon removal step as described before at the end of the etch process for the rims.

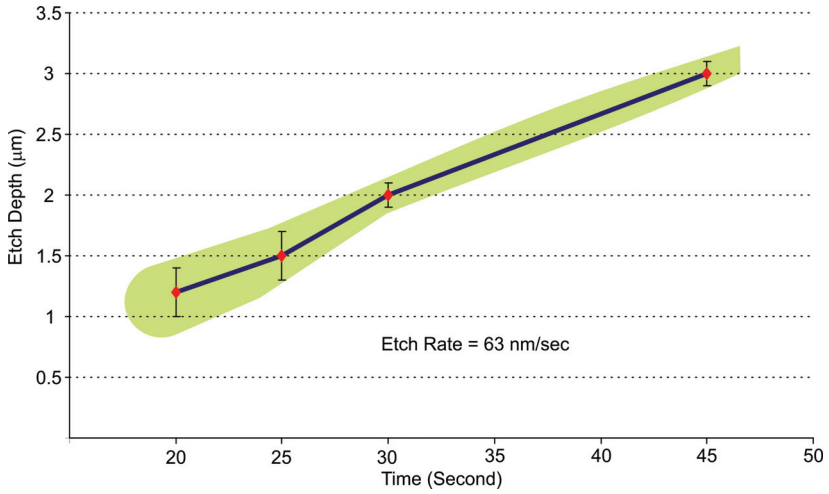

Figure 4.7 *Etch rate of polysilicon using B-HARS recipe[4] in Adixen AMS100-SE*

The lithography process is done using Olin 907/12. This resist forms a thinner layer which needs a shorter exposure time (3 sec) and provides better spatial resolution[5]. The mask in this step is a dark mask. Moreover, any bright area in the mask, which is necessary for the alignment, results in an etched crater (due to polysilicon layer etch in the next step) that affects subsequent lithography steps. This makes the normal alignment procedure impossible. To overcome this difficulty, "backside alignment" procedure is used to delineate a relevant pattern at the backside of the substrate. This pattern is then used to align the actual mask on the frontside of the wafer. This means two lithography steps are needed. In the next chapter we will discuss the use of negative tone SU-8 2 photoresist which results in a bright mask and, hence, a more convenient process.

[3] To completely close the isolation trenches, a 1.2 µm thick layer should be deposited. SiRN has been chosen since compare to Si_3N_4 it has much less (tensile) residual stress and hence thick layers can be deposited. Moreover, it is an electrical insulator and a good barrier against oxidation (see explanation of step e).
[4] The process parameters of this recipe are given in the relative process document in appendix VI.
[5] The light that passes through an aperture in a mask is subject to near-field diffraction as it propagates through the photoresist. For this reason, the image loses contrast with increasing depth into the photoresist.

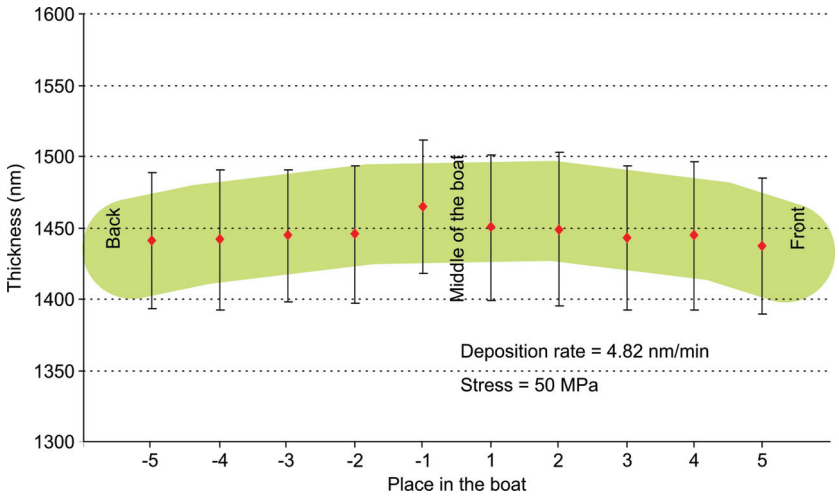

Figure 4.8 *Deposition rate and non-uniformity distribution of SiRN*

To fill these 2 µm wide trenches completely it is necessary to deposit at least 1.2 µm SiRN. The deposition is done in a tube with a temperature ramp from 820 (front) to 870 °C (back) at 150 mTorr chamber pressure. The flows of SiH_2Cl_2 and HN_3 are 77.5 and 20 sccm respectively. This layer additionally serves as a protecting cap during oxidation in *step e*. The non-uniformity distribution is shown in Figure 4.8.

Now, the whole stack of deposited materials is removed from the backside. The process is done in RIE-Electrotech (Etske). First, the thick SiRN layer is removed. Afterwards, without unloading the sample, the process variables are changed to etch polysilicon. At the end a short "Nitride/Oxide" etch step ensures the complete removal of the stack. Table 4-I shows the typical etch rates of the materials in these two processes.

Table 4-I. *Etch rates of different materials in Etske for backetch step*

Material	**SiO_2 (Thermal)**	**SiRN**	**Polysilicon**
Etch Rate in Nitride/Oxide process (nm/min)	30 to 35	55 to 60	16 to 18
Etch Rate in Poly process (nm/min)	~ 50	135 to 140	370 to 380

It should be noted that it is difficult to determine the complete removal of the stack by hydrophobicity of the surface because of the deposited fluorocarbon and the induced roughness. A fluorocarbon removal process at the end of *step c* is advisable.

Next, a special DRIE process (see the section 4.2.3) using standard photoresist as the mask material is done to reach the "etch ports". The selectivity of the process over silicon oxide is high. It does not affect the SiO_2 layer at the bottom of the

frontside "etch ports" and, therefore, after this step the "etch ports" stick out at the bottom of the etched vias (*step d*). The photoresist used as the masking material should be hard-baked for around two hours at 120 °C. This hardens the resist and removes all the water content which is essential to prevent cracking at cryogenic temperatures during the etching process. Moreover, the etch depth should be tuned according to the thickness of the wafer and the depth of the "etch ports" (*step a*; see above). The etch depth (and hence the etch rate), however, can only be measured by cutting a dummy wafer and observing the cross section.

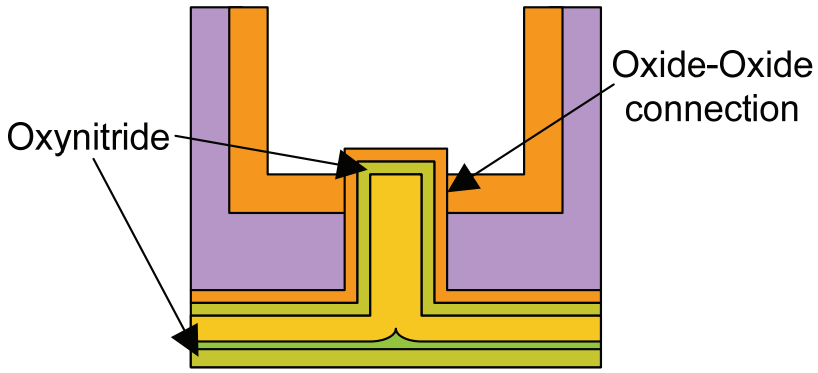

Figure 4.9 *Detailed schematic of the "etch ports" after step e. The 100 nm oxide grown at step b provides a suitable connection for 1 μm grown at step e and reduces the oxidation rate of the underlying* Si_3N_4

Afterwards the wafer is oxidized to grow a 1 μm thick oxide layer at the backside of the wafer and the sidewalls of the etched vias (*step e*). In this step, the frontside SiRN layer protects the polysilicon layer from oxidation. In the "etch ports", the 40 nm Si_3N_4 plays the same role [5]. Having the thin oxide layer at the sidewalls of the "etch ports" under the Si_3N_4 layer provides a compatible (oxide-oxide) connection to the grown oxide (see Figure 4.9). It also reduces the oxidation rate of the underlying Si_3N_4 layer. The thickness of Si_3N_4 layer is limited by the induced stress (see the next section).

Next, using a plasma etch with high directionality the backside is bombarded to remove the protecting SiO_2/Si_3N_4 stack from the bottom of the "etch ports" and expose the sacrificial polysilicon (*step f*). This step is discussed in more detail in the next section. It is followed by yet another anisotropic plasma blanket etch of SiRN on the frontside (*step g*) which should be as uniform as possible. This is done in an Oxford Plasmatherm 790 etcher using 12 and 100 sccm flow of Oxygen (O_2) and

Trifluoromethane (CHF_3) respectively. The pressure is set to 40 mTorr and the power to 250 W. Endpoint detection is used to stop the etching process at the onset of reaching the polysilicon surface.

In this stage, 100 nm aluminium is deposited and patterned to form electrodes, interconnects and bond pads (*step h*). This deposition is done in 10 mTorr chamber pressure to increase conformity. A lift off process is used to pattern aluminium. The reason is to make use of the resultant jagged edge of the structures, "ears", to enhance the connection of the aluminium lines and electrodes to the SU-8 membrane.

The process continues with a thin SU-8 2000.5 (500 nm thick) spin coat and pattern step to form the flexible membranes. The wafers should be cleaned within 100% fuming nitric acid and put in Oxygen plasma to increase adhesion. The thin SU-8 layer can be hard-baked to increase the resistance of the material to aquatic media [6]. This, however, will induce more tensile stress in the layer and increases the modulus of elasticity which translates into stiffer membranes.

Afterwards, a thick (~500 μm) SU-8 100 layer is processed to realize the hairs (*steps i*). This step can be repeated to increase the length of the hairs which results in higher drag force and mechanical sensitivity. The SU-8 process is very sensitive to the flatness and levelness of the hot plates used for soft and post-exposure bake. Therefore, the levelness of hot plates should be checked before each process. The detailed SU-8 processing is described in the next chapter.

The last step (*step j*) is to etch the sacrificial polysilicon layer within the rim boundaries by isotropic SF_6 plasma. To this end, the backside of the wafer is protected with the oxide grown in *step e* and the frontside with the thin SU-8 2000.5 membrane that covers the layer-stack everywhere except on the aluminium bond pads.

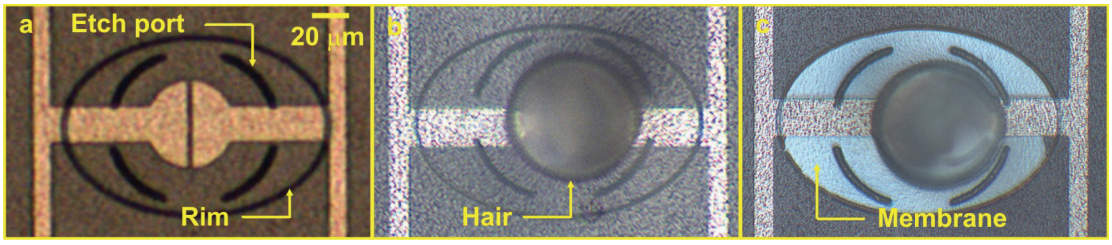

Figure 4.10 *Microscopic pictures from the last 3 fabrication steps*

Figure 4.10 shows a series of microscopic pictures from the last progressive stages of a single device during the fabrication process.

4.2.3 Results and Discussion

In this section we detail the fabrication steps that have been discussed in the previous part, present the results and indicate the important considerations for each step.

The thickness of stoichiometric silicon nitride (Si_3N_4) which is deposited in *step b* on the grown silicon oxide should be chosen carefully. The role of this layer has been discussed before.

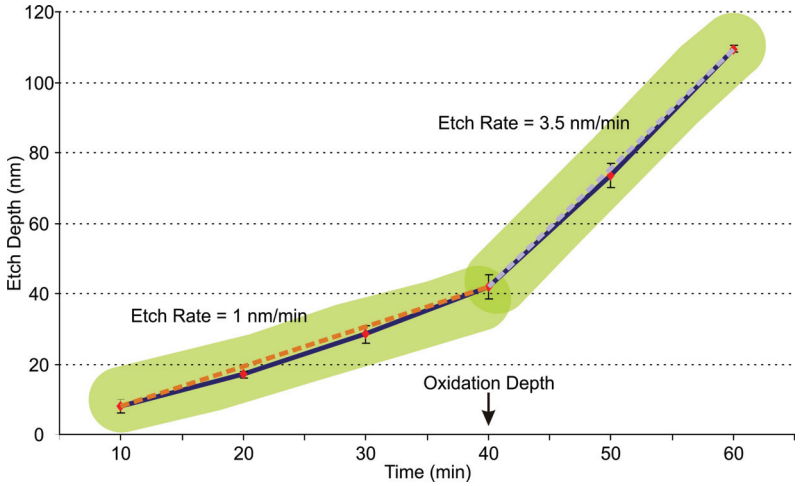

Figure 4.11 *The surface etch rate of oxidised Si_3N_4 in isotropic sacrificial layer etch*

Figure 4.11 shows the etch rate of oxidised Si_3N_4 on the surface. The oxidation is done at 1150 °C for the time needed to grow 1 µm oxide on (100) crystalline silicon wafers (about 2 hours and 40 minutes using wet oxidation furnace). The etch rate of thermal SiO_2 is 1 to 1.5 nm/min and that of LPCVD grown Si_3N_4 is 3.5 to 4.5 nm/min which increases rapidly with etching time. Therefore, during backside oxidation (*step e*) about 40 nm Si_3N_4 turns into silicon oxynitride. It follows that to prevent oxidation of sacrificial polysilicon a minimum of 40 nm Si_3N_4 needs to be deposited. A thicker layer can provide a better protection without hindering the etch process (because of the high etch rate). However, Si_3N_4 has a high tensile stress (~1.1 GPa) which can result in appreciable wafer curvature in later stages when the thick SU-8 layer is processed.

Figure 4.12 shows a SEM image of the membrane cross section after *step b*. The thickness of the polysilicon layer determines the electrode separation. To increase the electrical sensitivity we should minimise this distance but a minimum of 2.5 µm

thickness is needed to ensure complete closure of the "etch ports" and a smooth topography (which is important especially for the metal interconnects which are deposited later). However, it is possible to oxidize the sacrificial layer to some extend and remove the oxide to thin the layer while keeping the "etch ports" closed. This has been shown in the figure with a dotted line. Having a smooth surface helps to obtain low resistance metal lines. In addition, a thinner polysilicon layer decreases the chance of keyhole formation during *step c* when the rim is filled with SiRN.

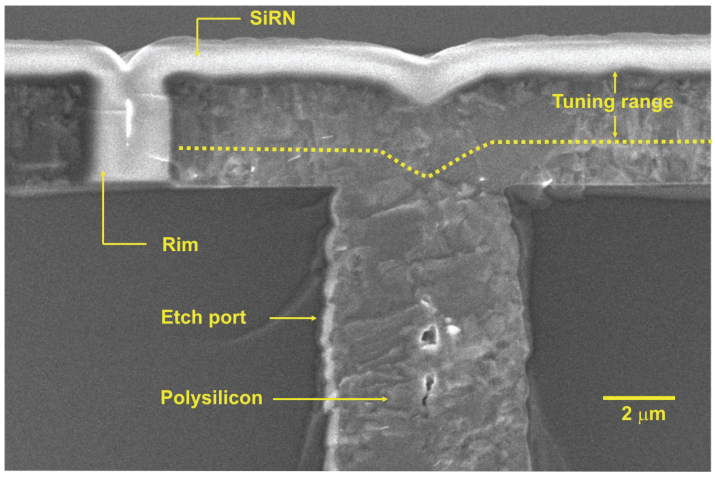

Figure 4.12 *SEM micrograph demonstrates tuning and SiRN plug as protection rim around sacrificial layer*

The oxidation steps are done at 1150 °C for 90 minutes. Consequently samples are dipped in 50% HF solution to remove the grown oxide. In each step approximately 430 nm of polysilicon is removed and, therefore, 4 to 5 oxidation runs are necessary to achieve a 1 μm thick polysilicon layer.

Figure 4.13 shows another SEM image of the cross section after the backside etch (*step d*). The insets are close ups of the bottom and mouth of the etch vias. The backside etch is the most critical step. First, the etch process should be selective enough over silicon oxide and/or silicon nitride to preserve the "etch ports". Otherwise, the sacrificial polysilicon in the ports which have a damaged protecting stack will be oxidized (in *step e*) and cannot be removed later on (*step f*)[6]. Second, the

[6] Note that for a successful release at step f, the thickness of the oxide on the port should be much less than the oxide which forms on the backside of the wafer and the sidewalls of the etch vias at step e. Polysilicon, if exposed, is oxidised faster than single crystalline substrate and, therefore, the protecting oxide at the backside is removed completely before the sacrificial layer is reached.

bottom of the etched holes should be as flat as possible or else, because of small misalignment, it might miss the port as indicated in Figure 4.14.

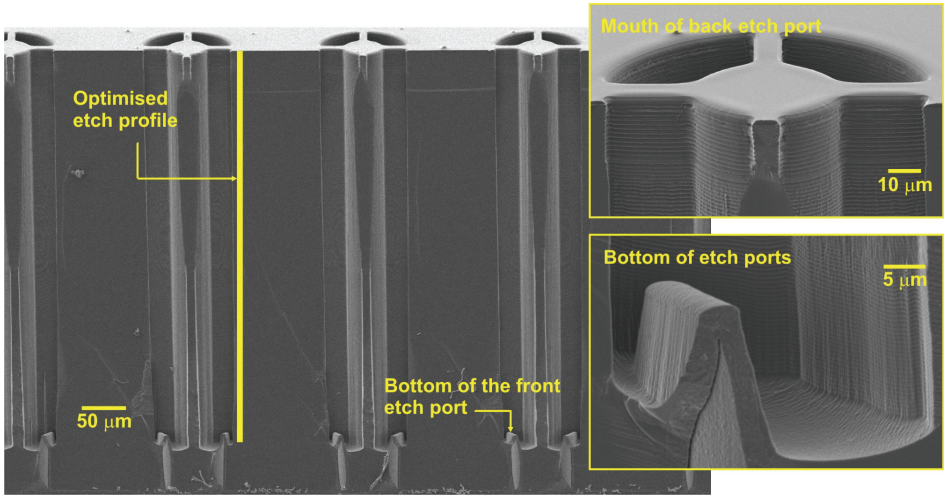

Figure 4.13 *SEM micrograph of etch vias. The flat bottom and uniformity are important for high yield (note: wafer is upside down)*

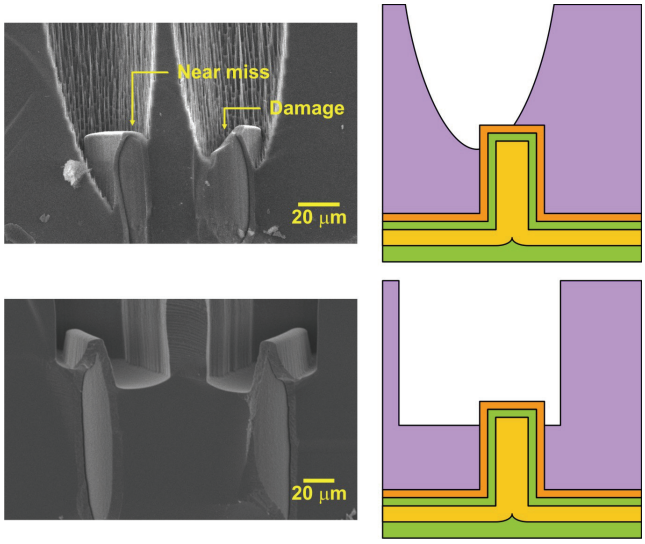

Figure 4.14 *Detail of backside etch profile*

Third, the etch time and selectivity should be such that photoresist can be used as the etch mask. It is hard to remove any other masking material from the backside of the wafer before the oxidation step (*step e*) without affecting the protection layers at the bottom of the "etch ports". And finally, the etch process has to be uniform over the entire wafer. This is because while the etch process should be done so that ports are well exposed, over-etch can remove the protecting SiO_2/Si_3N_4 stack and later

oxidation of polysilicon in the port at *step e*. Besides, under-etch results in closed ports. Consequently, in both cases, the membrane cannot be etched free.

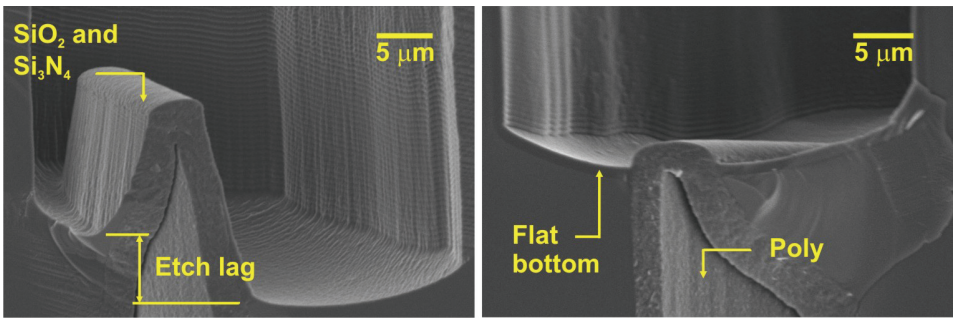

Figure 4.15 *The progress of backside etch after reaching the "etch ports"*

Figure 4.15 shows a close up of the bottom of an etch via. Note that the outer part of the etch vias are bigger (Figure 4.2) and this induces an intrinsic etch lag to the process. However, when the bottom of an etch via is flat, the etch lag or a small misalignment has no detrimental effect on the provided connection.

Table 4-II. *DRIE recipe (Pulsed CHF_3) for the backside "etch ports" using Adixen AMS100-SE*

Parameter	Etch	Deposition
Gas	SF_6	CHF_3
Flow (sccm)	400	200
Time (s)	4	0.5
Priority	2	1
APC (%)	15	15
Power ICP (W)	2500	2500
Power CCP LF (W)	20	20
Pulsed LF (ms)	20 on / 180 off	20 on / 180 off
He Pressure (mBar)	10	10
SH (mm)	110	110
Electrode Temperature (°C)	-110	-110

To fulfil all these requirements, a new DRIE process for high aspect ratio etching of silicon was developed to make a flat bottom with vertical sidewalls [7]. This new process uses CHF_3 as inhibitor. Inlet holes with an aspect ratio of ~22.5 are uniformly (±2%) etched over the wafer, with an etch rate of 10 µm/min. Selectivity over the SiO_2/Si_3N_4 stack is sufficient to stop on it: the etch rate of oxide is smaller than 1 nm/min. In practice, it is essential to increase the Capacitively Coupled Plasma

(CCP) power to 50 W for one minute at the beginning of the process or else the native oxide layer on the surface of the substrate prevents the etch process to proceed. The etch rate for photoresist is 15 nm/min. Sidewall profile (taper) and shape of the bottom is mainly controlled by the electrode temperature, on/off time and power of the CCP. Table 4-II indicates the parameters that have been used in this specific DRIE process. This recipe is highly sensitive to temperature and etching load. Fine adjustments may be needed to use the recipe for a different pattern.

In the oxidation step (*step e*), the thickness of the grown oxide is based on the selectivity of the etch recipe for the sacrificial layer etch, stress considerations and more importantly the oxidation rate of the protecting SiO_2/Si_3N_4 stack on the bottom of the "etch ports" and the SiRN layer on the frontside of the wafer. Short oxidation times will not provide sufficiently thick oxide layers whilst long time oxidation will oxidize the sacrificial layer. Experiments have shown that the minimum required thickness of the oxide is about 1 μm. This oxide layer should be thick enough to withstand the anisotropic etch process of *step f* and the release etch process of *step j*.

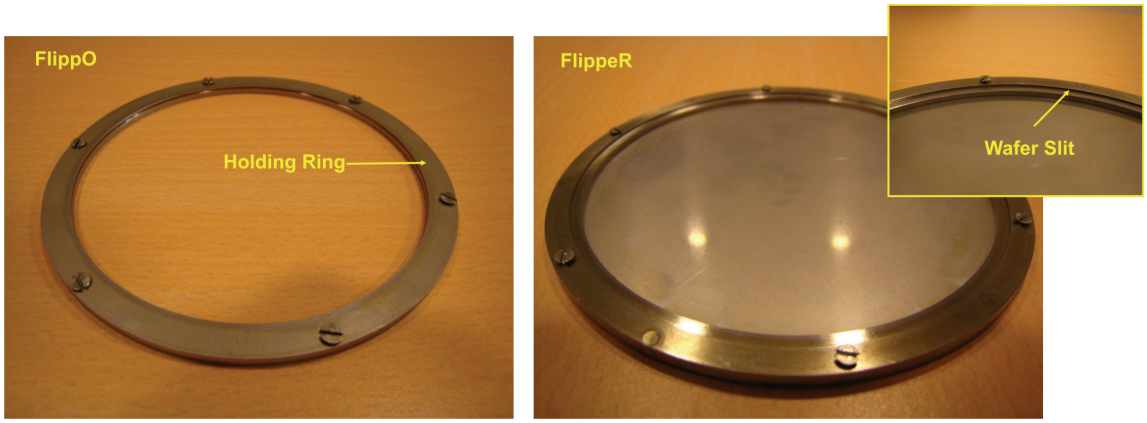

Figure 4.16 *The first prototypes of the carrier*

To protect the hair structures during the backside etch process a special holder is needed. The carrier was initially made of stainless steel in two variations as shown in Figure 4.16. Loading and unloading of the substrate in these carriers are easy, they are not influenced by the SF_6 plasma and hence can be reused without any problem. However, conductivity of stainless steel influences the plasma. In addition, it is difficult to obtain the same flatness as for silicon wafers. The holder shown on the right side (FlippeR) causes more trouble as the thin bottom plate bulges. The one on the left

(FlippO), however, doesn't protect the structures when the wafer is lifted by the fork of the etcher during loading and unloading.

To overcome these difficulties using oxidised silicon wafers another carrier has been designed as is shown in Figure 4.17. The rings provide the necessary distance and the bottom carrier is to protect the hair structures during wafer transfer. The fork which lifts the substrate does not damage the SU-8 hairs. The holes in the carrier are essential to let cooling gas (He) contact the frontside of the wafer. Apart from temperature stabilization, He dilutes the SF_6 radicals and prevents the front side to be etched through pin holes in the membrane layer. However, the carrier should be disassembled, cleaned and oxidised again after approximately fifteen hours of operation since the protecting oxide is etched (1 nm/min) during the process.

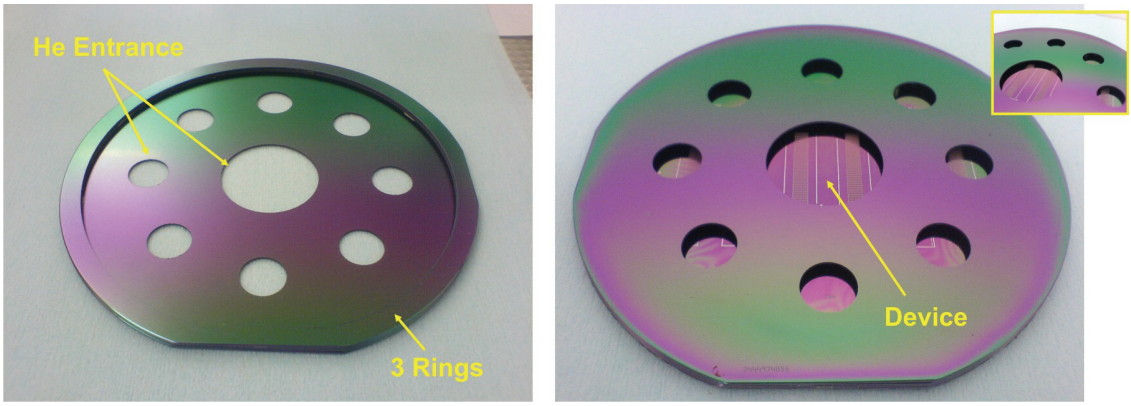

Figure 4.17 *The wafer holder for backside etch, left: the holder, right: the holder is glued to the device wafer*

Table 4-III. *Recipe (for Oxford Plasmalab 100) to remove SiO_2/Si_3N_4 stack from the bottom of fronside "etch ports" in steps f and j*

Parameter	Anisotropic	Isotropic
SF_6 (sccm)	50	120
He (mTorr)	20	20
Power ICP (W)	600	600
Power CCP (W)	50	0
Pressure (mTorr)	10	15
Temperature (°C)	20	20
Etch Rate SiO_2 (nm/min) On the surface	~ 70	~ 1
Etch Rate polysilicon (nm/min) On the surface		145-150

Table 4-III summarizes the etch recipe for opening the "etch ports" and sacrificial layer etch (steps *f* and *j* respectively) using SF_6 plasma [8, 9]. In the anisotropic process ion bombardment will remove the SiO_2/Si_3N_4 protection stack and then the isotropic process will selectively remove the sacrificial polysilicon within the rim boundaries.

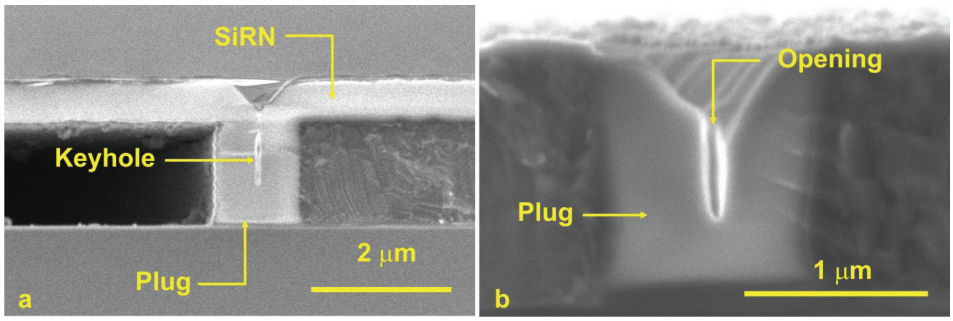

Figure 4.18 *The keyhole in deposited SiRN in the rim can result in a sharp opening which can cause electrical discontinuity. Left: before blanket etch, right: after blanket etch*

A problem that can arise during *step g* is the sharp opening in the SiRN layer which fills the rim because of the keyhole formation during the SiRN deposition step (Figure 4.18). This opening can cause discontinuity in the aluminium interconnects. To prevent this, the etch profile should be positively tapered or deposition of SiRN should be tuned not to leave a keyhole. The obtained electrical resistivity of aluminium wires is around 6.5×10^{-8} Ω·m and does not change upon crossing the rim.

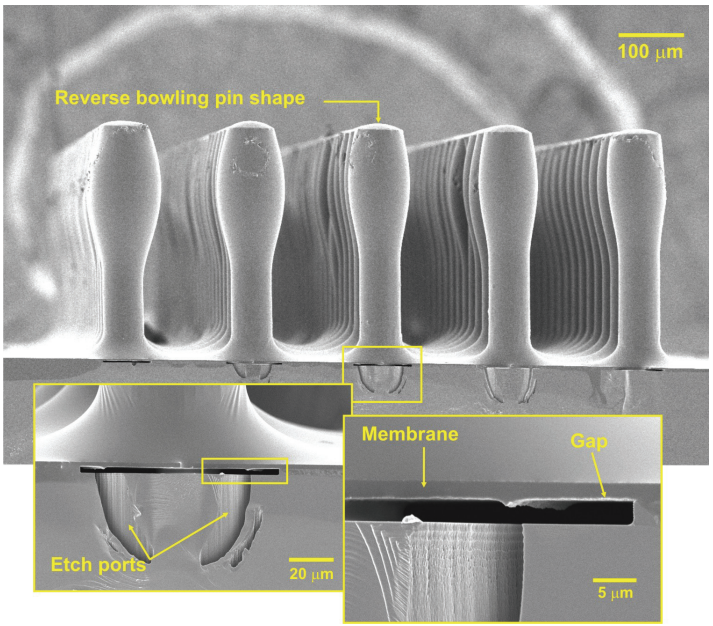

Figure 4.19 *SEM micrograph of a sensor array. Note the bigger top of the hairs increases the drag force on them*

Figure 4.19 shows a final device. The close up of the gap and the base of the hairs are shown in the insets. The shape of the hairs, using negative tone characteristics of SU-8, has been tuned to increase the drag force on them. In this device a single SU-8 layer is used for realization of the hair.

It is possible to repeat *step i* of the process to realize longer hairs. We have used a double layer process and successfully increased the length of the hair structures to 900 μm. The results are shown in Figure 4.20.

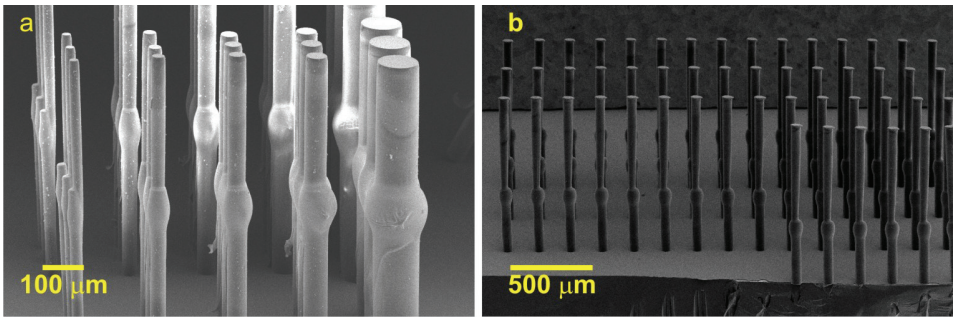

Figure 4.20 *Two layers hair structures*

4.2.4 Process variations

4.2.4.1 Negative Profile for the Frontside "Etch Ports"

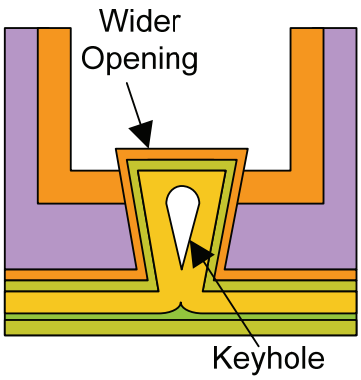

Figure 4.21 *Schematic of the keyhole formation and wider openings of the "etch ports" using a negatively tapered profile*

Formation of keyholes is desirable in *step h* when depositing the polysilicon layer. The polysilicon in the "etch ports" act as sacrificial layer and, therefore, is etched away later (*step j*). The keyhole formation makes the etching process faster. For this reason, the etching process of frontside "etch ports" can be tailored to negative profile to enhance the keyhole formation. This also provides a larger cross section at the

bottom of the port which is desirable for diffusion of the etch species during sacrificial layer etch process. Furthermore, it also decreases the chance of closed port formation due to misalignment.

4.2.4.2 Using Amorphous Silicon

For a better uniformity and surface roughness, instead of polysilicon, an amorphous silicon (a-Si) layer can be used. However, a-Si exhibits higher residual stress and its deposition rate is almost half that of polysilicon. Higher residual stress increases the chance of substrate deformation during later high temperature processes especially when the backside stack has been etched away in *step c*. The lower deposition rate translates to longer deposition time to achieve the minimum thickness required for "etch ports" closure.

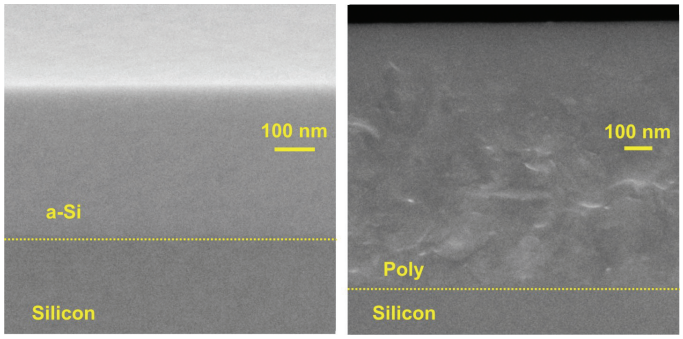

Figure 4.22 *The local roughness of the a. amorphous silicon and b. polysilicon layer*

4.2.4.3 Isotropic Step to Open the "Etch Ports"

The anisotropic process in *step f* while removing the oxide/oxynitride layer at the bottom of the "etch ports" thins the protecting oxide layer at the backside of the wafer. However, since the etch rate on the surface is much higher than in the high aspect ratio etched vias, this process removes more than 90 percent of the oxide layer. This may leave an oxide layer which is not thick enough to protect the wafer during the isotropic sacrificial layer etch (*step j*). Additionally, the severe ion bombardment on the backside of the wafer may cause pinholes in the oxide layer which, during the isotropic etch step, change the loading of the system and have detrimental effects on the etch process.

Table 4-IV. *Etch rates of different materials in ISO process*

Material	Thermal Oxide (SiO_2)	Si_3N_4	Oxidised Si_3N_4	Polysilicon
Etch Rate in ISO process (nm/min)	1 to 1.5	4 to 8	0.8 to 1	145 to 150

To overcome all these, one may consider using an isotropic step and remove the protecting stack of materials at the bottom of the "etch ports" using only the chemical component of the etch recipe. Yet, this means a very long etching process. We used the same isotropic process used in *step j*. The etch rates of the materials on the surface of the wafer are given in Table 4-IV. There is about 50% reduction in etch rate at the bottom of the high aspect ratio etch vias. Therefore, a minimum of 3 hours isotropic etch process is needed to open the protecting stack. On the other hand, during this time only 20 percent of the protecting oxide at the backside is removed. This will also provide the possibility to grow a thinner oxide in *step e* which in turn means the thickness of the oxidized nitride layer decreases.

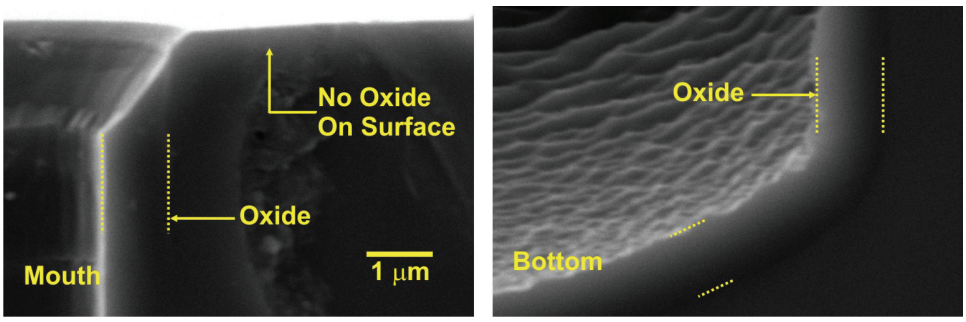

Figure 4.23 *The effect of ion bombardment using RIBE to remove the stack at the bottom of the vias*

This whole process is further justified by investigating the effect of the directional ion bombardment. To this end, an experiment was conducted using Reactive Ion Beam Etcher (RIBE). In RIBE, the chamber's pressure is very low (0.3 mTorr) and the directionality is very high. It uses only the accelerated ions and involves no chemical component in etching process. The result shows that there is no significant change in the thickness of the oxide layer at the bottom of the vias.

Figure 4.24 below shows the open "etch ports" which are obtained using only the isotropic step. The membrane in these pictures is (~1 μm thick) silicon nitride. The flow of He from the bottom side dilutes SF_6 etch species so that they have no visible effect on the front side. This is important since the polysilicon can be attacked through a pinhole in the covering SU-8 membrane. Moreover, it should be noted that once the polysilicon layer is exposed, the etch rates of oxide and nitride layers decrease substantially. This is due to the great difference between the etch rates; polysilicon is etched and depletes the SF_6 etch species.

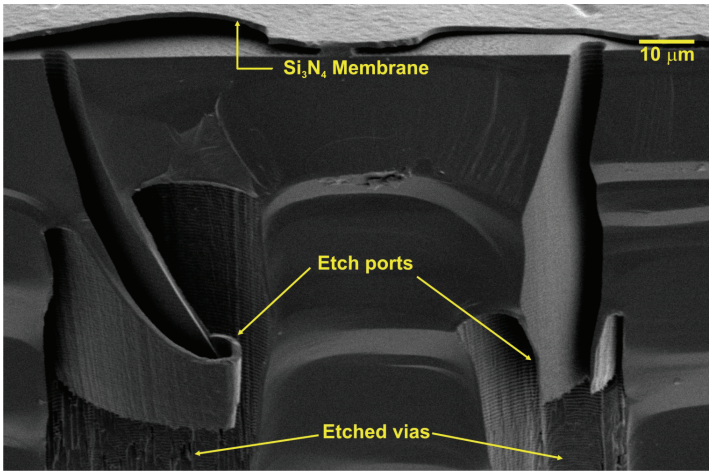

Figure 4.24 *The "etch ports" can be opened using only the isotropic step. Once polysilicon is exposed the protective SiO_2 and SiRN are not etched further.*

4.2.4.4 DRIE Step for Highly Doped Substrates

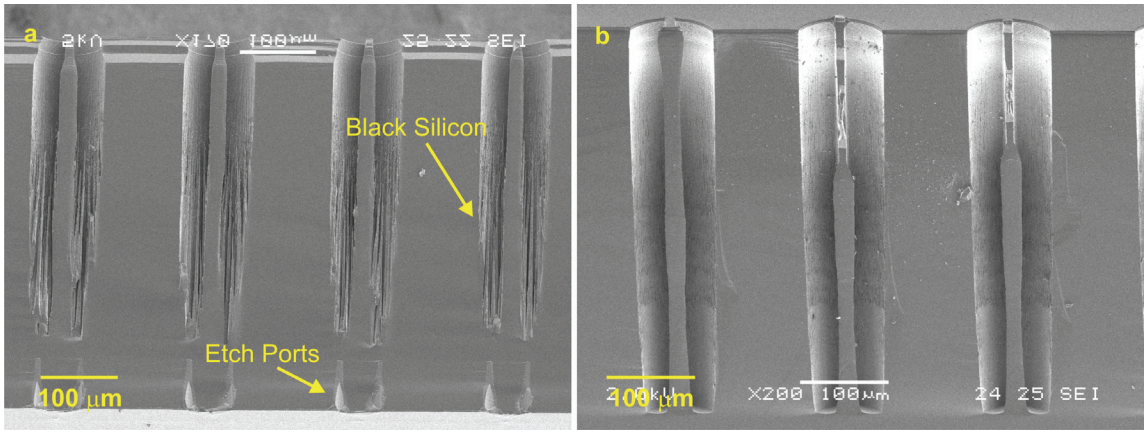

Figure 4.25 *Effect of the CCP power in DRIE on highly doped silicon substrate: a. CCP LF=20 W, b. CCP LF=25 W*

The DRIE process (*step d*) is a critical step. Slight variation of the processing condition affects the etch rate and the resulting profile. Interestingly, it has been observed that the doping level of the substrate plays a clear role in the etch rate and profile. Figure 4.25 shows the etch profile for a highly doped substrate. At the left the resulting profile using the recipe given in Table 4-II is shown. This recipe results in vertical sidewalls and a flat bottom when an undoped wafer is used (see e.g. Figure 4.13). However, the profile changes substantially, as can be seen in the figure, using a highly doped substrate. It is believed that the excessive image charges deflect the incoming fluorine radicals and, hence, the profile degrades. This can be overcome by

an increase in the CCP power. At the right of the figure the resulting profile using the same recipe but with a CCP power equal to 25 W (in contrast to 20 W of the original recipe) is shown. This slight change has a considerable effect on the outcome of the process.

4.2.4.5 Sacrificial Layer Etch Process using XeF_2

The isotropic etch process (*step j*) can be done using XeF_2. Xenon difluoride offers a very high selectivity and etch rate. However, as shown in Figure 4.26, this results in a very rough surface of the substrate (common electrode) and may have detrimental effects on electrical properties of the device. This effect can be controlled as discussed in [10]. The required elevated temperature is in the range which can be used safely without affecting the polymer structures.

Using SF_6 plasma, however, results in a smooth surface as shown at the left side of the figure. Note that the particles seen in the picture are due to cutting procedure. On the other hand, when, the etch time should be increased to ensure complete release of the membrane, SF_6 can completely remove the protecting oxide at the sidewalls of "etch ports" and the surface of the substrate. This exposes the silicon substrate which etches fast and, clearly, affects the device.

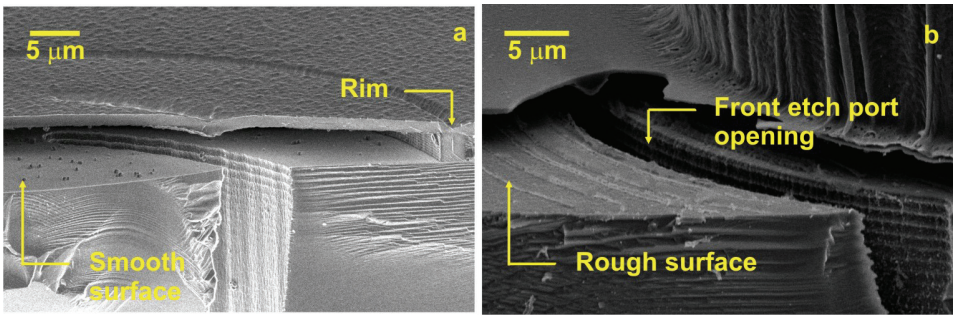

Figure 4.26 *The silicon surface under the membrane. a: SF_6 isotropic plasma recipe, b: roughness of the surface caused by XeF_2. Note that few particles on the surface of the sample etched with SF_6 (left side) are probably due to mechanical breaking of the chip.*

4.2.5 Conclusion

A fabrication process was presented that allowed us to successfully realize dense arrays of fully supported flexible SU-8 membranes with hairs on top. These flow sensors mimic the mechanoreceptors in lateral line of fish. The operation environment enforces the insulation of the electrodes from the fluid and a number of design rules which have been met. The process needs careful consideration and fine tuning in each

step beforehand. A number of optimization processes resulting in more robust and/or faster processing have been pointed out. The fabrication process, although seemingly complex, offers several possibilities for particular adjustments of the characteristics of the sensors on a single wafer. It also can be used as a more general fabrication scheme for backside sacrificial layer etching.

4.3 Canal Embedded Sensors

In this part we present the fabrication process for the canal embedded artificial neuromasts. The concept and the design of this device have been discussed in chapter three. The hair-like structure resembles a cantilever with a rigid tip: a thin flexible beam connected to the top of the canal at one end and to a wider part at the other end. This wider part is the seat of a floating electrode. SU-8 is a negative tone photoresist. Therefore, the basal part of the two segmented structure can be directly exposed on the wider part without affecting the underneath layer. On the other hand, to fabricate the top of the channel which also serves as the base of the hair-like structure a reflector needs to be used. The presented results serve as a feasibility study as the final prototype of the device including the readout electrodes has not been fabricated yet.

4.3.1 Fabrication Procedure and Results

The intent of the canal embedded sensors' design and technology is to have a simpler and faster to execute fabrication process than what is used for the artificial superficial neuromasts presented in the previous section. Moreover, it is intended to make channel embedded flow-sensors. The procedure mainly consists of low temperature polymer processing steps. A doped polysilicon layer functions as bottom electrode with connection lines and bond pads. The deposition of this layer is even unnecessary when using SOI (Silicon On Insulator) substrates (with a thin device layer). In addition, an amorphous silicon (a-Si) layer is deposited as the sacrificial layer between the hair and the substrate. XeF_2 based etching offers a highly selective and dry method to etch this layer later in the process. The hairs and channel are built in the same SU-8 layer at the same time. Being a negative tone photoresist, SU-8 also provides the possibility for fabrication of the mace shaped hanging structures. The schematic exploded view of the sensor is shown in Figure 4.27.

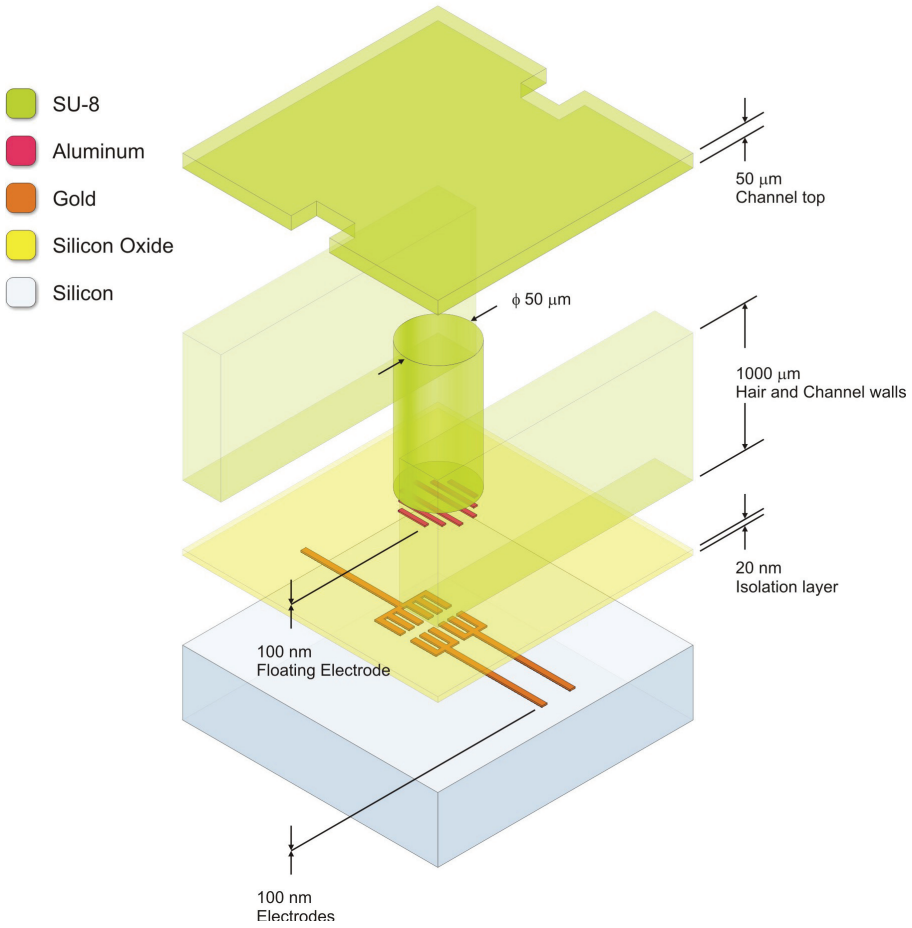

Figure 4.27 *Exploded view of a canal embedded artificial neuromast*

The outline of the process is shown in Figure 4.28. The process begins with a Single Side polished (SSP) silicon wafer. The wafer is oxidized to form a 1 µm thick insulating SiO_2 layer on the surface (*step a*). Subsequently, a 200 nm polysilicon layer is deposited. Solid Source Diffusion (SSD) at 1050°C is used to dope the polysilicon layer and make it conductive (i.e. resistivity of about 0.002 Ω·cm). These steps can be avoided using SOI wafers with highly conductive (i.e. resistivity of about 0.02 Ω·cm) device layers. Thereafter, the polysilicon layer (or the device layer of the SOI wafer) is patterned to realize the bottom electrodes, connection wires and bond pads.

A 100 nm thick silicon dioxide (SiO_2) is deposited using Plasma Enhanced Chemical Vapour Deposition (PECVD) and patterned to provide access to the bond pads (*step b*). This deposition is done at low temperatures to avoid boron segregation at

the Si-SiO_2 interface [11]. The layer is required to prevent the electrodes having electrical contact with liquid.

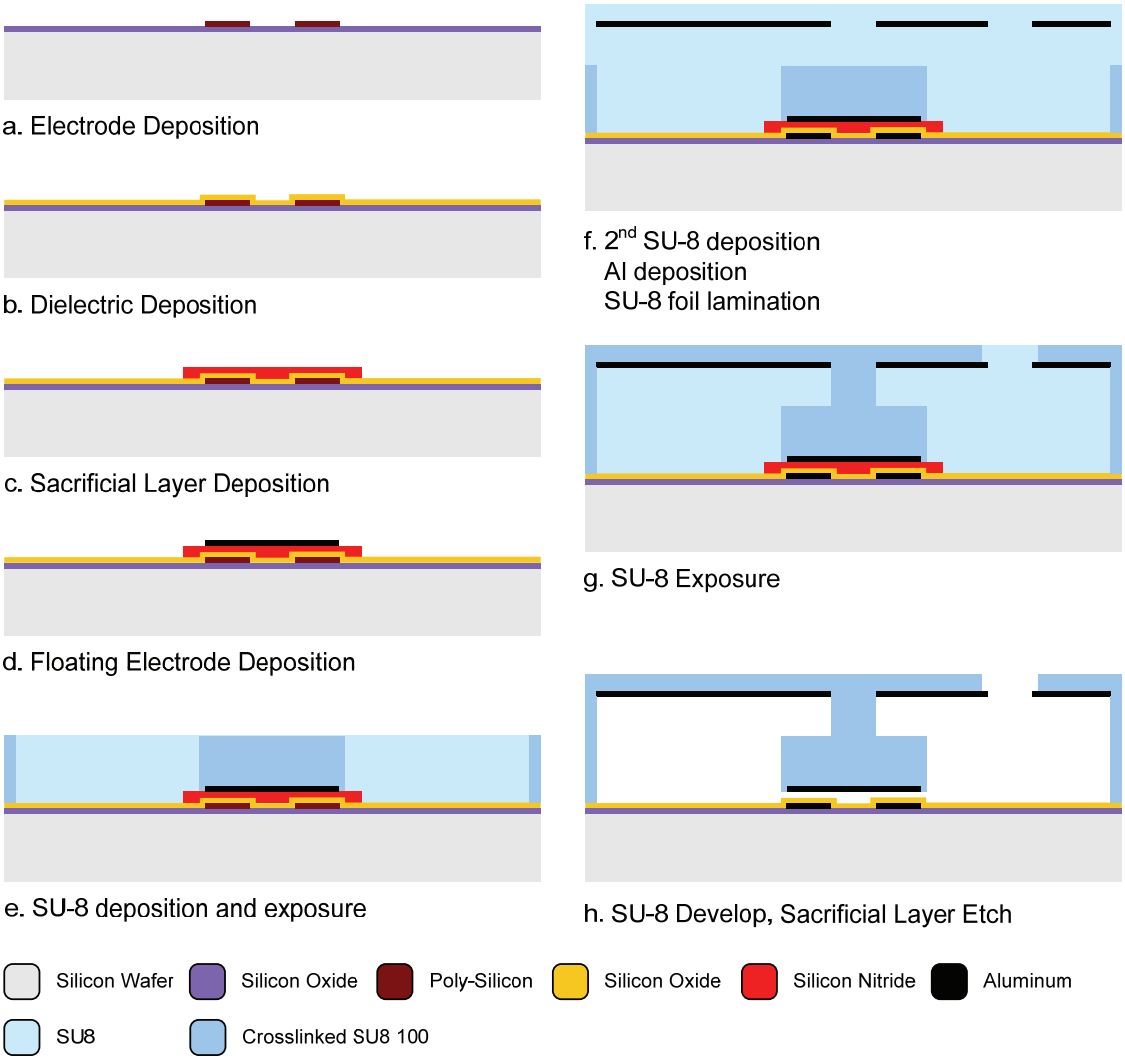

Figure 4.28 *Process scheme for fabrication of canal embedded flow sensors*

Subsequently, a 500 nm thick layer of amorphous silicon (a-Si) is deposited and patterned (*step c*). This layer serves as the sacrificial layer and its thickness determines the separation of electrodes and can be tuned according to the design criteria. A large gap reduces the sensitivity and a very small one, increases the chance of stiction to the substrate. Amorphous silicon is deposited at lower temperatures than polysilicon and gives a smoother surface. Therefore, in spite of lower deposition rates, it is preferred.

At *step d*, a layer of aluminium, which forms the floating electrode on the tip of the hair, is deposited and patterned. Gold is a better conductor but it has weak adhesion to SU-8 [12] and is, therefore, not suitable in the current design. Although following this procedure the floating electrode is not shielded, it is possible to grow a thin layer of oxide (or deposit a thin layer of nitride) before aluminium sputtering step and pattern it to insulate the floating electrode from the liquid medium as well.

The next step (*step e*) is to spin and expose the SU-8 layer which forms both the hair segment and the walls of the channel. The surface area of these structures should be wide enough to cover the floating electrode. The thickness of the layer determines the length of the hair, i.e. L_h. Therefore, the thicker this layer, the larger the drag force on the structure and, thus, the higher the sensitivity.

Subsequently, another thick layer of SU-8 is spun and soft-baked (*step f*). This layer forms the stem of the structure and its thickness determines the length of the stem, L_s. At the same time this layer forms the second part of the channel walls. After the soft-bake process of the SU-8 layer, a 200 nm thick aluminium layer is sputtered and patterned to delineate the stems and the pores resembling a canal lateral line. This aluminium layer acts as a barrier during UV exposure to keep the underneath SU-8 uncrosslinked.

After aluminium deposition substrate features are not visible and the features on the underlying SU-8 layer may not exhibit enough resolution or contrast. Therefore, it is usually troublesome to align the mask to pattern the aluminium layer (as well as other subsequent masks). A simple but effective way is to etch a suitable pattern on the backside of the wafers as the first fabrication step and use a bottom alignment procedure for all the following lithographic steps.

To encapsulate the channel and provide a base for the hair, a 20 μm thick SU-8 foil (Microform 1000 DF20 from MicroChem© which has now been changed to DuPont™ PerMX™ 3000 [13]) is rolled over the wafer. The use of a dry foil in this step is crucial. The normal soft-bake process for a SU-8 layer that is spun on the substrate causes the underneath SU-8 to reflow and the aluminium reflector to wrinkle and crack as can be seen in Figure 4.29 below. These wrinkles in turn result in undesirable cross linked structures inside the canal. On the other hand, the epoxy foil does not need a long soft-bake process at high temperature and keeps the aluminium layer intact. However, even when using the foil, the area on the surface covered by aluminium

should be minimised. SU-8 outgases during post-exposure bake and the aluminium, which covers a big area, hinders the process.

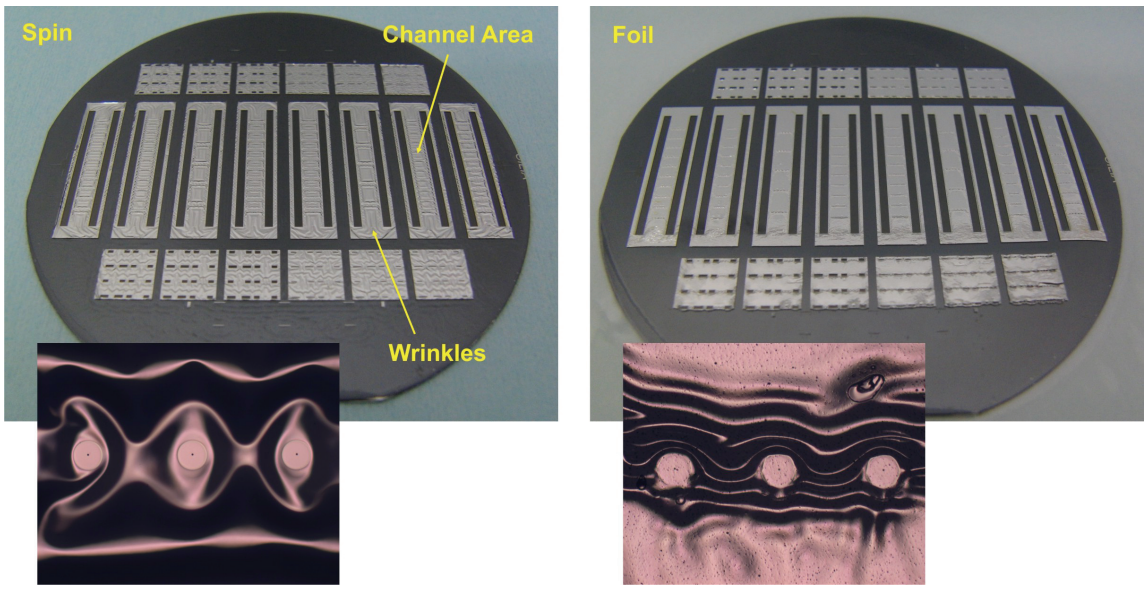

Figure 4.29 *Right: Epoxy foil laminated on the substrate; Left: SU-8 spun and soft-baked. In both cases the underlying SU-8 is baked after exposure and before aluminium deposition. The insets show a microscopic view of the patterns.*

The channel walls are made from all the layers of SU-8 previously spun and the foil. Therefore, the structure is made inside a canal. In addition, the cumulative thickness determines the canal height, which is equal to the structure length plus the gap between the electrodes.

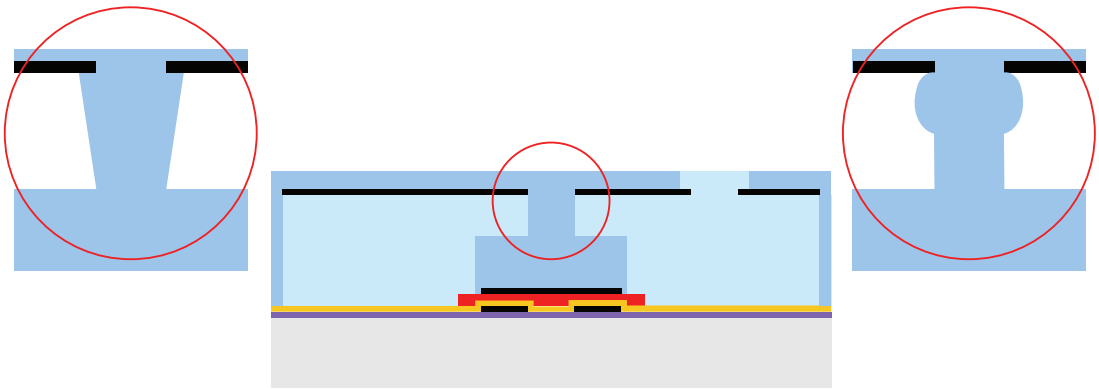

Figure 4.30 *The result of over exposure in the profile of the stem. The thicker part decreases the flexibility.*

Following this, the structure is exposed using a mask protecting the pores (*step g*). The exposure time depends on the stem length and should be optimized. A long

exposure time needed for very thick layers can cause a bulge at the base and results in degradation of performance. This situation is shown in Figure 4.30.

Note the increase in the hair base diameter and the negatively tapered shape of the stem on the left side of the schematic drawing and a bulge at the base on the right side.

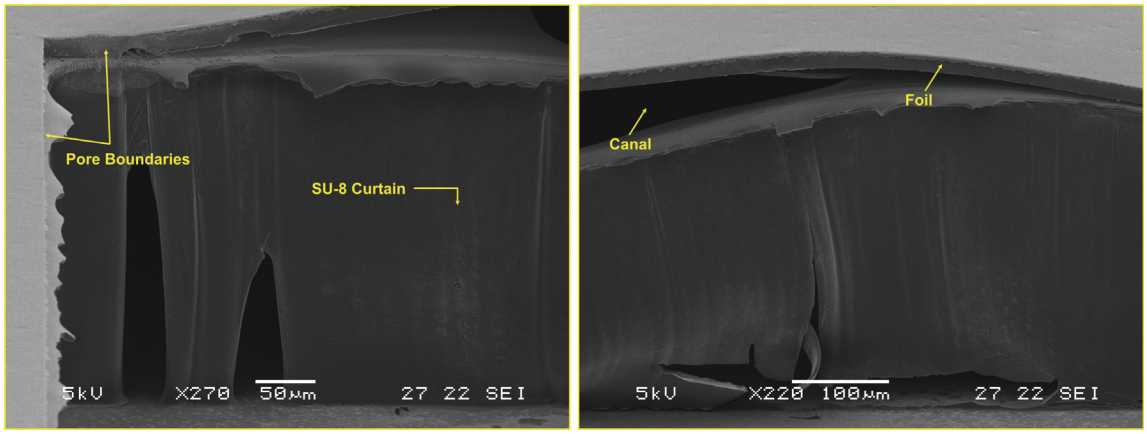

Figure 4.31 *Misalignment of the last mask may result in a curtain of SU-8 hanging at the edge of the pore openings*

It is important that the dimensions of the features representing the pores on the mask in the last lithography step are bigger than the opening in the aluminium layer. Otherwise, because of a small misalignment, the SU-8 at the edge of the pores will be exposed and forms a curtain-like barrier in the canal as is shown in Figure 4.31.

The next step is to develop SU-8 in an ultrasonic bath of RER600 (*step h*). In this stage the chips can be diced out of the wafer and treated individually. The ultrasonic bath is needed to remove all undeveloped SU-8 from inside the canal in a reasonable time. After the development, the hard-bake process is carried out to harden the SU-8 and increase its resistance to aquatic environment.

The last step is to etch the sacrificial a-Si layer and release the hairs. This step is done using a Xenon Difluoride (XeF_2) etcher. A wet etch process can end up to hair stiction after drying[7]. Besides, XeF_2 etch process is highly selective and will not affect the floating aluminium electrodes and SiO_2 insulating layers. However, the selectivity is so high that even a native oxide layer can prevent etching to proceed. Therefore, a HF

[7] Note that stiction occurs when the channel dries out. Therefore, once these sensors have been put inside the water the channel should always be kept filled.

(Hydrofluoric Acid) dip, or a short plasma treatment in SF_6 immediately before the etch process, is needed.

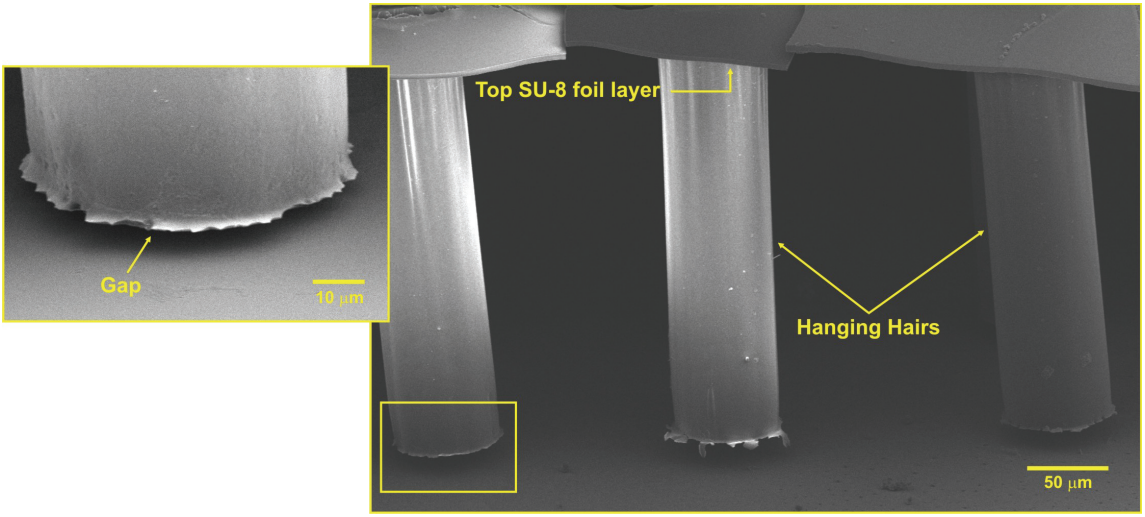

Figure 4.32 *SEM image of free hanging hair structures. The larger gaps are a result of the mechanical deformation in the top membrane due to the cut. The fabricated gap is 1 μm.*

It is also possible to etch the protecting aluminium layer but it has the risk of attacking the aluminium that forms the floating electrode. This process should be carried out before the sacrificial layer etch. The prototype is shown in Figure 4.33

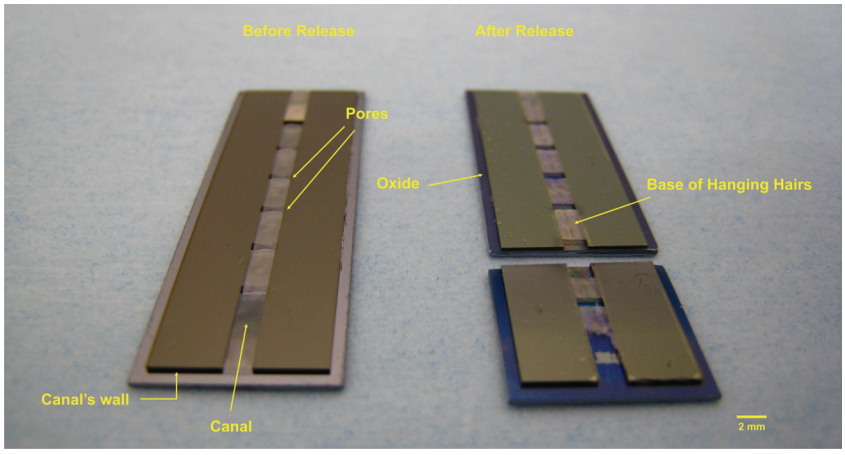

Figure 4.33 *The sensor chip before (left) and after (right) release*

4.3.2 Conclusion

The fabrication results presented in the previous section demonstrates the feasibility of realisation of a long structure having a short distance to the substrate with

no major stumbling blocks. Nevertheless, the very small gap between the electrodes, especially when compared to the length of the hanging hairs, makes the structures susceptible to stiction when liquid in the canal dries out. Good adhesion of aluminium to SU-8 after sacrificial layer removal has been shown in section 5.1.2 of the next chapter.

Unfortunately the actual prototype of the sensor including the electrodes has not been fabricated up to now and hence no measurements are available to confirm the device principle. While this may be true, the fabrication process for a final prototype has been started. It is expected that this device will be completed and tested in the near future. The results presented above provide us with a practical guide for optimisation of the final prototype.

4.4 The BooT

In this part we focus on the fabrication procedure of hair-like structures supported by a laterally moving shuttle. The shuttle includes fingers which form capacitors with other fixed fingers on the substrate. These fixed fingers are anchored to the substrate to prevent their in-plane bending due to the fluid drag and shear forces. The fabrication procedure of the shuttle and the fingers greatly resembles that of shear stress sensors with a high aspect ratio SU-8 cylinder on the shuttle. As in most shear stress sensors [14], using SOI wafers simplifies the process and avoids out of plane bending due to stress gradients. However, in that case the stationary fingers are not anchored to the substrate.

4.4.1 Fabrication Procedure

The outline of the fabrication process is shown schematically in Figure 4.34. The process starts using single side polished (SSP) silicon substrates. The substrate should be conductive and is set to ground potential during sensor operation.

In the first step (*step a*), the anchors are etched into the substrate with a depth of 50 to 60 μm. For this step, a similar etch process is used as in *step a* of the closed membrane fabrication introduced in section 4.2.2. A fluorocarbon removal step is done before the wafers are oxidised at 900 °C to grow a 100 nm thick oxide. It is known that at higher temperature, the produced stress is further relaxed due to viscous flow of the oxide [15, 16]. This has appreciable effect on the geometry of the grown oxide specially at the corners of the structures on a shaped silicon surface [17].

However, in different steps of the presented process, both single and poly crystalline silicon layers are being oxidised. To avoid possible differences in mechanical characteristics of the layers, wet oxidation is chosen over dry oxidation since it can be done at lower temperatures. On the other hand, dry oxidation at higher temperatures offers more uniformity and better control over the oxide thickness. The effects of high temperature oxidation on the produced stress gradient in the structures in this case have to be further investigated.

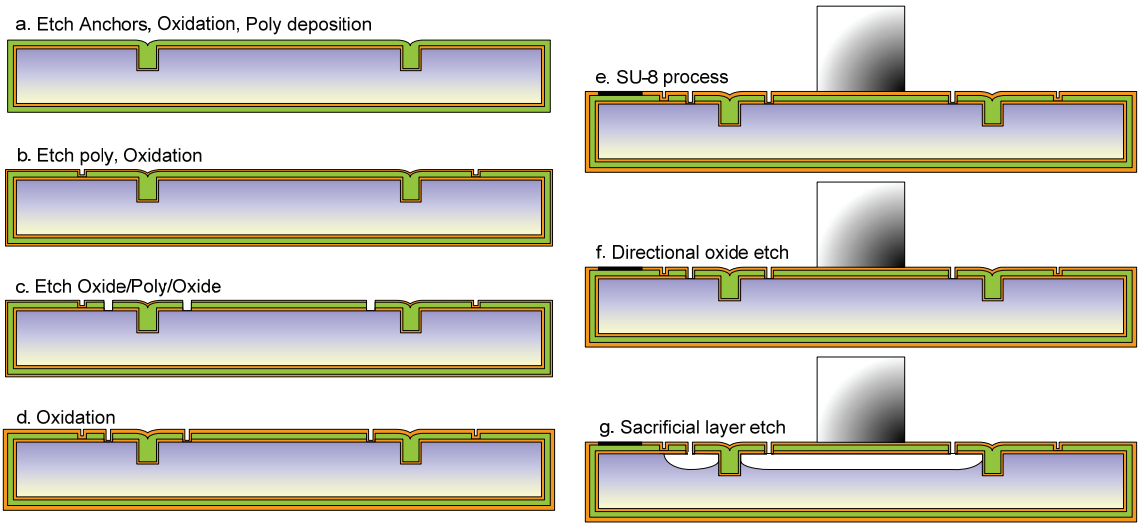

Figure 4.34 *Schematic outline of the fabrication process*

Next, a 2 μm thick polysilicon layer is deposited. A minimum of 1.2 μm polysilicon is needed to completely close the anchor trenches etched in the previous step to avoid lithography problems at the later stages. The thickness of this layer, on the other hand, determines the height of the beams and the fingers. The polysilicon is also used as the structural material for the springs. Therefore, an annealing process at 1100 °C is carried out to lower the stress gradient in the layer. In addition, because this layer is used to conduct electrical signals, it is doped. Solid Source Diffusion (SSD) at 1050 °C is used to decrease the resistivity to 0.002 Ω·cm (it is calculated, considering a 3 μm thick layer, from the measured sheet resistance, $R_{\square}$, which is around 6.8 Ω/□). To ensure homogenous distribution of the dopants and zero stress gradient, the samples are annealed at 1100 °C for 3 hours. However, before this annealing step, to protect the polysilicon layer from being oxidised during the process, a capping oxide is deposited using PECVD and is annealed at 800 °C. This low temperature annealing

before the actual high temperature step causes H_2 outgassing from the capping oxide and prevents cracking. The capping oxide is removed afterwards using BHF (Buffered HF) solution.

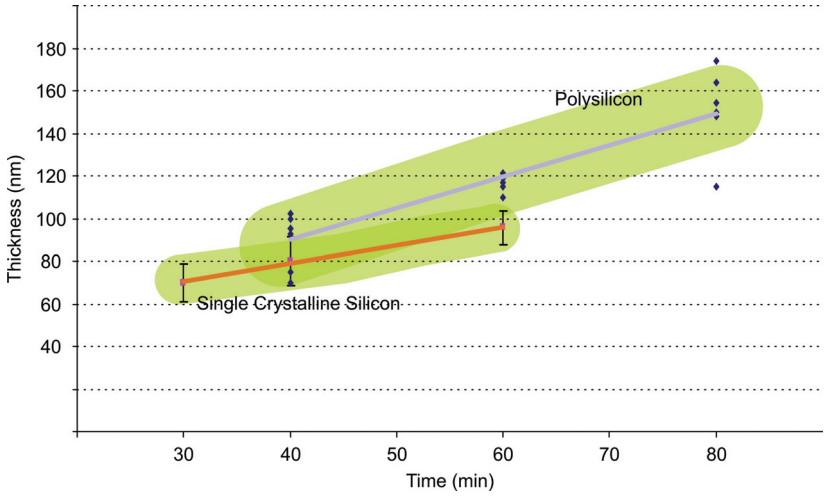

Figure 4.35 *Comparison between oxide thickness grown by wet oxidation at 900 °C of the oxide grown on single crystalline silicon and polysilicon layers*

Isolation trenches are then etched into the polysilicon layer (*step b*). These trenches electrically separate structural parts. The etch process is chosen to be selective with respect to the underneath oxide. The wafer is then oxidised, at 900 °C, to grow 110 nm thick oxide on the polysilicon layer. The oxidation rate of polysilicon is shown in Figure 4.35. This oxide acts as an etch stop during later device release. At the end of the process, the thickness of the oxide at the top and bottom of the polysilicon layer should be equal. This is to avoid stress gradient in the released structure which results in structural bending. Therefore, the thickness of the oxide grown in *step b* plus that in *step d* and minus the etched thickness by RIE in *step f* should be equal to the thickness of the oxide grown at *step a*.

The process continues with another etching step (*step e*) to remove a stack of SiO_2/polysilicon/SiO_2 and delineate the shuttle and the fingers. Two recipes are used which are selective to silicon and oxide respectively. Table 4-V shows the recipe that is used to remove the oxide layer.

The formed openings (access ports) are used at the last step to etch the underneath bulk of silicon. To protect the sidewalls of the fingers and the shuttle, a thin (~50 nm) thermal oxide is grown afterwards (*step d*). The openings are, therefore,

covered with this thin oxide which should be removed prior to device release using directional etching (see below).

Table 4-V. *RIE recipe (C-Nitride) for oxide removal using Adixen AMS100-SE*

Parameter	Etch
Gas	Ar / CHF_3
Flow (sccm)	100 / 100
APC (%)	100
Power ICP (W)	1200
Power CCP LF (W)	150
He Pressure (mBar)	10
SH (mm)	200
Electrode Temperature (°C)	-100

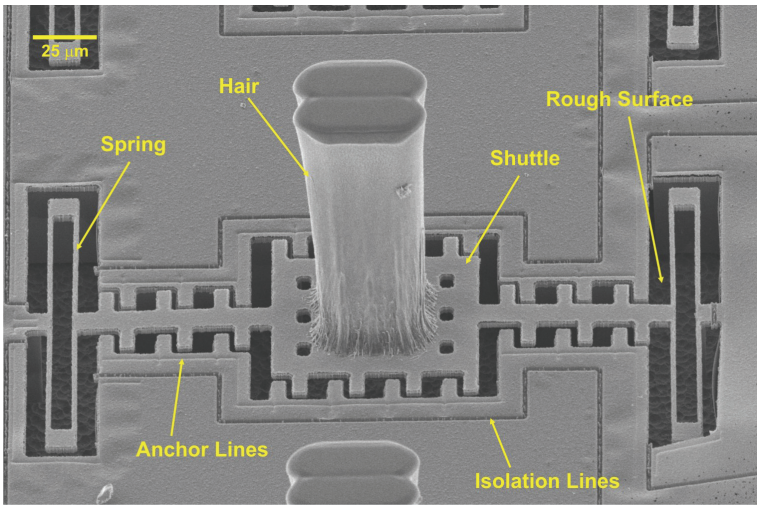

Figure 4.36 *SEM picture of a fabricated demo structure. The length of the hair is about 200 µm, each spring arm is 100 µm. The anchor and the rough surface of silicon due to the XeF_2 etch process are clearly visible.*

In the next step (*step e*), the covering oxide on the bond pads is removed and a thin aluminium layer is deposited and patterned. The aluminium can be used to cover the connection lines and lower the electrical resistance. These aluminium lines, however, should be insulated to prevent electrical contact to the liquid later on. For this purpose, a thin (~500 nm) layer of SU-8 2000.5 is used. The hair-like structure is then fabricated using SU-8 100 as has been discussed before in section 4.2.2. The grown oxide on the access ports (at *step d*) is removed using the same recipe presented in Table 4-V (*step f*). At the end (*step g*), XeF_2 is used to release the structure. Figure

4.36 shows a released device made on a single side polished (100) wafer. The springs and the shuttle, though covered with protecting SiO_2, are in the plane of the fixed fingers and exhibit no bending.

4.4.2 Discussion

The fabrication process of the BooT design is rather simple. Using SOI wafers and thick fingers which are not anchored to the substrate along their length, the process will become basically that of shear stress sensors which is well-established. The addition of hair structure does not change this fact. However, in that case the sacrificial layer would be silicon dioxide and the electrical insulation should be provided by conformal deposition of a dielectric (e.g. Parylene-C). The geometrical characteristics of the springs, among others, are determining factors of the performance of the sensor and can be adjusted to provide a wide dynamic range for the sensory array. Nevertheless, to achieve a low detection threshold the cross section of the springs should decrease while their length should increase. However, thin, compliant springs are more prone to bending due to residual stresses. The realised springs are 2 μm wide, which is limited by the lithography facilities, and ~2.5 μm thick. The springs with folded design show no out-of-plane bending even when they are very long. The springs with simple design, however, tend to buckle due to the stress gradient produced by the oxide layer as is shown in Figure 4.37. In addition, long and thin shuttles also exhibit out-of-plane bending, as is shown at the right side of the figure, even though their folded springs are flat. A solution to the residual stress, apart from using SOI wafers, is the complete removal of the protecting oxide after the last step. The device then needs to be coated, for example with Parylene-C, to provide insulation from the aquatic medium.

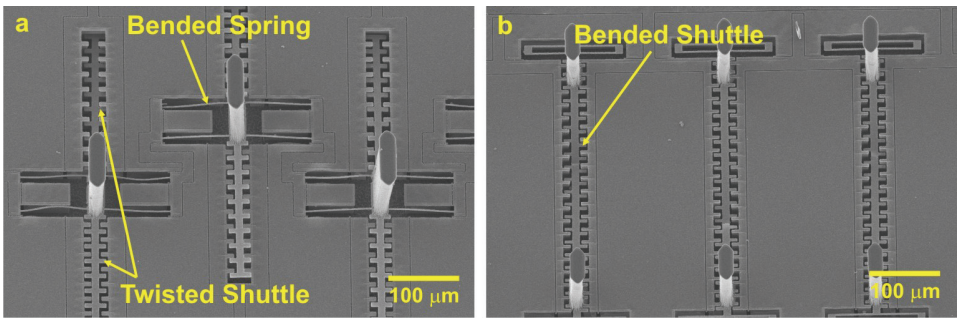

Figure 4.37 *The bending and rotation of the structures after release due to stress gradient*

Figure 4.38 shows a close up of the shuttle and the fingers. The rotation of the shuttle is shown at the left side. The obvious consequence is misplacement of the electrodes which degrades the capacitive performance. When the area of the shuttle increases it exhibits less bending. Another problem that may arise due to misalignment is the exposure of the polysilicon that fills the anchor trenches (see right side of the figure). When exposed, this layer is etched in the release step and opens a way for the liquid to enter the anchor trenches. The liquid is then in contact with the doped polysilicon layer which carries the signal and, therefore, may cause short circuits and electrolysis.

The last thing to consider is the effect of the bulk of fluid which fills the etched well under the shuttle. Since the well is rather deep the squeeze film damping should be relatively small. It may also increase the drag force on the structure due to reduction of the boundary layer thickness of the boundary layer.

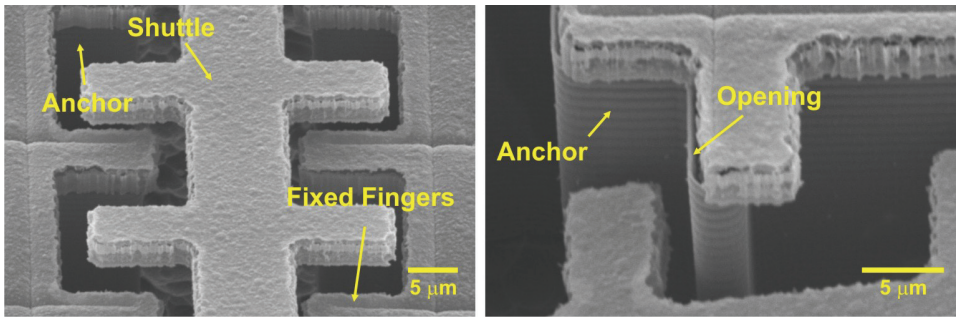

Figure 4.38 *Closer view of the fingers. Left: The shuttle has rotated upward, Right: The misalignment results in undesired opening*

4.4.3 Conclusion

The fabrication process of the BooT design presented in chapter three has been discussed. The laterally moving shuttle is connected to the substrate with four 2 μm wide, ~2.5 μm thick springs. The whole structure is made of polysilicon covered with a thin oxide layer which acts both as an etch barrier during device release and as an electrical insulation during operation. The nonuniformity of the insulating oxide layer, however, results in buckling of the springs. Two different designs for springs are presented: the simple springs and folded springs. While the former are more prone to buckling, the latter can release their axial stress and, therefore, do not show out-of-plane displacement. The shuttle carries the hair-like structure made of SU-8. To further stiffen the fixed fingers they are anchored to the substrate along their whole length.

This is because in water shear and drag forces on the fingers are higher than in a medium like air.

As this is a comparably new design, like the canal embedded sensors, the actual prototype including the electrodes has not been fabricated up to now. The presented fabrication results demonstrate the feasibility of the critical steps in the process. A complete device will be ready in near future.

4.5 Conclusion

The fabrication process for three different sensor designs has been presented. Among these, the sensor based on fully supported membranes has been realised successfully and is currently tested. The preliminary fabrication results of the other two prove the presented fabrication concepts by demonstrating the feasibility of the more challenging steps. In Table 4-VI the three fabrication processes are compared. The high temperature steps are important since they tend to induce thermal stress in the structure which needs to be carefully taken care of. The robustness against process parameter variations indicates the necessity of recalibration and optimisation of the obtained parameters for every step when the process is run multiple times. The critical steps are the ones in which one or more issues like uniformity, selectivity and endpoint detection are important. Unconventional steps are all the steps which cannot be categorised as lithography, deposition (including coating) or etching steps.

Table 4-VI. *Qualitative comparison between presented fabrication procedures*

Parameter	Membrane	Canal	BooT
Number of masks	8	6	8
High temperature (>500 °C) steps	5	4	4
Uniformity of steps (excluding SU-8 process)	Critical	Not Critical	Fairly Critical
Robustness against process parameter variations (excluding SU-8 process)	Poor	Very Good	Good
Reliability of SU-8 process	Good	Poor	Good
Critical steps	5	2	4
Costume made accessories	1	-	-
Unconventional steps	-	1	-
Overall difficulty of fabrication process	High	Average	Average
Yield	~100%	<100%	<100%

The fabrication of the closed membrane design exhibits a high yield and robust process. However, some of the critical fabrication steps are sensitive to the process parameters which should be tuned precisely. The thickness of the membrane is limited to 500 nm because thinner SU-8 layers cannot be spun defect free. An isotropic oxygen plasma etching process can be used to further thin the layer but the resulting thickness is not uniform. The process for canal embedded sensors is comparably simple and does not involve major critical steps. The diameter of the basal part of the hanging hair greatly determines the performance of the sensor. The use of negative tone SU-8 epoxy for realisation of this thin and long SU-8 beam has been demonstrated. On the other hand the very narrow gap between a high aspect ratio structure and the substrate may cause stiction problem. In addition, a major part of the process involves SU-8 structures for which the uniformity and repeatability are of concern. The laterally moving structures (BooT) have a relatively easier fabrication scheme as well. They are conceptually similar to shear stress sensors but the shuttle carries a high aspect ratio hair-like structure to turn them into drag-force sensors. In the presented fabrication process the fixed fingers are anchored to the substrate to provide further stiffness. The out-of-plane bending of the structures due to the stress gradient in the thin films is a major concern of the design. This problem may be alleviated when using SOI wafers with sufficiently thick device layer.

4.6 Reference

[1] N. Maluf and K. Williams, *An Introduction to Microelectromechanical Systems Engineering*, 2nd ed. Norwood, MA: Artech House, 2004.

[2] G. J. M. Krijnen*, et al.*, "Cricket Inspired Flow-Sensor Arrays," in: *Proceedings of the IEEE Sensors*, 2007, pp. 539-546.

[3] M. Uematsu*, et al.*, "Simulation of wet oxidation of silicon based on the interfacial silicon emission model and comparison with dry oxidation," *Journal of Applied Physics,* vol. 89, pp. 1948-1953, 2001.

[4] B. E. Deal and A. S. Grove, "General Relationship for the Thermal Oxidation of Silicon," *Journal of Applied Physics,* vol. 36, pp. 3770-3778, 1965.

[5] T. Enomoto*, et al.*, "Thermal-Oxidation Rate of a Si3N4 Film and Its Masking Effect against Oxidation of Silicon," *Japanese Journal of Applied Physics,* vol. 17, pp. 1049-1058, 1978.

[6] V. M. B. Carballo, "Rdiation Imaging Detectors Made by Wafer Post-processing of CMOS Chips," Ph. D. Dissertation, University of Twente, Enschede, 2009.

[7] H. V. Jansen*, et al.*, "Black silicon method X: A review on high speed and selective plasma etching of silicon with profile control: An in-depth comparison between Bosch and cryostat DRIE processes as a roadmap to next generation equipment," *Journal of Micromechanics and Microengineering,* vol. 19, 2009.

[8] M. J. de Boer*, et al.*, "Guidelines for etching silicon MEMS structures using fluorine high-density plasmas at cryogenic temperatures," *Microelectromechanical Systems, Journal of,* vol. 11, pp. 385-401, 2002.

[9] H. Jansen*, et al.*, "A survey on the reactive ion etching of silicon in microtechnology," *Journal of Micromechanics and Microengineering,* vol. 6, p. 14, 1996.

[10] K. Sugano and O. Tabata, "Reduction of surface roughness and aperture size effect for etching of Si with XeF2," *Journal of Micromechanics and Microengineering,* vol. 12, p. 911, 2002.

[11] J. W. Colby and L. E. Katz, "Boron Segregation at Si-SiO2 Interface as a Function of Temperature and Orientation," *Journal of the Electrochemical Society,* vol. 123, pp. 409-412, 1976.

[12] M. Nordstrom*, et al.*, "Investigation of the bond strength between the photo-sensitive polymer SU-8 and gold," *Microelectronic Engineering,* vol. 78-79, pp. 152-157, Mar 2005.

[13] DuPont. (2009, *PerMX 3000 series Data Sheet.* Available: http://www2.dupont.com/WLP/en_US/assets/downloads/pdf/PerMX3000_datasheet.pdf

[14] J. W. Naughton and M. Sheplak, "Modern developments in shear-stress measurement," *Progress in Aerospace Sciences,* vol. 38, pp. 515-570, 2002.

[15] C. H. Hsueh and A. G. Evans, "Oxidation induced stresses and some effects on the behavior of oxide films," *Journal of Applied Physics,* vol. 54, pp. 6672-6686, 1983.

[16] E. Kobeda and E. A. Irene, "SiO2 film stress distribution during thermal oxidation of Si," *Journal of Vacuum Science & Technology B: Microelectronics and Nanometer Structures,* vol. 6, pp. 574-578, 1988.

[17] R. B. Marcus and T. T. Sheng, "The Oxidation of Shaped Silicon Surfaces," *Journal of the Electrochemical Society,* vol. 129, pp. 1278-1282, 1982.

5

SU-8 Process

Due to its importance in all fabrication schemes introduced, in this chapter the SU-8 process is reviewed in detail. First the parameters and practical considerations for realisation of SU-8 structures are presented. Then, fabrication of passive canal embedded hair-like cylindrical structures from SU-8 on glass wafers is described. These structures are intended for use in Particle Image Velocimetry (PIV) measurements. Differences in structural and thermal properties between glass and silicon substrates require considerable adaptation of SU-8 process parameters.

5.1 SU-8

SU-8 has originally been developed for photolithography [1] but its use has now been successfully extended to a wide range of applications [2] (see also the bibliography at the end of chapter three). It has been introduced in chapter three section 3.3.7.1 as a suitable material for fabrication of the membrane and the hair structures in aquatic hair-based flow sensors. In the latter a thick layer of highly viscous SU-8 100 is used to fabricate high aspect ratio structures that sparsely cover the substrate. On the other hand, the thin SU-8 2000.5 used as the membrane covers the whole substrate. In another design, i.e. the canal embedded sensors, it also has been used as a building block to fabricate the wall of the canal. Here big SU-8 islands cover a relatively large area of the substrate. In addition, later in this chapter SU-8 utilization for fabrication of passive canal embedded hair-like cylindrical structures on glass wafers is presented. This diversity of applications imposes a wide range of requirements, which call for a careful consideration of the processing details in each case. In this chapter each of these steps is described.

5.1.1 Processing

The basic SU-8 process consist of pre-treatment of the substrate, spin coat, soft-bake, exposure, post-exposure bake (PEB), development and hard-bake as shown in Figure 5.1 below. The boxes indicate the process steps. The objective of each step has been described at the top of the box and the influential parameters are listed below. The actual parameters for each SU-8 process in the various fabrication schemes are presented in the process documents in the appendix. In the next sections the practical considerations that have lead to specific values of the many parameters are described.

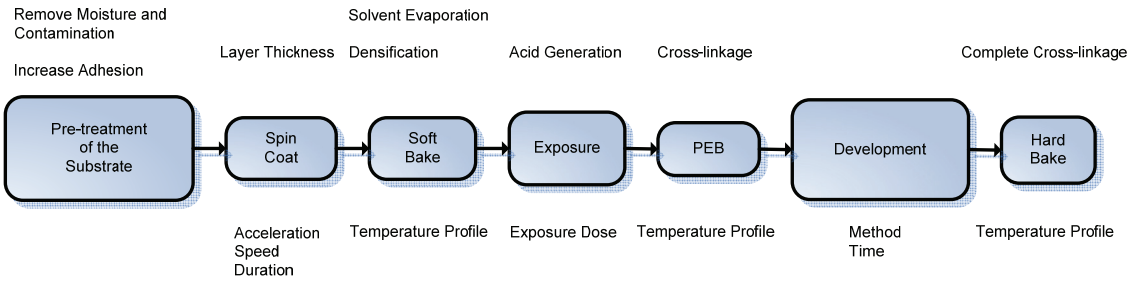

Figure 5.1 *The flow chart of basic SU-8 processing*

5.1.2 The Thin Membrane

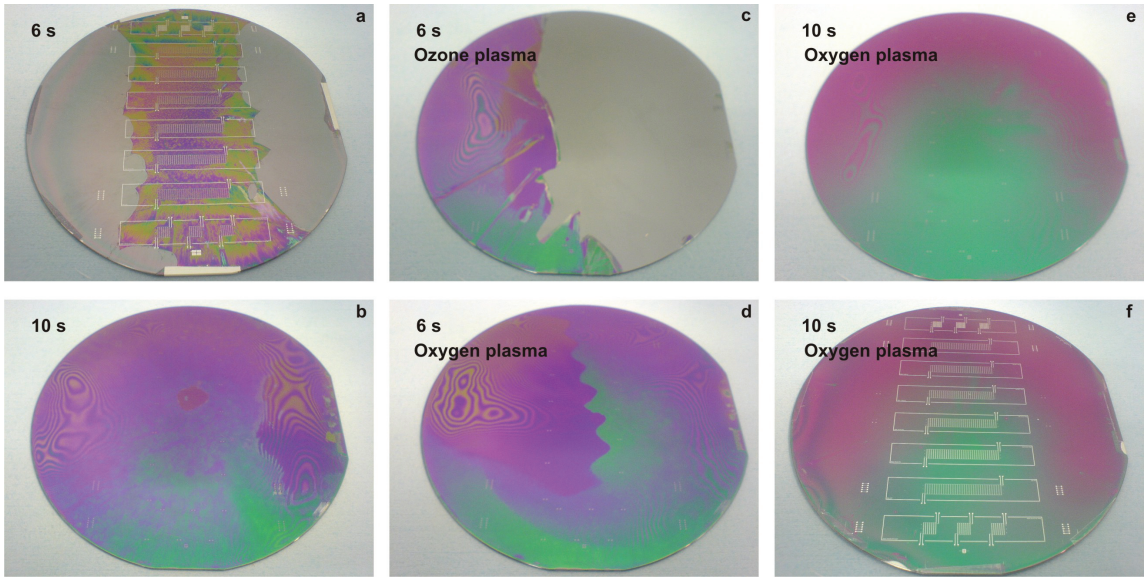

Figure 5.2 *The effect of surface pre-treatment and exposure dose (both indicated in the figure) on the adhesion of SU-8 2000.5 to the substrate. e and f are the same except that the latter is a processed wafer.*

The most important requirement in this case is the good adhesion to the substrate and aluminium electrodes underneath. The uniformity of the layer is important as well. For these reasons, as well as the sensitivity of thin layers to particles, the substrate should be thoroughly cleaned before the polymer is spin coat. The cleaning procedure increases the wettability and the adhesion. It is common to use Piranha cleaning on the substrate but the presence of an aluminium layer does not allow this procedure. Ozone plasma treatment [3] did not show any considerable improvement as well. We, therefore, used a standard cleaning procedure in fuming nitric acid (HNO_3) followed by an isotropic oxygen plasma treatment (10 minutes, 1000 ml/min O_2 flow, 800 W). The result is shown in Figure 5.2. Although it is the exposure dose that seems to have the strongest impact (see below), pre-treatment of the substrate results in visible improvement of the adhesion.

The layer thickness is determined by the rotational speed of the spin coating program. Figure 5.3 shows the obtained thickness versus rotational speed. The thin SU-8 layer is highly sensitive to particles present on the surface. The very thin layers, indicated by an orange oval in the figure, have visible defects and the highest non-uniformity. SU-8 does not wet the silicon surface (and other substrates with low surface energy) well. This results in a non-uniform coating of the substrate especially

when the SU-8 layer is thin. Therefore, to ensure full coverage of the surface, SU-8 should be poured on and cover the whole surface before the spin process starts. The wetting can be improved by applying commercial primers to the substrate before spin coating [2].

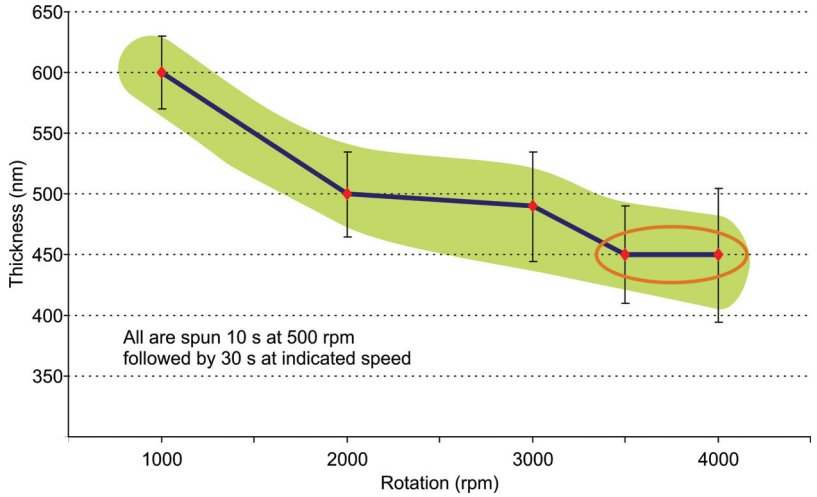

Figure 5.3 *Thickness vs. Rotational speed of the spin program for SU-8 2000.5*

After spinning, the wafers should be left for about an hour on a flat surface for levelling. The soft-bake is done at 95 °C by putting the substrate directly on a hot plate for one minute. Before one proceeds to the exposure step, the samples should be left for more than 24 hours on a flat surface for stress relaxation [4]. This will also result in a dry skin at the surface of the SU-8 layer and prevents the sticking to the mask during exposure. This is especially important when using a bright mask.

The exposure time is an important factor in the adhesion of the layer. Underexposure causes the layer to peel off from the substrate and overexposure results in the loss of resolution. The calculated exposure time using the data sheet from Microchem© [5] and an EVG 620 mask aligner is

$$\frac{Required\ Eposure\ Energy}{Lamp\ Power} = \frac{60\ mJ/cm^2}{12\ mW/cm^2} = 5\ s$$

But this exposure time is not sufficient. The necessary exposure time was determined to be at least 10 s which results in a stable coverage. It should be noted that after exposure a latent image should appear in the layer. The contact modes, soft or hard,

show no observable difference but chances of the substrate sticking to the mask are higher in the "hard contact" mode.

Although exposure itself does not produce stress in the layer [6], better results are obtained when the samples are allowed to relax on a flat substrate for some hours at room temperature before the post-exposure bake. This time potentially can reduce the effect of non-uniform exposure dose. The post-exposure bake (PEB) itself is done for one minute at 95 °C on a flat hot plate[1]. Lowering the PEB temperature substantially reduces the stress in the layer and hence prevents extra stiffening of the membrane [7]. This is followed by development of the SU-8 layer in RER 600 by immersion in a bath and manual agitation for 10 seconds. Long development time may cause delamination of the layer from the substrate. The samples are then put in a dry spinner and rinsed with IPA (2-Isopropanol) and blow dried with nitrogen.

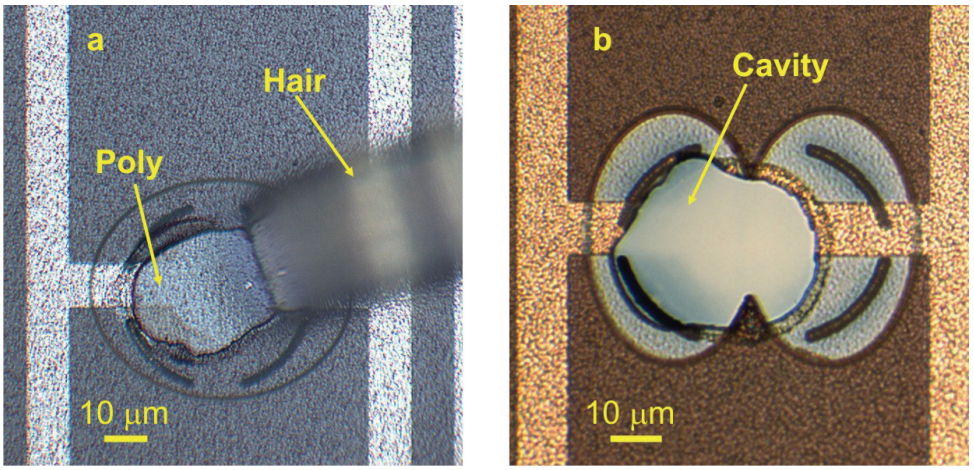

Figure 5.4 *The adhesion of aluminium electrodes to SU-8 membranes. Left: A hair has been cut and the aluminium electrode remained attached to it, not to the underlying poly; Right: After sacrificial layer etch and membrane release the aluminium remains attached to the membrane.*

Aluminium adhesion to SU-8 is illustrated in Figure 5.4. When a hair is ripped off the substrate, aluminium thin film always remains attached to the SU-8 hair. This is important when the sacrificial layer is etched, since any delamination of the aluminium film destroys the functionality of the device.

SU-8 is a thermal resin and its properties will change when subject to temperatures higher than it has seen before. In addition, as has been said, to decrease

[1] Note that the wafer is put on a pre-heated plate and is taken away after the intended time. It cools down on a flat surface at the room temperature.

the water absorption it is advisable to do a hard-bake process. This can be done at 150 °C for 10 to 30 minutes. When SU-8 is not properly cross-linked after the PEB process, its mechanical properties may vary and swelling due to humidity may occur [8]. The hard-bake process, however, increases the modulus of elasticity of the membrane.

5.1.3 The Hair

In the fabrication process of the sensors having a closed membrane, thick SU-8 100 which forms the hair structures is spun over the thin SU-8 2000.5 which forms the membrane. Although there is a visible boundary between the two layers (see Figure 5.5) the adhesion is strong and basically the two layers fuse into each other. As a result the fracture and peel off usually happen in the thin layer. Therefore, there is no need for pre-treatment of the surface. However, a short exposure to oxygen plasma can increase the wettability of the surface. This exposure further thins the membrane which, when controlled, is desirable since it increases the membrane flexibility. It should be noted that there is no visible difference between SU-8 100 connection with SU-8 2000.5 or SU-8 2 in SEM pictures or simple peel off test.

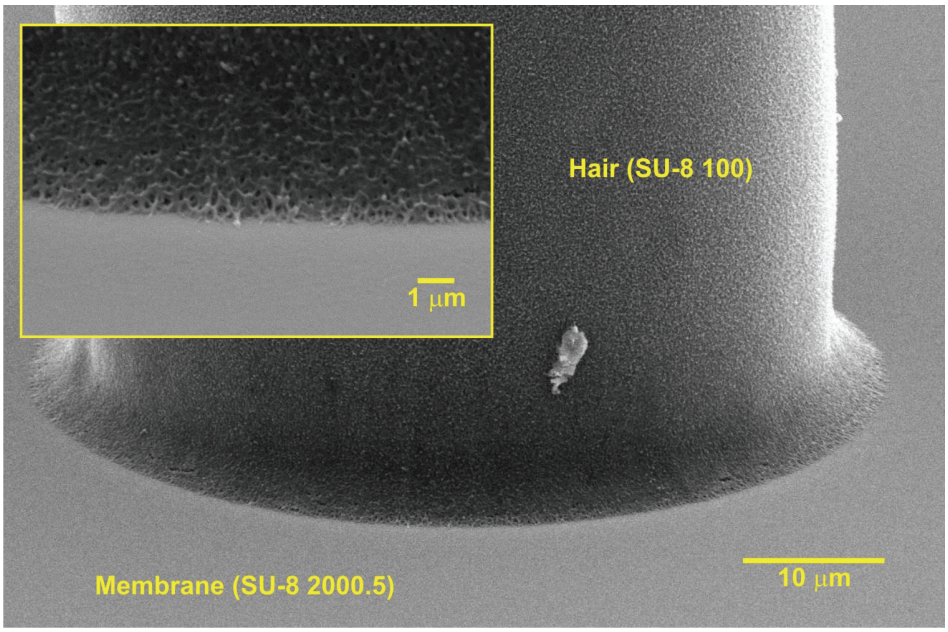

Figure 5.5 *The connection between hair-like structure and the membrane*

The substrate should be left on the chuck of the spin coater for 3 to 5 minutes to allow SU-8 to retract from the edges to the surface. Afterwards the substrate should be left on a flat and levelled surface for couple of hours before the soft-bake process. The large thickness has the advantage that it decreases the sensitivity to small particles but, on the other hand, its sensitivity to unlevel surfaces is much higher. For the conditions indicated above, there can be topographical variations of more than 350 μm if the surface of the hot plate is not levelled.

As discussed in the previous chapter, the high aspect ratio hair structures are achieved using two or three layers of SU-8. After the first layer is soft-baked, the second layer is spun. The exposure takes places after the desired height has been reached. The time for the soft-bake process of all the layers including the first layer is more than when using just a single layer to reduce the amount of solvent and has to be optimised by experiment [9, 10].

The soft-bake process is followed by 48 to 72 hours stress relaxation at room temperature and to further dry the top surface to prevent sticking. However, to ensure that the sticking will not occur, it is possible to put strips of Scotch tape (~50 μm thick) on the layer especially at the centre of the wafer and at the edges. While this approach helps to prevent sticking, the glue solvent of Scotch tape affects the SU-8. It can be seen that SU-8 thins on places where the tape is used. Another approach is to put the strips directly on the mask. In this case the SU-8 layer does not stick and is not affected.

The alignment should be done using a "large gap" procedure because of the high non-uniformity in the SU-8 layer. For a single SU-8 layer a soft contact and 110 seconds exposure are used. The maximum aspect ratio is limited by the available lithography source to 20. Therefore, for a 400 μm thick layer the minimum hair diameter is 20 μm. The stress relaxation after exposure is very important [4]. Typically a two hours relaxation at room temperature (in an environment without UV radiation) on a flat plate is done before the post-exposure bake.

The second layer can be processed with repetition of the above mentioned steps. However, in that case no post-exposure bake for the first layer is necessary since the thermal cycles used to soft-bake the second layer are sufficient to complete the cross linking of the first layer as well. In addition, the exposure time of the second layer should increase to 150 s because of the lack of a reflecting layer at the bottom.

When three layers of SU-8 are spun on top of each other and the exposure is done after the whole stack is pre-baked, the exposure time is high as 475 s.

The development is done using a spray gun developer for 20 cycles of one minute. Long development times can cause the delamination of the thin membrane underneath or cause mechanical damage of the hairs. After development the surface is carefully rinsed with IPA and is dried in a low speed spin drier without nitrogen flushing. When the development has not been complete, the substrate turns milky as it is rinsed by IPA. In such instances, it should be rinsed with RER600 again and the development continues for a few minutes more in the solution.

A commonly observed phenomenon is the formation of "ears" on top of the hair-like structures as shown in Figure 5.6. These annexa are not omnipresent, not even on a single wafer, but when they occur there are always four ears on each structure. It is believed the non-uniformity of the SU-8 thickness is responsible for this effect. This non-uniformity results in nonzero (and variable) gap between the mask and the layer which in turn changes the light diffraction through the aperture. Although the aperture is a circular opening, the four sided extensions show the characteristics of a square aperture.

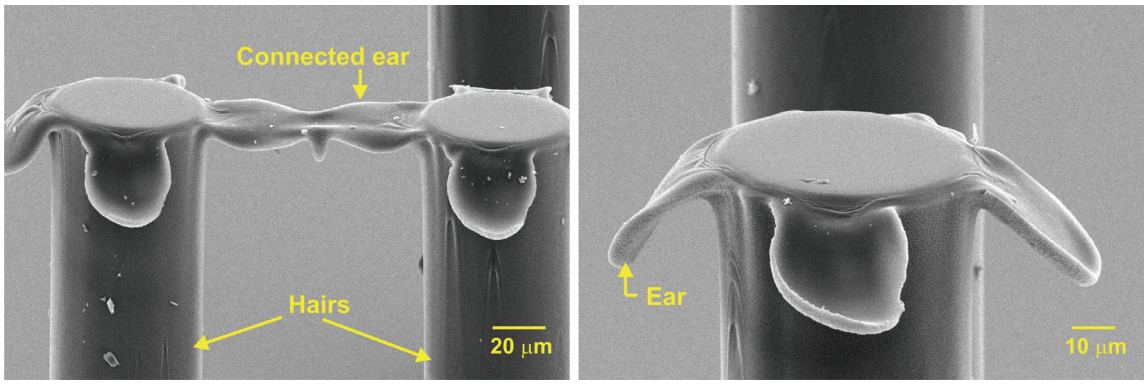

Figure 5.6 *The "ears" of SU-8*

It was mentioned before that in order to realise a long hair having a thin bottom part one can use three layers of SU-8. After each spin process the layer is soft-baked and then the next layer is spun. The exposure time in this case increases substantially. Longer exposure time also increases the chance of "ear" formation. However, using an i-line filter alleviates this problem.

5.1.4 Process Alternatives for Closed Membrane Sensors

5.1.4.1 Using SU-8 as a Masking Material

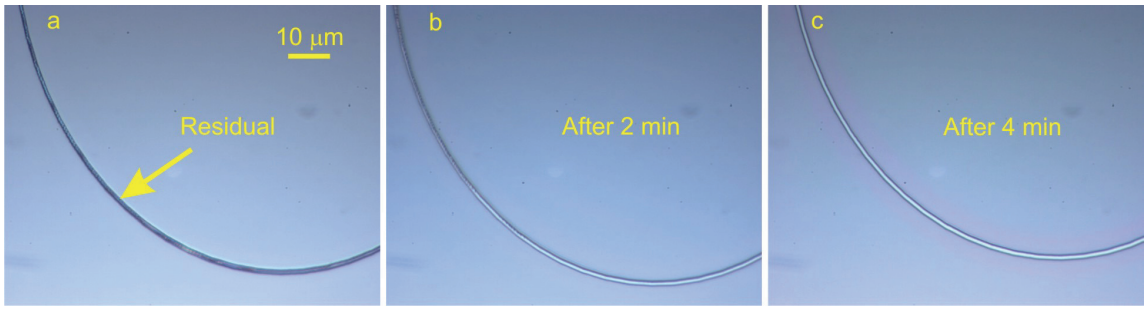

Figure 5.7 *Successive images of SU-8 2 residual removal from the rim using O_2 RIE*

Negative tone photoresist can be used to simplify some of the photolithography steps for the sensors with closed membrane. Particularly, using SU-8 2 as a masking material in *step c* (see previous chapter, section 4.2.2) when etching the rim will result in a bright mask which is easier to align and will eliminate an extra lithography step which is needed when using normal positive resist. The SU-8 2 process used is summarised in Table 5-I below. However, there always remain residuals of the resist in the patterned area due to diffraction of the light and small lateral dimensions of the features. A Reactive Ion Etching (RIE) process (20 sccm O_2 flow, zero pressure, 50 W) is done to remove the resist in the patterned structures and the result is shown in Figure 5.7. In this process the etch rate of SU-8 before hard-bake is 180 to 200 nm/min.

Table 5-I. *SU-8 2 process recipe*

Parameter	Value	Comments
Dehydration (min)	5	Optional
Spin	10 s at 500 rpm 30 s at 3000 rpm	Program #5
Soft-Bake (min)	2	at 95 °C
Exposure (sec)	10	12 mW/cm² source
Post-exposure Bake (min)	2	at 95 °C
Develop (s)	20	Immersion

A descum process in an isotropic oxygen plasma etcher (600 ml/min O_2 flow, 300 W) is used as an alternative approach to remove the residuals. It is more difficult to control the etch rate in this process and the lateral resolution of the features

decreases. Moreover, there is a clear delamination of the resist at the edge of the patterned structures as shown in Figure 5.8.

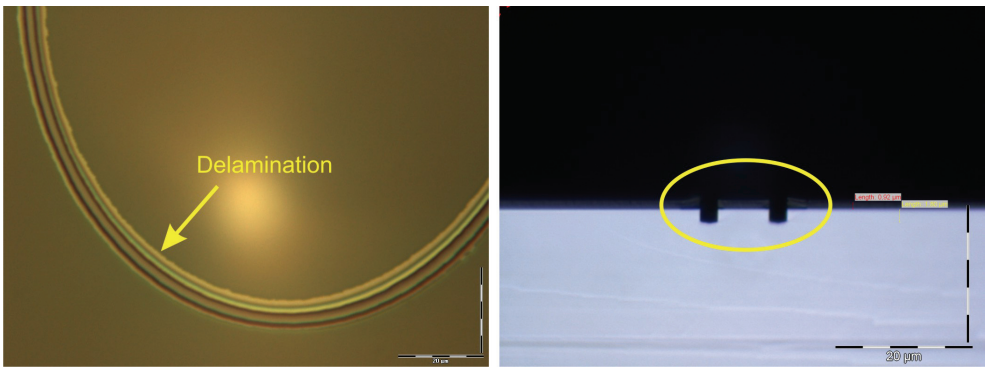

Figure 5.8 *a. Delamination of thin SU-8 layers at the edge of the patterned features in isotropic oxygen plasma, b. This has minor effect on the etching process*

Sometimes after the development of SU-8 there is a ribbon of cross linked material left on the pattern as shown in Figure 5.9. This can be easily removed in isotropic or anisotropic oxygen plasma in a short time without affecting the structure.

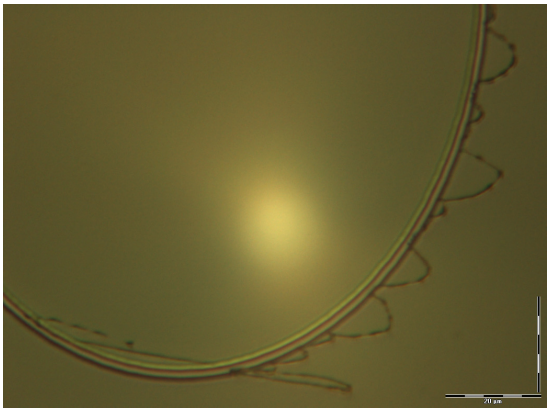

Figure 5.9 *Black Ribbon around the features patterned in SU-8 2*

In addition to using thin SU-8 2 layers as the masking material for rim lithography, SU-8 5 can be used in *step d* for the backside DRIE process (see chapter four section 4.2.2). SU-8 5 is more robust and its use once again results in a bright mask which is more convenient for the lithography process. It should be noted that in spite of the big difference between the thermal expansion coefficients of SU-8 and silicon (52×10^{-6} and 2.6×10^{-6} /°C respectively), the thin SU-8 layers stay on the surface at the cryogenic temperature of the backside etch process. However, thicker layers shatter immediately in the etch chamber.

5.1.4.2 Thinner Membrane

As it has been shown in chapter three, thinner and more compliant membranes allow for higher anti-symmetric deflection which is desirable. However, the achievable thickness is limited to around 500 nm as discussed before (see Figure 5.3). The isotropic or anisotropic oxygen plasma etching provides the possibility to etch back some of the developed SU-8 layer and thin the membrane further. Both of the O_2 plasma etch steps introduced in section 5.1.4.1 can be used. The etch rate of SU-8 2000.5 in oxygen plasma using the descum process in the barrel etcher strongly depends on the temperature and is approximately 50 nm/min between 40 to 50 °C. Moreover, the etch rate depends on the wafer orientation in the holder. Using the directional O_2 plasma offers better control on the etch rate. However, the process exhibits non-uniformity as the etch depth increases.

In chapter three Parylene-C has also been introduced as an alternative material for the membrane. Unfortunately, at the time of writing there is no facility for Parylene deposition in the MESA$^+$ institute. However, in near future the incorporation of Parylene in the process can be investigated, either in collaboration with Philips Research Laboratories, Minimally Invasive Healthcare division, or by the new Parylene equipment recently acquired.

5.1.4.3 Mace Shape SU-8

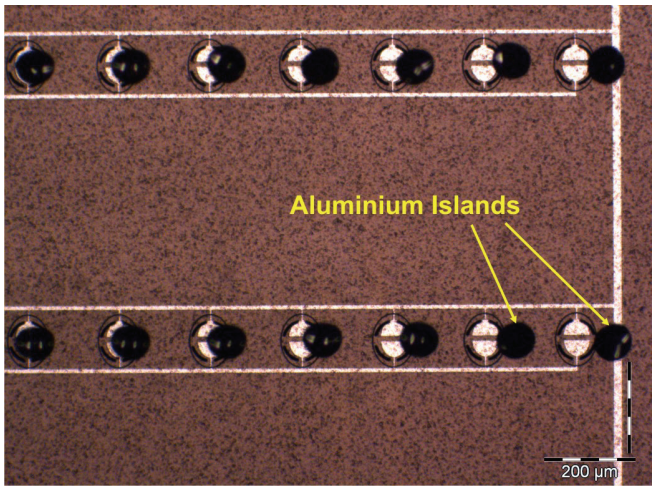

Figure 5.10 *Displacement of the aluminium reflectors after the soft-bake process for the second SU-8 layer*

In chapter three we also introduced the mace shape SU-8 hair structure and discussed its advantages. Since SU-8 is a negative resist exposing a wider area in the top

layer will affect the bottom structure. To prevent undesirable cross linked SU-8 in the first layer a thin layer (100 nm) of aluminium is deposited and patterned to function as a reflector under the exposed area of the second layer. However, because of SU-8 reflow during the soft-bake process of the second layer, aluminium wrinkles (see also Figure 4.29 section 4.3.1 in the previous chapter). To avoid any crack in the reflector layer, the area covered with aluminium should be minimized. Yet, small aluminium islands displace substantially during the soft-bake process of the second layer as shown in Figure 5.10. The displacement increases at the sides and strangely is only in one direction. More detailed study is needed to characterise and control this effect. Therefore, the reflector layer is not used at the moment.

Figure 5.11 shows the two layer structures on one wafer without the aluminium reflector layer. Two distinct profiles are observed: At the left, the smooth and negatively tapered hair and at the right the hair that has a bulge at the connection point between the two layers. As it can be seen in the right picture, the first part of the hair is shorter and wider than intended. This is due to the non-uniformity in the SU-8 layer.

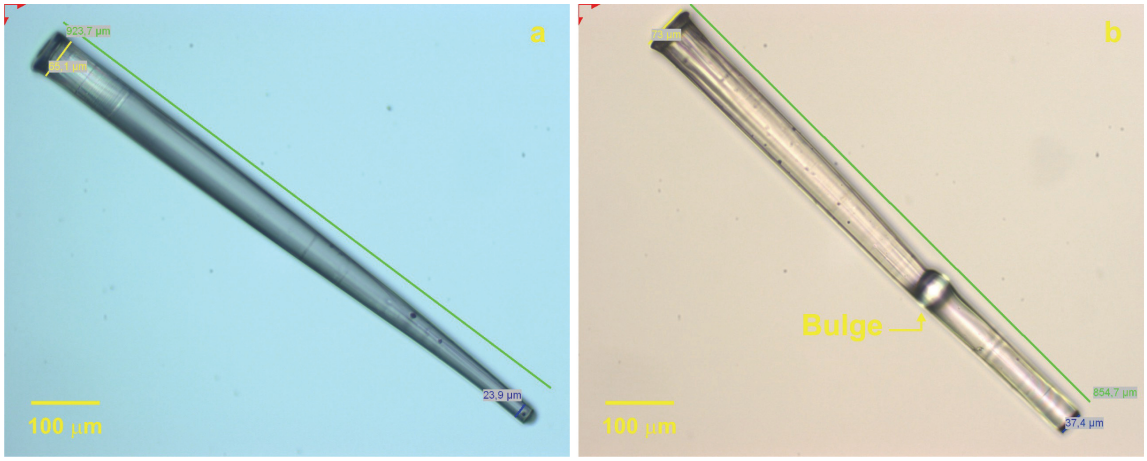

Figure 5.11 *Exposure of a larger area on top of a smaller one produces negatively tapered hair structures. These structures have two common shape profiles shown above.*

In order to realise reproducible long structures of the form shown at the left side of Figure 5.11 and to better control the profile, another method is used. Three layers of SU-8 100 are spun and soft-baked subsequently. Next a long exposure (475 s) is done followed by a prolonged post-exposure bake. In this case, it is essential to use an i-line filter to prevent ears on top of the hairs (see section 5.1.3). Figure 5.12 shows the results of a non-optimised process. The exposure dose (hence exposure time)

should be carefully tuned. When the stems of the hairs are too thin the hairs usually bend during the spray development. Using immersion technique they may survive the development process but will collapse due to capillary forces when taken out of the developer or their tip are joint together. In some cases the resulting hairs are not straight and exhibit a half-S curve. Although the reason is not fully clear, this can be due to excessive stresses during the PEB process, which considerably displace the material. Note that the outlines of the electrodes and membrane are visible in part *d* of the figure due to the charging of the thin SU-8 membrane in the SEM instrument.

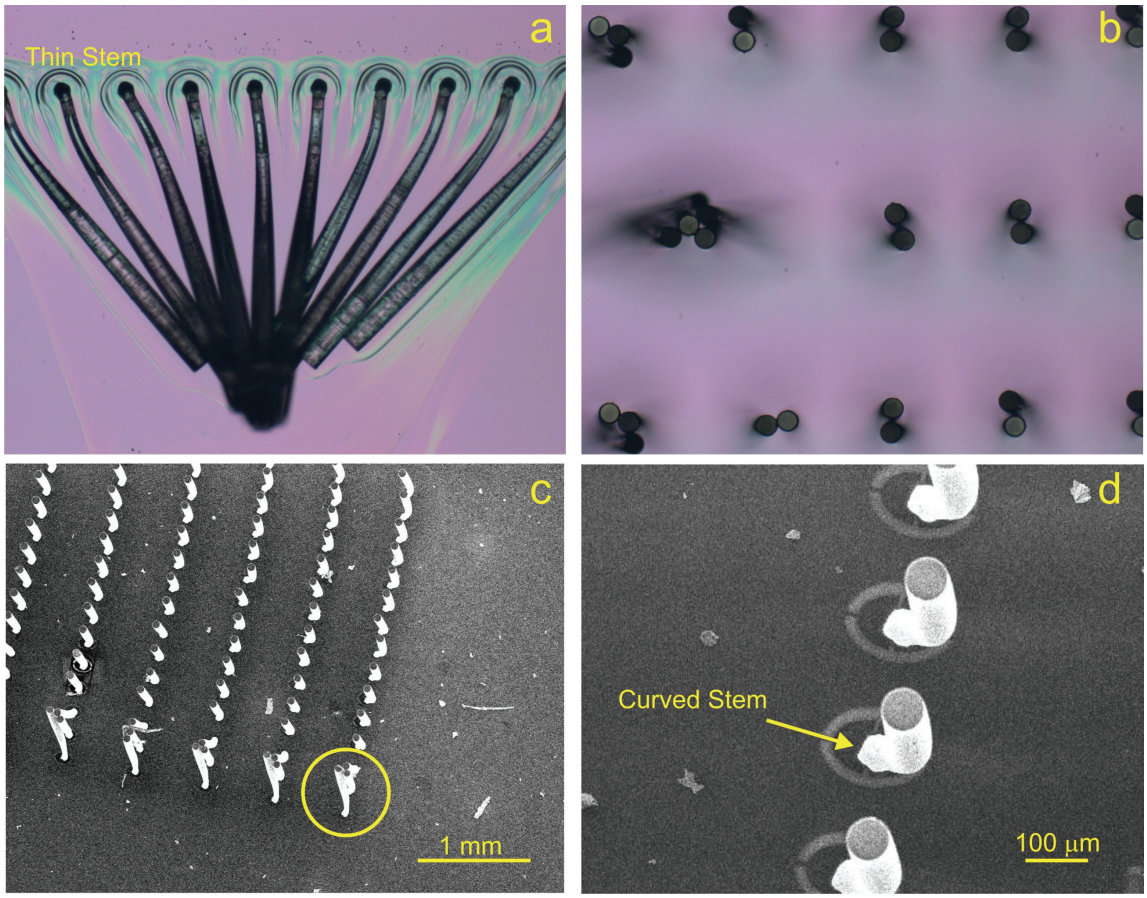

Figure 5.12 *SU-8 hair arrays. a: during spray development the hairs with very thin stem bend, b: during spin dry process surface tension joins the tips of closely spaced long hairs, c: SEM picture of the array with some joint hairs and d: close up of a hair with a thin curved stem*

5.2 The Flow Box

To investigate the fluid movement around hairs by Particle Image Velocimetry (PIV) a Flow Box is designed. PIV is an optical method to measure fluid movement. For this purpose the fluid is seeded with tracer particles. A high power double-pulsed laser unit is used to generate a thin sheet of light in which the injected, fluid borne particles become visible by reflection. Pairs of images, shot with short intervals (e.g. 200 μs), allow the tracking of particle movement from which the local flow velocities can be determined. The method is not invasive, has sub pixel accuracy (due to the use of many particles and correlation techniques) and produces two dimensional vector fields lying in the sheet of the laser light [11, 12]. The information gained from this method is beneficial for the study of the dynamic interactions between fluid and mechanoreceptors.

MicroPIV is designed to measure velocity fields of particle seeded flows with micron scale spatial resolution using PIV techniques. Since MicroPIV can only be used with small particles embedded in liquids, fixed SU-8 hairs have been made inside a sealed canal with inlet and outlet openings for this application. The top and bottom surfaces need to be transparent for the laser used in the MicroPIV technique. Although these structures were specifically designed and fabricated to allow for the study of fluid and fixed hairs interactions, the experience gained is also used for the fabrication of canal embedded sensors which have been discussed before. In the following sections the fabrication process is briefly reviewed and the obtained results are presented.

5.2.1 Fabrication

The schematic of the process flow is presented in Figure 5.13. The substrate chosen is a 1.1 mm thick Borofloat® wafer. These wafers are transparent for the wavelength of the laser used in the PIV setup (532 nm). Moreover, as we shall see shortly, the structures are made of SU-8 which, when cross-linked and hard baked, exhibits a high tensile stress. Thinner glass wafers bend under the induced stress and make the successive lithography steps troublesome.

The SU-8 adhesion to the glass substrate is not very good. To increase this adhesion, it is necessary to clean the wafers first in fuming nitric acid and then in Piranha solution. A dehydration bake at 250 to 300 °C for two hours is then carried out to remove all the moisture on the surface. Although following these measures

results in better adhesion, the wide SU-8 islands, e.g. the canal walls, delaminate from the substrate when hard baked. To overcome the delamination problem, a thin (~2 μm) SU-8 2 layer is spun and exposed to fully cover the surface of the wafer before the first thick SU-8 layer, which forms the hair-like structures as well as the walls of the canal, is applied. The initial thin SU-8 coating not only prevents the delamination of the canal walls but also increases the adhesion of the thin SU-8 hairs to the substrate. In addition it prevents water to creep between the SU-8 wall and the glass substrate.

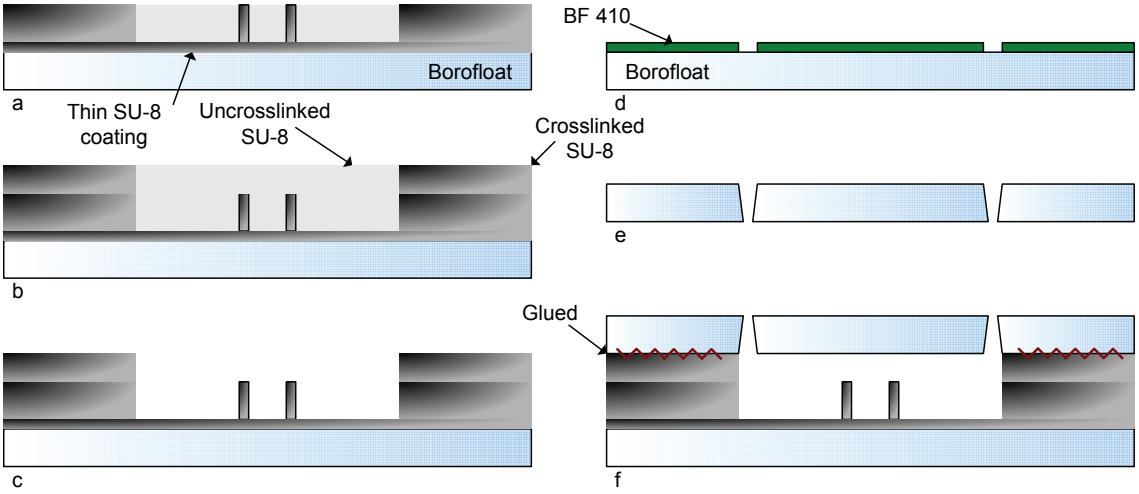

Figure 5.13 *The schematic fabrication process of the Flow Box*

The second SU-8 layer is processed as has been discussed before in detail. However, a longer soft bake step is needed. From this layer the cylindrical hairs and the bottom part of the canal walls are formed (*step a*). After post exposure bake, the third SU-8 layer is spun (*step b*). The thickness of this layer is tuned to the necessary gap between the hair-like structures and the top of the canal. When the third layer process is finished, the entire structure is developed (*step c*). A hard bake process is optional to increase the resistance of the SU-8 to humidity [8]. However, it should be noted that this process increases the internal stress of the SU-8 structures.

The lithography process on a transparent substrate is problematic. The reflection or absorption of UV by the chuck is not controllable and has noticeable effects on the SU-8. To control this, a thin layer of chromium (or aluminium) is deposited at the backside of the wafer before the first, thick SU-8 layer is spun. Deposition of chromium needs to be done after piranha cleaning and the thin SU-8

layer processing steps. Another advantage of a thin reflecting chromium layer is that it increases the contrast between cross-linked and uncross-linked SU-8 and eases the alignment procedure. An alternative approach is to put the substrate on a bare silicon wafer during the exposure. In these two approaches, the reflected UV from the metal layer or silicon wafer travels through the thickness of the Borofloat® wafer, reflects and changes the resolution of the SU-8 pattern close to the substrate. It usually results in some cross-linked SU-8 at the base of the hairs. A third option is to use a black, absorbing surface under the substrate during the lithography process. The exposure time in this case needs to be increased for the hair base to receive a sufficient exposure dose. Figure 5.14 shows the result of a standard lithography step using a black absorber at the back and a chromium layer.

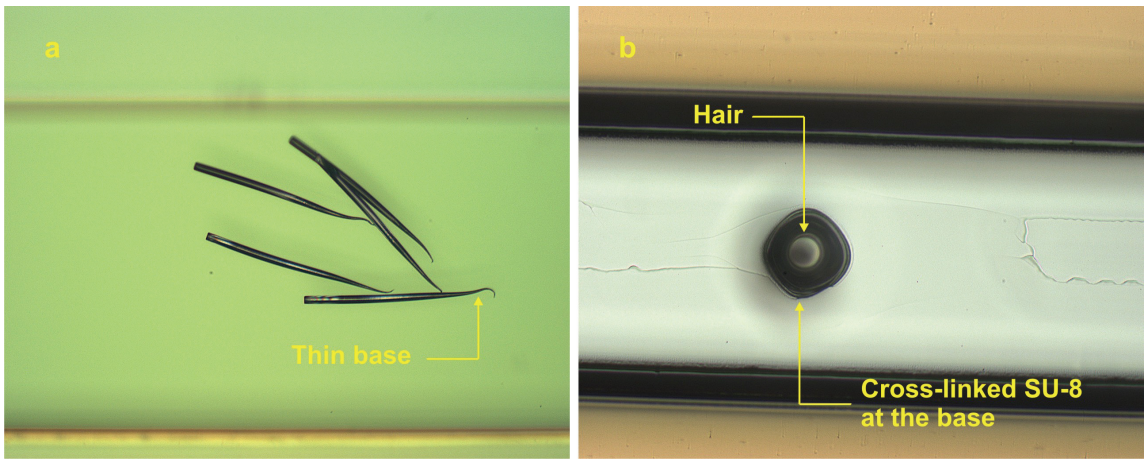

Figure 5.14 *a. The SU-8 hair profile using a dark absorber at the back and the standard exposure time, b. Additional cross-linked SU-8 polymer at the hair base using a chromium reflector*

A large tensile residual stress is build up in thick SU-8 layers during the processing which is associated with the large difference between the room and baking temperatures. This stress causes cracks in the sharp corners of the channel, which act as stress concentration points (see Figure 5.15). The cracks, however, only become visible after development. To overcome this, the process temperature specially for the soft bake step should be reduced [13]. The cracking problem is also shown to decrease by altering the chemical composition of the SU-8 [14]. In our case we have observed the cracks at the corners even at lower soft bake temperatures (95 °C) and slow temperature ramps. Fortunately these cracks do not degrade the intended performance of the device. However, to further decrease this problem the sharp concave corners

should be avoided in the mask [13, 15]. This is easily done by rounding the corners to form quarter circles.

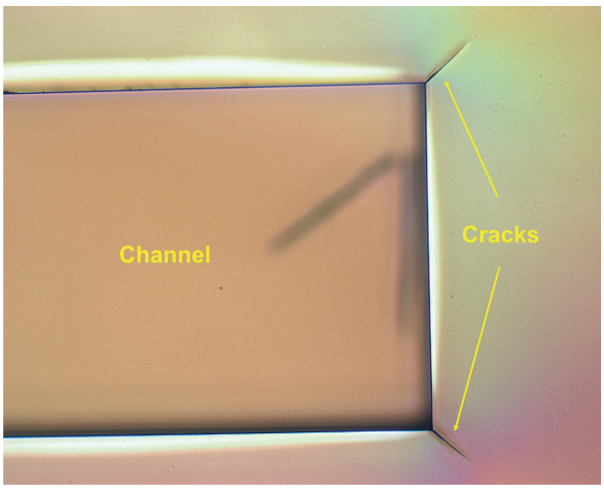

Figure 5.15 *The crack in SU-8 layer at the sharp corners*

The top of the canal is made from another glass wafer. The standard 500 µm thick Pyrex® wafers are suitable as there is no chance of bending in this phase of the process. These wafers are covered with a thick laminate foil (Ordyl BF410) and 29 µm Al_2O_3 particles are used in a powder blasting technique [16] to etch inlet and outlet holes. Then the foil is removed in an ultrasonic acetone bath and the wafers are cleaned and diced. Subsequently the top glass and the chip are attached using epoxy glue. The final device is shown in Figure 5.16.

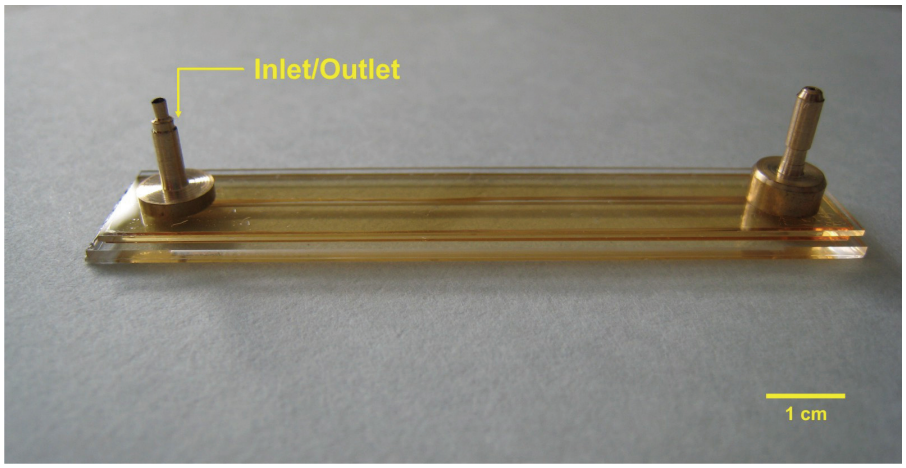

Figure 5.16 *The Flow Box*

An important consideration is to minimise the area covered by thick SU-8 layers on wafer scale. This is to decrease the generated stress in the layer stack. In addition, in individual chips, the area covered with canal walls should be small or otherwise the induced curvature hinders the assembly steps.

5.2.2 Discussion

Although the current application requires passive hair-like structures in a canal, the design and technology process described above offer a platform for realisation of canal embedded hair-based flow sensors. The question is what are the advantages and disadvantages of this method? The SU-8 canals have smooth sidewalls and connection to the bottom surface. They are made side by side of the hair structures from the same SU-8 layer by lithography process and, therefore, are cheap and easy to fabricate. In addition, their geometrical parameters can be changed easily with a change of the exposure mask. On the other hand, the somehow large non-uniformity of the top surface, where the cap is glued, makes the assembly process difficult. The stress generated during thermal treatment of the SU-8 layer can cause several problems most importantly the delamination from the substrate. Moreover, the behaviour of the SU-8 layer when in contact with water for a long time has to be investigated.

An alternative approach can be machining of the canal in a transparent plastic block and gluing it to the substrate where the hairs are based. Although in this approach it is more difficult to tune the geometry and obtain the smooth sidewalls, the connection between the two parts is potentially better due to the flatter finish of both surfaces. However this has to be verified by experiment. In this case, the canal properties will not change when in contact with water. Note that to align the canal with the hairs proper marks can be patterned into the substrate or some alignment features can be realised using the 2nd SU-8 layer.

5.2.3 Conclusion (Flow Box Design)

To investigate the fluid flow around hairs using micro Particle Image Velocimetry (μPIV) leak free canals with embedded hair-like structures were realised on glass substrates using three SU-8 layers. The canal is sealed with a pre-etched glass cap, which also provides inlet and outlet ports to the canal. The differences between structural and thermal properties of glass and silicon substrates result in considerable variation of the process parameters, which should be carefully tuned for each

application. The lower stiffness (Borofloat: 63 GPa, Silicon: 150 GPa), higher thermal expansion coefficient (Borofloat: 3.25×10^{-6} K^{-1}, Silicon: 2.6×10^{-6} K^{-1}) and the transparency of the glass wafers significantly affect the processing parameters. In addition, the low adhesion strength of SU-8 to the Borofloat glass and the high residual tensile stress may result in delamination of SU-8 films. This problem has been solved using a thin SU-8 film under the structure. The fabrication of canals, despite the various adaptations, has been successfully demonstrated.

To realise a canal embedded sensor using above procedure however has a disadvantage. The top of the canal is glued to the SU-8 walls and although through careful consideration leak free channels are possible to build but the process is not robust. This is mainly because of the large variation in the thickness of SU-8 walls. This also results in formation of cavities due to non uniform topography of the connection edges which may have some undesired effects on the flow profile.

5.3 Conclusion

SU-8 processing is pivotal in all the design and fabrication schemes that were presented in this thesis. It is used in largely varying situations to form layers as thin as 500 nm and high aspect ratio structures more than 1 mm long. In this chapter the subtle process consideration for realisation of all the SU-8 structures were reviewed.

SU-8 processing conditions affect the final results substantially. As a result there can be a large deviation in the mechanical properties of the structural elements made of SU-8 from one experiment to the other. It is important to understand the root cause of these changes and control the process to achieve uniform outcomes. On the other hand, as has been pointed out before, SU-8 seems the only possible material at hand from which thin membranes and long hairs can be made simultaneously. It can be handled easily in standard cleanroom facilities and has favourable mechanical characteristics. To the author's knowledge no other material offers the flexibility for the proposed structures. These properties make SU-8 the primary material choice for hair structures in all the designs, for the membrane of the sensors with closed membrane and for the walls of the canal in the canal embedded hairs. Admittedly, the optimisation of SU-8 fabrication procedure can be troublesome at times. However, once the influential factors are determined, they can be tuned to achieve the desired results.

5.4 References

[1] J. D. Gelorme*, et al.*, "Photoresist composition and printed circuit boards and packages made therewith," US Patent 4882245, 1989.

[2] A. del Campo and C. Greiner, "SU-8: a photoresist for high-aspect-ratio and 3D submicron lithography," *Journal of Micromechanics and Microengineering,* vol. 17, pp. R81-R95, Jun 2007.

[3] N. J. Sniadecki and C. S. Chen, "Microfabricated Silicone Elastomeric Post Arrays for Measuring Traction Forces of Adherent Cells," in *Methods in Cell Biology*. vol. Volume 83, W. YuLi and E. D. Dennis, Eds., ed: Academic Press, 2007, pp. 313-328.

[4] J. Hammacher*, et al.*, "Stress engineering and mechanical properties of SU-8-layers for mechanical applications," *Microsystem Technologies-Micro-and Nanosystems-Information Storage and Processing Systems,* vol. 14, pp. 1515-1523, Oct 2008.

[5] Microchem. *SU-8 Data Sheets*. Available: http://www.microchem.com/products/su_eight.htm

[6] H. Lorenz*, et al.*, "Mechanical characterization of a new high-aspect-ratio near UV-photoresist," *Microelectronic Engineering,* vol. 42, pp. 371-374, 1998 1998.

[7] B. Li*, et al.*, "Low-stress ultra-thick SU-8 UV photolithography process for MEMS," *Journal of Microlithography, Microfabrication, and Microsystems,* vol. 4, pp. 043008-6, 2005.

[8] R. Feng and R. J. Farris, "Influence of processing conditions on the thermal and mechanical properties of SU8 negative photoresist coatings," *Journal of Micromechanics and Microengineering,* vol. 13, p. 80, 2003.

[9] Z. Cui*, et al.*, "Profile control of SU-8 photoresist using different radiation sources," Edinburgh, United Kingdom, 2001, pp. 119-125.

[10] J. Zhang*, et al.*, "Polymerization optimization of SU-8 photoresist and its applications in microfluidic systems and MEMS," *Journal of Micromechanics and Microengineering,* vol. 11, pp. 20-26, Jan 2001.

[11] M. Raffel*, et al.*, *Particle Image Velocimetry: A Practical Guide*, 2 ed.: Springer-Verlag, 2007.

[12] S. T. Wereley and C. D. Meinhart, "Recent Advances in Micro-Particle Image Velocimetry," *Annual Review of Fluid Mechanics,* pp. 557–576, 2010.

[13] A. A. Thomas and et al., "The effect of soft bake temperature on the polymerization of SU-8 photoresist," *Journal of Micromechanics and Microengineering,* vol. 16, p. 1819, 2006.

[14] D. W. Johnson*, et al.*, "Improving the Process Capability of SU-8. Part II," *Journal of Photopolymer Science and Technology,* vol. 14, pp. 689-694, 2001.

[15] S. Bystrova*, et al.*, "Study of crack formation in high-aspect ratio SU-8 structures on silicon," *Microelectronic Engineering,* vol. 84, pp. 1113-1116.

[16] H. Wensink, "Fabrication of microstructures by powder blasting," Ph.D. Dissertation, University of Twente, Enschede, 2002.

6
Measurements

In this section the results of the experimental work are presented. The experimental setup is described and results of mechanical characterisation of the membranes in air are presented first. The capacitive sensor function of the design is confirmed in air as well. Finally some observations of the sensor in water are reported.

6.1 Introduction

Various types of experiments for evaluation of the sensor performance are carried out and discussed in this chapter. First, a laser vibrometer is employed to characterise the mechanical properties of the membranes. The results can be used to evaluate and adjust the analytical model for the mechanical sensitivity as developed in chapter 3. Second, electrical (capacitive) measurements are carried out. Here the effect of parasitic capacitances and the transduction of mechanical displacement to electrical signal are investigated. Finally some measurements on a sensor in water are performed using a specially designed measurement rig.

6.2 In Air

When the sensors are operated in water it is expected that parasitic capacitances formed between the signal lines and ground will be more pronounced than in air. Moreover, since characterisation in air delivers important information with respect to the mechanical properties of the sensor, it is beneficial to evaluate the electrical performance in air prior to testing in water. In addition, since the use of a laser vibrometer on a sensor that is placed in the water is troublesome the mechanical performance in air can be used to predict the sensor behaviour in water.

6.2.1 Laser Vibrometer Measurements

The initial experiments are aimed at measuring the characteristics of the sensors that incorporate the fully supported membranes. This characterisation is carried out with the sensors in air using a Polytec MSA-400 laser vibrometer. The air flow is generated by a loudspeaker and is guided through a funnel to increase the flow velocities. Figure 6.1 shows the measurement setup. The funnel output is placed at a few centimetres distance to the sample which is fixed on a positioning table.

The laser beam from the vibrometer is aimed at and reflected by the membrane. The vibration amplitude, phase and frequency are obtained from the Doppler shift of the laser beam frequency due to the motion of the surface [1]. However, as the SU-8 is almost transparent the laser beam needs to be focused on the electrode area to provide enough reflection. In addition, the SU-8 hair-like structure in the middle, which is not always an ideal straight cylinder, requires the laser beam to be well separated from the

centre of the membrane. Therefore there is a limited space available to measure the displacement.

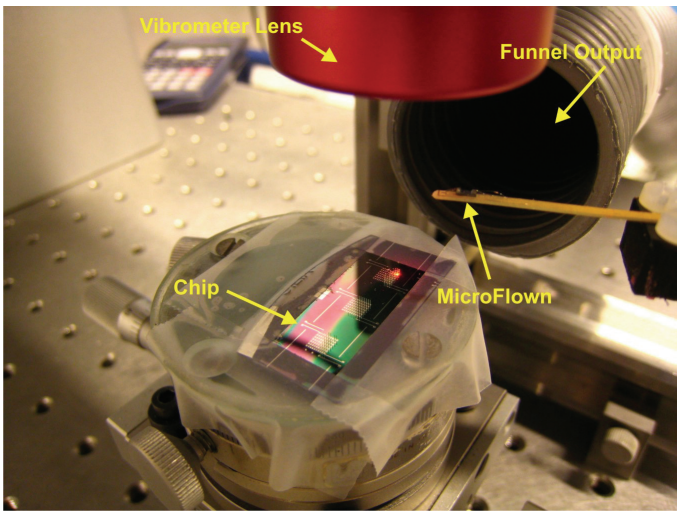

Figure 6.1 *A funnel is used to generate low frequency flow with large amplitude*

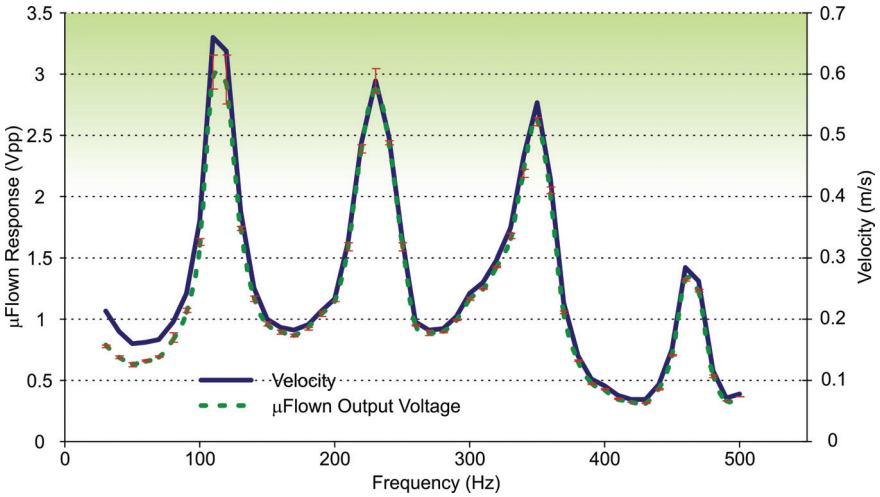

Figure 6.2 *Frequency response of the funnel as measured using a MicroFlown*

The flow velocity is characterised at different frequencies using a MicroFlown® [2] and the result is presented in Figure 6.2. Clearly the funnel helps to increase the flow velocity to relative high values, however, only at the cost of rather large fluctuations in the generated flow as function of frequencies. Given the fact that the sensors are designed for operation in water, rather than in air, clear membrane movement can be best observed at velocities of 0.5 m/s and higher. Figure 6.2 shows that this condition is met for a reasonable bandwidth, especially in the funnel induced

peaks. Moreover, the simultaneous use of a MicroFlown when measuring on a flow-sensor allows for proper normalisation of the sensors response to the applied flow-field.

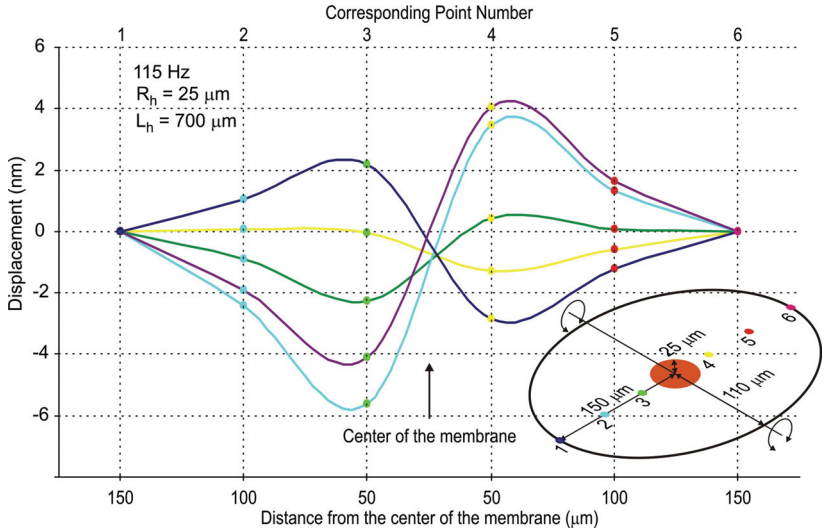

Figure 6.3 *Displacement of the membrane measured across its semi-major axis with laser vibrometer at 115 Hz*

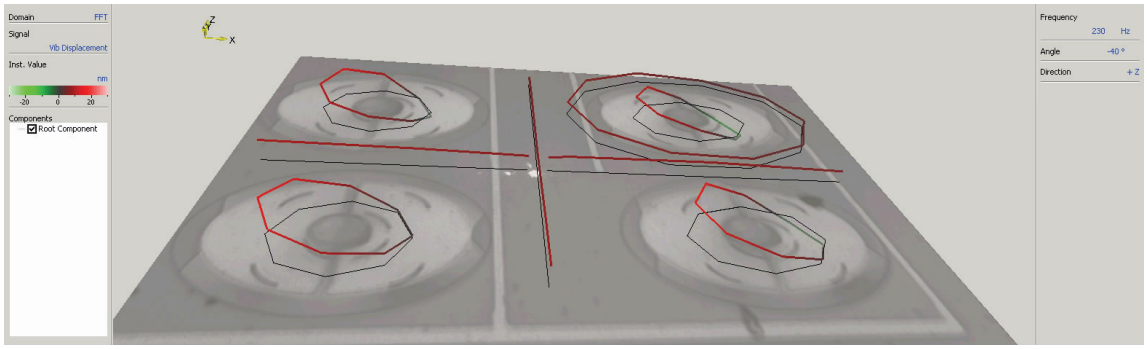

Figure 6.4 *A snapshot from the laser vibrometer screen during measurements (using 230 Hz oscillatory air flow)*

Figure 6.3 shows the measured membrane deflection in the half cycle of oscillation at different phases for an excitation flow at 115 Hz. The points correspond to the same colour point on the small inset of the graph which shows the outline of the membrane. The hair (50 µm in diameter) is situated between points 3 (green) and 4 (yellow). A flow velocity of 0.6 m/s at 115 Hz was realised. This velocity, considering identical Reynolds numbers, corresponds to 37 mm/s in water. The mechanical sensitivity in this frequency is therefore 2.7×10^{-3} rad/(m/s). It should be noted that the small asymmetric deflections of the membranes are a result of slight misalignment of the hair relative to the membrane and/or the remaining sacrificial layer under the

membrane at the edges. Figure 6.4 depicts a snapshot of typical laser vibrometer output.

6.2.2 Capacitive Measurements

The sensor has also been tested using the capacitive readout circuitry that has been introduced in chapter three. The sensor is fixed to a custom made PCB and two lead wires are bonded to the pads (from backside to *A* and *B* pads shown in Figure 6.5). These lead-wires are used to feed two 1 MHz signals, one phase and one anti-phase, to the two sides of the sensors allowing for the differential capacitive measurement (as described in chapter three).

It should be noted that there is always SU-8 residue left on the bond pads after fabrication. To connect the wires, this residue needs to be removed e.g. mechanically using the tip of a pair of tweezers. This should be done carefully minimising the chances of removing the aluminium pads by scratching. A better choice is to use an acetone drenched swab to rub the SU-8 off the pads.

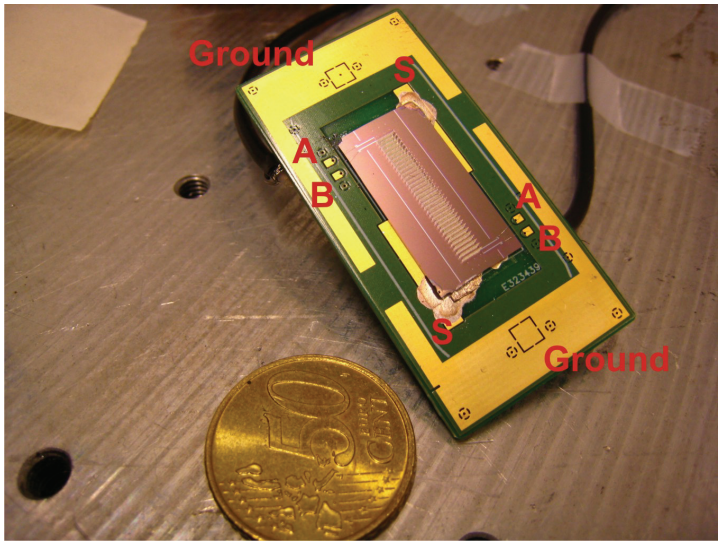

Figure 6.5 *The PCB and bond pads' configuration*

Since the common electrode of the sensor is the silicon substrate itself, a conductive silver paste is used to provide connection from the edge of the chip to the PCB pad (*S* in Figure 6.5). The side of the chip should be scratched to remove any native oxide before the paste is applied. The resistance between the two A or two B pads is about 300 to 500 Ω. This is primarily the resistance of the aluminium layer

which forms the upper electrode. The resistance measured between two signal lines (*S* pads) is 30 to 50 Ω. These measurements have been done several times within a time span of two months. No change of resistance or degradation of the aluminium lines has been observed.

Using the above values for the resistances and theoretical values for capacitances the electrical cut-off frequency is estimated to be between 2.89 and 4.82 MHz. Therefore the use of 1 MHz carrier signals is justified. The measurement setup is shown in Figure 6.6. The air flow is again provided using the funnel which is connected to a power amplifier and a signal generator. The output signal of a sensory array is fed to a charge amplifier and then passes through a demodulator and is displayed on an oscilloscope. A lock-in amplifier is used to extract the response at the applied frequency from the output. The magnitude of both carrier frequency signals is adjusted to minimise the noise at the charge-amplifier output. This accounts for asymmetry in the two capacitance values of the sensor. The flow is again characterised using MicroFlown flow measurements. To make sure that the output is indeed a result of the generated flow and not caused by any secondary interactions, the flow was blocked shortly leading to a largely diminished sensor output, as expected.

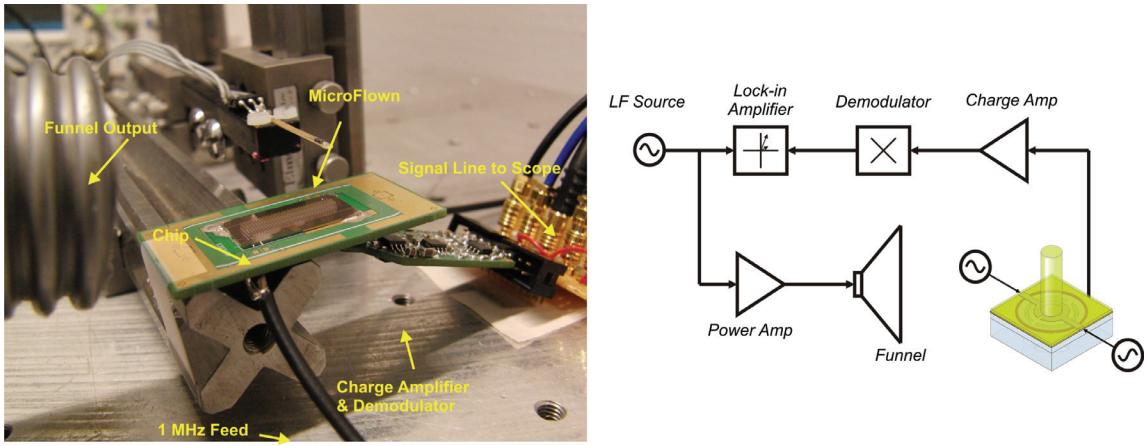

Figure 6.6 *The setup for electrical measurements in the air. The schematic of measurement setup is shown at the right.*

The frequency response of the system, using 10 seconds integration time on the lock-in amplifier, is shown in Figure 6.7. The output is measured from 50 to 300 Hz and is normalised using the flows as determined by the MicroFlown readout.

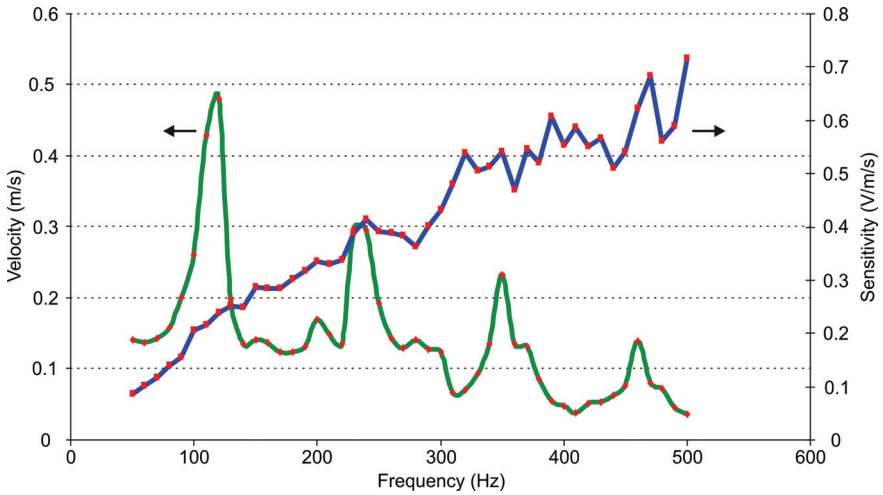

Figure 6.7 *A typical frequency response of the sensor*

The flow amplitude dependency of the sensor is shown in Figure 6.8 where the sensor output is plotted as a function of flow-velocity. Apart from some fluctuations that are attributed to measurement uncertainties the lines are more or less straight over the tested flow amplitude interval showing no signs of nonlinearity. Additionally Figure 6.8 shows the rms noise floors for 100, 500 and 1000 Hz measurement bandwidth.

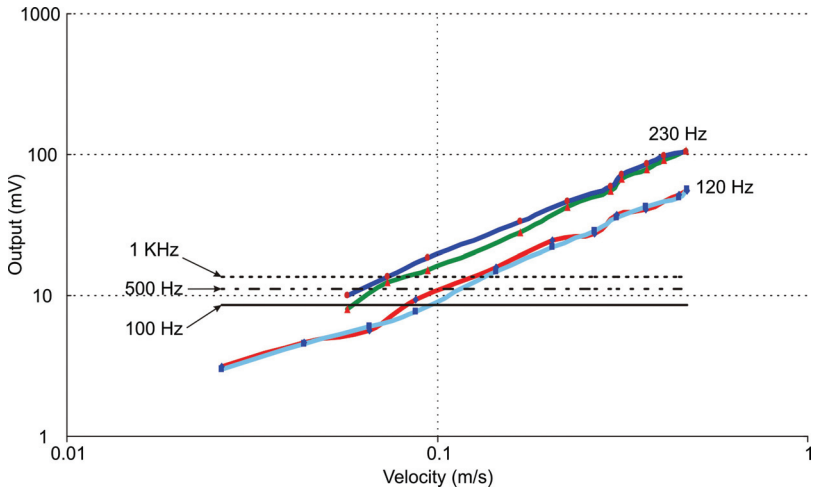

Figure 6.8 *Flow amplitude dependency*

The angle dependence of the responsivity is determined by measuring the sensor response at 120 Hz at various angles (every 10 degrees) between the funnel-axis and the rotational axis of the hair-sensors (0 degrees meaning both axes coincide, i.e. the air-flow is perpendicular to the intended direction of highest responsivity). Due to

the charge-amplifier PCB, holding fixtures and additional wiring hooked up to the sensor, not all angles were equally favourable and at some angles the flow was partly perturbed. Therefore the resulting angle dependence shows a slightly distorted figure of eight as shown in Figure 6.9. The angles show the direction of the flow toward the centre of a two centimetre long array of sensors.

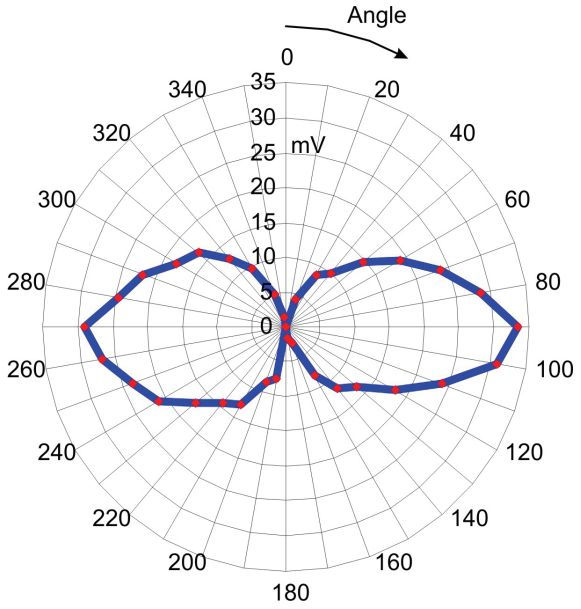

Figure 6.9 *Figure of eight*

In one experiment, after a few minutes of continuous operation using high air flow velocities, the sensor lost its sensitivity. Figure 6.10 shows a membrane of the used chip before and after the measurement. At left the membrane is smooth and the light blue colour of the SiO_2/Si_3N_4 stack is clear. On the other hand, on the right side the membrane seems crocked. Although this can be due to mechanical fatigue in the polymeric membrane [3], a SEM picture is needed for better understanding of the phenomena. Interestingly only half of the membranes in the chip, especially those that were close to the funnel output, show degradation; the other half were intact. The resistance between the pads was measured as well but did not show any difference relative to the resistances measured before the experiment.

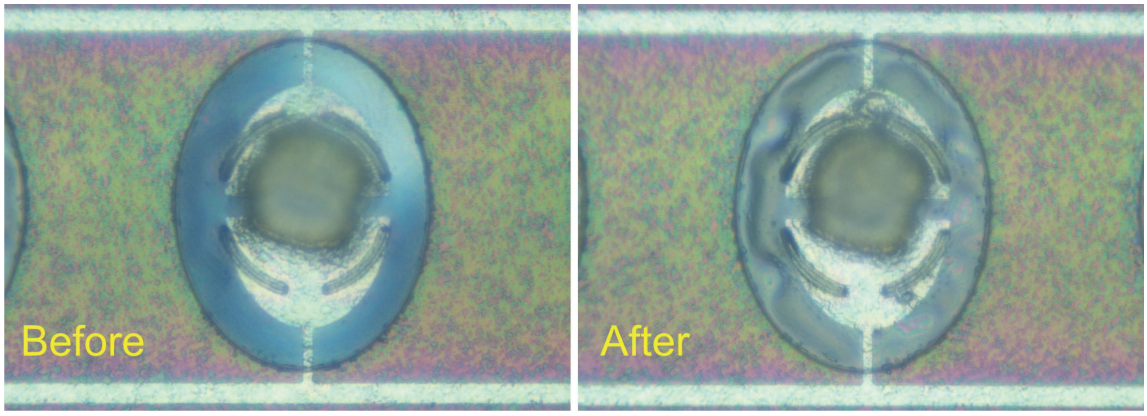

Figure 6.10 *The membrane before (left) and after (right) operation. Note that before operation smooth surface of the membrane reveals the blue colour of the oxide/nitride stack underneath.*

6.3 In Water

To generate low frequency oscillatory water flows one can use a dipole source in a water tank. However, to be able to use a vibrometer for mechanical characterisation and to avoid putting the charge amplifier and demodulator board in water, a special setup was designed. It consists of two loudspeakers with water resistant diaphragms which are connected to both ends of a tube and are actuated by anti-phase driving signals. There is an opening at the top of the tube to put the PCB with the chip (upside down) for electrical measurements or an optical grade glass for laser vibrometer measurements. The sensor is fixed on a block of aluminium to prevent lateral vibration of the chip.

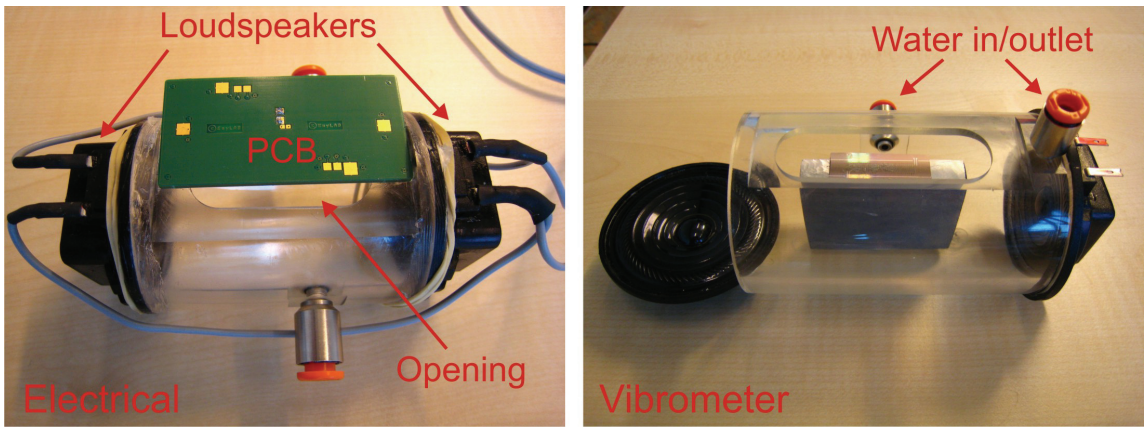

Figure 6.11 *Two different configurations of BoomBox*

The static pressure in water increases by about 100 Pa for each centimetre in depth. This is important when a closed structure with a different inner pressure is submerged. The structure may collapse due to high static pressure differences.

At the time of writing only preliminary experiments in water had been conducted. Figure 6.12 shows the effect of water on the electrodes when it penetrates through the openings under the membranes. In this case some of the membranes were broken before the sample was put in the water for two and half days. Having all the membranes intact, another sample shows no sign of degradation. Although the overall time that this sensor has been in water is lower, but it has been put and taken out of the water three times.

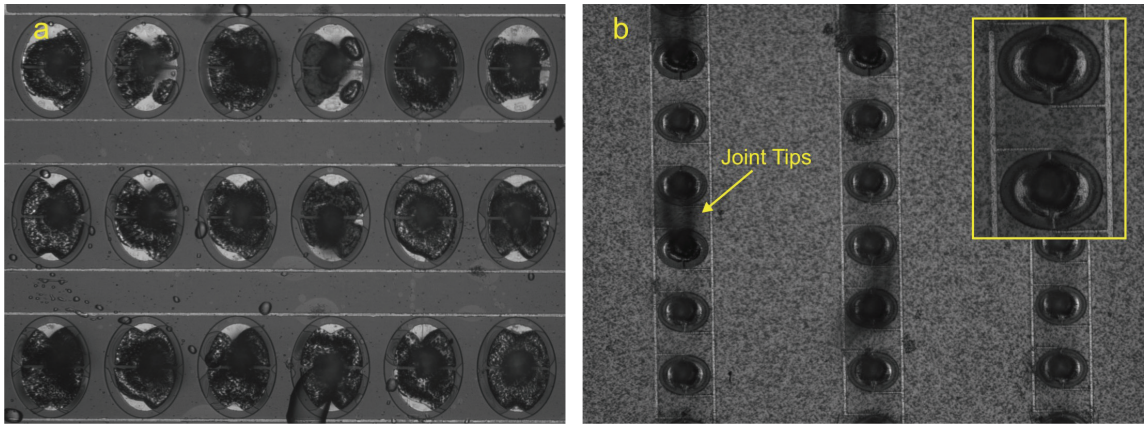

Figure 6.12 *a: The effect of water when it penetrates under the membrane, b: A sensor with intact membranes after being in water*

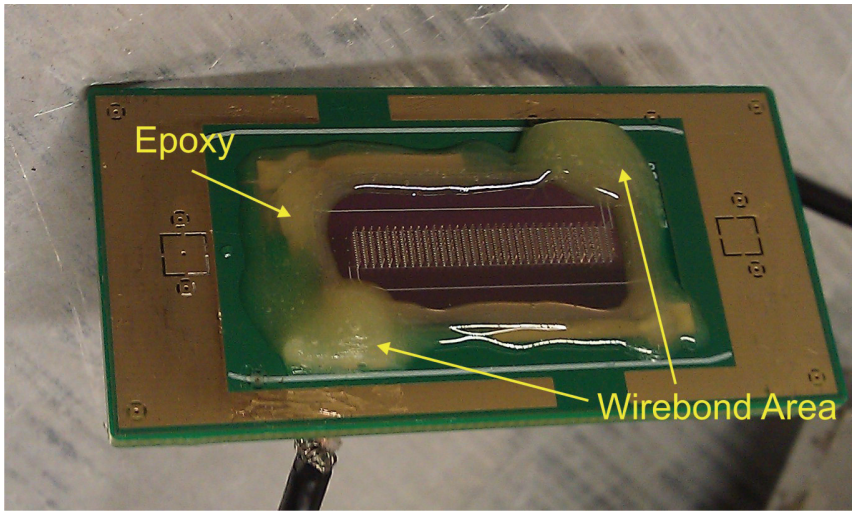

Figure 6.13 *The insulated device with epoxy to be put in water*

A stumbling block is the insulation of the sensor without affecting the thin wire bonds. Figure 6.13 shows the sample which has been put in the water. A two component epoxy was used to cover the sides and bond wires of the sensor to protect them from water contact. However, the shrinkage of epoxy while cured results in disconnection of thin wires. A sample that has been prepared even exhibits a short circuit between the feed pads and the signal. Further experiments with more careful consideration of the peripheral components, are scheduled to be done soon.

6.4 Discussion

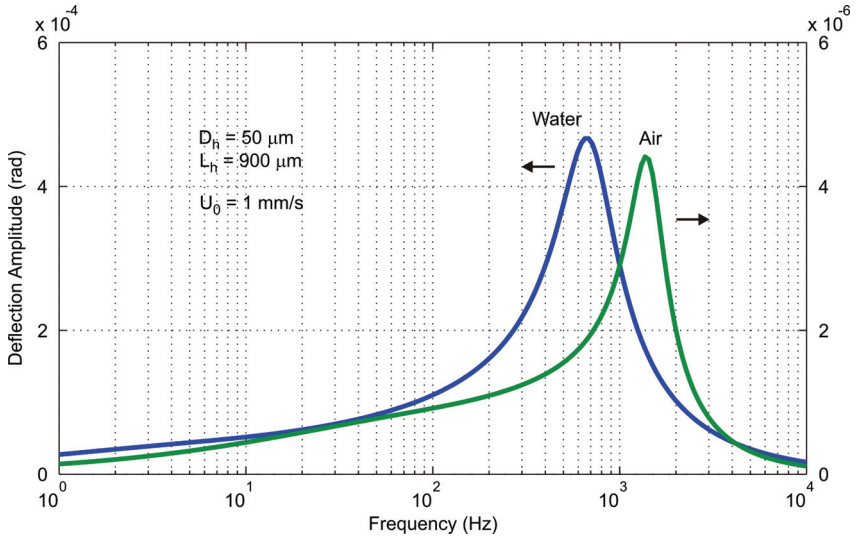

Figure 6.14 *Comparison of the deflection amplitude of the sensor in air and water*

Although no measurements has been successfully carried out in water one can deduce some information about the sensitivity of the sensor using the previous presented results obtained in air. Figure 6.14 above shows the maximum deflection amplitude of the sensor considering water and air as the medium and the flow velocity of 1 mm/s. It is the lower density and kinematic viscosity of air that result in lower drag torques, by two orders of magnitude, and lower damping, hence higher resonance frequency. Note that here the stiffness of the sensor has been considered eight times higher than the stiffness as calculated in chapter three to account for residual stress of the membrane.

Figure 6.15 shows the ratios of drag-torque and deflection amplitude of the sensor in water relative to those in air. It can be seen that oscillatory flow of 1 mm/s induces a minimum of 100 times more torque on the hair structure in water than in air.

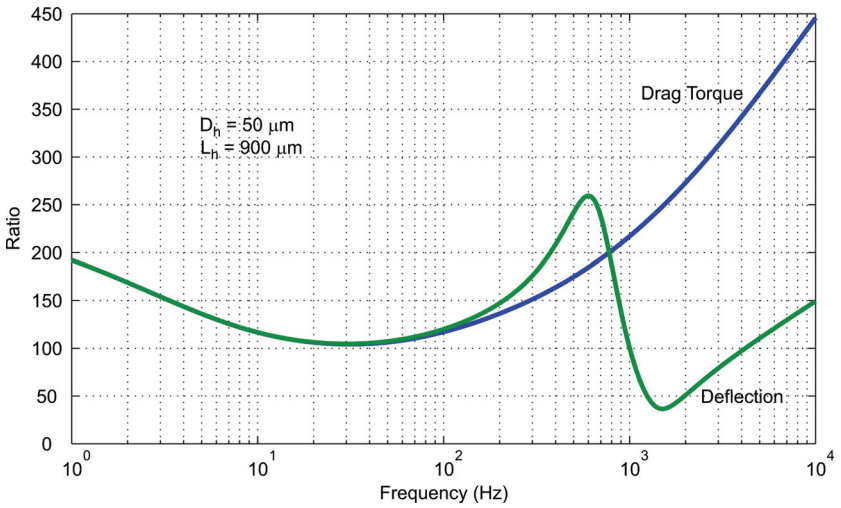

Figure 6.15 *Ratio of the drag torque and deflection amplitude in water and air*

Using data from Figure 6.8 we can see that detection threshold at 120 Hz fluid flow using a 500 Hz measurement bandwidth is about 0.1 m/s in air. The torque in water at 120 Hz is about 110 times larger than in air (see Figure 6.15). Therefore, given the noise originated from parasitic capacitances stays the same, the detection threshold in water at 120 Hz is about 0.9 mm/s.

Let us calculate thermal noise induced flow threshold of the sensor. It can be shown that [4] for a harmonic oscillator

$$d\left\langle \varphi^2 \right\rangle = \frac{4k_B \cdot T}{Q \cdot \omega_0 \cdot k_\varphi} \tag{3.1}$$

in which φ is the rotation of the hair, k_B is the Boltzmann constant, T is the absolute temperature in Kelvin, Q is the quality factor, ω_0 is the resonance frequency and k_φ is the stiffness of the system given in chapter three. Using the values obtained in chapter three (for water) one can calculate the rms deflection of 8×10^{-7} rad which translates to 15.4 μm/s at 10 Hz. This low value is due to high stiffness of the sensor. Considering in the air the quality factor and resonance are higher, the thermal noise limits the sensor even less. Therefore, it is obvious that the electronics are the dominant source of the noise in the system.

The first attempts to submerge the sensor in water demonstrate that a fully covered chip is essential to prevent water to penetrate under the membranes. When water creeps under the membranes the aluminium electrodes clearly degrade. A complete chip however is fairly water tight and robust. Several immersion and

subsequent dry out cycles did not damage the sensor. Moreover, water did not enter the backside of the chip. Although when the sensor is taken out of the water, surface tension joins the tip of some hairs, this does not produce damage to the membranes.

6.5 Conclusion

Various measurements have shown the following:

- The fabricated sensors display a clear mechanical response. This implies that the membranes are etched free, showing the overall purpose of the technology to fabricate cavities using etch-ports from the backside of the sensors.
- Output versus flow-amplitude and output versus flow direction as measured capacitively both show results entirely in line with expected responses and confirm the proper functioning of the differential capacitive measurement scheme and the actual sensor concept.
- The higher detection threshold obtained from the measurements in air suggests that the membrane is stiffer than the ideal design. As it has been discussed in chapter three, this can be due to internal residual stress.
- The output of the sensor was observed to carry more than expected noise. It is hypothesized that this may be due to the existence of parasitic capacitances that have a magnitude in the same order or larger than the sensor's capacitance. It is expected that these parasitics may be reduced by proper shielding as shown e.g. in a comparable hair based flow-sensor design where the noise was largely reduced using SOI wafers [5].
- The failure observed after continuous operation for a while, may be a result of fatigue in the SU-8 membrane. This, however, should be examined more carefully.

In conclusion we have demonstrated proper mechanical and electrical operation of our hair-sensors. The developed technology and proof of concept open up future possibilities for this type of aquatic flow-sensors. However, to materialise this potential further investigation into the fabrication technology and mechanical properties of the SU-8 membranes is needed to improve the sensitivity of these flow-sensors.

6.6 References

[1] *Polytec GmbH*. Available: http://www.polytec.com/eu/

[2] H.-E. de Bree*, et al.*, "Novel device measuring acoustical flows," 1995, pp. 536-539.

[3] J. Sauer and G. Richardson, "Fatigue of polymers," *International Journal of Fracture,* vol. 16, pp. 499-532, 1980.

[4] M. C. Elwenspoek*, et al.*, *Introduction To Mechanics And Transducer Science.* Enschede: University of Twente, 2008.

[5] A. M. K. Dagamseh*, et al.*, "Engineering of Biomimetic Hair-Flow Sensor Arrays Dedicated to High-Resolution Flow Field Measurements," presented at the IEEE Sensors, Hawaii, USA, 2010.

7
Conclusions and Outlook

Wonders shall never end…

7.1 Discussion and Conclusion

In this work, for the first time, design and fabrication of aquatic flow sensors with capacitive readout using MEMS technology has been shown. Water has a high dielectric permittivity, viscosity and density. An important question to be asked is whether capacitive readout is a suitable mechanism for sensors in such environment? Using capacitive readout in a potentially conductive and highly viscous medium imposes strict constrains on the designs. Considering the former, the electrodes should be insulated from the medium. A conductive contact will result in electrolysis and short circuiting. This insulation can be obtained by complete separation of electrodes or by covering them with a dielectric layer. On the other hand, the high viscosity and high density of water increase the damping and inertia of the moving objects immersed in it. This results in a considerable smaller bandwidth and potentially a highly damped system (depending on the stiffness and inertia of the device). Capacitive changes in our designs are achieved when electrodes move with respect to each other. It is beneficial if the length scale of the electrodes is small to limit the added mass and damping. However, small electrodes construct a small capacitor which is hard to interrogate with discrete readout circuitry. The effect of the added damping is even more pronounced when the liquid is confined in the narrow gap between the two electrodes. The resulting squeeze film damping would substantially restrict the frequency response. These effects are less pronounced at low frequencies but increase rapidly at higher frequencies. Moreover, any movement in water requires higher energy than in air. Therefore naturally a capacitive sensor is more limited in bandwidth in water than in air (compare the results of chapter three with those presented in [1, 2]).

On the other hand, thermal anemometry and piezoresistivity can be considered as alternatives which are not affected by any of the above mentioned constraints. However, thermal anemometer sensors are limited at low flow velocities as well as higher frequencies (due to the heat capacity of the medium). The bandwidth of a double wire anemometer, e.g. MicroFlown®, is especially limited in a medium with high thermal capacity. Moreover, the power consumption in such a medium increases dramatically. As reviewed in chapter two, the majority of underwater flow transducers use piezoresistive readout. Despite this fact, capacitive readout is still more accurate, consumes low power, is less sensitive to temperature changes and is relatively easy to

implement [3]. Therefore it is a favourable mechanism especially for continuous operation and large sensor arrays. The three proposed designs use the differential capacitive readout mechanism and have their own advantages and disadvantages. Their performance and fabrication have been evaluated and compared in chapters three and four (see tables 3.VIII and 4.VII).

The closed membrane configuration completely separates the electrodes from the medium. Therefore, the sensor's capacitance is well defined and controlled. The design and fabrication processes yield to a robust sensor of which the frequency response is close to a critically damped system. The fabrication process is however complicated and the mechanical transduction relies on polymeric parts (i.e. the membrane is made of polymer for higher flexibility; see also the next part). A highly flexible membrane is required for a high sensitivity. This flexibility is achieved mainly with thinner and larger membranes which are more difficult to fabricate. A more compliant material is clearly favourable as well. In any case there is a trade-off between higher flexibility (and therefore higher sensitivity) and the bandwidth. Another important feature of the design is the possibility to adjust the back chamber pressure. As the squeeze film damping due to the air in between the electrodes does not have a significant effect on the performance of the sensor at the frequency range of interest, the back chamber pressure can be adjusted to avoid downward membrane deflection. This alleviates the effects of nonlinear stiffening or collapse of the membrane due to static pressure difference across it. Theoretically, the detection threshold of an optimised sensor based on closed membrane structure is below 1 mm/s, which is comparable to the sensors found in literature (see chapter two). Preliminary measurements however demonstrate that the sensor is stiffer than the ideal prediction. As it has been discussed in chapter three, this can be due to internal residual stress and the effect of aluminium electrodes on the flexibility of the membrane. The combination of these effects can stiffen the membrane around 24 times.

The canal embedded sensor design is relatively simple and cheap. It exhibits a comparably high sensitivity and very low detection threshold. Most of the fabrication steps are at low temperature. Although the electrodes are electrically insulated from the medium, the properties of the intermediate dielectric (i.e. water) substantially change the sensor's capacitance. The fabrication process heavily relies on SU-8 which is a polymer. Therefore any change in the processing conditions directly reflects in the

characteristics of this polymer and therefore the fabrication scheme is critical; each step should be optimised for each batch. Moreover, like the pervious case, the mechanical part is built of a polymer (SU-8) which properties can change over time. Overall the characteristics of this sensor depend on the exact processing and working conditions and its realisation is risky.

In the BooT design the flexibility of the sensor is detached from the hair geometry. This provides a great opportunity for fine tuning of the sensors' characteristics. Moreover, as the mechanical parts (i.e. springs) are not made of a polymer their structural properties are more defined and reliable. The design is fairly simple and has a familiar configuration. On the down side, the calculated frequency response of the sensor exhibits a large resonance peak which is not desirable. The proposed fabrication procedure has to be further optimised to overcome deformations due to stress gradients. As has been pointed out before, the existence of water in between the electrodes potentially requires the sensor to be often recalibrated. Although in order to further assess the performance a functional prototype has to be built, the theoretical results are promising.

7.2 Outlook

Being a principally two port transduction mechanism, capacitive sensing opens the gates toward "active detection". It provides the possibility for incorporation of electrostatic spring softening, parametric amplification and stochastic resonance [4]. Capacitive sensing also offers the chance to employ FDM (Frequency Division Multiplexing) when monitoring an array of sensors [5]. I believe the capacitive readout mechanism can be more adapted to liquid media using, among others, an integrated readout. When the basic function of charge amplification is done on chip level rather than with a discrete board, the effects of parasitics will decrease substantially, i.e. coupling through the medium will be less problematic. In this case the parasitics contribute less to the total capacitance and, therefore, considering a constant resolvable relative change, much lower fluid induced changes are detectable. If possible, changes of the capacitance should be due to parallel motion of thin plates with respect to each other. This not only reduces the fluid resistance against the plates but also provides a linear modulation of the signal (although for small signal modulation this is of little concern).

As has been said, the increase in mass and damping of moving objects in water are limiting factors associated with the enlargement of the electrodes' area. This has been overcome with the structures in which many individual receptors are connected in parallel. The array therefore functions just as a single sensor and the cumulative response is the average of all the receptors which have minute phase differences with respect to each other. Using an integrated readout removes the need for this parallel connection by providing the possibility to measure much lower capacitances. The wiring problems namely space limitations, cross talks and insulation also can be reduced substantially using on chip sensor-interfacing electronics.

In the closed membrane configuration the thickness of the membrane has a dominant effect on the flexibility of the membrane. A material that can increase the flexibility by forming thinner, stress free layers is Parylene-C which has been discussed in chapter three. Ultrathin, pinhole free Parylene-C membranes using conformal deposition can be realised [6]. A 200 nm Parylene-C membrane is about 20 times more compliant than the current 500 nm SU-8 membranes given that the Young's modulus of both materials are more or less the same. This results in a 15 times higher low frequency sensitivity. However the internal loss of Parylene-C membranes should be evaluated. In the same way, the use of a material which has a higher Young's modulus but can be deposited in much lower thickness can potentially be beneficial. A low temperature deposition which does not affect the aluminium electrodes underneath is needed. For example, poly-SiGe is deposited at 450 °C and has a Young's modulus of 155 GPa. A 50 nm poly-SiGe membrane is 30 times more flexible compared to a 500 nm SU-8 membrane. In addition, the mechanical loss of such a material is much less than for SU-8 and its conformal deposition provides the possibility to use corrugated membranes [7]. The mechanical properties of poly-SiGe are more stable over time. It is also more resistant towards water in contrast to SU-8 for which water absorption [8], however small, changes its mechanical characteristics. Moreover, poly-SiGe low temperature deposition is CMOS compatible and allows for the use of integrated readout. Therefore, further research should be done regarding the more flexible membranes using thinner, non-polymer materials.

The mechanical impedance matching and viscous coupling are other areas which should be further explored. Material and mechanics of the drag pickup

mechanism (including the fabrication procedure of mace shaped hairs) should be optimised to increase the energy transfer from the medium.

The BooT design also deserves some more attention. Instead of protective oxide layer, Parylene-C has to be used for insulation of the device from the water to prevent deformation of long, thin springs due to stress gradients. The springs and shuttle can be made of single crystalline silicon to eliminate internal stresses. To this end, using SOI wafers simplifies the fabrication process. In the current scheme the thickness of the springs is the same as the thickness of the fingers since they are made of the same polysilicon layer. By using an extra etch step these can be decoupled. This provides the possibility to use thicker fingers without adversely affecting the flexibility of the device.

7.3 References

[1] C. M. Bruinink*, et al.*, "Advancements in Technology and Design of Biomimetic Flow-Sensor Arrays," in: *Micro Electro Mechanical Systems, 2009. MEMS 2009. IEEE 22nd International Conference on*, 2009, pp. 152-155.

[2] G. J. M. Krijnen*, et al.*, "Biomimetic micromechanical adaptive flow-sensor arrays," in: *Proceedings of SPIE - The International Society for Optical Engineering*, 2007.

[3] L. K. Baxter, *Capacitive sensors: Design and application*: Wiley-IEEE Press, 1997.

[4] H. Droogendijk and G. J. M. Krijnen, "Simulation Studies of Parametric Amplification in Bio-inspired Flow Sensors," presented at the 21st Micromechanics and Micro systems Europe workshop, Enschede, The Netherlands, 2010.

[5] A. Dagamseh*, et al.*, "Array of biomimetic hair sensor dedicated for flow pattern recognition," in: *Design Test Integration and Packaging of MEMS/MOEMS (DTIP), 2010 Symposium on*, 2010, pp. 48-50.

[6] M. A. Spivack and G. Ferrante, "Determination of the Water Vapor Permeability and Continuity of Ultrathin Parylene Membranes," *Journal of the Electrochemical Society,* vol. 116, pp. 1592-1594, 1969.

[7] C. V. Hoof*, et al.* (2004) The Best Materials for Tiny, Clever Sensors. *Science*. 986-987.

[8] C. Liu*, et al.*, "Diffusion of water into SU-8 microcantilevers," *Physical Chemistry Chemical Physics,* vol. 12, pp. 10577-10583, 2010.

Summary

The lateral line, known from 19th century, is an unorthodox but essential sensory organ in fish and amphibians. It is used to detect flow fluctuations in surrounding water; on which many ecological behaviour of the animal depend. Its usefulness is best demonstrated considering an environment with minimal visual information (e.g. in deep waters, cave, etc). In engineering terms, lateral line consists of an array of flow sensors (neuromasts) which are sensitive to fluid particle velocity. It is robust and has a high sensitivity at low frequencies. The lateral line system can therefore be used for source localisation and mapping of the immediate surrounding.

We began with a description of biomimetic practice in engineering and its potentials (chapter one). The importance of a fluid particle velocity sensor has been pointed out. The morphology and structure of lateral line and neuromasts have been briefly discussed in chapter two. The nature of fluid flow in the range of interest has also been discussed. In the next two chapters three different designs for realisation of aquatic flow sensors which are inspired by the superficial and canal neuromast organ of the lateral line system of fish were proposed. The designs are based on differential capacitive readout motivated by accuracy and low power consumption.

The first device is based on a flexible fully supported membrane with electrodes underneath carrying a hair like structure on top. Using this configuration both separates the electrodes from water and avoids the liquid in between them. The structure has been introduced and analysed thoroughly. Various aspects of the device performance have been optimised by understanding the influential parameters. These can be adjusted in parallel (from sensor to sensor even in one array) or in wafer scale to tune the characteristics of the sensor. Using Micro-Electro-Mechanical Systems technology, a prototype has been fabricated. The fabrication steps have been described in detail and optimised to achieve a high yield and robust process. The uniformity and outcome of many steps have to be checked each time that they are used. However, this complicated process consumed a lot time and effort. The sensory chips are now ready for characterisation. The performance of the sensor in air has been successfully demonstrated. The higher detection threshold obtained from these measurements suggests that the membranes are stiffer than the ideal design. In addition signal to

noise ratio is lower than expected. This is due to large parasitic capacitances. The laser vibrometer and electrical measurements in water are to follow.

Another scheme has been presented for the realisation of canal embedded sensors. To use the above mentioned sensors (i.e. sensors which incorporate a close membrane) in a canal they should be inlaid in a separately fabricated channel. Using canal embedded configuration the sensors are built directly in an enclosing canal. In this scheme, although water is present in between the two capacitor's plates, the movement is small and lateral. Therefore, at low frequencies of interest, squeeze film damping is negligible. Further, the high dielectric permittivity of water increases the capacitance and, therefore, fewer individual sensors need to be connected in parallel. One of the electrodes is insulated and the one in contact with water is a floating electrode. Thus no electrolysis is expected. The presented fabrication results of the canal embedded structure demonstrate the capability of polymer processing for the simple realisation of the sensors. As the integration of electrodes and wiring should not influence the established steps, I expect no major stumbling block in the realisation of the final prototype. This process offers a great tuning potential as the dynamic response strongly depends on the diameters of the two parts of the hanging structures. The presented fabrication steps, however, required a great deal of experiments and optimisation; especially the realisation of the channel top. Although these steps have been successfully carried out, they strongly depend on process conditions which need to be carefully taken into account.

Resembling capacitive shear-stress sensors to benefit from extensive existing knowledge about their design and fabrication, a laterally moving structure (BooT) has been also suggested. This relatively simpler design utilises a shuttle which has conductive (but insulated) fingers and moves with respect to a set of fixed plates. The small length scale of the fingers lessens the squeeze film damping effect of the water which is allowed in between them. Furthermore, fixed fingers are anchored to the substrate to omit any deflection due to water movement. As this scheme is relatively new, only a few aspects of the fabrication have yet been investigated. Reliable realisation of thin, flexible and stress free springs should be further examined. In addition, although each finger has a small area the movement is limited by the total area of all the fingers facing the medium in the direction of flow. The moving structures however are made of polysilicon whose mechanical characteristics are well

known and reliable. Unfortunately at the time of writing none of the prototypes for the last two schemes are ready for characterisations but the results achieved during fabrication processes are very promising.

Samenvatting

De laterale lijn, bekend sinds de 19e eeuw, is een essentieel zintuig voor vissen en amfibieën. Dit orgaan maakt het voor de vis mogelijk stromingsfluctuaties waar te nemen in het omliggende water, welke voor een groot deel het ecologisch gedrag van het dier bepalen. Dit orgaan is van groot belang in een omgeving waar minimale visuele informatie beschikbaar is (bijv. diepe wateren, grotten, etc.). Vanuit technisch oogpunt bestaat de laterale lijn uit een reeks van stromingssensoren (neuromasten) die gevoelig zijn voor de deeltjessnelheid van de vloeistof waarin het dier zich bevindt. De laterale lijn is robuust en heeft een hoge gevoeligheid bij lage frequenties en is geschikt voor bronlokalisatie en het in kaart brengen van de directe omgeving middels het nabije veld.

Hoofdstuk één van dit proefschrift beschrijft de rol van biomimetica in de ingenieurswetenschappen en de mogelijkheden hiervan. Het belang van een sensor voor deeltjessnelheid in vloeistoffen wordt toegelicht en de vorm en structuur van de laterale lijn en de neuromasten wordt beschreven in hoofdstuk twee. In de daarop volgende hoofdstukken worden drie verschillende ontwerpen beschreven voor de realisatie van stromingssensoren in water. Deze ontwerpen zijn allen geïnspireerd op de oppervlakte- en kanaalneuromasten van het laterale lijn orgaan. Deze ontwerpen zijn gebaseerd op een differentiële capacitieve uitlezing waarmee een hoge nauwkeurigheid en een laag vermogensverbruik haalbaar is.

De eerste sensor is gebaseerd op een gesloten flexibel membraan. Bovenop het membraan bevindt zich een haarstructuur en onder dit membraan bevinden zich elektrodes voor de capactieve uitlezing. In deze configuratie zijn de elektrodes gescheiden van het water en kan er geen water tussen de elektrodes komen. De structuur van de sensor wordt beschreven en uitvoerig geanalyseerd. Middels deze analyse worden de parameters verkregen om een optimale werking van de sensor te verkrijgen. Deze parameters kunnen per sensor in een rij worden aangepast of op wafer-niveau, om de eigenschappen van de sensor te optimaliseren. Met Micro-Electro-Mechanical Systems (MEMS) technologie is een prototype gefabriceerd. De fabricagestappen worden beschreven en zijn zodanig geoptimaliseerd dat er een robuust proces is ontwikkeld met een hoge opbrengst. De gefabriceerde sensoren zijn

klaar voor karakterisatie en de werking van de sensor in lucht is experimenteel aangetoond. Uit het experiment komt naar voren dat de detectielimiet hoger is dan verwacht, wat suggereert dat de gefabriceerde membranen stijver zijn dan in het ontwerp is aangenomen. Ook is de signaal-ruis verhouding lager dan verwacht door de aanwezigheid van grotere parasitaire capaciteiten. Metingen en karakterisatie van de sensor in water moeten nog worden verricht.

Om de eerder genoemde sensoren in te bedden in een kanaal wordt een nieuw concept geïntroduceerd. Dit omvat plaatsing van de eerder beschreven sensoren (sensoren met een gesloten membraan) in een afzonderlijk gefabriceerd kanaal of door een concept te kiezen waarbij de sensoren reeds in een kanaal zijn geïntegreerd. In het laatst genoemde concept bevindt zich water tussen de twee elektrodes van de uitleescapaciteiten. De invloed van water op de demping van het systeem (squeezed film demping) wordt bij lage frequenties verwaarloosbaar geacht omdat de bewegingen klein en lateraal zijn. Door de hoge diëlektrische constante van water wordt de capaciteit vergroot waardoor er minder sensoren nodig zijn in een parallelle configuratie. Daarnaast is een van de elektrodes geïsoleerd om elektrolyse te voorkomen. De beschreven fabricageresultaten van dit nieuwe concept laten de potentie zien van een polymeerproces op basis van SU-8 voor de realisatie van deze sensoren. Naar verwachting zal integratie van elektrodes en bedrading de tot dusver ontwikkelde fabricagestappen niet beïnvloeden waardoor de realisatie van het uiteindelijke prototype haalbaar moet zijn. Het ontwerp biedt de mogelijkheid voor optimalisatie van de sensor doordat de dynamische responsie sterk afhangt van de mechanische eigenschappen van de ophanging, die eenvoudig zijn aan te passen. De beschreven fabricagestappen vereisen een groot aantal experimenten en optimalisatie; in het bijzonder de realisatie van een kanaal rondom de sensoren. De processtappen zijn succesvol uitgevoerd maar hangen sterk af van de procescondities. Deze moeten zorgvuldig in acht worden genomen tijdens de fabricage.

Gezien het feit dat capacitieve sensoren die gebaseerd zijn op het meten van afschuifspanningen al geruime tijd bestaan en om te profiteren van het feit dat er veel bekend is over het ontwerp en de fabricage hiervan wordt er ook een lateraal bewegende structuur (BooT) voorgesteld. Dit relatief eenvoudig ontwerp maakt gebruik van een schijf met elektrisch geleidende vingers, die beweegt ten opzichte van gefixeerde platen. De beperkte lengte van de vingers verminderd de viskeuze demping

t.g.v. het water dat zich tussen de vingers bevindt. Ook zijn de gefixeerde vingers verbonden met het substraat, zodat er geen uitwijking plaatsvindt door beweging van het water. Gezien het feit dat dit een relatief nieuw idee is, zijn er slechts enkele aspecten van de fabricage onderzocht. De betrouwbare realisatie van dunne flexibele en spanningsvrije veren moet verder worden onderzocht. Hoewel elke vinger een klein oppervlak heeft, is de beweging hiervan beperkt door het totale oppervlak van de vingers in de richting van de stroming. De bewegende structuren worden echter gemaakt van polisilicium en hiervan zijn de mechanische eigenschappen goed gedefinieerd. Helaas zijn op moment van schrijven van dit proefschrift geen prototypes van de genoemde concepten beschikbaar voor karakterisatie maar de behaalde resultaten tijdens de fabricage zijn veelbelovend.

Appendices

I. On the static deflection of a fully supported membrane

The governing equation for the deflection of a circular membrane is [1]

$$D \cdot \nabla^4 w = q(r,\theta) \tag{1.1}$$

where ∇^2 is the Laplace operator,

$$\nabla^2 = \frac{\partial^2}{\partial r^2} + \frac{1}{r} \cdot \frac{\partial}{\partial r} + \frac{1}{r^2} \cdot \frac{\partial^2}{\partial \theta^2} \tag{1.2}$$

q is the density of the distributed force, w is the deflection, r and θ are coordinates in polar system and D is the flexural rigidity of the membrane. In the following, positive direction of the z axis and hence positive w are considered to be downward.

When due to symmetry, there is no dependency on angular position, successive integration of (1.1) leads to [2]

$$D \cdot w(r) = F(r) + c_1 \cdot \frac{r^2}{4}(\log r - 1) + c_2 \cdot \frac{r^2}{4} + c_3 \cdot \log r + c_4 \tag{1.3}$$

where

$$F(r) = \int \frac{1}{r} \int r \int \frac{1}{r} \int r \cdot q(r) \cdot dr \cdot dr \cdot dr \cdot dr \tag{1.4}$$

The problem is further divided into two parts as shown in Figure 1. The total solution is the superposition of the deflection obtained in each case.

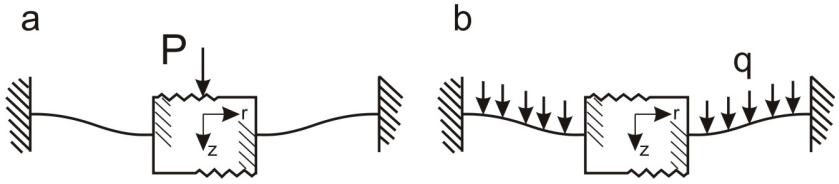

Figure 1 *Decomposition of the downward deflection*

I.I. Circular plate clamped to a rigid circular shaft inclusion at the centre, and subjected to a point load P at the centre

This configuration shown in left side of Figure 1. The boundary conditions can be written as

$$\begin{aligned} w|_{r=a} &= 0, \qquad \left.\frac{\partial w}{\partial r}\right|_{r=a} = 0 \\ \left.\frac{\partial w}{\partial r}\right|_{r=b} &= 0, \qquad (2\pi \cdot r) \cdot Q_r|_{r=b} = -P \end{aligned} \tag{1.5}$$

where a is the radius of the membrane, b is the radius of the inclusion and Q_r is the shear force and is given by

$$-r \cdot Q(r) = \int r \cdot q(r) \cdot dr + c \tag{1.6}$$

in which c is a constant. The other variables are shown in the figure. This leads to

$$\begin{aligned} c_1 &= \frac{P}{2\pi} \\ c_2 &= \frac{P}{4\pi}\left(1 + \frac{2\zeta^2}{1-\zeta^2} \cdot \ln b - \frac{2}{1-\zeta^2} \cdot \ln a\right) \\ c_3 &= -\frac{P \cdot b^2}{4\pi} \cdot \frac{\ln \zeta}{1-\zeta^2} \\ c_4 &= \frac{P \cdot a^2}{16\pi} \cdot \left(1 - \frac{2\zeta^2}{1-\zeta^2} \cdot \ln \zeta \cdot (1 - 2\ln a)\right) \end{aligned} \tag{1.7}$$

in which $\zeta = b/a$. The resulting deflection is therefore

$$w(\rho) = \frac{P \cdot a^2}{16\pi} \cdot \left(1 - \rho^2 + 2\rho^2 \cdot \ln \rho - \frac{2\zeta^2 \cdot \ln \zeta}{1-\zeta^2} \cdot (1 - \rho^2 + 2\ln \rho)\right) \tag{1.8}$$

in which $\rho = r/a$ is the normalised radial coordinate. Note that (1.8) is valid when $\zeta \le \rho \le 1$.

I.II. Circular plate clamped to a rigid circular shaft inclusion at the centre, and subjected to a uniformly distributed load q

For the configuration shown on the right side of Figure 1, the boundary conditions are

$$\begin{aligned} w\big|_{r=a} &= 0, \qquad \left.\frac{\partial w}{\partial r}\right|_{r=a} = 0 \\ \left.\frac{\partial w}{\partial r}\right|_{r=b} &= 0, \qquad (2\pi \cdot r) \cdot Q_r\big|_{r=b} = 0 \end{aligned} \tag{1.9}$$

Therefore (1.3) leads to

$$
\begin{aligned}
c_1 &= \frac{-q\cdot b^2}{2}\\
c_2 &= -\frac{q\cdot a^2}{8\left(1-\zeta^2\right)}\left(1+2\zeta^2\cdot\left(1-2\ln a\right)+\zeta^4\cdot\left(-3+4\ln b\right)\right)\\
c_3 &= \frac{q\cdot a^2\cdot b^2}{16}\cdot\left(1-\frac{4\zeta^2}{1-\zeta^2}\cdot\ln\zeta\right)\\
c_4 &= \frac{q\cdot a^4}{64\left(1-\zeta^2\right)}\cdot\left(1-\zeta^2\cdot\left(3+4\ln a\right)+2\zeta^4\cdot\left(1+2\ln a\right)+8\zeta^4\cdot\ln\zeta\cdot\left(1-2\ln a\right)\right)
\end{aligned}
\tag{1.10}
$$

and the deflection is obtained as

$$
\begin{aligned}
w(\rho) = \frac{q\cdot a^4}{64}\cdot\Bigg(&\frac{1}{\left(1-\zeta^2\right)}+\rho^4+4\zeta^2\cdot\ln\rho\cdot\left(1-2\rho^2\right)-2\rho^2\cdot\left(1-\zeta^2\right)+\\
&8\zeta^4\cdot\ln\zeta\cdot\left(1-\rho^2-2\ln\rho\right)-\zeta^2\cdot\left(3-2\zeta^2\right)\Bigg)
\end{aligned}
\tag{1.11}
$$

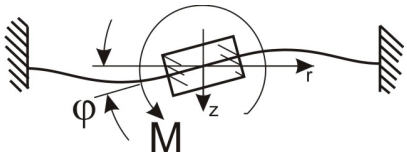

Figure 2 *Anti-symmetric deflection under linearly varying load*

I.III. Anti-symmetric deflection of a clamped circular plate with a rigid inclusion at the centre

When a moment of magnitude M is applied to the inclusion as shown in Figure 2, the complete general solution to (1.1) has been shown to be

$$
w(\rho,\theta) = \left(A\cdot\rho + B\cdot\rho^3 + C\cdot\rho^{-1} + H\cdot\rho\cdot\ln(\rho)\right)\cdot\cos(\theta) \tag{1.12}
$$

where $\rho = r/a$ is the normalised radial distance.

The boundary conditions can be written as

$$
\begin{aligned}
w\big|_{\rho=1} &= \left.\frac{\partial w}{\partial r}\right|_{\rho=1} = 0\\
w\big|_{\rho=\zeta} &= \varphi\cdot b\cdot\cos(\theta)\\
\left.\frac{\partial w}{\partial \rho}\right|_{\rho=\zeta} &= \left.\frac{w}{\rho}\right|_{\rho=\zeta}
\end{aligned}
\tag{1.13}
$$

in which φ is the angular deflection of the inclusion. The above boundary layer condition leads to

$$\begin{aligned} &A+B+C=0 \\ &A+3B-C+H=0 \\ &A\cdot\zeta+B\cdot\zeta^3+C\cdot\zeta^{-1}+H\cdot\zeta\cdot\ln(\zeta)=\varphi\cdot a \\ &2B\cdot\zeta^2-2C\cdot\zeta^{-2}+H=0 \end{aligned} \tag{1.14}$$

which, therefore, gives

$$w(\rho,\theta)=\frac{M}{8\pi\cdot D}\cdot\frac{a\cdot\left(\rho^2\cdot\left(1-\zeta^2-\rho^2+2\ln(\rho)+2\ln(\rho)\cdot\zeta^2\right)+\zeta^2\right)\cdot\cos(\theta)}{\rho\cdot\left(1+\zeta^2\right)} \tag{1.15}$$

in which M is related to the bending moment and shearing force of the membrane in radial direction as [3]

$$M=a\int_{-\pi}^{\pi}M_r\big|_{\rho=1}\cdot\cos(\theta)\cdot d\theta-a^2\int_{-\pi}^{\pi}Q_r\big|_{\rho=1}\cdot\cos(\theta)\cdot d\theta \tag{1.16}$$

where

$$\begin{aligned} &Q_r=-D\cdot\frac{\partial}{\partial r}\left(\nabla^2 w\right) \\ &M_r=-D\cdot\left(\frac{\partial^2 w}{\partial r^2}+\nu\cdot\left(\frac{1}{r}\frac{\partial w}{\partial r}+\frac{1}{r^2}\frac{\partial^2 w}{\partial\theta^2}\right)\right) \end{aligned} \tag{1.17}$$

Using above equalities one can easily derive that

$$M=\left(-4\pi\cdot D\cdot\frac{1+\zeta^2}{1-\zeta^2+\ln\zeta\cdot\left(1+\zeta^2\right)}\right)\cdot\varphi \tag{1.18}$$

which gives the torsional stiffness of the membrane as defined by $K_\varphi=M/\varphi$.

The analytical solution of anti-symmetric deflection is compared to simulation results (COMSOL Multiphysics 3.5a) at different ζ ratios in Figure 3 below. Solid lines are the analytical results and dots depict the maximum of a curve. Simulation results are shown as dashed lines. It is clear that analytical approximation slightly underestimates the deflection.

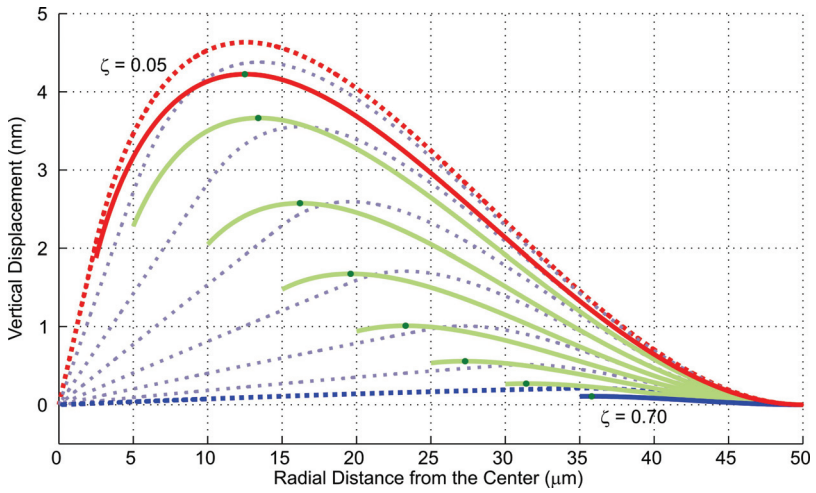

Figure 3 *Comparison of analytical results and simulation for different ζ ratio. Solid lines illustrate the analytical solution and dashed lines are simulation results.*

[1] S. Timoshenko and S. Woinowsky-Krieger, *Theory of Plates and Shells*, 2 ed.: McGraw-Hill, 1959.

[2] J. N. Reddy, *Theory and Analysis of Elastic Plates and Shells*, 2nd ed. Boca Raton: CRC Press, 2007.

[3] E. Ollerton, "Thin Annular Plates Having an Inner Clamp Carrying Bending Moments," *Journal of Strain Analysis for Engineering Design,* vol. 12, pp. 192-&, 1977.

II. On the derivation of squeeze film damping coefficient

The general form of the Reynold's equation by neglecting the lateral movement of the surfaces is obtained [1] as

$$\vec{\nabla}\cdot\left(\frac{\rho\cdot h^3}{\mu}\cdot\nabla p\right)=12\frac{\partial(\rho\cdot h)}{\partial t} \tag{2.1}$$

where p is the pressure, ρ is the density, μ is the dynamic viscosity and h is the thickness. It should be noted again that this equation is derived under steady[1] and isothermal[2] conditions. It is also important that the Reynold's number

$$R=\frac{\omega\cdot\rho\cdot h^2}{\mu} \tag{2.2}$$

is much smaller than unity which is satisfied in our case of interest. Moreover in isothermal conditions the density is proportional to the pressure and therefore introducing dimensionless parameters, (2.1) can be written as

$$\vec{\nabla}\cdot\left(H^3\cdot P\cdot\nabla P\right)=\sigma\cdot\frac{\partial(P\cdot H)}{\partial t} \tag{2.3}$$

where $H=h/h_0$, $P=p/p_0$ and σ is the squeeze number, $\sigma=12\mu/p_0\cdot h_0^2$.

For small displacement of a surface around its balance position, one can introduce perturbations [2] as

$$\begin{aligned} P&=1+\delta\bar{P}\\ H&=1+\delta\bar{H}\end{aligned} \tag{2.4}$$

$(\delta\ll 1)$ and linearise (2.3) as

$$\nabla^2\bar{P}=\sigma\cdot\left(\frac{\partial\bar{P}}{\partial t}+\frac{\partial\bar{H}}{\partial t}\right) \tag{2.5}$$

in which for polar coordinates

$$\nabla^2=\frac{\partial^2}{\partial r^2}+\frac{1}{r}\cdot\frac{\partial}{\partial r}+\frac{1}{r^2}\cdot\frac{\partial^2}{\partial\theta^2} \tag{2.6}$$

Green functions can be used [3] to solve inhomogeneous diffusion equation of (2.5). For the diffusion equation of the form

[1] Steady flow means that the time derivative of velocities and inertia of fluid are ignored.
[2] Isothermal condition is when the thermal gradient through the film thickness is negligible. This is valid if the thermal conductivity of the plates is high.

$$\nabla^2 P(\vec{r}) - \alpha^2 \cdot \frac{\partial P(\vec{r})}{\partial t} = f(\vec{r},t) \tag{2.7}$$

it can be shown that

$$P(\vec{r},t) = \int_0^t \int_{V'} G(\vec{r},t,\vec{r}',t') \cdot f(\vec{r}',t') \cdot dt' \cdot dV' - \alpha^2 \cdot \int_{V'} G(\vec{r},t,\vec{r}',0) \cdot P(\vec{r},0) \cdot dV' \tag{2.8}$$

in which the Green's function, *G*, is defined as

$$G(\vec{r},t,\vec{r}',t') = \frac{-1}{\alpha^2} \cdot \sum_{m,n} e^{\frac{-k_{mn}^2 \cdot (t-t')}{\alpha^2}} \cdot \psi_{mn}(\vec{r}) \cdot \psi_{mn}^*(\vec{r}') \tag{2.9}$$

where ψ_{mn} are the eigenfunctions and k_{mn} are the eigenvalues of the two dimensional Helmholtz equation (if the pressure in z direction is considered constant)

$$\nabla^2 \psi_{mn} + k_{mn}^2 \cdot \psi_{mn} = 0 \tag{2.10}$$

for which the orthonormality dictates

$$\int_V \psi_{mn}(\vec{r}) \cdot \psi_{m'n'}^*(\vec{r}) \cdot dV = \delta_{n,n'} \cdot \delta_{m,m'} \tag{2.11}$$

$$\sum \psi_{mn}(\vec{r}) \cdot \psi_{mn}^*(\vec{r}') = \delta(\vec{r} - \vec{r}') \tag{2.12}$$

To begin, consider the Helmholtz equation of (2.10) with

$$\left. \frac{\partial \psi}{\partial r} \right|_{r=a} = 0 \tag{2.13}$$

as the boundary condition which results from the zero flow constrain due to the fully supported membrane. Here *a* is the membrane radius.

Now using the method of separation of variables

$$\psi_{mn} = R(r) \cdot \Theta(\theta) \tag{2.14}$$

in which uniqueness requires that Θ is periodic with periodicity 2π and replacing (2.14) in (2.10) results in

$$\begin{aligned} &\frac{\partial^2 \Theta}{\partial \theta^2} + n^2 \cdot \Theta = 0 \\ &r^2 \cdot \frac{\partial^2 R}{\partial r^2} + r \cdot \frac{\partial R}{\partial r} + \left(k_{mn}^2 \cdot r^2 - n^2\right) \cdot R = 0 \end{aligned} \tag{2.15}$$

for $n = 0,1,2,\ldots$ and therefore

$$\begin{aligned} \Theta &= A \cdot \cos(n \cdot \theta) + B \cdot \sin(n \cdot \theta) \\ R &= C \cdot J_n(k_{mn} \cdot r) \end{aligned} \tag{2.16}$$

where J_n is the Bessel function of the first kind of n^{th} order and the Bessel function of the second kind is omitted because R should be finite at the centre of the membrane. Applying the boundary condition at (2.13) one gets

$$J_n'\left(k_{mn}\cdot a\right)=0 \tag{2.17}$$

and therefore

$$k_{mn}=\frac{\rho_m}{a} \tag{2.18}$$

where ρ_m is the m^{th} extremum of the function J_n. Therefore

$$\psi=\sum_{m,n}C_{mn}\cdot J_n\left(k_{mn}\cdot r\right)\cdot\left(A_{mn}\cdot\cos\left(n\cdot\theta\right)+B_{mn}\cdot\sin\left(n\cdot\theta\right)\right) \tag{2.19}$$

In addition the condition of ortonormality in (2.11) leads to

$$\begin{aligned}\psi_{m0}&=\frac{1}{\sqrt{\pi}}\cdot\frac{J_0\left(k_{m0}\cdot r\right)}{a\cdot J_0\left(k_{m0}\cdot a\right)}\\ \psi_{mn}&=\frac{\sqrt{2}\cdot k_{mn}}{\sqrt{\pi\cdot\left(k_{mn}^2-n^2\right)}}\cdot\frac{J_n\left(k_{mn}\cdot r\right)}{a\cdot J_n\left(k_{mn}\cdot a\right)}\cdot\cos\left(n\cdot\theta\right)\end{aligned} \tag{2.20}$$

in which the phase of cosine term, $\tan^{-1}\left(B/A\right)$, is arbitrary and therefore is taken zero for convenience.

Therefore in this case noting that $\alpha^2=\sigma$ the green function is constructed according to (2.9). Due to the time dependent exponential factor in the function the second term on the right hand side of (2.8) is zero in steady state and therefore assuming

$$H\left(r,\theta,t\right)=H'\left(r\right)\cdot\cos\left(\theta\right)\cdot\left(A\cdot\cos\left(\omega\cdot t\right)+B\cdot\sin\left(\omega\cdot t\right)\right) \tag{2.21}$$

we have

$$f\left(\vec{r},t\right)=\sigma\cdot\frac{\partial H}{\partial t}=\sigma\cdot H'\left(r\right)\cdot\cos\left(\theta\right)\cdot\omega\cdot\left(-A\cdot\sin\left(\omega\cdot t\right)+B\cdot\cos\left(\omega\cdot t\right)\right) \tag{2.22}$$

and one can derive

$$\begin{aligned}\bar{P}\left(r,\theta,t\right)=&\sum_m\frac{-2\cdot\left(k_{m1}\cdot a\right)^2}{\left(\left(k_{m1}\cdot a\right)^2-1\right)}\cdot\frac{\cos\left(\theta\right)\cdot J_1\left(k_{m1}\cdot r\right)}{\left[J_1\left(k_{m1}\cdot a\right)\right]^2}\times\\ &\times\frac{\omega}{\lambda^2+\omega^2}\left(\left(A\cdot\omega-B\cdot\lambda\right)\cdot\cos\left(\omega\cdot t\right)+\left(A\cdot\lambda+B\cdot\omega\right)\cdot\sin\left(\omega\cdot t\right)\right)\times\\ &\times\int_0^a J_1\left(k_{m1}\cdot r'\right)\cdot H'\left(r'\right)\cdot r'\cdot dr'\end{aligned} \tag{2.23}$$

in which

$$\lambda = \frac{-k_{m1}^2}{\sigma} \tag{2.24}$$

and the exponential part of the time dependant term,

$$e^{\lambda t} \cdot \left(-A \cdot \omega + B \cdot \lambda\right) \tag{2.25}$$

is zero at steady state.

Now the damping torque is calculated from

$$T_d = \int_A \bar{P} \cdot p_0 \cdot r \cdot \cos(\theta) \cdot dA \tag{2.26}$$

which using the identity

$$\int_0^z r^{\upsilon} \cdot J_{\upsilon-1}(r) \cdot dr = z^{\upsilon} \cdot J_{\upsilon}(z) \quad \upsilon > 0 \tag{2.27}$$

results in

$$\begin{aligned} T_d(t) = {} & \frac{p_0}{h_0} \cdot 2\pi \cdot a^4 \cdot \sum_m \frac{k_{m1}}{k_{m1}^2 \cdot a^2 - 1} \cdot \frac{J_2(k_{m1} \cdot a)}{\left[J_1(k_{m1} \cdot a)\right]^2} \times \\ & \times \omega \cdot \frac{(A \cdot \omega - B \cdot \lambda) \cdot \cos(\omega \cdot t) + (A \cdot \lambda + B \cdot \omega) \cdot \sin(\omega \cdot t)}{\lambda^2 + \omega^2} \times \\ & \times \int_0^a J_1(k_{m1} \cdot r') \cdot \frac{w(r')}{M_0} \cdot r' \cdot dr' \end{aligned} \tag{2.28}$$

The function $w(r)$ is

$$\begin{cases} r \cdot \tan\left(\dfrac{M_0}{K_\varphi}\right) & r \le R_h \\ \dfrac{-M_0}{8\pi \cdot D} \cdot \dfrac{R_h \cdot \left(\zeta^2 + \rho^2 \cdot \left(1 - \zeta^2 - \rho^2 + 2\ln(\rho) + 2 \cdot \zeta^2 \cdot \ln(\rho)\right)\right)}{\rho \cdot \zeta \cdot \left(1 + \zeta^2\right)} & R_h \le r \le a \end{cases} \tag{2.29}$$

where

$$\zeta = \frac{R_h}{a}, \quad \rho = \frac{r}{a}, \quad M_0 = \sqrt{A^2 + B^2} \tag{2.30}$$

and K_φ is the stiffness of the membrane (for derivation see Appendix I) and D is the flexural rigidity. The resulting torque is shown in figure 1 below.

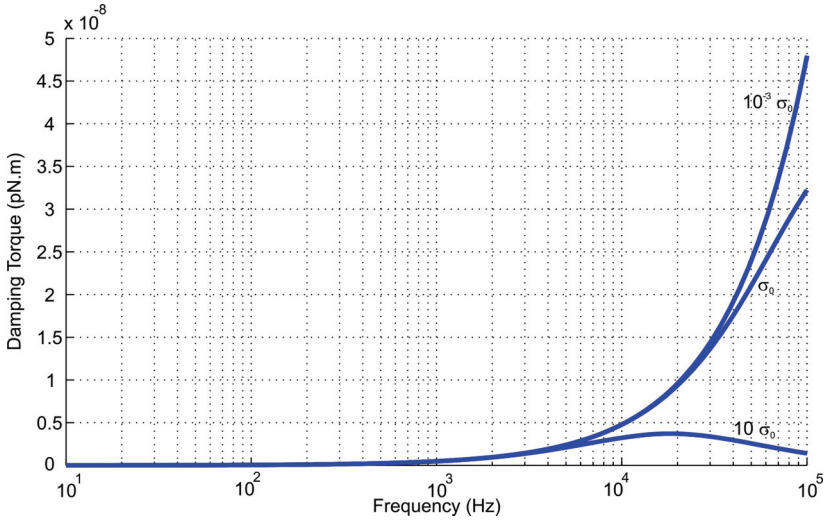

Figure 4 *Squeeze film damping torque generated by the air in the closed chamber under the membrane*

[1] M. Bao, "Air Damping," in *Analysis and design principles of mems devices*, ed Amsterdam: Elsevier, 2005.

[2] F. Pan*, et al.*, "Squeeze film damping effect on the dynamic response of a MEMS torsion mirror," *Journal of Micromechanics and Microengineering,* vol. 8, pp. 200-208, Sep 1998.

[3] R. B. Darling*, et al.*, "Compact analytical modeling of squeeze film damping with arbitrary venting conditions using a Green's function approach," *Sensors and Actuators A: Physical,* vol. 70, pp. 32-41, 1998.

III. On the vibration of a two segmented cantilever beam

The Euler-Bernoulli beam equation can be derived easily from the Hamilton principle as

$$EI \cdot \frac{\partial^4 w}{\partial x^4} + \rho \cdot A \cdot \frac{\partial^2 w}{\partial t^2} + \eta \cdot \frac{\partial w}{\partial t} = f(x,t) \tag{4.1}$$

where E is the Young's modulus, I is the moment of inertia, $A = \pi R_s^2$ is the constant cross sectional area, ρ is the density, η is the structural damping coefficient and f is the distributed drag force. Here we investigate vibration of an stepped cantilever beam.

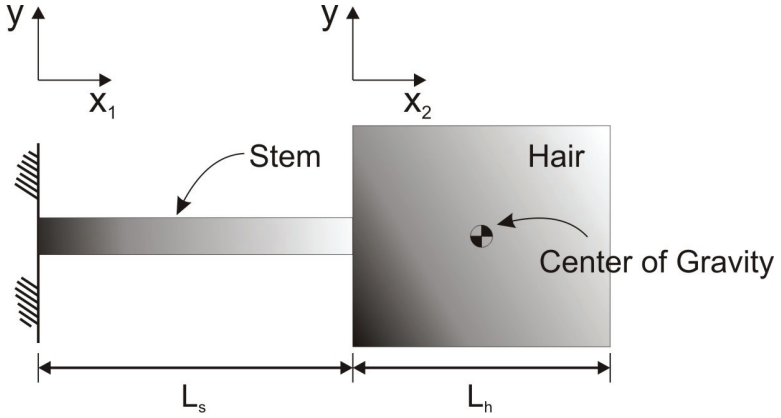

Figure 5 *A cantilever beam with a tip mass whose centre of gravity does not coincide with the connection point*

Consider a beam composed of two parts which show different static and dynamic behaviour due to the difference in their flexural rigidity, EI, as shown Figure 5. For this beam the dynamic PDE (Partial Differential Equation) of motion is therefore

$$\begin{cases} E_s \cdot I_s \cdot \dfrac{\partial^4 w_1}{\partial x_1^4} + \rho_s \cdot A_S \cdot \dfrac{\partial^2 w_1}{\partial t^2} + \eta \cdot \dfrac{\partial w_1}{\partial t} = f_s(x_1,t) & 0 \le x_1 \le L_s \\ E_h \cdot I_h \cdot \dfrac{\partial^4 w_2}{\partial x_2^4} + \rho_s \cdot A_h \cdot \dfrac{\partial^2 w_2}{\partial t^2} + \eta \cdot \dfrac{\partial w_2}{\partial t} = f_h(x_2,t) & 0 \le x_2 \le L_h \end{cases} \tag{4.2}$$

where the s and h indices denote the basal and apical parts respectively. In our case of interest Young's moduli, density and structural damping pertaining to both parts are the same. The boundary conditions are

$$
\begin{aligned}
&w_1(0,t)=0 \qquad \frac{\partial w_1}{\partial x_1}(0,t)=0\\
&\frac{\partial^2 w_2}{\partial x_2^2}(L_h,t)=0 \quad \frac{\partial^3 w_2}{\partial x_2^3}(L_h,t)=0
\end{aligned}
\tag{4.3}
$$

and in the junction of two parts,

$$
\begin{aligned}
&w_1(L_s,t)=w_2(0,t)\\
&\frac{\partial w_1}{\partial x_1}(L_s,t)=\frac{\partial w_2}{\partial x_2}(0,t)\\
&E_s\cdot I_s\cdot\frac{\partial^2 w_1}{\partial x_1^2}(L_s,t)=E_h\cdot I_h\cdot\frac{\partial^2 w_2}{\partial x_2^2}(0,t)\\
&E_s\cdot I_s\cdot\frac{\partial^3 w_1}{\partial x_1^3}(L_s,t)=E_h\cdot I_h\cdot\frac{\partial^3 w_2}{\partial x_2^3}(0,t)
\end{aligned}
\tag{4.4}
$$

Let us first derive the natural resonance frequencies and mode shapes of the beam. To this end, the method of separation of variables is employed. Consider the particular solution to homogenous and undamped equation in the form

$$
\begin{cases}
w_1(x_1,t)=X_1(x_1)\cdot T(t)\\
w_2(x_2,t)=X_2(x_2)\cdot T(t)
\end{cases}
\tag{4.5}
$$

where we considered the time dependency of the two functions identical. Therefore, substituting (4.5) in (4.4) one gets

$$
\begin{aligned}
&\frac{\partial^2 T_n}{\partial t^2}=-\omega_n^2\cdot T_n\\
&\frac{E_s\cdot I_s}{\rho_s\cdot A_s}\cdot\frac{\partial^4 X_{1n}}{\partial x_1^4}=\omega_n^2\cdot X_{1n}\\
&\frac{E_h\cdot I_h}{\rho_h\cdot A_h}\cdot\frac{\partial^4 X_{2n}}{\partial x_2^4}=\omega_n^2\cdot X_{2n}
\end{aligned}
\tag{4.6}
$$

in which n denotes the n^{th} vibrational mode. This result in

$$
\begin{aligned}
&T_n(t)=a_n\cdot\sin(\omega_n\cdot t)+b_n\cdot\cos(\omega_n\cdot t)\\
&X_{1n}(x_1)=A_{1n}\cdot\sin(k_{1n}\cdot x_1)+B_{1n}\cdot\cos(k_{1n}\cdot x_1)+\\
&\qquad C_{1n}\cdot\sinh(k_{1n}\cdot x_1)+D_{1n}\cdot\cosh(k_{1n}\cdot x_1)\\
&X_{2n}(x_2)=A_{2n}\cdot\sin(k_{2n}\cdot x_2)+B_{2n}\cdot\cos(k_{2n}\cdot x_2)+\\
&\qquad C_{2n}\cdot\sinh(k_{2n}\cdot x_2)+D_{2n}\cdot\cosh(k_{2n}\cdot x_2)
\end{aligned}
\tag{4.7}
$$

in which the dispersion relations relate the wave numbers, k_{1n} and k_{2n}, to the natural frequency, ω_n, as

$$\omega_n^2 = \frac{E_s \cdot I_s}{\rho_s \cdot A_s} \cdot k_{1n}^4, \quad \omega_n^2 = \frac{E_h \cdot I_h}{\rho_h \cdot A_h} \cdot k_{2n}^4 \tag{4.8}$$

Note that one can consider the apical part (the hair) completely rigid. In this case the boundary conditions presented by (4.3) and (4.4) are rewritten as [1]

$$\begin{aligned} & X(0,t) = 0 \\ & \frac{dX}{dx}(0,t) = 0 \\ & EI_s \cdot \frac{d^2X}{dx^2}(L_s,t) = \left(J + M_h \cdot \left(\frac{L_h}{2} \right)^2 \right) \cdot \omega_n^2 \cdot \left. \frac{dX}{dx} \right|_{x=L_s} + M_h \cdot \frac{L_h}{2} \cdot \omega_n^2 \cdot X|_{x=L_s} \\ & EI_s \cdot \frac{d^3X}{dx^3}(L_s,t) = -M_h \cdot \omega_n^2 \cdot X|_{x=L_s} - M_h \cdot \frac{L_h}{2} \cdot \omega_n^2 \cdot \left. \frac{dX}{dx} \right|_{x=L_s} \end{aligned} \tag{4.9}$$

where the index *1* is dropped for simplicity and in which $M_h = \rho \cdot \pi R_h^2 \cdot L_h$ is the mass and $J = M_h \cdot \left(3R_h^2 + L_h^2\right)/12$ is the moment of inertia of the wide part at the tip (the hair). The wave numbers (hence the natural frequencies) and the mode shapes can be obtained accordingly by using (4.9) and the relations for X_{1n} in (4.6) to (4.8). The frequency equation is

$$\begin{aligned} & \cos(k \cdot L_s) \cdot \sinh(k \cdot L_s) \cdot \left(k^3 \cdot M \cdot m \cdot l^2 + k^3 \cdot J \cdot m - k \cdot M \cdot m\right) + \\ & \sin(k \cdot L_s) \cdot \cosh(k \cdot L_s) \cdot \left(k^3 \cdot M \cdot m \cdot l^2 + k^3 \cdot J \cdot m + k \cdot M \cdot m\right) + \\ & \cos(k \cdot L_s) \cdot \cosh(k \cdot L_s) \cdot \left(k^4 \cdot J \cdot M - m^2\right) + k^4 \cdot J \cdot M + \\ & \sin(k \cdot L_s) \cdot \sinh(k \cdot L_s) \cdot \left(2k^2 \cdot M \cdot m \cdot l\right) - m^2 = 0 \end{aligned} \tag{4.10}$$

in which $m = \rho_s \cdot A_s$. The roots of this equation determine the wave numbers and thus the natural frequencies. Using this approximation the solution can also been found considering the Timoshenko beam theory [2].

The complete problem (and similar problems with more steps in the beam) can be solved using the transfer matrix [3] or the receptance coupling [4] methods. Here we take another approach and incorporate the method used by [5]. The boundary conditions at $x_1 = 0$ lead to

$$A_{1n} + C_{1n} = 0, \qquad B_{1n} + D_{1n} = 0 \tag{4.11}$$

and therefore

$$X_{1n}(x_1) = A_{1n}\cdot\left(\sin(k_{1n}\cdot x_1) - \sinh(k_{1n}\cdot x_1)\right) + B_{1n}\cdot\left(\cos(k_{1n}\cdot x_1) - \cosh(k_{1n}\cdot x_1)\right) \quad (4.12)$$

from the continuity relations given by(4.4)

$$\begin{bmatrix} A_{1n}\cdot F_1 + B_{1n}\cdot F_3 \\ A_{1n}\cdot F_3 - B_{1n}\cdot F_2 \\ A_{1n}\cdot F_2 + B_{1n}\cdot F_4 \\ -A_{1n}\cdot F_4 + B_{1n}\cdot F_1 \end{bmatrix} = \begin{bmatrix} 0 & 1 & 0 & 1 \\ \beta & 0 & \beta & 0 \\ 0 & \beta^2\cdot EI & 0 & -\beta^2\cdot EI \\ -\beta^3\cdot EI & 0 & \beta^3\cdot EI & 0 \end{bmatrix}\cdot\begin{bmatrix} A_{2n} \\ B_{2n} \\ C_{2n} \\ D_{2n} \end{bmatrix} \quad (4.13)$$

in which

$$\beta^4 = \frac{\rho_h\cdot A_h}{E_h\cdot I_h}\cdot\frac{E_s\cdot I_s}{\rho_s\cdot A_s}, \qquad EI = \frac{E_h\cdot I_h}{E_s\cdot I_s} \quad (4.14)$$

and

$$\begin{aligned} F_1 &= \sin(k_{1n}\cdot L_s) - \sinh(k_{1n}\cdot L_s) \\ F_2 &= \sin(k_{1n}\cdot L_s) + \sinh(k_{1n}\cdot L_s) \\ F_3 &= \cos(k_{1n}\cdot L_s) - \cosh(k_{1n}\cdot L_s) \\ F_4 &= \cos(k_{1n}\cdot L_s) + \cosh(k_{1n}\cdot L_s) \end{aligned} \quad (4.15)$$

therefore for the hair part

$$\begin{aligned} X_{2n}(x_2) = A_{1n}\cdot(T_1\cdot\sin + T_2\cdot\cos + T_3\cdot\sinh + T_4\cdot\cosh) + \\ B_{1n}\cdot(V_1\cdot\sin + V_2\cdot\cos + V_3\cdot\sinh + V_4\cdot\cosh) \end{aligned} \quad (4.16)$$

where the argument of trigonomic and hyperbolic functions is $k_{2n}\cdot x_2$ and

$$\begin{aligned} T_1 &= \frac{1}{2}\cdot\left[\frac{F_3}{\beta} + \frac{F_4}{\beta^3\cdot EI}\right] & V_1 &= \frac{1}{2}\cdot\left[\frac{-F_2}{\beta} - \frac{F_1}{\beta^3\cdot EI}\right] \\ T_2 &= \frac{1}{2}\cdot\left[F_1 + \frac{F_2}{\beta^2\cdot EI}\right] & V_2 &= \frac{1}{2}\cdot\left[F_3 + \frac{F_4}{\beta^2\cdot EI}\right] \\ T_3 &= \frac{1}{2}\cdot\left[\frac{F_3}{\beta} - \frac{F_4}{\beta^3\cdot EI}\right] & V_3 &= \frac{1}{2}\cdot\left[\frac{-F_2}{\beta} + \frac{F_1}{\beta^3\cdot EI}\right] \\ T_4 &= \frac{1}{2}\cdot\left[F_1 - \frac{F_2}{\beta^2\cdot EI}\right] & V_4 &= \frac{1}{2}\cdot\left[F_3 - \frac{F_4}{\beta^2\cdot EI}\right] \end{aligned} \quad (4.17)$$

Now using the boundary condition at $x_2 = L_h$ one will have

$$\begin{cases} A_{1n}\cdot Z_1 + B_{1n}\cdot Z_2 = 0 \\ A_{1n}\cdot Z_3 + B_{1n}\cdot Z_4 = 0 \end{cases} \quad (4.18)$$

for which

$$\begin{bmatrix} Z_1 \\ Z_2 \\ Z_3 \\ Z_4 \end{bmatrix} = \begin{bmatrix} -k_{2n}^2 \cdot T_1 & -k_{2n}^2 \cdot T_2 & k_{2n}^2 \cdot T_3 & k_{2n}^2 \cdot T_4 \\ -k_{2n}^2 \cdot V_1 & -k_{2n}^2 \cdot V_2 & k_{2n}^2 \cdot V_3 & k_{2n}^2 \cdot V_4 \\ k_{2n}^3 \cdot T_2 & -k_{2n}^3 \cdot T_1 & k_{2n}^3 \cdot T_4 & k_{2n}^3 \cdot T_3 \\ k_{2n}^3 \cdot V_2 & -k_{2n}^3 \cdot V_1 & k_{2n}^3 \cdot V_4 & k_{2n}^3 \cdot V_3 \end{bmatrix} \cdot \begin{bmatrix} \sin(k_{2n} \cdot L_h) \\ \cos(k_{2n} \cdot L_h) \\ \sinh(k_{2n} \cdot L_h) \\ \cosh(k_{2n} \cdot L_h) \end{bmatrix} \tag{4.19}$$

To have nontrivial solution for (4.18) the determinant of the system's matrix should be zero which leads to the frequency equation of the form

$$Z_1 \cdot Z_4 - Z_2 \cdot Z_3 = 0 \tag{4.20}$$

The corresponding mode shapes are then obtained by substituting $B_{1n} = -A_{1n} \cdot Z_1 / Z_2$ in (4.12) and (4.16). Let us assume that the obtained mode shapes are orthogonal and we shall normalise them to have an orthonormal set. Therefore,

$$A_{1n}^{-2} = \rho_s \cdot A_s \cdot \int_0^{L_s} X_{1n}^2 + \rho_h \cdot A_h \cdot \int_0^{L_h} X_{2n}^2 \tag{4.21}$$

The table below compares the natural resonance frequencies (given in Hz) calculated analytically using (4.20) and using Comsol MultiPhysics®.

	First	Secons	Third	Forth	Fifth
Analytical	826	13.1×10^3	4.3×10^5	1.1×10^6	1.2×10^6
Simulation	723	12.9×10^3	4.1×10^5	9.3×10^5	1.1×10^6

Now we shall consider the problem of forced vibration of the stepped cantilever. We shall use modal analysis and consider the forced response to be a linear combination of the all mode shapes obtained previously as

$$w(x,t) = \sum_0^\infty q_i(t) \cdot X_i(x) \tag{4.22}$$

where q_i are the generalised coordinate and X_i consist of X_{1i} and X_{2i} computed previously for the appropriate range. In addition, the forces resisting the motion at any point depend on the velocity and are opposite in the direction to the velocity. Therefore, we can write

$$f(x,t) = f_u(x,t) - f_c(x,t) \tag{4.23}$$

and considering the Stokes' mechanical impedance,

$$f_c(x,t) = Z(x) \cdot \frac{\partial w}{\partial t} \tag{4.24}$$

Now, substituting (4.22) in (4.1), multiplying by X_j and integrate over the length of the cantilever one can derive

$$\begin{aligned}&\sum_i q_i \cdot \int_0^L E \cdot I \cdot \frac{\partial^4 X_i}{\partial x^4} \cdot X_j \, dx + \sum_i \frac{\partial^2 q_i}{\partial t^2} \cdot \int_0^L \rho \cdot A \cdot X_i \cdot X_j \, dx + \\ &\sum_i \frac{\partial q_i}{\partial t} \cdot \int_0^L \eta \cdot X_i \cdot X_j \, dx = \int_0^L f_u \cdot X_j \, dx - \sum_i \frac{\partial q_i}{\partial t} \cdot \int_0^L Z \cdot X_i \cdot X_j \, dx\end{aligned} \tag{4.25}$$

in which L is the total length of the cantilever and the dependency of E, I, ρ, A and η on the spatial coordinate is implicit. The orthonormality condition specifies that

$$\int_0^L \rho \cdot A \cdot X_i \cdot X_j \, dx = \delta_{ij} \tag{4.26}$$

where δ_{ij} is the Kronecker delta. Using the relations given for the mode shapes in (4.6), this also results in

$$\int_0^L E \cdot I \cdot \frac{\partial^4 X_i}{\partial x^4} \cdot X_j = \hat{\omega}_i^2 \cdot \delta_{ij} \tag{4.27}$$

and hence (4.25) is rewritten as

$$\hat{\omega}_j^2 \cdot q_j + \ddot{q}_j + \sum_i \dot{q}_i \cdot \int_0^L \eta \cdot X_i \cdot X_j \, dx + \sum_i \dot{q}_i \cdot \int_0^L Z \cdot X_i \cdot X_j \, dx = \int_0^L f_u \cdot X_j \, dx \tag{4.28}$$

in which the dots on q show temporal derivatives. Moreover, as the Stokes' impedance can be written as $Z = Z_{re} + j\,\omega \cdot Z_{im}$ we have

$$\sum_i \dot{q}_i \cdot \int_0^L Z \cdot X_i \cdot X_j \, dx = \sum_i \dot{q}_i \cdot \int_0^L Z_{re} \cdot X_i \cdot X_j \, dx + \sum_i \ddot{q}_i \cdot \int_0^L Z_{im} \cdot X_i \cdot X_j \, dx \tag{4.29}$$

To seek an approximate solution one should truncate the series which leads to a set of coupled differential equations. However, when the coupling is weak one can use a further approximation and neglect it. The q is then obtained using

$$\left(1 + m_j\right) \ddot{q}_j + \left(1 + d_j\right) \dot{q}_j + \hat{\omega}_j^2 \cdot q_j = F_j \tag{4.30}$$

in which

$$m_j = \int_0^L Z_{re} \cdot X_j^2 \, dx, \qquad d_j = \int_0^L Z_{im} \cdot X_j^2 \, dx, \qquad F_j = \int_0^L f_u \cdot X_j \, dx \tag{4.31}$$

Note that each of these integrals have to be evaluated in both sections, e.g.

$$m_j = \int_0^{L_s} Z_{re1} \cdot X_{1j}^2 \, dx + \int_0^{L_h} Z_{re2} \cdot X_{2j}^2 \, dx \tag{4.32}$$

[1] B. Rama Bhat and H. Wagner, "Natural frequencies of a uniform cantilever with a tip mass slender in the axial direction," *Journal of Sound and Vibration,* vol. 45, pp. 304-307, 1976.

[2] R. E. Rossi and P. A. A. Laura, "Vibrations of a timoshenko beam clamped at one end and carrying a finite mass at the other," *Applied Acoustics,* vol. 30, pp. 293-301, 1990.

[3] L. Meirovitch, *Analytical Methods in Vibrations*. New York: The Macmillan Company, 1967.

[4] R. Bishop and D. Johnson, *The mechanics of vibration*. Cambridge: Cambridge university press, 1960.

[5] M. A. Koplow*, et al.*, "Closed form solutions for the dynamic response of Euler-Bernoulli beams with step changes in cross section," *Journal of Sound and Vibration,* vol. 295, pp. 214-225, 2006.

IV. On the fluid drag on a straight cylinder

Generally the in-line force on a straight stationary cylinder immersed in an oscillatory fluid and perpendicular to the velocity is described by the semi-empirical Morison equation [1]

$$F_H = \frac{1}{2}\rho \cdot D \cdot C_D \cdot U \cdot |U| + \frac{1}{4}\pi \rho \cdot D^2 \cdot C_M \cdot \frac{\partial U}{\partial t} \tag{5.1}$$

in which ρ is the density of the fluid, D is the diameter of the cylinder, U is the free stream velocity and C_D and C_M are the drag and inertia coefficients respectively. In case of an oscillatory cylinder in a stationary fluid, coefficient C_M is replaced by C_I which is called the coefficient of added mass and is related to inertia coefficient by

$$C_M = C_I + 1 \tag{5.2}$$

Various flow regimes has been observed, among others, by Tatsuno and Bearman [2] that depend on Keulegan-Carpenter number and Reynolds number or Stokes number. These parameters are defined as

$$KC = \frac{U_m \cdot T}{D}$$
$$Re = \frac{U_m \cdot D}{\nu} \tag{5.3}$$
$$\beta = \frac{Re}{KC} = \frac{D^2}{\nu \cdot T}$$

in which U_m is the maximum flow velocity, T is the period of oscillation and ν is the kinematic viscosity of the fluid. Reynolds number shows the relative importance of inertia and to viscous forces. Equivalently one can use Strouhal number instead of Keulegan-Carpenter number which is defined as

$$St = \frac{2\pi}{KC} = \frac{\omega \cdot D}{U} \tag{5.4}$$

and indicates the importance of local inertia forces relative to convective inertia forces. Figure 6 shows the magnitude of these parameters. The blue solid line and the green dashed line are for a cylindrical structure of diameter 6 and 50 μm respectively.

For an oscillatory flow, it is β which plays the same rule ($\pi\beta/2$ is sometimes called the kinetic Reynolds number). When β is very large the viscous forces are

negligible and the flow is considered inviscid for any practical case. In case that β is very small, the analytical expression for drag and inertia coefficients first provided by Stokes [3] which was presented and discussed in chapter 3. Wang [4] has extended the Stokes analysis and shown that

$$C_D = \frac{3\pi^3}{2KC}\cdot\left((\pi\beta)^{-\frac{1}{2}} + (\pi\beta)^{-1} - \frac{(\pi\beta)^{-\frac{3}{2}}}{4}\right) \tag{5.5}$$

$$C_M = 2 + 4(\pi\beta)^{-\frac{1}{2}} + (\pi\beta)^{-\frac{3}{2}}$$

When $Re \ll 1$ and $\beta \gg 1$.

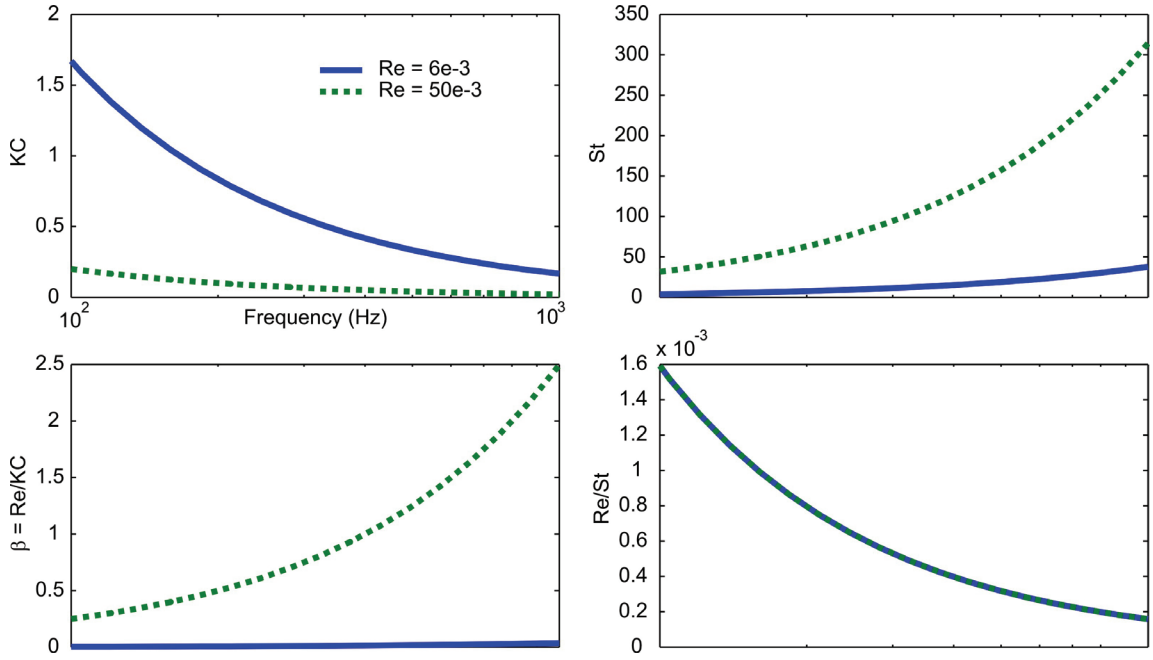

Figure 6 *The important parameters for hydrodynamic behaviour of an immersed cylinder*

It is clear from Figure 6 that at higher frequencies the Stokes analysis is only valid for cylindrical structures with very small diameter. As the diameter becomes larger the Strouhal number grows rapidly and the condition is not satisfied anymore (for more discussion see [4, 5]).

The diameter of the fabricated MEMS structures is determined by technologically limited maximum aspect ratio in lithography process. That is, to achieve a longer cylindrical hair-structure (which penetrates further into and above the boundary layer and hence provides larger drag induced torque) the diameter of the

structure is about 40 to 50 μm as has been discussed in chapters 3 and 4. Consequently, the Stokes' analysis, in spite of the fact that it results in a more or less correct qualitative measure of the frequency response, greatly underestimates the quantitative behaviour.

For a large Strouhal number, the governing continuity and Navier-Stokes equations are written as

$$\begin{aligned} &\nabla \cdot \vec{V} = 0 \\ &\rho \cdot \frac{\partial \vec{V}}{\partial t} = -\nabla P + \mu \cdot \nabla^2 \vec{V} \end{aligned} \tag{5.6}$$

where V is the velocity vector, P is the pressure, ρ and μ are the density and absolute viscosity of the fluid and t is the time. Note that the nonlinear convective inertial term and gravity are neglected in (5.6). When the amplitude of oscillation is much smaller than the characteristic length of the flow (i.e. the radius of the cylinder), the force per unit length of an oscillating cylinder in an otherwise still fluid is given by [6]

$$F_H' = \pi \cdot \rho \cdot \frac{D^2}{4} \cdot \omega \cdot \Gamma(\omega) \cdot U \tag{5.7}$$

in which Γ is called the "hydrodynamic function" and given by

$$\Gamma(\omega) = j \cdot \left(1 + \frac{4 K_1\left(\sqrt{j \cdot \beta'}\right)}{\sqrt{j \cdot \beta'} \cdot K_0\left(\sqrt{j \cdot \beta'}\right)} \right) \tag{5.8}$$

where $\beta' = \pi \beta / 2$ and K_0 and K_1 are modified Bessel functions of the second kind. Considering the real and imaginary parts of the hydrodynamic function, $\Gamma = \Gamma' + j\Gamma''$, and comparing the results to (5.1) one will get

$$\begin{aligned} C_D &= \frac{\pi D \cdot \omega \cdot \Gamma'}{2 U_m} = \frac{\pi^2}{KC} \cdot \Gamma' \\ C_M &= 1 + \Gamma'' \end{aligned} \tag{5.9}$$

Figure 7 shows the real and imaginary part of the flow impedance derived from Stokes (see chapter 3) and Rosenhead theories. It can be easily shown that at higher frequencies, Wang estimation is in very good agreement with (5.9).

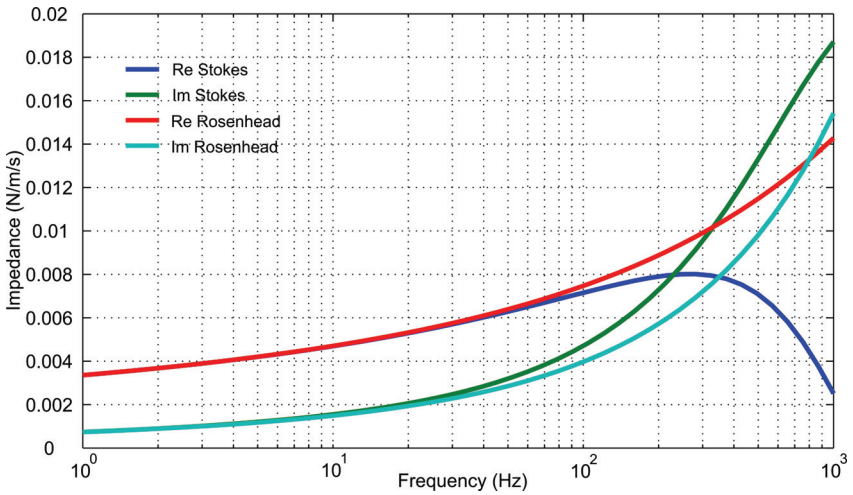

Figure 7 *Comparison between Stokes' and Rosenhead's theory*

[1] J. R. Morison, *et al.*, "The Force Exerted by Surface Waves on Piles," *Petroleum Transactions, AIME,* vol. 189, pp. 149-154, 1950.

[2] M. Tatsuno and P. W. Bearman, "A visual study of the flow around an oscillating circular cylinder at low Keulegan-Carpenter numbers and low Stokes numbers," *Journal of Fluid Mechanics,* vol. 211, pp. 157-182, 1990.

[3] G. G. Stokes, "On the effect of the internal friction of fluids on the motion of pendulums," *Transactions of the Cambridge Philosophical Society,* vol. 9, pp. 8-106, 1851.

[4] C.-Y. Wang, "On high-frequency oscillatory viscous flows," *Journal of Fluid Mechanics Digital Archive,* vol. 32, pp. 55-68, 1968.

[5] J. A. C. Humphrey, *et al.*, "Dynamics of Arthropod Filiform Hairs. I. Mathematical Modelling of the Hair and Air Motions," *Philosophical Transactions: Biological Sciences,* vol. 340, pp. 423-444, 1993.

[6] Y. Shi and J. E. Sader, "Lattice Boltzmann method for oscillatory Stokes flow with applications to micro- and nanodevices," *Physical Review E,* vol. 81, p. 036706, 2010.

V. Process Documents

Table I. *The process document for closed membrane fabrication*

Step	Process	Parameters	Remarks
01	Substrate selection - Silicon <100> DSP (low resistance)	Orientation: <100> Diameter: 100mm Thickness: 525 +/- 25 µm Polished: Double side Resistivity: 0.010-0.015 Ω·cm Type: p	To be used as common electrode Use at least 6 dummy wafers (SSP)
02	Wafer thickness measurement	HeidenHahn	
03	Cleaning Standard	HNO_3 (100%) Selectipur: MERCK HNO_3 (69%) VLSI: MERCK • Beaker 1: fumic HNO_3 (100 %), 5 min • Beaker 2: fumic HNO_3 (100 %), 5 min • Quick Dump Rinse <0.1 µS • Beaker 3: boiling (95 °C) HNO_3 (69 %), 10 min • Quick Dump Rinse <0.1 µS • Spin drying	Start from beaker 2
04	Lithography - Priming (liquid)	HexaMethylDiSilazane (HMDS) • Dehydration bake (120 °C): 5 min • Spin program: 4 (4000 rpm, 20 sec)	
05	Lithography - Coating Olin907-17	• Spinning acceleration: 4000 rpm/s • Spinning speed: 4000 rpm • Spinning time: 20 s • Prebake (95 °C): 90 s	Wait 30 min before exposure to avoid stiction
06	Lithography - Alignment & Exposure Olin 907-17 (EVG 20)	Electronic Vision Group 20 Mask Aligner • Hg-lamp: 12 mW/cm² • Exposure Time: 3.5 sec	Mask: FrontHole Soft contact
07	Lithography - Development Olin Resist	Developer: OPD4262 • After Exposure Bake (120 °C): 60 sec Development: • Time: 30 sec in Beaker 1 • Time: 15-30 sec in Beaker 2 • Quick Dump Rinse <0.1 µS • Spin drying	No Post Bake required because reflow of the resist decreases the resolution
08	Optical microscopic inspection - Lithography	Microscope	
09	Plasma etching of Si B-ADIX	Adixen AMS 100 SE See MIS homepage for etch profile	Depth: 60 to 70 µm Etch rate must be determined in each run

<table>
<tr><td></td><td></td><td><table>
<tr><th>Parameters</th><th>Etch</th><th>Deposition</th></tr>
<tr><td>Gas</td><td>SF_6</td><td>C_4F_8</td></tr>
<tr><td>Flow(sccm)</td><td>300</td><td>150</td></tr>
<tr><td>Time sec</td><td>7</td><td>2</td></tr>
<tr><td>Priority</td><td>2</td><td>1</td></tr>
<tr><td>APC %</td><td>25</td><td>25</td></tr>
<tr><td>ICP Watt</td><td>1800</td><td>1800</td></tr>
<tr><td>CCP Watt (LF)</td><td>80</td><td>80</td></tr>
<tr><td>Pulsed (LF) ms.</td><td>10on/90off</td><td>10on/90off</td></tr>
<tr><td>He mBar</td><td>10</td><td>10</td></tr>
<tr><td>SH mm</td><td>200</td><td>200</td></tr>
<tr><td>Electrode temp.°C.</td><td>10</td><td>10</td></tr>
</table></td><td>Use patterned dummy wafers
Uniformity is important
Time: ~to be determined at each run (use highly doped dummies)</td></tr>
<tr><td>10</td><td>Stripping of Olin PR by oxygen plasma</td><td>Tepla 300
Barrel Etcher (2.45 GHz)
Ultra clean system only (no metals except Al)
• See list with recipes in CR
• O_2 flow: 200 sccm (50 %)
• Power: up to 1000 W
• Pressure: 1 mbar
• Time: see recipes on the wall</td><td>Program 06</td></tr>
<tr><td>11</td><td>Cleaning Standard</td><td>HNO_3 (100%) Selectipur: MERCK
HNO_3 (69%) VLSI: MERCK
• Beaker 1: fumic HNO_3 (100 %), 5 min
• Beaker 2: fumic HNO_3 (100 %), 5 min
• Quick Dump Rinse <0.1 µS
• Beaker 3: boiling (95 °C) HNO_3 (69 %), 10 min
• Quick Dump Rinse <0.1 µS
• Spin drying</td><td></td></tr>
<tr><td>12</td><td>Dry Oxidation (DOX) at 800 °C of Silicon</td><td>Standby temperature: 800°C
• Program: DOX-800
• Temp.: 800°C
• Gas: O_2
• Flow: 4 l/min</td><td>For Fluorocarbon removal
Time: 30 min in B3</td></tr>
<tr><td>13</td><td>Etching HF (50%) SiO_2</td><td>HF (50%) VLSI: MERCK
• Etch time: >1 min
• Quick Dump Rinse <0.1 µS
• Spin drying</td><td>For Fluorocarbon removal
Time: ~1 min</td></tr>
<tr><td>14</td><td>Dry Oxidation (DOX) at 1100 °C of Silicon</td><td>Standby temperature: 800 °C
• Program: DOX-1100
• Temp.: 1100 °C
• Gas: O_2
• Flow: 4 l/min</td><td>Thickness: 100 nm
Time: ~42 min
Or Wet Oxidation at 900 °C for ~53 min (Check water level and temperature of bubbler)</td></tr>
</table>

15	Ellipsometer Measurement	Thin Film Mapper	
16	LPCVD Si_3N_4 stoichiometric	Tempress LPCVD F1 Tube: F1 • Program: Nitr01 • SiH_2Cl_2 flow: 22 sccm • NH_3 flow: 66 sccm • Temperature: 800 °C • Pressure: 200 mTorr • Stress: 1,09±40 MPa Deposition rate: 4-6 nm/min N_f: 2.008	Use blank dummies Thickness: 30 nm Time: ~5:30 min Having 100 nm of dry oxide the color is turquoise Stoichiometric nitride has less oxidation rate
17	Ellipsometer Measurement	Thin Film Mapper	On blank dummies
18	Micro Balance Measurement	Satotius Micro Balance	
19	LPCVD Poly Si - 590°C	Tempress LPCVD/HC Tube: G1 • SiH_4 flow: 50 sccm • Temperature: 590 °C • Pressure: 250 mTorr • Program: Poly590C Deposition rate: 5.5-7.5 nm/min	Use blank dummies Two days deposition Thickness: 3 µm It must just close the trenches! With F2, 15h, 3.3 nm/min
20	Micro Balance Measurement	Satotius Micro Balance	For 4" wafer poly deposition $\delta(nm)=26.5\times\Delta m(mg)$
21	Annealing	Furnace B3 Standby temperature: 800 °C • Program: ANN-1100-N_2 • Temp.: 1100 °C • Gas: N_2 • Flow: 1 l/min • Ramp: 20 °C/min	To lower stress Time: 2 hrs
22	Wet Oxidation of Silicon at 1150°C	Furnace B2 Standby temperature: 800 °C Check water level of bubbler • Program: WET1150B • Temp.: 1150 °C • Gas: $H_2O + N_2$ (Bubbler)	Check water level and temperature of the bubbler To decrease the gap
23	Micro Balance Measurement	Satotius Micro Balance	For 4" wafer poly deposition $\delta(nm)=26.5\times\Delta m(mg)$ Repeat 22 until the desired thickness is reached
24	Cleaning Standard	HNO_3 (100%) Selectipur: MERCK HNO_3 (69%) VLSI: MERCK • Beaker 1: fumic HNO_3 (100 %), 5 min • Beaker 2: fumic HNO_3 (100 %), 5 min • Quick Dump Rinse <0.1 µS	

<table>
<tr><td></td><td></td><td>• Beaker 3: boiling (95 °C) HNO_3 (69 %), 10 min
• Quick Dump Rinse <0.1 µS
• Spin drying</td><td></td></tr>
<tr><td>25</td><td>Lithography - dehydration SU-8</td><td>Hotplate
• 2 hrs at 120 °C</td><td>Time: 10-30 min</td></tr>
<tr><td>26</td><td>Lithography - Coating SU-8 2 (Delta20)</td><td>Süss MicroTec Spinner Delta 20
• Spin program: 5
10 sec at 500 rpm, acc. 100 rpm/min
30 sec at 3000 rpm, acc. 100 rpm/min
• Thickness: 2 µm
• Prebake (95 °C): 2 min</td><td>Wait 1 hr before exposure to avoid stiction</td></tr>
<tr><td>27</td><td>Lithography - Alignment & Exposure SU-8 2 (EVG)</td><td>Electronic Vision Group 20 Mask Aligner
• Hg-lamp: 12 mW/cm²
• Exposure Time: 10 sec</td><td>Mask: Rim
Soft contact</td></tr>
<tr><td>28</td><td>Lithography - Development SU-8 2</td><td>Developer: RER600
• After Exposure Bake (95 °C): 2 min
Development:
• Time: 20 sec
• Method: Immersion
• IPA Rinse
• Spin drying</td><td></td></tr>
<tr><td>29</td><td>Plasma cleaning (Etske)</td><td>Elektrotech PF310/340
Clean chamber
Styros electrode
• Electrode temp.: 10 °C
• O_2 flow: 20 sccm
• Pressure: 0 mTorr
• Power: 50 W
Etch rate SU-8 = 150 nm/min</td><td>Removal of Residues
Time: 4:15 min:sec</td></tr>
<tr><td>30</td><td>Optical microscopic inspection - Lithography</td><td>Microscope</td><td>Check; if SU-8 residues are in the lines do previous step again</td></tr>
<tr><td>31</td><td>Plasma etching of Si B-HARS-1</td><td>Adixen AMS 100 SE
See MIS homepage for etch profile
<table><tr><th>Parameters</th><th>Etch</th><th>Deposition</th></tr><tr><td>Gas</td><td>SF_6</td><td>C_4F_8</td></tr><tr><td>Flow(sccm)</td><td>250</td><td>200</td></tr><tr><td>Time sec</td><td>3</td><td>1</td></tr><tr><td>Priority</td><td>2</td><td>1</td></tr><tr><td>APC %</td><td>100</td><td>100</td></tr><tr><td>ICP Watt</td><td>1500</td><td>1500</td></tr><tr><td>CCP Watt (LF)</td><td>80</td><td>80</td></tr><tr><td>Pulsed (LF) ms.</td><td>10on/90off</td><td>10on/90off</td></tr><tr><td>He mBar</td><td>10</td><td>10</td></tr></table></td><td>Or B-ADIX
Depth: ~3 µm; to reach the Si_3N_4 underneath
Etch rate must be determined in each run!
Use patterned dummy wafers
Uniformity is important
Time: ~71 s (depends on the thickness)
It is not critical if etch into silicon substrate</td></tr>
</table>

		<table><tr><td>SH mm</td><td>200</td><td>200</td></tr><tr><td>Electrode temp.°C.</td><td>10</td><td>10</td></tr><tr><td>Er Olin907</td><td>25-50 nm/min</td><td></td></tr><tr><td>Er silicon</td><td>1-5 µm/min</td><td></td></tr></table>	
32	Stripping of Olin PR by oxygen plasma	Tepla 300 Barrel Etcher (2.45 GHz) Ultra clean system only (no metals except Al) • See list with recipes in CR • O_2 flow: 200 sccm (50 %) • Power: up to 1000 W • Pressure: 1 mbar • Time: see recipes on the wall		Program 06
33	Cleaning Standard	HNO_3 (100%) Selectipur: MERCK HNO_3 (69%) VLSI: MERCK • Beaker 1: fumic HNO_3 (100 %), 5 min • Beaker 2: fumic HNO_3 (100 %), 5 min • Quick Dump Rinse <0.1 µS • Beaker 3: boiling (95 °C) HNO_3 (69 %), 10 min • Quick Dump Rinse <0.1 µS • Spin drying		
34	Dry Oxidation (DOX) at 800 °C of Silicon	Standby temperature: 800°C • Program: DOX-800 • Temp.: 800°C • Gas: O_2 • Flow: 4 l/min		For Fluorocarbon removal Time: 30 min in B3
35	Etching HF (1%)	HF (1%) VLSI: MERCK • Quick Dump Rinse <0.1 µS • Spin drying		For Fluorocarbon removal Time: ~1 min
36	LPCVD SiRN - low stress	Tempress LPCVD/HC Tube: G3 • SiH_2Cl_2 flow: 70 sccm • NH_3 flow: 18 sccm • Temperature: 830 °C • Pressure: 200 mTorr • Program: SiRN01 Deposition rate: 3.9~5.3 nm/min N_f: 2.14		Thickness: >1.5 µm Time: ~5:30 hr:min
37	Plasma etching SiN (Etske)	Elektrotech PF310/340 Dirty chamber Styros electrode • Electrode temp.: 10 °C • CHF_3 flow: 25 sccm • O_2 flow: 5 sccm • Pressure: 10 mTorr • Power: 75 W Etchrate SiN = 50 nm/min (for V_{DC}=-460V) Etchrate Olin resist = 95 nm/min If DC-Bias < 375V apply chamber clean		Backside Etch rate: 58 nm/min Time: 25 min

38	Plasma etching of polysilicon on SiO_2 (Etske)	Elektrotech PF310/340 Clean chamber Styros electrode • Electrode temp.: 10 °C • SF_6 flow: 30 sccm • CHF_3 flow: 7 sccm • O_2 flow: 11 sccm • Pressure: 100 mTorr • Power: 75 W Use etch steps of maximal 5 min. Vent system and continue. Small gaps exhibit RIE-lag!	Backside Etch rate: 58 nm/min Time: ~5:00 min:sec (depends on the thickness) Wait till Poly goes completely (it is visible) and a dark ring starts from outer edge.
39	Plasma etching SiN (Etske)	Elektrotech PF310/340 Dirty chamber Styros electrode • Electrode temp.: 10 °C • CHF_3 flow: 25 sccm • O_2 flow: 5 sccm • Pressure: 10 mTorr • Power: 75 W Etchrate SiN = 50 nm/min (for V_{DC}=-460V) Etchrate Olin resist = 95 nm/min If DC-Bias < 375V apply chamber clean	Backside Etch rate: 58 nm/min Time: 5 min
40	Cleaning Standard	HNO_3 (100%) Selectipur: MERCK HNO_3 (69%) VLSI: MERCK • Beaker 1: fumic HNO_3 (100 %), 5 min • Beaker 2: fumic HNO_3 (100 %), 5 min • Quick Dump Rinse <0.1 µS • Beaker 3: boiling (95 °C) HNO_3 (69 %), 10 min • Quick Dump Rinse <0.1 µS • Spin drying	
41	Dry Oxidation (DOX) at 800 °C of Silicon	Standby temperature: 800°C • Program: DOX-800 • Temp.: 800°C • Gas: O_2 • Flow: 4 l/min	For Fluorocarbon removal Time: 30 min in B3
42	Etching HF (50%) SiO_2	HF (50%) VLSI: MERCK • Etch time: >1 min • Quick Dump Rinse <0.1 µS • Spin drying	For Fluorocarbon removal Time: ~1 min The backside may not show hydrophobicity due to roughness
43	Lithography - dehydration SU-8	Hotplate • 2 hrs at 120 °C	Time: 10-30 min Or use positive resist as an alternative (see below)
44	Lithography - Coating SU-8 5 (Delta20)	Süss MicroTec Spinner Delta 20 • Spin program: 5 10 sec at 500 rpm, acc. 100 rpm/min 30 sec at 3000 rpm, acc. 100 rpm/min • Thickness: 5 µm • Prebake:	Backside Wait >2 hr before exposure to avoid stiction

<table>
<tr><td></td><td></td><td>1 min at 50 °C
1 min at 65 °C
3 min at 95 °C
let it cool down on the hot plate</td><td></td></tr>
<tr><td>45</td><td>Lithography - Alignment & Exposure SU-8 5 (EVG)</td><td>Electronic Vision Group 20 Mask Aligner
• Hg-lamp: 12 mW/cm²
• Exposure Time: 10 sec</td><td>Mask: BackHole
Backside alignment
Soft contact</td></tr>
<tr><td>46</td><td>Lithography - Development SU-8 5</td><td>Developer: RER600
• After Exposure Bake:
1 min at 50 °C
1 min at 65 °C
3 min at 95 °C
let it cool down on the hot plate
Development:
• Time: 2 min
• Method: Immersion
• IPA Rinse
• Spin drying</td><td></td></tr>
<tr><td>47</td><td>Optical microscopic inspection - Lithography</td><td>Microscope</td><td>Backside</td></tr>
<tr><td>48</td><td>Plasma etching of Si Pulsed CHF_3</td><td>CR125c/Adixen AMS 100 SE
See MIS homepage for etch profile
<table><tr><th>Parameters</th><th>Etch</th><th>Deposition</th></tr><tr><td>Gas</td><td>SF_6</td><td>CHF_3</td></tr><tr><td>Flow sccm</td><td>400</td><td>200</td></tr><tr><td>Time sec</td><td>4</td><td>0.5</td></tr><tr><td>Priority</td><td>2</td><td>1</td></tr><tr><td>APC %</td><td>15</td><td>15</td></tr><tr><td>ICP Watt</td><td>2500</td><td>2500</td></tr><tr><td>CCP Watt (LF)</td><td>20</td><td>20</td></tr><tr><td>Pulsed (LF) ms.</td><td>20on/180off</td><td>20on/180off</td></tr><tr><td>He mBar</td><td>10</td><td>10</td></tr><tr><td>SH mm</td><td>110</td><td>110</td></tr><tr><td>Electrode temp.°C.</td><td>-110</td><td>-110</td></tr><tr><td>Er Olin907</td><td><38 nm/min</td><td></td></tr><tr><td>Er silicon</td><td>10-20 µm/min</td><td></td></tr></table></td><td>Backside
Depth: ~460um (calculate according to front etch and the thickness of the wafer)
At first increase the CCP power to 50 for 1 min and then set it to 20
It is better not to etch continuously! Etch 30 min, take the wafer out, wait, and continue to etch again!</td></tr>
<tr><td>49</td><td>Stripping of Olin PR by oxygen plasma</td><td>Tepla 300
Barrel Etcher (2.45 GHz)
Ultra clean system only (no metals except Al)
• See list with recipes in CR
• O_2 flow: 200 sccm (50 %)
• Power: up to 1000 W
• Pressure: 1 mbar</td><td>Program 06</td></tr>
</table>

		• Time: see recipes on the wall	
50	Cleaning Standard	HNO_3 (100%) Selectipur: MERCK HNO_3 (69%) VLSI: MERCK • Beaker 1: fumic HNO_3 (100 %), 5 min • Beaker 2: fumic HNO_3 (100 %), 5 min • Quick Dump Rinse <0.1 µS • Beaker 3: boiling (95 °C) HNO_3 (69 %), 10 min • Quick Dump Rinse <0.1 µS • Spin drying	NO Fluorocarbon removal after this step since it will remove oxide of protection stack!
51	Wet Oxidation (WOX) at 1150°C of Silicon	Furnace B2 Standby temperature: 800 °C Check water level of bubbler • Program: WOX-1150 • Temp.: 1150 °C • Gas: $H_2O + N_2$ (Bubbler)	Check water level and temperature of the bubbler Thickness: ~800 nm Time: ~90 min
52	Plasma etching of SiN	Plasma Therm 790 • Alumnium electrode • Electrode temp.: 20 °C • CHF3: 27 sccm • O_2: 12 sccm • Pressure: 20 mTorr • Power: 350 Watt Silicon: 10 nm/min SiO_2: 34 nm/min SiN: 34 nm/min	Front side Use end point detection (1:30 to 2 min low etch rate of oxidized nitride) Etch rate: 52 nm/min
53	Lithography - Coating Olin907-17	• Spinning acceleration: 4000 rpm/s • Spinning speed: 4000 rpm • Spinning time: 20 s • Prebake (95 °C): 90 s	Wait 30 min before exposure to avoid stiction
54	Lithography - Alignment & Exposure Olin 907-17 (EVG 20)	Electronic Vision Group 20 Mask Aligner • Hg-lamp: 12 mW/cm² • Exposure Time: 3.5 sec	Mask: Electrodes Soft contact
55	Lithography - Development Olin Resist	Developer: OPD4262 • After Exposure Bake (120 °C): 60 sec Development: • Time: 30 sec in Beaker 1 • Time: 15-30 sec in Beaker 2 • Quick Dump Rinse <0.1 µS • Spin drying	No Post Bake required because reflow of the resist decreases the resolution
56	Optical microscopic inspection - Lithography	Microscope	
57	Sputtering of Al, resist compatible (Oxford)	Oxford PL 400 • Program: 100 nm Al pos 1 Change program parameters to: • Power: 700W • Pressure: 10 mTorr Deposition rate (100 mm wafer): 88 nm/min	Thickness: 100 nm Or sputterke 10 nm/min
58	Lithography - Lift-off	Aceton: Technical	We use lift-off to have ears

		IPA VLSI: MERCK • Beaker 1: Aceton, > 10 min • Beaker 2: Aceton, >10 min • Beaker 3: Isopropanol > 10min • Spin drying	as a clamp to SU-8 Use ultrasonic bath
59	Cleaning Short	HNO_3 (100%) Selectipur: MERCK HNO_3 (69%) VLSI: MERCK • Beaker 1: fumic HNO_3 (100 %), 5 min • Beaker 2: fumic HNO_3 (100 %), 5 min • Quick Dump Rinse <0.1 µS • Quick Dump Rinse <0.1 µS • Spin drying	
60	Oxygen plasma cleaning	Tepla 300 Barrel Etcher (2.45 GHz) Ultra clean system only (no metals except Al) • See list with recipes in CR • O_2 flow: 200 sccm (50 %) • Power: up to 1000 W • Pressure: 1 mbar • Time: see recipes on the wall	Program 04 Time: 10 min
61	Lithography - dehydration SU-8	Hotplate • 2 hrs at 120 °C	Time: 10-15 min
62	Lithography - Coating SU-8 2000.5 (Delta20)	Süss MicroTec Spinner Delta 20 • Spin program: 5 10 sec at 500 rpm, acc. 100 rpm/min 30 sec at 3000 rpm, acc. 100 rpm/min • Thickness: 2 µm • Prebake (95 °C): 2 min	Wait 1 hr before exposure to avoid stiction
63	Lithography - Alignment & Exposure SU-8 2000.5 (EVG)	Electronic Vision Group 20 Mask Aligner • Hg-lamp: 12 mW/cm² • Exposure Time: >12 sec	Mask: BondPads Soft contact
64	Lithography - Development SU-8 2000.5	Developer: RER600 • After Exposure Bake (95 °C): 2 min Development: • Time: 20 sec • Method: Immersion • IPA Rinse • Spin drying	Do not rinse with water
65	Lithography - Coating SU-8 100 (Delta20)	Süss MicroTec Spinner Delta 20 • Spin program: 5 30 sec at 500 rpm, acc. 100 rpm/min 30 sec at 3000 rpm, acc. 100 rpm/min • Thickness: >380 µm • Prebake (95 °C): 10 min at 50 °C 30 min at 65 °C 300 min at 95 °C let it cool down on the hot plate	First Layer Leave the wafers on the flat surface of the hot plate for 2 hrs before soft bake Wait overnight before exposure to avoid stiction (and use tape on the mask)
66	Lithography - Alignment &	Electronic Vision Group 20 Mask Aligner • Hg-lamp: 12 mW/cm²	Mask: Hair I

<table>
<tr><td></td><td>Exposure SU-8 100 (EVG)</td><td>• Exposure Time: 60 sec</td><td>Soft contact</td></tr>
<tr><td>67</td><td>Lithography - Coating SU-8 100 (Delta20)</td><td>Süss MicroTec Spinner Delta 20
• Spin program: 5
30 sec at 500 rpm, acc. 100 rpm/min
30 sec at 3000 rpm, acc. 100 rpm/min
• Thickness: >380 µm
• Prebake (95 °C):
10 min at 50 °C
30 min at 65 °C
300 min at 95 °C
let it cool down on the hot plate</td><td>Second Layer
Leave the wafers on the flat surface of the hot plate for 2 hrs before soft bake
Wait overnight before exposure to avoid stiction (and use tape on the mask)</td></tr>
<tr><td>68</td><td>Lithography - Alignment & Exposure SU-8 100 (EVG)</td><td>Electronic Vision Group 20 Mask Aligner
• Hg-lamp: 12 mW/cm^2
• Exposure Time: 60 sec</td><td>Mask: Hair II
Soft contact</td></tr>
<tr><td>69</td><td>Lithography - Development SU-8 100</td><td>Developer: RER600
• After Exposure Bake:
10 min at 50 °C
10 min at 65 °C
50 min at 75 °C
cool down in 5 °C steps each for 5 min
Development:
• Time: 20 min
• Method: Spray
• IPA Rinse
• Spin drying</td><td>Do not rinse with water
Do not use high speed spin drying</td></tr>
<tr><td>70</td><td>Plasma etching of poly-Silicon (Oxford Plasma Lab 100)</td><td>Oxford Plasma Lab 100
<table><tr><th>Parameters</th><th>Value</th></tr><tr><td>SF_6 (sccm)</td><td>120</td></tr><tr><td>He (sccm)</td><td>20</td></tr><tr><td>ICP (W)</td><td>600</td></tr><tr><td>CCP (W)</td><td>0</td></tr><tr><td>Pressure (mTorr)</td><td>15</td></tr><tr><td>Eelctrode temp. (°C)</td><td>20</td></tr><tr><td>Etch rate SiO_2 (µm/min)</td><td></td></tr><tr><td>Etch rate Olin 907 (µm/min)</td><td></td></tr><tr><td>Etch rate poly-Silicon (µm/min)</td><td></td></tr><tr><td>Etch rate SiRN (µm/min)</td><td></td></tr></table></td><td>Isotropic step
Use Special Holder to put the wafer upside down
V_{DC}=0
Time: ~6 hrs
Use steps of maximum 2 hrs and repeat until the membranes are free (~3 times)</td></tr>
<tr><td></td><td></td><td></td><td></td></tr>
</table>

Table II. *The process document for fabrication of canal embedded hairs*

Step	Process	Parameters	Remarks
01	Substrate selection - Silicon <100> SSP (low resistance)	Orientation: <100> Diameter: 100mm Thickness: 525 +/- 25 µm Polished: Single side Resistivity: 0.010-0.015 Ω·cm Type: p	Substrate should be grounded Number of Dummies: ?
02	Cleaning Standard	HNO_3 (100%) Selectipur: MERCK HNO_3 (69%) VLSI: MERCK • Beaker 1: fumic HNO_3 (100 %), 5 min • Beaker 2: fumic HNO_3 (100 %), 5 min • Quick Dump Rinse <0.1 µS • Beaker 3: boiling (95 °C) HNO_3 (69 %), 10 min • Quick Dump Rinse <0.1 µS • Spin drying	Start from beaker 2
03	Etching HF (50%) SiO_2	HF (50 %) VLSI: MERCK • Etch time: >1 min • Quick Dump Rinse <0.1 µS • Spin drying	
04	Dry Oxidation of Silicon at 800°C	Furnace B3 Standby temperature: 800 °C • Program: DOX-800 • Temp.: 800 °C • Gas: O_2 • Flow: 4 l/min	Electrical isolation layer Thickness: >100 nm
05	Ellipsometer Measurement	Thin Film Mapper	
06	Micro Balance Measurement	Satotius Micro Balance	
07	Cleaning Standard	HNO_3 (100%) Selectipur: MERCK HNO_3 (69%) VLSI: MERCK • Beaker 1: fumic HNO_3 (100 %), 5 min • Beaker 2: fumic HNO_3 (100 %), 5 min • Quick Dump Rinse <0.1 µS • Beaker 3: boiling (95 °C) HNO_3 (69 %), 10 min • Quick Dump Rinse <0.1 µS • Spin drying	
08	LPCVD Poly Si - 590°C	Tempress LPCVD Tube: F2 Program: senspoly • SiH_4 flow: 50 sccm • Temperature: 590 °C • Pressure: 250 mTorr • Deposition rate: 3.3 nm/min • Stress: 30 MPa	Thickness: 200 nm
09	Micro Balance	Satotius Micro Balance	For 4" wafer poly deposition

	Measurement		$\delta(nm)=26.5\times\Delta m(mg)$
10	Annealing	Furnace B3 Standby temperature: 800 °C • Program: ANN1100C • Temp.: 1100°C • Gas: N_2 • Flow: 1 l/min • Ramp: 20 °C/min	To lower stress Time: 2 hrs
11	Etching HF (1%) Native Oxide	HF (1%) VLSI: MERCK • Etch time: >1 min • Quick Dump Rinse <0.1 µS • Spin drying	
12	Solid Source Diffusion (SSD) of Boron at 1100°C	Furnace B1 Standby temperature: 700 °C • Program: SSD-1100 • Temp.: 1100 °C • Gas N_2: 3.80 SLM • Gas O_2: 0.20 SLM • Time:	Time: 60 min
13	Etching BHF (1:7) SiO_2	NH_4F:HF (1:7) VLSI: MERCK • Quick Dump Rinse <0.1 µS • Spin drying Etch rate thermal SiO_2 = 60-80 nm/min Etch rate PECVD SiO_2 = 125 nm/min Etch rate TEOS SiO_2 = 180 nm/min	10 min, wafer should be white and no colour rings should be present (B_2O_5 removal) Time: ~1 hr
14	Cleaning Standard	HNO_3 (100%) Selectipur: MERCK HNO_3 (69%) VLSI: MERCK • Beaker 1: fumic HNO_3 (100 %), 5 min • Beaker 2: fumic HNO_3 (100 %), 5 min • Quick Dump Rinse <0.1 µS • Beaker 3: boiling (95 °C) HNO_3 (69 %), 10 min • Quick Dump Rinse <0.1 µS • Spin drying	
15	Dry Oxidation at 800°C of Silicon	Furnace B3 Standby temperature: 800 °C • Program: DOX-800 • Temp.: 800 °C • Gas: O_2 • Flow: 4 l/min	Removal of residues Time: 30 min
16	Etching BHF (1:7) SiO_2	NH_4F:HF (1:7) VLSI: MERCK • Quick Dump Rinse <0.1 µS • Spin drying Etch rate thermal SiO_2 = 60-80 nm/min Etch rate PECVD SiO_2 = 125 nm/min Etch rate TEOS SiO_2 = 180 nm/min	Time: 1 hour
17	Sheet Resistance measurement	Resistance Measurement Equipment	$R_{sheat}=R_{meas}\cdot\pi/\ln(2)=4.532\cdot R_{meas}\ \Omega/\square$ $\rho=R_{sheat}/\text{thikness}<0.02$

<table>
<tr><td></td><td></td><td></td><td>Ω·cm</td></tr>
<tr><td>18</td><td>Lithography - Priming (liquid)</td><td>HexaMethylDiSilazane (HMDS)
• Dehydration bake (120 °C): 5 min
• Spin program: 5 (5000 rpm, 20 sec)</td><td></td></tr>
<tr><td>19</td><td>Lithography - Coating Olin907-12</td><td>• Spinning acceleration: 4000 rpm/s
• Spinning speed: 5000 rpm
• Spinning time: 20 s
• Prebake (95 °C): 90 s</td><td>Wait 30 min before exposure to avoid stiction</td></tr>
<tr><td>20</td><td>Lithography - Alignment & Exposure Olin 907-12 (EVG 20)</td><td>Electronic Vision Group 20 Mask Aligner
• Hg-lamp: 12 mW/cm²
• Exposure Time: 3.5 sec</td><td>Mask: BottomElectrodes
Soft contact</td></tr>
<tr><td>21</td><td>Lithography - Development Olin Resist</td><td>Developer: OPD4262
• After Exposure Bake (120 °C): 60 sec
Development:
• Time: 30 sec in Beaker 1
• Time: 15-30 sec in Beaker 2
• Quick Dump Rinse <0.1 µS
• Spin drying</td><td>No Post Bake required because reflow of the resist decreases the resolution</td></tr>
<tr><td>22</td><td>Optical microscopic inspection - Lithography</td><td>Microscope</td><td></td></tr>
<tr><td>23</td><td>Plasma etching of Si
B-HARS-1</td><td>Adixen AMS 100 SE
See MIS homepage for etch profile
<table><tr><th>Parameters</th><th>Etch</th><th>Deposition</th></tr><tr><td>Gas</td><td>SF_6</td><td>C_4F_8</td></tr><tr><td>Flow(sccm)</td><td>250</td><td>200</td></tr><tr><td>Time sec</td><td>3</td><td>1</td></tr><tr><td>Priority</td><td>2</td><td>1</td></tr><tr><td>APC %</td><td>100</td><td>100</td></tr><tr><td>ICP Watt</td><td>1500</td><td>1500</td></tr><tr><td>CCP Watt (LF)</td><td>80</td><td>80</td></tr><tr><td>Pulsed (LF) ms.</td><td>10on/90off</td><td>10on/90off</td></tr><tr><td>He mBar</td><td>10</td><td>10</td></tr><tr><td>SH mm</td><td>200</td><td>200</td></tr><tr><td>Electrode temp.°C.</td><td>10</td><td>10</td></tr><tr><td>Er Olin907</td><td>25-50 nm/min</td><td></td></tr><tr><td>Er silicon</td><td>1-5 µm/min</td><td></td></tr></table></td><td>Or B-ADIX
Etch rate must be determined in each run!
Use patterned dummy wafers
Uniformity is important
Time: ~21 s (depends on the thickness)</td></tr>
<tr><td>24</td><td>Stripping of Olin PR by oxygen plasma</td><td>Tepla 300
Barrel Etcher (2.45 GHz)
Ultra clean system only (no metals except Al)
• See list with recipes in CR
• O_2 flow: 200 sccm (50 %)</td><td>Program 06</td></tr>
</table>

		• Power: up to 1000 W • Pressure: 1 mbar • Time: see recipes on the wall	
25	Cleaning Standard	HNO_3 (100%) Selectipur: MERCK HNO_3 (69%) VLSI: MERCK • Beaker 1: fumic HNO_3 (100 %), 5 min • Beaker 2: fumic HNO_3 (100 %), 5 min • Quick Dump Rinse <0.1 µS • Beaker 3: boiling (95 °C) HNO_3 (69 %), 10 min • Quick Dump Rinse <0.1 µS • Spin drying	
26	Etching HF (1%)	HF (1%) VLSI: MERCK • Quick Dump Rinse <0.1 µS • Spin drying	Time: >1 min
27	Wet Oxidation (WOX) at 900 °C of Silicon	Furnace B2 Standby temperature: 800 °C Check water level of bubbler • Program: WOX-900 • Temp.: 900 °C • Gas: $H_2O + N_2$ (Bubbler)	Check water level and temperature of the bubbler Thickness: 100 nm
28	LPCVD Poly Si - 590°C	Tempress LPCVD Tube: F2 Program: senspoly • SiH4 flow: 50 sccm • temperature: 590 °C • pressure: 250 mTorr • deposition rate: xx nm/min • Stress: 30 MPa	or a-Si, 550°C Thickness: 500 nm
29	Lithography - Coating Olin907-17	• Spinning acceleration: 4000 rpm/s • Spinning speed: 4000 rpm • Spinning time: 20 s • Prebake (95 °C): 90 s	Wait 30 min before exposure to avoid stiction
30	Lithography - Alignment & Exposure Olin 907-17 (EVG 20)	Electronic Vision Group 20 Mask Aligner • Hg-lamp: 12 mW/cm² • Exposure Time: 3.5 sec	Mask: Sacrificial Layer Soft contact
31	Lithography - Development Olin Resist	Developer: OPD4262 • After Exposure Bake (120 °C): 60 sec Development: • Time: 30 sec in Beaker 1 • Time: 15-30 sec in Beaker 2 • Quick Dump Rinse <0.1 µS • Spin drying	No Post Bake required because reflow of the resist decreases the resolution
32	Optical microscopic inspection - Lithography	Microscope	
33	Sputtering of Al, resist compatible (Oxford)	Oxford PL 400 • Program: 100 nm Al pos 1 Change program parameters to: • Power: 700W	Thickness: 100 nm

		• Pressure: 10 mTorr Deposition rate (100 mm wafer): 88 nm/min	
34	Lithography - Lift-off	Aceton: Technical IPA VLSI: MERCK • Beaker 1: Aceton, > 10 min • Beaker 2: Aceton, >10 min • Beaker 3: Isopropanol > 10min • Spin drying	We use lift-off to have ears as a clamp to SU-8 Use ultrasonic bath
35	Cleaning Short	HNO_3 (100%) Selectipur: MERCK HNO_3 (69%) VLSI: MERCK • Beaker 1: fumic HNO_3 (100 %), 5 min • Beaker 2: fumic HNO_3 (100 %), 5 min • Quick Dump Rinse <0.1 µS • Quick Dump Rinse <0.1 µS • Spin drying	
36	Lithography - dehydration SU-8	Hotplate • 2 hrs at 120 °C	Time: 30 min
37	Lithography - Coating SU-8 100 (Delta20)	Süss MicroTec Spinner Delta 20 • Spin program: 5 30 sec at 500 rpm, acc. 100 rpm/min 30 sec at 1000 rpm, acc. 100 rpm/min • Thickness: >380 µm • Prebake (95 °C): 10 min at 50 °C 30 min at 65 °C 300 min at 95 °C let it cool down on the hot plate	First Layer Leave the wafers on the flat surface of the hot plate for 2 hrs before soft bake Wait overnight before exposure to avoid stiction (and use tape on the mask)
38	Lithography - Alignment & Exposure SU-8 100 (EVG)	Electronic Vision Group 20 Mask Aligner • Hg-lamp: 12 mW/cm² • Exposure Time: 60 sec	Mask: Hair Soft contact
39	Lithography - Coating SU-8 100 (Delta20)	Süss MicroTec Spinner Delta 20 • Spin program: 5 30 sec at 500 rpm, acc. 100 rpm/min 30 sec at 2500 rpm, acc. 100 rpm/min • Thickness: >380 µm • Prebake (95 °C): 10 min at 50 °C 30 min at 65 °C 300 min at 95 °C let it cool down on the hot plate	Second Layer Leave the wafers on the flat surface of the hot plate for 2 hrs before soft bake Wait overnight before exposure to avoid stiction (and use tape on the mask)
40	Lithography - Alignment & Exposure SU-8 100 (EVG)	Electronic Vision Group 20 Mask Aligner • Hg-lamp: 12 mW/cm² • Exposure Time: 60 sec	Mask: Stem Soft contact PEB is done later
41	Sputtering of Al, resist compatible (Oxford)	Oxford PL 400 • Program: 100 nm Al pos 1 Change program parameters to: • Power: 700W • Pressure: 10 mTorr Deposition rate (100 mm wafer): 88 nm/min	Thickness: 100 nm If necessary reduce the power

42	Lithography - Priming (liquid)	HexaMethylDiSilazane (HMDS) • Dehydration bake (120 °C): 5 min • Spin program: 5 (5000 rpm, 20 sec)	
43	Lithography - Coating Olin907-12	• Spinning acceleration: 4000 rpm/s • Spinning speed: 5000 rpm • Spinning time: 20 s • Prebake (95 °C): 90 s	Do NOT bake Leave wafers for 1 or 2 days for evaporation of solvent
44	Lithography - Alignment & Exposure Olin 907-12 (EVG 20)	Electronic Vision Group 20 Mask Aligner • Hg-lamp: 12 mW/cm² • Exposure Time: 3.5 sec	Mask: Reflector Soft contact
45	Lithography - Development Olin Resist	Developer: OPD4262 • After Exposure Bake (120 °C): 60 sec Development: • Time: 30 sec in Beaker 1 • Time: 15-30 sec in Beaker 2 • Quick Dump Rinse <0.1 µS • Spin drying	Do NOT bake
46	Optical microscopic inspection - Lithography	Microscope	
47	Lithography - Development Olin Resist	Developer: OPD4262 • After Exposure Bake (120 °C): 60 sec Development: • Time: 30 sec in Beaker 1 • Time: 15-30 sec in Beaker 2 • Quick Dump Rinse <0.1 µS • Spin drying	For Al removal Do NOT bake Do NOT rinse with water Etch rate: 14~20 nm/min
48	Stripping of Olin PR in Aceton	Aceton VLSI: MERCK • Method: Spray 5 sec • Spin drying • Visual microscopic inspection	
49	Lithography - Coating SU-8 foil	Laminator • Temperature: 80 °C • Speed: 2 • Bake: 5 min at 65 °C	Do NOT bake
50	Lithography - Alignment & Exposure (EVG)	Electronic Vision Group 20 Mask Aligner • Hg-lamp: 12 mW/cm² • Exposure Time: 110 sec	Mask: Pores Soft contact
51	Lithography - Development SU-8 100	Developer: RER600 • After Exposure Bake: 10 min at 50 °C 10 min at 65 °C 50 min at 75 °C cool down in 5 °C steps each for 5 min Development: • Time: 20 min • Method: Ultrasonic bath • IPA Rinse	Do not rinse with water It is better to dice the chips before this step and develop individually using ultrasonic bath

		• Spin drying	
52	Etching HF (1%)	HF (1%) VLSI: MERCK • Quick Dump Rinse <0.1 µS • Spin drying	Time: >1 min
53	XeF_2 Etching of Silicon	HF (1%) VLSI: MERCK • Expansion Chamber Temp.: 40 °C • Chamber Temp.: 35 °C • Pressure: 3 Torr • Step Time: 30 sec	~10 steps

Table III. *The process document for fabrication of laterally moving hairs (BooT)*

Step	Process	Parameters	Remarks
01	Substrate selection - Silicon <100> SSP (low resistance)	Orientation: <100> Diameter: 100mm Thickness: 525 +/- 25 µm Polished: Single side Resistivity: 0.010-0.015 Ω·cm Type: p	Substrate should be grounded Number of Dummies: ?
02	Cleaning Standard	HNO_3 (100%) Selectipur: MERCK HNO_3 (69%) VLSI: MERCK • Beaker 1: fumic HNO_3 (100 %), 5 min • Beaker 2: fumic HNO_3 (100 %), 5 min • Quick Dump Rinse <0.1 µS • Beaker 3: boiling (95 °C) HNO_3 (69 %), 10 min • Quick Dump Rinse <0.1 µS • Spin drying	Start from beaker 2
03	Lithography - Priming (liquid)	HexaMethylDiSilazane (HMDS) • Dehydration bake (120 °C): 5 min • Spin program: 4 (4000 rpm, 20 sec)	
04	Lithography - Coating Olin907-17	• Spinning acceleration: 4000 rpm/s • Spinning speed: 4000 rpm • Spinning time: 20 s • Prebake (95 °C): 90 s	Wait 30 min before exposure to avoid stiction
05	Lithography - Alignment & Exposure Olin 907-17 (EVG 20)	Electronic Vision Group 20 Mask Aligner • Hg-lamp: 12 mW/cm² • Exposure Time: 3.5 sec	Mask: Anchor Soft contact
06	Lithography - Development Olin Resist	Developer: OPD4262 • After Exposure Bake (120 °C): 60 sec Development: • Time: 30 sec in Beaker 1 • Time: 15-30 sec in Beaker 2 • Quick Dump Rinse <0.1 µS • Spin drying	No Post Bake required because reflow of the resist decreases the resolution

<table>
<tr><td>07</td><td>Optical microscopic inspection - Lithography</td><td>Microscope</td><td></td></tr>
<tr><td>08</td><td>Plasma etching of Si
B-ADIX</td><td>Adixen AMS 100 SE
See MIS homepage for etch profile
<table><tr><th>Parameters</th><th>Etch</th><th>Deposition</th></tr><tr><td>Gas</td><td>SF_6</td><td>C_4F_8</td></tr><tr><td>Flow(sccm)</td><td>300</td><td>150</td></tr><tr><td>Time sec</td><td>7</td><td>2</td></tr><tr><td>Priority</td><td>2</td><td>1</td></tr><tr><td>APC %</td><td>25</td><td>25</td></tr><tr><td>ICP Watt</td><td>1800</td><td>1800</td></tr><tr><td>CCP Watt (LF)</td><td>80</td><td>80</td></tr><tr><td>Pulsed (LF) ms.</td><td>10on/90off</td><td>10on/90off</td></tr><tr><td>He mBar</td><td>10</td><td>10</td></tr><tr><td>SH mm</td><td>200</td><td>200</td></tr><tr><td>Electrode temp. °C.</td><td>10</td><td>10</td></tr></table></td><td>Depth: 60 to 70 µm
Etch rate must be determined in each run
Use patterned dummy wafers
Uniformity is important
Time: ~13 min</td></tr>
<tr><td>09</td><td>Stripping of Olin PR by oxygen plasma</td><td>Tepla 300
Barrel Etcher (2.45 GHz)
Ultra clean system only (no metals except Al)
• See list with recipes in CR
• O_2 flow: 200 sccm (50 %)
• Power: up to 1000 W
• Pressure: 1 mbar
• Time: see recipes on the wall</td><td>Program 06</td></tr>
<tr><td>10</td><td>Cleaning Standard</td><td>HNO_3 (100%) Selectipur: MERCK
HNO_3 (69%) VLSI: MERCK
• Beaker 1: fumic HNO_3 (100 %), 5 min
• Beaker 2: fumic HNO_3 (100 %), 5 min
• Quick Dump Rinse <0.1 µS
• Beaker 3: boiling (95 °C) HNO_3 (69 %), 10 min
• Quick Dump Rinse <0.1 µS
• Spin drying</td><td></td></tr>
<tr><td>11</td><td>Dry Oxidation (DOX) at 800 °C of Silicon</td><td>Standby temperature: 800°C
• Program: DOX-800
• Temp.: 800°C
• Gas: O_2
• Flow: 4 l/min</td><td>For Fluorocarbon removal
Time: 30 min in B3</td></tr>
<tr><td>12</td><td>Etching HF (50%) SiO_2</td><td>HF (50%) VLSI: MERCK
• Etch time: >1 min
• Quick Dump Rinse <0.1 µS
• Spin drying</td><td>For Fluorocarbon removal
Time: ~1 min</td></tr>
<tr><td>13</td><td>Dry Oxidation (DOX) at</td><td>Standby temperature: 800 °C
• Program: DOX-1100</td><td>Thickness: 150 nm</td></tr>
</table>

	1100 °C of Silicon	• Temp.: 1100 °C • Gas: O_2 • Flow: 4 l/min	Time: ~53 min
14	Ellipsometer Measurement	Thin Film Mapper	
15	Micro Balance Measurement	Satotius Micro Balance	
16	LPCVD Poly Si - 590°C	Tempress LPCVD/HC Tube: G1 SiH_4 flow: 50 sccm temperature: 590 °C pressure: 250 mTorr • Program: Poly590C deposition rate: 5.5-7.5 nm/min	Use blank dummies Two days deposition Thickness: 3 µm It must close the trenches! With F2, 15h, 3.3 nm/min
17	Micro Balance Measurement	Satotius Micro Balance	For 4" wafer poly deposition $\delta(nm)=26.5\times\Delta m(mg)$
18	Annealing	Furnace B3 Standby temperature: 800 °C • Program: ANN-1050-N2 • Temp.: 1050 °C • Gas: N_2 • Flow: 1 l/min • Ramp: 20 °C/min	To lower stress Time: 2 hrs
19	Etching HF (1%) Native Oxide	HF (1%) VLSI: MERCK • Etch time: >1 min • Quick Dump Rinse <0.1 µS • Spin drying	
20	Solid Source Diffusion (SSD) of Boron at 1100°C	Furnace B1 Standby temperature: 700 °C • Program: SSD-1100 • Temp.: 1100 °C • Gas N_2: 3.80 SLM • Gas O_2: 0.20 SLM • Time:	Time: 60 min
21	Etching BHF (1:7) SiO_2	NH_4F:HF (1:7) VLSI: MERCK • Quick Dump Rinse <0.1 µS • Spin drying Etch rate thermal SiO_2 = 60-80 nm/min Etch rate PECVD SiO_2 = 125 nm/min Etch rate TEOS SiO_2 = 180 nm/min	10 min, wafer should be white and no colour rings should be present (B_2O_5 removal) Time: ~1 hr
22	Cleaning Standard	HNO_3 (100%) Selectipur: MERCK HNO_3 (69%) VLSI: MERCK • Beaker 1: fumic HNO_3 (100 %), 5 min • Beaker 2: fumic HNO_3 (100 %), 5 min • Quick Dump Rinse <0.1 µS • Beaker 3: boiling (95 °C) HNO_3 (69 %), 10 min • Quick Dump Rinse <0.1 µS • Spin drying	

23	Dry Oxidation at 800°C of Silicon	Furnace B3 Standby temperature: 800 °C • Program: DOX-800 • Temp.: 800 °C • Gas: O_2 • Flow: 4 l/min	Removal of residues Time: 30 min
24	Etching BHF (1:7) SiO_2	NH_4F:HF (1:7) VLSI: MERCK • Quick Dump Rinse <0.1 µS • Spin drying Etch rate thermal SiO_2 = 60-80 nm/min Etch rate PECVD SiO_2 = 125 nm/min Etch rate TEOS SiO_2 = 180 nm/min	Time: 1 hr
25	Cleaning Standard	HNO_3 (100%) Selectipur: MERCK HNO_3 (69%) VLSI: MERCK • Beaker 1: fumic HNO_3 (100 %), 5 min • Beaker 2: fumic HNO_3 (100 %), 5 min • Quick Dump Rinse <0.1 µS • Beaker 3: boiling (95 °C) HNO_3 (69 %), 10 min • Quick Dump Rinse <0.1 µS • Spin drying	or short
26	PECVD of SiO_2 (Oxford)	Oxford Plasmalab 80 + Multi-user system Apply purge sequence before and after use Purge sequence: 1 min N_2, pump down, apply three times Paramters: • Electrode temp. = 300 °C • 2% SiH_4/N_2 flow = 200 sccm • N_2O flow = 710 sccm • Pressure = 650 mTorr • APC = 33 • Power = 60 W LF • Capacitor = 850 • Deposition rate= 37 nm/min	Thickness: 1 µm Oxide capping mask on front side It is possible to use TEOS as capping as well
27	Annealing at 800 °C with N_2	Furnace B3 Standby temperature: 800 °C • Program: ANN800C • Temp.: 800 °C • Gas: N_2 • Flow: 1 l/min • Ramp: 10 °C/min	H_2 degassing
28	Annealing at 1050 °C with N_2 for diffusion of B or P	Furnace B3 Standby temperature: 800 °C • Program: ANN1050C • Temp.: 1050 °C • Gas: N_2 • Flow: 1 l/min • Ramp: 10 °C/min	For uniform boron distribution
29	Etching BHF (1:7) SiO_2	NH_4F:HF (1:7) VLSI: MERCK • Quick Dump Rinse <0.1 µS • Spin drying	Time: 12 min

<table>
<tr><td></td><td></td><td>Etch rate thermal SiO_2 = 60-80 nm/min
Etch rate PECVD SiO_2 = 125 nm/min
Etch rate TEOS SiO_2 = 180 nm/min</td><td></td></tr>
<tr><td>30</td><td>Sheet Resistance measurement</td><td>Resistance Measurement Equipment</td><td>$R_{sheat}=R_{meas}\cdot\pi/\ln(2)=4.532\cdot R_{meas}$ Ω/□
$\rho=R_{sheat}/\text{thikness}<0.02$ Ω·cm</td></tr>
<tr><td>31</td><td>Lithography - Priming (liquid)</td><td>HexaMethylDiSilazane (HMDS)
• Dehydration bake (120 °C): 5 min
• Spin program: 4 (4000 rpm, 20 sec)</td><td></td></tr>
<tr><td>32</td><td>Lithography - Coating Olin907-17</td><td>• Spinning acceleration: 4000 rpm/s
• Spinning speed: 4000 rpm
• Spinning time: 20 s
• Prebake (95 °C): 90 s</td><td>Wait 30 min before exposure to avoid stiction</td></tr>
<tr><td>33</td><td>Lithography - Alignment & Exposure Olin 907-17 (EVG 20)</td><td>Electronic Vision Group 20 Mask Aligner
• Hg-lamp: 12 mW/cm²
• Exposure Time: 3.5 sec</td><td>Mask: Isolation
Soft contact</td></tr>
<tr><td>34</td><td>Lithography - Development Olin Resist</td><td>Developer: OPD4262
• After Exposure Bake (120 °C): 60 sec
Development:
• Time: 30 sec in Beaker 1
• Time: 15-30 sec in Beaker 2
• Quick Dump Rinse <0.1 µS
• Spin drying</td><td>No Post Bake required because reflow of the resist decreases the resolution</td></tr>
<tr><td>35</td><td>Optical microscopic inspection - Lithography</td><td>Microscope</td><td></td></tr>
<tr><td>36</td><td>Plasma etching of Si B-HARS-1</td><td>Adixen AMS 100 SE
See MIS homepage for etch profile
<table><tr><th>Parameters</th><th>Etch</th><th>Deposition</th></tr><tr><td>Gas</td><td>SF_6</td><td>C_4F_8</td></tr><tr><td>Flow(sccm)</td><td>250</td><td>200</td></tr><tr><td>Time sec</td><td>3</td><td>1</td></tr><tr><td>Priority</td><td>2</td><td>1</td></tr><tr><td>APC %</td><td>100</td><td>100</td></tr><tr><td>ICP Watt</td><td>1500</td><td>1500</td></tr><tr><td>CCP Watt (LF)</td><td>80</td><td>80</td></tr><tr><td>Pulsed (LF) ms.</td><td>10on/90off</td><td>10on/90off</td></tr><tr><td>He mBar</td><td>10</td><td>10</td></tr><tr><td>SH mm</td><td>200</td><td>200</td></tr><tr><td>Electrode temp.°C.</td><td>10</td><td>10</td></tr><tr><td>Er Olin907</td><td>25-50 nm/min</td><td></td></tr></table></td><td>Or B-ADIX
Depth: ~3 µm; to reach the SiO_2 underneath
Etch rate must be determined in each run!
Use patterned dummy wafers
Uniformity is important
Time: ~71 s
It is not critical if etch into silicon substrate</td></tr>
</table>

		Er silicon | 1-5 µm/min	
37	Stripping of Olin PR by oxygen plasma	Tepla 300 Barrel Etcher (2.45 GHz) Ultra clean system only (no metals except Al) • See list with recipes in CR • O_2 flow: 200 sccm (50 %) • Power: up to 1000 W • Pressure: 1 mbar • Time: see recipes on the wall	Program 06
38	Cleaning Standard	HNO_3 (100%) Selectipur: MERCK HNO_3 (69%) VLSI: MERCK • Beaker 1: fumic HNO_3 (100 %), 5 min • Beaker 2: fumic HNO_3 (100 %), 5 min • Quick Dump Rinse <0.1 µS • Beaker 3: boiling (95 °C) HNO_3 (69 %), 10 min • Quick Dump Rinse <0.1 µS • Spin drying	
39	Dry Oxidation (DOX) at 1100 °C of Silicon	Standby temperature: 800 °C • Program: DOX-1100 • Temp.: 1100 °C • Gas: O_2 • Flow: 4 l/min	Thickness: 120 nm Time: ~60 min
40	Cleaning Standard	HNO_3 (100%) Selectipur: MERCK HNO_3 (69%) VLSI: MERCK • Beaker 1: fumic HNO_3 (100 %), 5 min • Beaker 2: fumic HNO_3 (100 %), 5 min • Quick Dump Rinse <0.1 µS • Beaker 3: boiling (95 °C) HNO_3 (69 %), 10 min • Quick Dump Rinse <0.1 µS • Spin drying	
41	Lithography - dehydration SU-8	Hotplate • 2 hrs at 120 °C	Time: 10-30 min
42	Lithography - Coating SU-8 2 (Delta20)	Süss MicroTec Spinner Delta 20 • Spin program: 5 10 sec at 500 rpm, acc. 100 rpm/min 30 sec at 3000 rpm, acc. 100 rpm/min • Thickness: 5 µm • Prebake: 2 min at 95 °C	Wait >1 hr before exposure to avoid stiction
43	Lithography - Alignment & Exposure SU-8 2 (EVG)	Electronic Vision Group 20 Mask Aligner • Hg-lamp: 12 mW/cm^2 • Exposure Time: 10 sec	Mask: Shuttle Soft contact
44	Lithography - Development SU-8 2	Developer: RER600 • After Exposure Bake: 3 min at 95 °C Development: • Time: 2 min • Method: Immersion • IPA Rinse • Spin drying	

<table>
<tr><td>45</td><td>Plasma cleaning (Etske)</td><td>Elektrotech PF310/340
Clean chamber
Styros electrode
• Electrode temp.: 10 °C
• O_2 flow: 20 sccm
• pressure: 0 mTorr
• power: 50 W
Etch rate SU-8 = 150 nm/min</td><td>Removal of Residues
Time: 4:15 min:sec</td></tr>
<tr><td>46</td><td>Optical microscopic inspection - Lithography</td><td>Microscope</td><td>Check; if SU-8 residues are in the lines do previous step again</td></tr>
<tr><td>47</td><td>Plasma etching of SiO_2
C-Nitride</td><td>Adixen AMS 100 SE
See MIS homepage for etch profile
<table><tr><th>Parameters</th><th>Etch</th></tr><tr><td>Gas Ar (sccm)</td><td>100</td></tr><tr><td>Gas CHF_3 (sccm)</td><td>100</td></tr><tr><td>APC %</td><td>100</td></tr><tr><td>ICP Watt</td><td>1200</td></tr><tr><td>CCP Watt (LF)</td><td>150</td></tr><tr><td>He mBar</td><td>10</td></tr><tr><td>SH mm</td><td>200</td></tr><tr><td>Electrode temp. °C.</td><td>-100</td></tr></table></td><td></td></tr>
<tr><td>48</td><td>Plasma etching of Si
C-Cryo 500</td><td>Adixen AMS 100 SE
See MIS homepage for etch profile
<table><tr><th>Parameters</th><th>Etch</th></tr><tr><td>Gas SF_6 (sccm)</td><td>100</td></tr><tr><td>Gas O_2 (sccm)</td><td>10</td></tr><tr><td>APC %</td><td>100</td></tr><tr><td>ICP Watt</td><td>500</td></tr><tr><td>CCP Watt (LF)</td><td>20</td></tr><tr><td>Pulsed (on/off)</td><td>20/80</td></tr><tr><td>He mBar</td><td>10</td></tr><tr><td>SH mm</td><td>200</td></tr><tr><td>Electrode temp. °C.</td><td>-100</td></tr></table></td><td></td></tr>
<tr><td>49</td><td>Plasma etching of SiO_2
C-Nitride</td><td>See step 47</td><td></td></tr>
<tr><td>50</td><td>Stripping of SU-8 PR by oxygen plasma</td><td>Tepla 300
Barrel Etcher (2.45 GHz)
Ultra clean system only (no metals except Al)
• See list with recipes in CR</td><td>Program 06</td></tr>
</table>

		• O_2 flow: 200 sccm (50 %) • Power: up to 1000 W • Pressure: 1 mbar • Time: see recipes on the wall	
51	Cleaning Standard	HNO_3 (100%) Selectipur: MERCK HNO_3 (69%) VLSI: MERCK • Beaker 1: fumic HNO_3 (100 %), 5 min • Beaker 2: fumic HNO_3 (100 %), 5 min • Quick Dump Rinse <0.1 µS • Beaker 3: boiling (95 °C) HNO_3 (69 %), 10 min • Quick Dump Rinse <0.1 µS • Spin drying	
52	Dry Oxidation (DOX) at 1100 °C of Silicon	Standby temperature: 800 °C • Program: DOX-1100 • Temp.: 1100 °C • Gas: O_2 • Flow: 4 l/min	Thickness: 50 nm Time: ~20 min
	Al wires (if necessary)		
	Cleaning Standard	HNO_3 (100%) Selectipur: MERCK HNO_3 (69%) VLSI: MERCK • Beaker 1: fumic HNO_3 (100 %), 5 min • Beaker 2: fumic HNO_3 (100 %), 5 min • Quick Dump Rinse <0.1 µS • Beaker 3: boiling (95 °C) HNO_3 (69 %), 10 min • Quick Dump Rinse <0.1 µS • Spin drying	
	Lithography - dehydration SU-8	Hotplate • 2 hrs at 120 °C	Time: 30 min
53	Lithography - Coating SU-8 100 (Delta20)	Süss MicroTec Spinner Delta 20 • Spin program: 6 30 sec at 500 rpm, acc. 100 rpm/min 30 sec at 2500 rpm, acc. 100 rpm/min • Thickness: ~200 µm • Prebake (95 °C): 10 min at 50 °C 30 min at 65 °C 120 min at 95 °C let it cool down on the hot plate	First Layer Leave the wafers on the flat surface of the hot plate for 2 hrs before soft bake Wait overnight before exposure to avoid stiction (and use tape on the mask)
54	Lithography - Alignment & Exposure SU-8 100 (EVG)	Electronic Vision Group 20 Mask Aligner • Hg-lamp: 12 mW/cm² • Exposure Time: 60 sec	Mask: Hair I Soft contact
55	Lithography - Coating SU-8 100 (Delta20)	Süss MicroTec Spinner Delta 20 • Spin program: 8 30 sec at 500 rpm, acc. 100 rpm/min 30 sec at 1000 rpm, acc. 100 rpm/min • Thickness: >380 µm • Prebake (95 °C): 10 min at 50 °C 30 min at 65 °C 300 min at 95 °C	Second Layer Leave the wafers on the flat surface of the hot plate for 2 hrs before soft bake Wait overnight before exposure to avoid stiction (and use tape on the mask)

		let it cool down on the hot plate	
56	Lithography - Alignment & Exposure SU-8 100 (EVG)	Electronic Vision Group 20 Mask Aligner • Hg-lamp: 12 mW/cm² • Exposure Time: 70 sec	Mask: Hair II Soft contact
57	Lithography - Development SU-8 100	Developer: RER600 • After Exposure Bake: 10 min at 50 °C 10 min at 65 °C 50 min at 75 °C cool down in 5 °C steps each for 5 min Development: • Time: 20 min • Method: Spray • IPA Rinse • Spin drying	Do not rinse with water Do not use high speed spin drying
49	Plasma etching of SiO_2 C-Nitride	See step 47	
54	XeF_2 Etching of Silicon	HF (1%) VLSI: MERCK • Expansion Chamber Temp.: 40 °C • Chamber Temp.: 35 °C • Pressure: 3 Torr • Step Time: 30 sec	~5 steps

Acknowledgement

"Life moves pretty fast. If you don't stop and look around once in a while, you could miss it.[1]" And there it is; the end of an experience of four years as a graduate student. I have had a great time in MicMac, an experience to treasure.

There are so many whom I should thank here; people who have affected my life in some way. In fact so many whom I have not met at all. I can start counting them from the day I was born. I am grateful to all of them and feel that I owe this to them. Naturally, I would like to name a few here.

First of all is my supervisor, Gijs. Thank you for your support, your guidance, patience, intensive discussions we have had and all you have taught me; and for the freedom you gave me to follow my path while showing me the pitfalls. I have always envied your broad knowledge and command of the subject discussed, scholarly or else.

Then are other MicMac-ers: Remco W., Theo, Meint and Erwin; for the time you always spent whenever I knocked on your door, for your invaluable help and share of experience. Joost and Vitaly; for taking the time to completely and precisely explain physics to me when I thought it is weird or too complicated. I wish I could teach like you. Marcel D.; for all your help and being such a nice office-mate. The way you work has always inspired me. Remco S. and Henk; for always being there to help and provide all that was needed in the lab. Kees; for spending your time in the cleanroom and for helping me out with the car. Marcel K.; for all I have learned from you about measurements. Once in a while I still ask myself "ben ik AIO of …". Susan and Satie; for restlessly taking care of virtually every type of administration and doing more than was your job. I would have been certainly lost without your kindness. Ahmed and Harmen; for our fruitful conversations. Robert; for translating the summary of the thesis to Dutch. Shahina; for your pleasant company. I shall never forget your insightful demonstration of noise. Ram; for your unmatched friendship which I wish to hold forever. It was always nice to hear you ask "which machine Nima?" Henry, Mubassira, Yiping, Hadi and Narges and the rest of the TST group. I should also mention the MESA+ cleanroom staff who were always more than helpful and all the

[1] From the movie "Ferris Bueller's Day Off" 1986

committee members. Then of course my friends, Amir, Waqqar, Irene, Esly, Andre, Somy, Saba, Robin and all the rest with whom I hardly ever felt homesick. I am very thankful to Anna for designing the cover in such a short notice. I should also thank my parents and Golnar, my sister, whose loving support reaches me easily over the long distance.

And then you, my dear Katja. Your presence in my life brings me more than I can mention or even count. Your constant encouragements and understanding made the Ph.D. crusade not bearable but pleasant. When asked what I have done, I always say "was making parking sensors for submarines", repeating you. So here, all of this to your smile.

I cannot say that this work has finished; actually it has just begun. But anyway "Dissertations are not finished; they are abandoned."[2]

[2] Fred Brooks